UNIVERSITY OF THE FREE STATE
UNIVERSITEIT VAN DIE VRYSTAAT
YUNIVESITHI YA FREISTATA

# Monte Carlo evaluation of the dose perturbation effect of various hip prostheses during pelvic megavoltage photon radiotherapy


**Department of Medical Physics**

**School of Medicine**

**Faculty of Health Sciences**

**University of the Free State**


A dissertation submitted in fulfilment of the requirements for the degree of

**Master of Medical Science in Medical Physics**

by


**Courage Mahuvava**

Supervisor: Dr. F.C.P du Plessis


07 November 2016

# Abstract

**Introduction:** Hip prostheses (HPs) are routinely used in hip augmentation surgery to replace painful or dysfunctional hip joints, especially in the elderly population. A number of patients with HPs are undergoing pelvic radiotherapy (RT) for localised prostate cancer. However, radiographic discrepancies between high-density and high-atomic-number (Z) inserts and surrounding tissue may cause considerable dose perturbations within the target volume and in regions where tissues interface with the prosthetic device. Furthermore, conventional treatment planning systems (TPSs) do not accurately predict dose effects incurred around metallic implants. Therefore, concerns regarding dose inhomogeneities near the prosthesis always arise, especially in patients with bilateral hip prostheses (bHPs) who require teletherapy of prostate cancer, where the tumour typically lies between the prostheses. The aim of this study was to evaluate the dosimetric effect of various HPs during 3D conformal prostate RT using Monte Carlo (MC) simulations.

**Materials and methods:** The MC radiation transport simulation user-code BEAMnrc was used to simulate an Elekta Prec*i*se linear accelerator (linac) head, based on the manufacturer's specifications. The MC linac model was validated by comparing dosimetric features including depth dose and dose profile data simulated in a cubic water tank (WT) with measured values. DOSXYZnrc was used to calculate 3D absorbed dose distributions in a CT based phantom (patient model) with and without HPs. Simulations were performed for 6, 10, 15 and 20 MV conformal photon beams using different beam arrangements. Three treatment plans were generated by XiO TPS and incorporated into MC simulations: a four–field (4F) box plan, a five–field (5F) plan and a six–field (6F) plan. The planning target volume (PTV) was generated by a 1 cm expansion of the prostate alone. The HP materials used were stainless steel (SS316L), titanium (Ti6Al4V) and ultra-high-molecular-weight-polyethylene (UHMWPE). These prosthetic models were manually drawn into the CT dataset from actual CT images of the patient pelvis using MCSHOW graphical user interface (GUI). The prosthesis was made part of the patient using a locally-developed Interactive Data Language (IDL) code that converts the density of the drawn volume into the desired HP material density. Both unilateral and bilateral models were considered in the simulations and dose perturbation factors (DPFs) were calculated on the proximal and distal interfaces of the implant. The dose reduction in the PTV as well as the dose to critical organs was also evaluated.

**Results:** Results indicated that the central axis depth dose within and beyond the inhomogeneity drops significantly due to beam attenuation. For patients with bHPs, the dose contribution from lateral ports at 6 MV was attenuated by up to 23% and 17% for SS316L and Ti6Al4V, respectively. For a unilateral HP (uHP), the respective dose attenuations were 19% and 12%. The dose perturbation was always < 1% for a patient fitted with UHMWPE. Up to 38% dose increase was found at the proximal bone–HP interface due to backscattered electrons from the metal implant. There was a weak dependence of dose distribution on beam energy at the target isocenter, with the maximum dose reduction ranging only from 22.8 to 16.9% from 6 to 20 MV in a patient with bilateral steel HPs. However, interface effects were more pronounced at higher beam energies. However, increasing the number of treatment beams improved the plan quality. The greatest PTV dose perturbation was observed in a 4F box and lowest in a 6F plan. Production of scatter radiation was found to be larger for backscatter compared to forward scatter in this study.

**Conclusions:** The dose perturbation effect of metallic HPs is significant and must be taken into account during treatment planning. UHMWPE poses no significant dose perturbation in the shadow of the implant and on the interface with tissue or bone. The use of MC–based TPSs is recommended for treatments using beam portals passing through HPs. MCSHOW allows the addition of HP contours in the virtual phantom from CT dataset of a patient without a HP. This allows one to carry out MC calculations for several implant models without metal artefacts. Results also highlight the significant influence of the implant's composition and the beam position relative to the HP as well as beam energy on the dose distribution. Increasing the beam energy may help overcome the attenuation effects of metallic HPs and to improve target coverage. Therefore this study recommends plans with a larger number of beams that would allow avoiding the hip inhomogeneity in order to effectively compensate for dose attenuated in fields passing through HPs. It is also evident from the results that the shadowing effect is density-dependent, and its maximum value is for the SS316L HP. A more sophisticated, non-coplanar beam orientation may be necessary to avoid the HPs whilst sparing organs at risk (OARs) and giving sufficient target coverage.

***Key words*:** Prostate cancer, Hip prosthesis, Pelvic radiotherapy, Dose perturbation, Treatment planning, Monte Carlo.

# Abstrak

**Inleiding:** Heup prostese (HPS) word gereeld gebruik in heupvervanging chirurgie om pynlike of abnormale heupgewrigte te vervang, veral in die bejaarde bevolking. 'n Aantal pasiënte met HPS ondergaan bekken bestraling (RT) vir gelokaliseerde prostaat of servikskanker. Dit kan egter radiografiese verskille veroorsaak tussen ‘n hoë-digtheid materiaal met 'n hoë atoomgetal (Z) en omliggende weefsel. Die effek veroorsaak aansienlike dosis versteurings binne die teiken volume. Konvensionele behandeling beplanning stelsels (BPSs) bereken dosis effekte nie akkuraat rondom metaal inplantings nie. Daarom bestaan daar kommer oor dosis nie-homogeniteite naby die prostese, veral in pasiënte met bilaterale heup prostese (bHPs) wat teleterapie van prostaatkanker ontvang, waar die gewas gewoonlik tussen die prostese geleë is. Die doel van hierdie studie is om die dosimetriese effek van verskillende HPS tydens 3D konforme prostaat bestraling met behulp van Monte Carlo (MC) simulasies te evalueer.

**Materiale en metodes:** Die MC bestralingstransport simulasie kode, BEAMnrc, is gebruik om 'n Elekta Precise lineêre versneller (linac) se kop na te boots, en is gebaseer op die vervaardiger se spesifikasies. Die MC linac model is getoets deur dit te vergelyk met diepte dosis en dosis profiel data soos gesimuleer in 'n kubiese waterbad (WB) en gemete waardes. DOSXYZnrc is gebruik om 3D geabsorbeerde dosis te bereken in 'n RT-gebaseerde fantoom (pasiënt model) met en sonder HPS. Simulasies is uitgevoer vir 6, 10, 15 en 20 MV foton velde met verskillende kofigurasies. Drie behandelingsplanne is opgestel deur ‘n Xio BPS naamlik 'n vier-veld (4F) kubiese plan, 'n vyf-veld (5F) plan en 'n ses-veld (6F) plan. Die beplannings parameters vanaf XiO is in die MC simulasies gebruik vir die studie. Die beplannings teiken volume (PTV) is gegenereer deur 'n 1 cm uitbreiding van die prostaatrand. Die HPS materiaal was vlekvrye staal (SS316L), titanium (Ti6Al4V) en ultra-hoë-molekulêre gewig-poliëtileen (UHMWPE). Hierdie prostetiese modelle is ingetrek in die RT beelde vanaf werklike RT beelde van die pasiënt pelvis, met behulp van die MCSHOW grafiese gebruikerskoppelvlak (GGK). Die prostese is deel van die pasiënt gemaak met behulp van 'n plaaslik ontwikkelde Interaktiewe Data vertaler kode (IDL) wat die digtheid van die gemete volume in die gewenste HPS materiaal digtheid omskakel. Beide eensydige en bilaterale modelle is oorweeg in die simulasies en dosis versteuringsfaktore (DVFs) is bereken op grond van die proksimale en distale koppelvlakke van die inplanting. Die vermindering in dosis in die PTV sowel as die dosis om kritieke organe is ook geëvalueer.

**Resultate:** Die resultate dui daarop dat die diepte dosis binne en buite die nie-homogeniteit beduidend val weens bundel attenuasie. Vir pasiënte met bHPs, is die dosis bydrae deur laterale velde op 6 MV verswak met tot 23% en 17% vir SS316L en Ti6Al4V, onderskeidelik. Vir 'n enkele HPS, was die dosis verswakking 19% en 12% onderskeidelik. Die dosis versteuring was < 1% vir 'n pasiënt wat toegerus is met UHMWPE HPS. Tot ‘n 38% verhoogde dosis is gevind by die proksimale been–HPS–koppelvlak te danke aan terug verstrooide elektrone van die metaal inplanting. Daar was 'n geringe afhanklikheid van die verspreiding van dosis op m.b.t bundel energie by die beplannings teiken geleë by die iso-senter, met die maksimum dosis verlaging wat wissel tussen 22,8 tot 16,9% van 6 tot 20 MV in 'n pasiënt met bilaterale staal HPS. Koppelvlak effekte was egter meer opgemerk teen hoër straal energie. ‘n Toename van die aantal behandelings velde het die plan gehalte verbeter. Die grootste PTV dosis versteurings is waargeneem in 'n 4F kubus en laagste in 'n 6F plan. Die produksie van verstrooide strale was geneig om meer te wees a.g.v die prostese soos vergelyk met fotone wat voorwaarts verstrooi.

**Gevolgtrekkings:** Die dosis versteurings effek van metaal HPs is betekenisvol en moet tydens die behandeling beplanning in ag geneem word. UHMWPE het geen beduidende dosis versteuring in die skaduwee van die inplanting en op die koppelvlak met weefsel of been nie. Die gebruik van MC-gebaseerde BHP word aanbeveel waar stralings behandelings gebruik word wat deur HPS beweeg. MCSHOW stel ons instaat om HP kontoere op die RT data van die pasient toe tevoeg. Dit stel ons in staat om MC berekeninge vir 'n paar inplanting modelle uit te voer sonder metaal artefakte. Resultate beklemtoon die belangrike invloed van die inplanting se samestelling en die veld posisie relatief tot die HPS asook bundel energie op die verspreiding dosis. Die verhoging van die bundel energie kan ons help om die attenuasie effek van metaal HPS te oorkom en om teikendosis te verbeter. Hierdie studie beveel aan planne met meer velde om nie-homogeniteite te omseil wat vir bundel attenuasie verantwoordelik is soos HPS. Dit is ook duidelik uit die resultate dat die grootste effek die digtheidsafhanklik is en dat sy maksimum waarde is vir die SS316L HP. 'n Meer gesofistikeerde, nie-saamvlakkige dosis oriëentasie mag nodig wees om die HPS vermy, terwyl organe bespaar word.

***Sleutel woorde*:** Prostaatkanker, Heup prostese, Pelvis bestraling, Dosis storing, beplanning van behandeling, Monte Carlo.

# Acknowledgements

Research is never done alone. First and foremost, I would like to thank Almighty God for granting me the opportunity to conduct this study, and because of His providence throughout my research work, I have been able to successfully complete this degree.

The following document summarizes a two-year's worth of effort, frustration and achievement. However, apart from my personal efforts, the successful completion of this dissertation is attributed to the extensive support and assistance from several people and I take this opportunity to express my gratitude to everyone who has been instrumental in the development of this project.

I would like to express my special appreciation for the effort put forth by my supervisor Dr. F.C.P du Plessis for his continuous guidance, motivation, charisma and patience, not to mention his unsurpassed knowledge in computational dosimetry. I particularly thank him for teaching me "how independent research should be conducted" and for his insightful comments about my research work, which have been the primary resource for getting my research focus on the right track. One could simply not wish for a better supervisor.

I also owe my deepest gratitude to Prof. W.I.D Rae for entrusting me to pursue this interesting study and for his ever readiness to respond to my personal issues and queries so promptly. He has been very generous with his time and provided invaluable advice on academic issues.

Working with a team of research scientists at Universitas Academic Hospital Annex has been a great privilege, and I take this opportunity to thank the medical physics research team: Dr. F.C.P du Plessis, Prof. William Rae, Dr. Willie Shaw, Dedri O'Reilly, Lourens Strauss, Jacobus Smit, Itumeleng Setilo, Stalyn Mutsakanyi, Michael Oderinde, Nicholas Ade as well as various interns in the department for the brilliant suggestions they made during our "Tuesday meetings". The exposure and the experience were invaluable and

their unequivocal cooperation and constant source of support has been extremely indispensable to my growth as a research scientist and as a team player. The enthusiasm they had for research was contagious and motivational for me, even during tough times during the research.

I particularly thank Lourens Strauss for helping me to develop 3D conformal radiotherapy (3DCRT) plans for prostate treatment on XiO TPS for use in MC phantom simulations. He also helped me with the development of a FORTRAN code to combine dose files when multiple beams were used during phantom irradiation. A word of thanks also goes to the hospital technician Ben Kriel, who provided me with Elekta Prec*i*se linac specifications and also to the medical physics interns for giving me water tank dose measurement results for standardizing my Monte Carlo linac model.

This research project was funded by the South African Medical Research Council (MRC) with funds from National Treasury under its Economic Competitiveness and Support Package. This research and the publication thereof is the result of funding provided by the MRC of South Africa in terms of the MRC's Flagship Awards Project SAMRC-RFA-UFSP-01-2013/HARD.

I would also like to acknowledge the South African Zimmer Orthopaedics Institute for providing me with the detailed information about the shape, design, positioning and composition of various HPs for use in the CT dataset.

My very profound gratitude also goes to my family for their support while I was away during my studies. Their prayers for me are what sustained me thus far, and my mere expression of thanks cannot suffice. Also special thanks to my friend and Monte Carlo colleague, Stalyn Mutsakanyi, who made my stay away from home pleasant and for sharing ideas with me throughout the duration of our studies.

Finally, I am thankful to all those not mentioned here for their direct or indirect assistance towards fulfilling this Master's programme.

# Declaration

I, *Courage Mahuvava*, declare that the master's research dissertation or interrelated, publishable manuscripts/published articles that I herewith submit at the University of the Free State, is my independent work and that I have not previously submitted it for a qualification at another institution of higher education. I hereby declare that I am aware that the copyright is vested in the University of the Free State. All royalties as regards intellectual property that was developed during the course of and/or in connection with the study at the University of the Free State, will accrue to the University.

# Abbreviations and acronyms

| | |
|---|---|
| 3D | Three-dimensional |
| 4F | Four-field |
| 5F | Five-field |
| 6F | Six-field |
| 3DCRT | Three-dimensional conformal radiation therapy |
| AAPM | American Association of Physicists in Medicine |
| ADAC | Advanced Diagnosis, Automation, and Control |
| AE | Lower electron energy limit for cross section calculation |
| ASCII | American Standard Code for Information Interchange |
| BEV | Beam's eye view |
| BEAMDP | BEAM Data Processor |
| bHP | Bilateral hip prostheses |
| BSDF | Back-scattered dose perturbation factor |
| CAX | Central axis |
| CS | Compton scattering |
| CT | Computed tomography |
| DBS | Directional bremsstrahlung splitting |
| DEF | Dose enhancement factor |
| DICOM | Digital Imaging and Communications in Medicine |
| DRF | Dose reduction factor |
| DVH | Dose volume histogram |
| ECUT | Global electron energy cut-off |
| EGS4/5 | Electron Gamma Shower v4.0/5.0 |
| EGSnrc | Electron Gamma Shower National Research Council of Canada |
| EGSnrcMP | Multi-platform environment for EGSnrc |
| FS | Field size |
| FWHM | Full width at half maximum |

| | |
|---|---|
| GEANT4 | GEometry ANd Tracking 4 |
| GUI | Graphical user interface |
| IAEA | International Atomic Energy Agency |
| ICRU | International Commission on Radiation Units and Measurements |
| IDL | Interactive Data Language |
| IMRT | Intensity modulated radiation therapy |
| KE | Kinetic energy |
| LINAC | Linear accelerator |
| MC | Monte Carlo |
| MCNP | Monte Carlo N-Particle Transport Code |
| MLC | Multi–leaf collimator |
| MRI | Magnetic resonance imaging |
| OAR | Organ at risk |
| OMEGA | Ottawa Madison Electron Gamma Algorithm |
| PCUT | Global photon energy cut–off |
| PDD | Percentage depth dose |
| PEA | Photoelectric absorption |
| PEGS4 | Pre-processor for Electron Gamma Shower v4.0 |
| PENELOPE | Penetration and ENErgy Loss of Positrons and Electrons |
| PP | Pair production |
| PS | Phase space |
| PTV | Planning target volume |
| RT | Radiotherapy/radiation therapy |
| SLAC | Stanford Linear Accelerator Centre |
| THR | Total hip replacement |
| TP | Treatment planning |
| TPS | Treatment planning system |
| UHMWPE | Ultra-high molecular weight polyethylene |
| uHP | Unilateral hip prostheses |

| | |
|---|---|
| VMAT | Volumetric Modulated Arc Therapy |
| Voxel | Volume element |
| WT | Water tank |
| Z | Atomic number |

# Table of contents

# List of figures

# List of tables

# 1. Introduction

## 1.1 Background

Prostate cancer is one of the most frequently diagnosed male malignancies worldwide (Agapito 2001; Su *et al.* 2005). Over 1.1 million new cases were recorded in 2012, and that accounts for 8% of all new cancer cases and 15% in men. The incidence of prostate cancer increases dramatically with age, with more than 90% of cases detected in men over 50 years of age (Martin *et al.* 2012). This older population is furthermore affected by other age-related co-morbidities such as osteoarthritis, for which a common treatment is metallic hip replacement (Rana & Pokharel 2014).

Due to increasing life expectancy, a growing number of patients requiring pelvic RT for localised prostate cancer have unilateral or bilateral hip prostheses. Depending on risk, treatment options for such patients include: radical prostatectomy, interstitial brachytherapy and external beam radiotherapy (Martin *et al.* 2012). In many cases, combinations of these treatment options are applied depending on the clinical protocols used. Such treatments include adjuvant teletherapy following radical prostatectomy to reduce the risk of loco-regional recurrence. This study will focus on prostate external beam radiotherapy. However, this work could equally well apply to all pelvic malignancies (e.g., bladder, rectum, etc.) in the proximity of the femoral heads.

## 1.2 Hip prostheses and pelvic irradiation

External beam radiation therapy of prostate cancer frequently makes use of lateral fields (Ding & Christine 2001). The presence of high-density and high-Z prostheses causes dosimetric calculation errors when setting up a RT treatment plan. This can be attributed to streak artefacts in the CT dataset, radiation attenuation through the prosthesis and alterations in the scatter dose in the neighbourhood of the prosthetic device. This may

create unacceptable dose distributions in the PTV and thus compel planners to compromise between target coverage and avoidance of beam entry through the prostheses (Martin *et al.* 2012).

The American Association of Physicists in Medicine: Radiation Therapy Committee Task Group 63 (AAPM TG 63) report (Reft *et al.* 2003) advocates using special beam arrangements that completely avoid the prosthesis in the beam's eye view (BEV) due to dose calculation uncertainties near the prostheses for most conventional TPSs. While this approach circumvents dosimetric complications due to metallic inhomogeneity, it restricts the choice of exploitable gantry angles, and the resultant dose distributions suffer from poor dosimetric conformality, especially for patients with bHP, since primarily only anterior-posterior beams can be selected. The feasibility of oblique beam orientation is further limited by its escalation of bladder and rectal tissue dose. When gantry angles are limited, dose conformality may be substantially improved by IMRT techniques (Kung *et al.* 2002; Su *et al.* 2005; Rosewall *et al.* 2009).

Therefore, when a prostate carcinoma develops in a patient with prosthetically augmented hips, it is a challenging task to achieve dose uniformity across the PTV without compromising the dose-volume constraints of critical structures contiguous to it. The concern is whether the presence of the prosthesis would impair local tumour control in patients undergoing radical treatment of tumours in the pelvic region because of target dose reduction from shadowing of the prosthesis, or an increase in complication rates due to induced scattered dose by the presence of the radiation exposed metallic implant.

Dose reduction in megavoltage (MV) x-ray beams can be as high as 64% for the target volume on the distal side of the prosthesis (Eng 2000). However, these dose effects may not be accurately predicted in most commercially available TPSs. Actually, only MC simulation has the ability to accurately quantify the dosimetric effect of a HP during RT (Buffard *et al.* 2006).

## 1.3 The Monte Carlo method

Although the physics of particle interactions with matter is well understood, it is generally impossible to develop an analytic expression to describe radiation transport in a medium due to the complex and probabilistic behaviour of radiation in matter. Analytical dose calculations through media can be performed only in very simple geometries and under severe approximations e.g., solving the Boltzmann transport equation. For problems of practical importance, it is therefore necessary to resort to numerical methods. One widely used technique is the MC method, which uses knowledge of probability distributions governing the individual interactions of particles in matter to simulate their individual random trajectories.

MC is a numerical tool commonly used in research areas involving stochastic event modelling e.g., radiation transport in matter, in disciplines such as nuclear medicine, radiation protection, diagnostic radiology, radiation shielding and dosimetry (Andreo 1998; Kafi, Maalej & Naqvi 2006). It is used to model any statistical process by sampling the individual probability distribution of the events that compose the process until the result converges, simulated in a defined geometry of source and medium. Computer–generated random numbers are used to determine which interaction will occur by comparing probabilities (i.e. cross-sections) of each interaction, and each particle is tracked until it deposits all its energy in the medium or escapes from the region of interest (Xu, Chao & Bozkurt 2000).

MC is widely recognized as the most accurate method available in computing dose distributions in non-tissue-equivalent materials. It is particularly useful in heterogeneous regions where the effects of electron/photon transport cannot be accurately handled with conventional, deterministic dose algorithms (Deng *et al.* 2000; Rogers 2002). MC maps the spatial distribution of charged particle energy as a result of primary photon interactions (Mackie, Scrimger, & Battista 1985). It provides a practical way to determine accurate 3D dose distributions in complex, heterogeneous targets such as bone augmented with a

metallic prosthesis where direct measurements are difficult or in some cases impossible to perform (Chetty *et al.* 2007; Deng *et al.* 2000).

The traditionally long calculation times previously associated with MC simulations rendered this method as a clinically unfeasible approach for routine clinical TP. With the development of faster codes optimized for RT calculations, computer processor technology and variance reduction techniques, the MC method is becoming a fast, powerful, and the current state-of-the-art technique in computational dosimetry. This study uses the EGSnrc-based MC user-codes BEAMnrc (Rogers, Walters and Kawrakow 2004) and DOSXYZnrc (Walters, Kawrakow & Rogers 2005) for linac head simulation and dose calculation in the phantom respectively.

## 1.4 Aims of the study

The main aim of this study is to evaluate the dose perturbation in the vicinity of various HPs during high energy conformal x-ray treatment of the prostate using MC simulations. This work adds more current data on the dosimetric effect of titanium, stainless steel and UHMWPE prosthetic hip devices at beam energies 6, 10, 15 and 20 MV.

Since heterogeneous media is introduced into the patient-CT phantom in a synthetic way, there is luxury to evaluate the absorbed dose with and without the prosthesis and quantities like dose enhancement factors (DEFs) and dose reduction factors (DRFs) can be obtained. This study therefore demonstrates the powerful application of the MC method in studying complex dosimetric problems.

## 1.5 Scope and layout of dissertation

This thesis consists of eight chapters. In consideration of the major parameters influencing MV photon beam therapy, a review of the production of photons in a linac as well as their interactions with matter will be introduced in Chapter 2. An introduction to electron interactions will be given and some dosimetric quantities and their units will also be discussed.

Chapter 3 starts off by discussing the general composition and design of HPs. It also touches on the various types of HPs and their mechanical and physiological properties in tissue. A detailed description of the dose attenuation effect of HPs on the photon beam dose distribution during RT and the diagnostic effect of metallic devices on imaging will then be presented in the next chapter.

The MC method is presented in more detail in Chapter 5, as well as its various applications in Medical Physics. BEAMnrc and DOSXYZnrc MC user-codes are described in this chapter, as well as the various variance reduction techniques to reduce the simulation time.

Chapters 6 through 8 present the research part of this thesis. The materials and methods used to conduct this research are discussed in Chapter 6. The results are put forth in chapter 7, where percentage depth doses (PDDs), dose profiles (DPs), dose volume histograms (DVHs), isodose data and dose perturbation factors (DPFs) obtained from the MC simulations are presented. The results are discussed in the same chapter and then conclusions of the research are presented in the final Chapter. Chapter 8 also summarizes the results and provides suggestions for improvement and future work.

# 2. Basic Radiation Physics

## 2.1 Background

X-rays possess intrinsic energy that may be imparted to the matter they interact with. When traversing matter, the photons will penetrate, scatter, or be absorbed. The photon interactions may be with a tightly bound electron, with a free orbital electron or with the nuclear electromagnetic field of the atom (Podgorsak 2005). In this study, a tightly bound electron is defined as an orbital electron whose binding energy is of the order of, or slightly larger than, the photon energy ($hv$), while a free electron is an electron with a binding energy that is much smaller than the photon energy.

This chapter introduces the basic interaction processes which may occur when ionization radiation, particularly ionizing photons and electrons, interact with matter. Some dosimetric quantities will also be discussed.

## 2.2 Mechanisms of photon interaction

When a photon beam passes through matter, three general interaction processes can occur:

- It can penetrate through the section of matter without interacting (transmission).
- It can interact with the matter and be completely absorbed by depositing all its energy (absorption).
- It can interact and be redirected or deflected from its original trajectory and deposit some of its energy (scattering).

### 2.2.1 Scattering

Scattering is a physical process whereby the interaction of a radiation beam in a medium with one or more localized non-uniformities results in the deflection of a particle or photon from its original direction into a random course.

A scattering event in which the total kinetic energy (KE) of the colliding particles is unchanged is called *elastic* e.g., coherent scattering. When scattering occurs with a loss of KE, the interaction is said to be *inelastic* e.g., Compton scattering (Khan 2010).

### 2.2.2 Absorption

During absorption, the photon is totally or significantly extinguished by the interaction, losing a substantial proportion of its energy (e.g., photoelectric absorption and pair production).

## 2.3 Energy transfer

The transfer of energy from the photon field to the medium can be considered as a two-step process:

- In the first stage, the indirectly ionizing radiation (photon) transfers energy to the secondary charged particles (electrons) in the medium through various photon interactions (photoelectric absorption, Compton scattering, pair production, etc.), setting one or more charged particles in motion.
- In the second stage, the charged particles transfer energy to the medium through *excitations* and *ionizations* of atoms in the medium, resulting in absorbed dose along the range of the primary electron, and lose some of their KE in the form of radiative losses (through bremsstrahlung, annihilation in flight).
    - During ionization, the incident radiation liberates an electron from an atom or molecule, leaving the material with a net positive charge.
    - During excitation, some of the photon's energy is transferred to the target material, leaving it in an excited (more energetic) state.

The energy transferred to electrons by photons can be expended in two distinct ways:

- Through collision interactions (soft collisions and hard collisions);
- Through radiative interactions (bremsstrahlung and electron-positron annihilation).

During *hard collisions* between incident and atomic electrons, the kinetic energy acquired by the ejected electrons is sufficient to cause further ionization a significant distance away from the track of the primary particle. These electrons are termed *secondary electrons* or *delta rays*, and also contribute to the buildup of dose. A *soft collision* occurs when a charged particle passes an atom at a considerable distance, resulting in only a very small amount of energy being transferred from the incident electron to orbital electrons in a single collision. During *bremsstrahlung*, x-rays are produced as electrons undergo Coulombic interactions with atomic nuclei in the target (Podgorsak 2005).

## 2.4 Photon beam attenuation

The intensity $I(x)$ of a narrow monoenergetic photon beam, attenuated by a homogenous material of thickness $x$ is given by the following equation:

$$I(x) = I(0)e^{-\mu x} \tag{1}$$

Where:

$I(0)$ is the beam intensity incident on the absorber and μ is the linear attenuation coefficient of the material being traversed.

There are five basic mechanisms in which ionizing photons interact with matter (Curry, Dowdey & Murry 1990). These processes are:

- Photoelectric absorption (PEA)
- Compton scattering (CS)
- Pair production (PP)
- Coherent scattering (C)
- Photonuclear reactions

Each of these interaction processes can be represented by its own attenuation coefficient, which varies in its specific way with the photon energy and with the Z–number of the attenuating medium (Khan 2003). The total mass-attenuation coefficient is the sum of individual coefficients for these processes:

$$\mu_{tot}/\rho = \tau_{PEA}/\rho + \sigma_{CS}/\rho + \kappa_{PP}/\rho + \sigma_{C}/\rho \tag{2}$$

Where $\tau_{PEA}, \sigma_{CS}, \kappa_{PP}, \sigma_C$ are linear attenuation coefficients for photoelectric absorption, Compton scattering, pair production and coherent scattering, respectively (Khan 2010). The linear attenuation coefficient is dependent on the photon energy ($hv$), the atomic-number ( $Z$), as well as the density ($\rho$) of the medium. Since coherent scattering is only important at very low photon energies (< 10 KeV) and high-Z materials, it is usually omitted from the sum at therapeutic energies.

### 2.4.1 Photoelectric absorption

The photoelectric effect is the mechanism by which photons are absorbed by matter. An incident photon collides with an inner–shell electron of the absorbing medium, resulting in total absorption of the incident photon. During this process, a complete transfer of the photon energy to a bound orbital electron occurs, creating a vacancy with the ejection of an energetic *photoelectron* from one of the atomic shells whilst the photon itself completely disappears (Fern`andez and Scot 2007). The recoil electron escapes its orbit with KE equal to the difference between the incident photon energy and the binding energy of the electron:

$$KE = hv - E_b \tag{3}$$

Where:

$KE$ is the kinetic energy of the photoelectron

$hv$ is the energy of the incident x-ray photon

$E_b$ is the binding energy of the photoelectron in its original shell.

The vacancy in the ionized (excited) atom is then filled by means of an electronic transition from a higher energy level of the atom (*atomic relaxation*). This creates another vacancy, which, in turn, is filled by an electron from an even lower binding energy shell. Thus, an electron cascade from outer to inner shells occurs (Mayles *et al.* 2008). The de-excitation energy can be carried off with the emission of *characteristic* x-rays, or in some cases, the emission of *Auger electrons*, which are monoenergetic electrons produced by

the absorption of characteristic x-rays internally by the atom (Podgorsak 2005). The probability of emission of a characteristic x-ray is called the *fluorescence yield*. The ejected free electron produced by the photoionization process may be sufficiently energetic to produce further ionization and excitation in subsequent atoms or molecules until all its energy is expended.

Photoelectric absorption is the most probable fate of an x-ray photon having energy slightly higher than the binding energy of atomic electrons and is most important for photons below 100 keV if the absorbing medium is water or biological tissue (Patra *et al.* 2014). However, in high–Z materials such as lead, photoelectric absorption is important for photons up to about 1 MeV. The production of photoelectrons and Auger electrons is shown diagrammatically in figure 2.1:

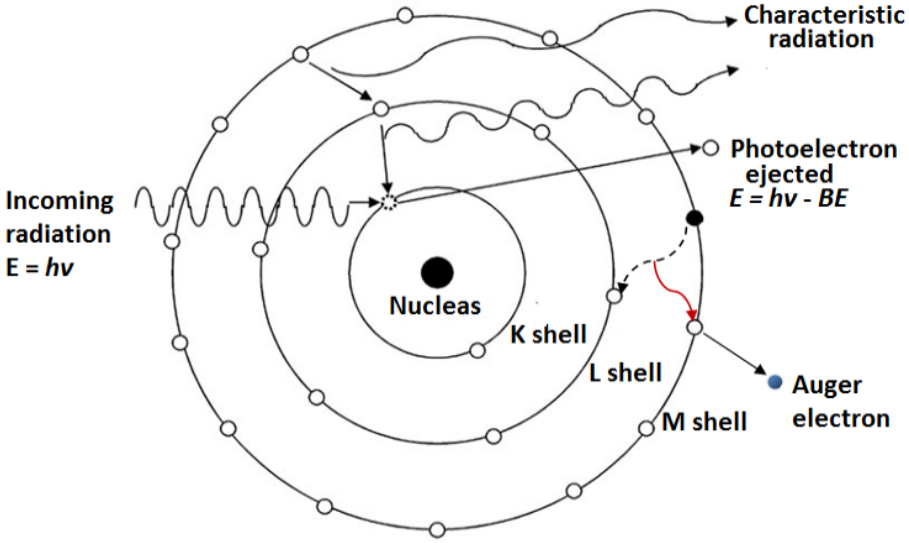


**Figure 2.1:** Diagram illustrating the photoelectric effect

In order for photoelectric absorption to occur, the energy of the incident photon must be greater than or equal to the binding energy of the electron with which it interacts. Photoelectric absorption can take place with electrons in the K, L, M, or N shells (Khan 2003) and cannot take place with free electrons. For sufficiently energetic photons, the most probable origin of the photoelectron is the most tightly bound K-shell of the atom.

## 2.4.2 Compton scattering

Compton scattering (CS), also known as incoherent scattering, is the most common type of inelastic scattering, and represents a photon with relatively high energy interacting with an essentially *'free and stationary'* orbital electron (Podgorsak 2005). The incident photon imparts some of its KE to the electron, ejecting it from its orbit as a recoil/Compton electron, whilst the photon is scattered through some scattering angle $\theta$ with respect to its original direction (Khan 2003) as shown in Figure 2.2.

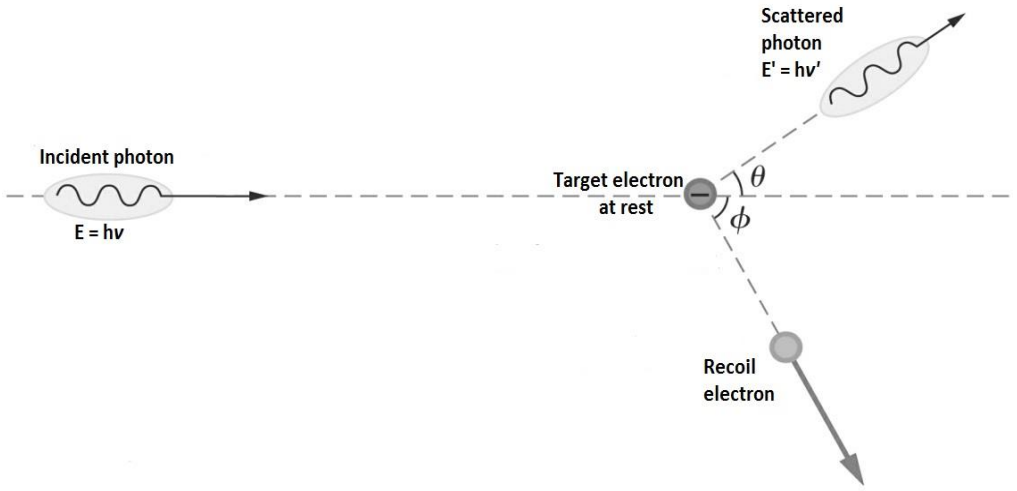


**Figure 2.2:** Diagram illustrating Compton scattering

The scattered x-ray photon may undergo another interaction, but since it is now less energetic, it is more feasible that it will enter into a photoelectric or coherent interaction. The recoil electron produced by the Compton process may be sufficiently energetic to produce secondary excitations and ionizations before coming to rest. In the case of maximum energy transfer, the recoil electron travels forward and the photon is backscattered 180° in the opposite direction (Podgorsak 2005).

The rest of the energy is retained by the scattered photon, depending on its initial energy ($h\nu$) and the deflection angle of the recoil electron $\theta$ (Curry, Dowdey & Murry 1990). By writing simultaneous equations for the conservation of energy and momentum and the

relativistic relationship between energy and momentum, the final expressions for the energy of the scattered photon $hv'$ and the kinetic energy of the recoil electron $E_k$ are given as follows:

$$hv' = \frac{hv}{1 + \alpha(1 - \cos\theta)} \quad \text{and} \quad E_k = hv\frac{\alpha(1 - \cos\theta)}{1 + \alpha(1 - \cos\theta)} \tag{4}$$

Where $\alpha = hv/(m_0c^2)$ and $m_0$ is the rest mass of the electron. The photon scattering angle $\theta$ and the deflection angle of the recoil electron $\phi$ are related by the following relationship:

$$\cot\phi = (1 + \alpha)\tan(\frac{\theta}{2}) \tag{5}$$

### 2.4.3 Pair production

During pair production, an x-ray photon with energy greater than 1.022 MeV passes near the nucleus of the atom and interacts strongly with the nuclear electromagnetic field in such a manner that its energy is converted into matter (Curry, Dowdey & Murry 1990; Khan 2003). The photon disappears and an electron ($e^-$) – positron ($e^+$) pair with a combined KE equal to $hv - 2m_0c^2$ is produced in the nuclear Coulomb field. The process can be represented as follows:

$$\gamma = e^- + e^+ \tag{6}$$

When pair production occurs in the field of an orbital electron, the effect is referred to as *triplet production* (threshold energy 2.044 MeV), and the electron – positron pair and the orbital electron share the available energy. The pair production process is an example of an event which involves conversion of energy into mass, as predicted by Einstein's equation $E = mc^2$. The reverse process in which mass is converted into energy, occurs when a positron combines with a *'free'* and stationary electron, producing two anti-parallel annihilation quanta with energies of 0.511 MeV each (Khan 2003). The

annihilation of a positron before it has expended all of its KE is referred to as *annihilation in flight* and produces photons with energies > 0.511 MeV (Podgorsak 2005).

Because the rest mass energy of the electron ($m_0c^2$) is equivalent to 0.511 MeV, a minimum energy of $2m_0c^2$ = 1.022 MeV is required to create the pair of electrons (Khan 2003; Mayles *et al.* 2008). Pair production is thus energetically infeasible unless the incident photon energy exceeds 1.022 MeV (reaction threshold), and pair production becomes the dominant interaction process when high–energy photons pass through materials of high atomic number. The pair production process is illustrated in figure 2.3:

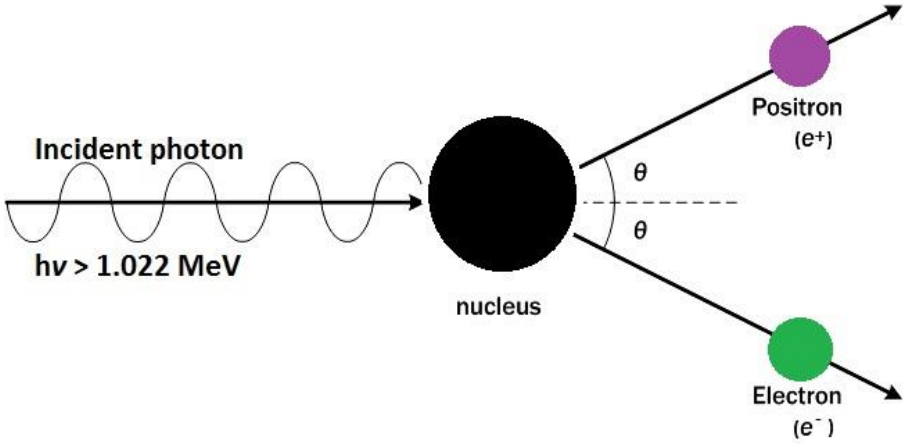


**Figure 2.3:** Diagram illustrating pair production

### 2.4.4 Coherent scattering

In coherent scattering, radiation undergoes a change in direction without a change in wavelength (Curry, Dowdey & Murry 1990). The photon interacts with a bound orbital electron and essentially no energy transfer occurs from the photon to charged particles and hence no ionization occurs. There are two types of Coherent scattering – Thomson scattering and Rayleigh scattering:

- **Thomson scattering**

  Thomson scattering refers to elastic scattering from the free electron or nucleus. If the scattering takes place from bound electron, then it is termed Rayleigh

scattering. In the Thomson process, a single electron is involved in the interaction (Curry, Dowdey & Murry 1990) and the oscillating electromagnetic field of the incident photon sets the electron into vibrations in the direction of its electric vector. The interaction results in the absorption of energy from the incident wave by the electron and its re-emission as electromagnetic radiation of the same frequency as the incident photon.

- **Rayleigh scattering**

  In Rayleigh scattering (RS), the incident photon interacts with and excites the total atom, as opposed to individual electrons in Compton scattering or photoelectric absorption. This interaction consists of a very low energy photon interacting with a tightly bound orbital electron, and being unable to eject it, the electron is only set into oscillation at the frequency of the incident photon. The vibrating electron responds by ejecting an electromagnetic photon of equal wavelength and frequency to the incident photon but in a random direction, while the atom itself is left in its ground state after the scattering process (Curry, Dowdey & Murry 1990).

  Unlike Thomson scattering where a single electron is involved in the interaction, Rayleigh scattering results from a cooperative interaction with all the electrons of the atom (Curry, Dowdey & Murry 1990). The scattering from different parts of the atomic cloud of electrons combine in phase to give coherent scattering. Rayleigh scattering is an elastic scattering process since the incident photon energy is conserved (no loss of energy), but redirection of the photon through a small angle occurs.

Coherent scattering only occurs when the energy of the photon is less than the binding energy of the electron it strikes, and is the main scattering process for very low photon energies passing through high–Z materials, but it is still much less predominant than photoelectric absorption.

### 2.4.5 Photonuclear reactions

Photonuclear reactions can also occur when a high energy photon is absorbed by the nucleus, resulting in the emission of a neutron, a proton, an alpha particle, or a cluster of particles, and the transformation of the nucleus into a radioactive product (Curry, Dowdey & Murry 1990). However, Podgorsak (2005) states that the probability for photonuclear reactions is much smaller compared to other photon interactions and do not play an active role in photon attenuation considerations. However, this process is of great consideration in shielding calculations due to photoneutron contamination of therapy beams of energy greater than 10 MV (Khan 2003). For photonuclear reactions to occur, the photon must have sufficient energy to overcome the strong nuclear binding energy of ~7 to 15 MeV (Curry, Dowdey & Murry 1990). Photonuclear reactions are also called *photodisintegration* reactions or the *nuclear photo effect*. Since their contribution to the total attenuation coefficient amounts to only a few per cent at photon energies above the reaction threshold, photonuclear reactions are omitted in the rest of the discussion.

## 2.5 Relative predominance of individual processes

The relative importance of each interaction process is dependent on the mass absorption characteristics of the absorbing medium (which is directly related to the density ($\rho$) and Z–number) as well as the photon energy $h\nu$, as shown schematically in figure 2.4.

The lines show the values of Z and h$\nu$ for which the two neighbouring effects are just equal (Podgorsak 2005). The left curve represents the energy at which Photoelectric absorption and Compton scattering are equally probable as a function of the atomic number. The line at the right represents the energy at which Compton scattering and pair production are equally probable. Compton scattering is usually the principal interaction mechanism in soft tissue and low–Z targets at h$\nu$ ranging from 100 keV to 10 MeV.

For a fixed value of the energy, the attenuation coefficient increases with the atomic number of the substance. Table 2.1 shows the energy dependence and linear interaction coefficients for the photoelectric effect, Rayleigh scattering, Compton scattering and pair production.

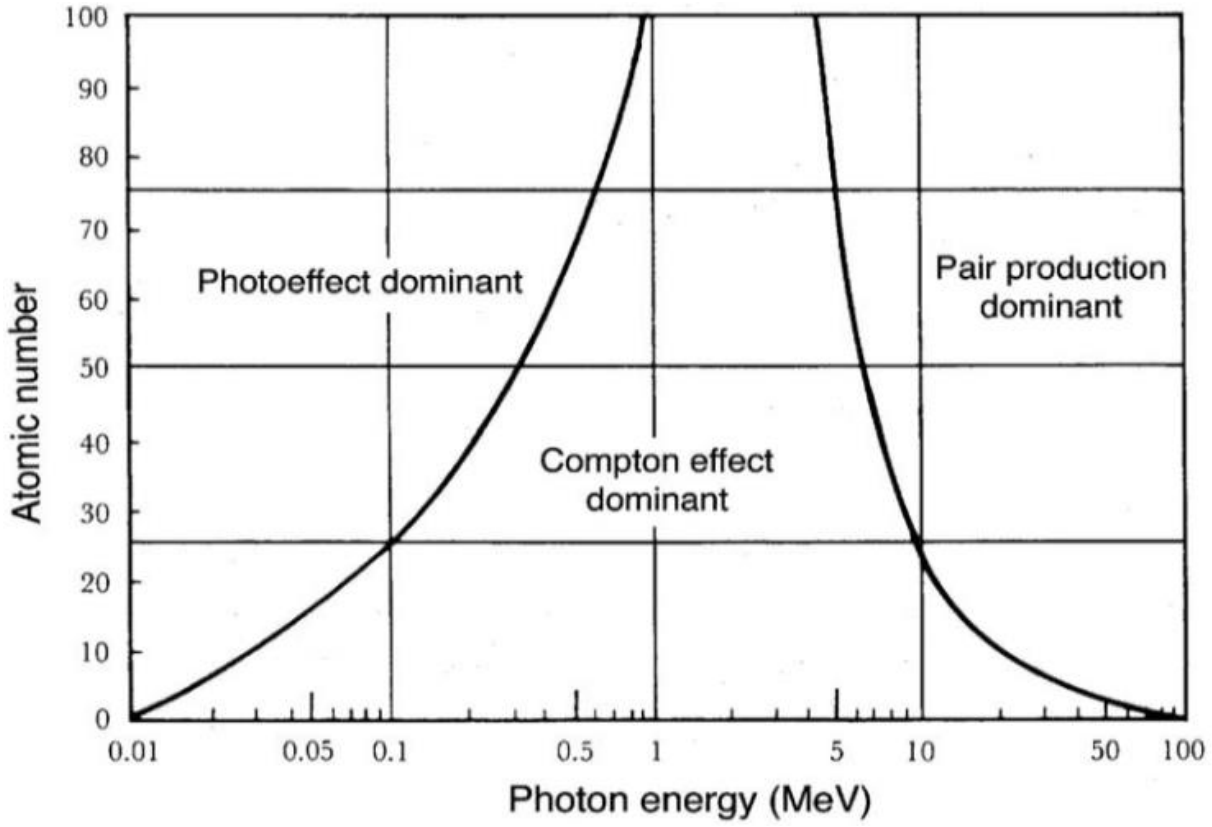


**Figure 2.4:** Relative predominance of PEA, CS and PP for different Z and hν (Podgorsak 2005)

The photoelectric absorption probability increases as the 4$^{th}$ power of the Z–number and is inversely proportional to the 3$^{rd}$ power of photon energy. This explains the strong impact of photoelectric absorption at low photon energies, especially in high atomic-number targets. An example would be the high contrast difference observed between bone and soft tissue in x-ray radiography. In general, the photoelectric process is the predominant mode of photon interaction at relatively low photon energies, Compton scattering predominates at intermediate energies, and pair production at high photon energies.

**Table 2.1:** Cross sections and attenuation coefficients of PEA, CS, PP and RS (Podgorsak 2005)

| Interaction Mechanism | Energy Dependence | Atomic coefficient Z-dependence | Mass coefficient Z-dependence |
|---|---|---|---|
| **Photoelectric Effect** | $\frac{1}{(h\nu)^3}$ | ${}_a\tau \propto Z^4$ | $\frac{\tau}{\rho} \propto Z^3$ |
| **Compton Scattering** | decreases with energy | ${}_a\sigma_C \propto Z$ | independent |
| **Pair Production** | increases with energy | ${}_a\kappa \propto Z^2$ | $\frac{\kappa}{\rho} \propto Z$ |
| **Rayleigh Scattering** | $\frac{1}{(h\nu)^2}$ | ${}_a\sigma_R \propto Z^2$ | $\frac{\sigma_R}{\rho} \propto Z$ |
| $\boldsymbol{h}$ **= Planck's constant,** $\boldsymbol{\nu}$ **= frequency,** $\boldsymbol{\rho}$ **= density and** $\boldsymbol{Z}$ **= atomic number** | | | |

$\tau$, $\sigma_C$, $\kappa$ and $\sigma_R$ are linear attenuation coefficients for photoelectric absorption, Compton scattering, pair production and Rayleigh scattering, respectively. The linear attenuation coefficient describes the fraction of a beam of x-rays that is absorbed or scattered per unit thickness of the absorber. The mass attenuation coefficient is a more fundamental coefficient than the linear coefficient, since the density has been factored out and its dependence on the nature of the material does not involve density but rather the atomic composition.

## 2.6 Some dosimetric quantities

Measurements and investigations of radiation effects require various specifications of the radiation field at the point of interest. In this section, a number of dosimetric quantities and units have been defined for describing a directly or indirectly ionizing radiation beam and the quantity of energy it may deposit in a given medium. The dosimetric quantities and their units are defined according to ICRU reports on radiation quantities and units (Landberg *et al.* 1993; Wambersie & Landgerg 1999).

### 2.6.1 Particle fluence and energy fluence

The *particle fluence* $\Phi$ is the quotient dN by dA, where dN is the number of particles incident on a sphere of cross–sectional area dA:

$$\Phi = \frac{\mathrm{dN}}{dA} \tag{7}$$

The unit of particle fluence is $m^{-2}$. The rate at which the particles pass through a unit area per unit time is defined as the *fluence rate* or *flux density*:

$$\dot{\Phi} = \frac{\mathrm{d}\Phi}{dt} \tag{8}$$

The *energy fluence* $\Psi$ is similarly defined as the quotient of dE by dA, where dE is the radiant energy incident on a sphere of cross–sectional area dA:

$$\Psi = \frac{\mathrm{dE}}{dA} \tag{9}$$

The unit of energy fluence is $\mathrm{J}/m^2$ for photons or $\mathrm{MeV}/m^2$ for electrons. The increment of the energy fluence per unit time $dt$ is called the *energy fluence rate* and is given by:

$$\dot{\Psi} = \frac{\mathrm{d}\Psi}{dt} \tag{10}$$

Energy fluence is also referred to as *intensity* or *energy flux density*.

### 2.6.2 Kerma and Cema

Kerma is an acronym for kinetic energy released per unit mass of an absorber. It is a non-stochastic quantity that quantifies the average amount of energy $dE_{tr}$ transferred from indirectly ionizing radiation (e.g., photons or neutrons) to charged particles (e.g., electrons) per unit mass $dm$. Kerma ($K$) is mathematically defined as:

$$K = \frac{dE_{tr}}{dm} \tag{11}$$

Cema ($C$) is an acronym for converted energy per unit mass, and it gives the energy lost by charged particles $dE_c$, except secondary electrons, in collisions in a mass $dm$ of a material:

$$C = \frac{dE_c}{dm} \tag{12}$$

The units for kerma and cema are Joules per kilogram (J/kg) or gray (Gy).

### 2.6.3 Absorbed dose

The absorbed dose ($D$) is the mean energy $\overline{\mathrm{E}}$ imparted by ionizing radiation to matter of mass $dm$ in a finite volume (Podgorsak 2005):

$$D = \frac{\mathrm{d}\overline{\mathrm{E}}}{dm} \tag{13}$$

The unit for absorbed dose is also J/kg (Gy).

### 2.6.4 Relationship between kerma and absorbed dose

Since kerma represents the energy transferred from photons to directly ionizing electrons, the kerma is maximal at the irradiated material's surface and decreases with depth due to the decrease in the photon energy fluence (figure 2.5). Conversely, the absorbed dose first escalates with depth as the energetic electrons ejected at various depths travel downstream. Consequently, there is an electronic buildup with depth. However, as the dose depends on the electron fluence, it reaches a maximum at a depth approximately equal to the range of electrons in the medium.

Beyond this depth, the dose decreases as kerma continues to drop, resulting in diminished secondary electron production and hence a net reduction in electron fluence. The kerma curve in figure 2.5 is initially higher than the dose curve but drops slightly below the dose curve beyond the buildup region. This effect is explained by the fact that the areas under the two curves taken to infinity must be equal. The buildup region in the dose curve is responsible for the skin sparing effect when high-energy photon beams are

used. The surface dose is due to electron contamination in the beam due to photon interactions in the media upstream from the phantom or due to charged particles generated in the accelerator head and beam modifying devices.

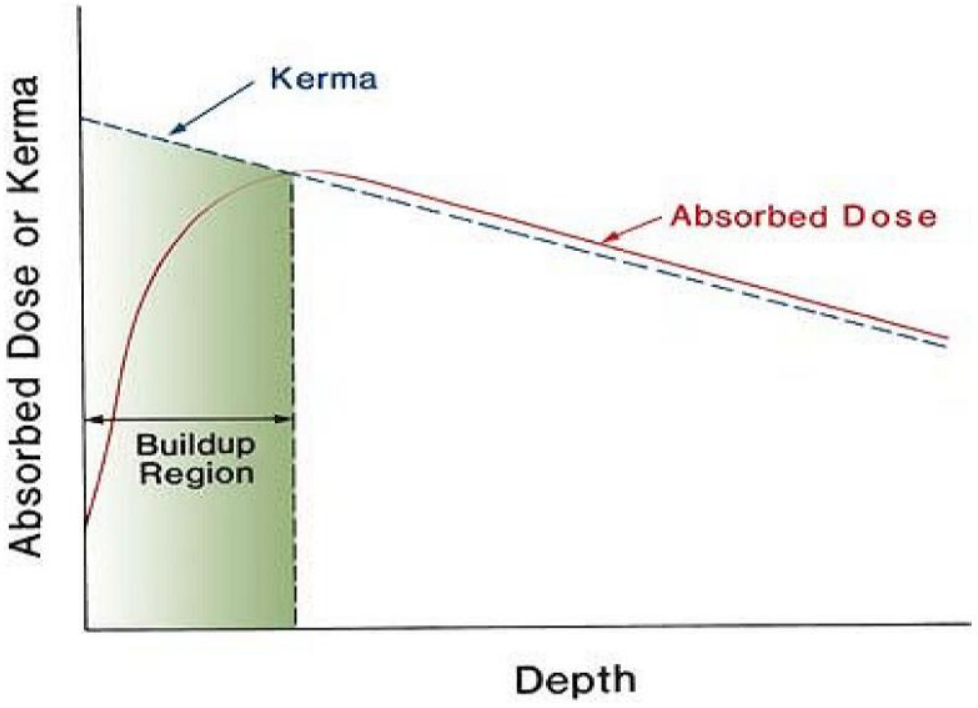


**Figure 2.5:** Absorbed dose and kerma as functions of depth (Khan 2010)

## 2.7 Photon production in a linear accelerator

The linear accelerator is based on increasing the KE of charged subatomic particles such as electrons to relativistic velocities by subjecting them to a series of oscillating electric potentials along a linear beamline (Khan 2003).

The accelerator waveguide serves as a conductor to microwaves and is the main structure in which the electrons are accelerated. The microwaves are produced in a klystron or in a magnetron in form of short temporal pulses and then supplied to the waveguide. The electron gun shoots monoenergetic electrons from a hot cathode at a specific velocity (about 50 KeV) (Khan 2003) in pulses that are synchronized with the microwave pulses into the accelerating waveguide. Heating the cathode releases electrons from the

material via thermionic emission. A block diagram of typical medical linac is shown in figure 2.6.

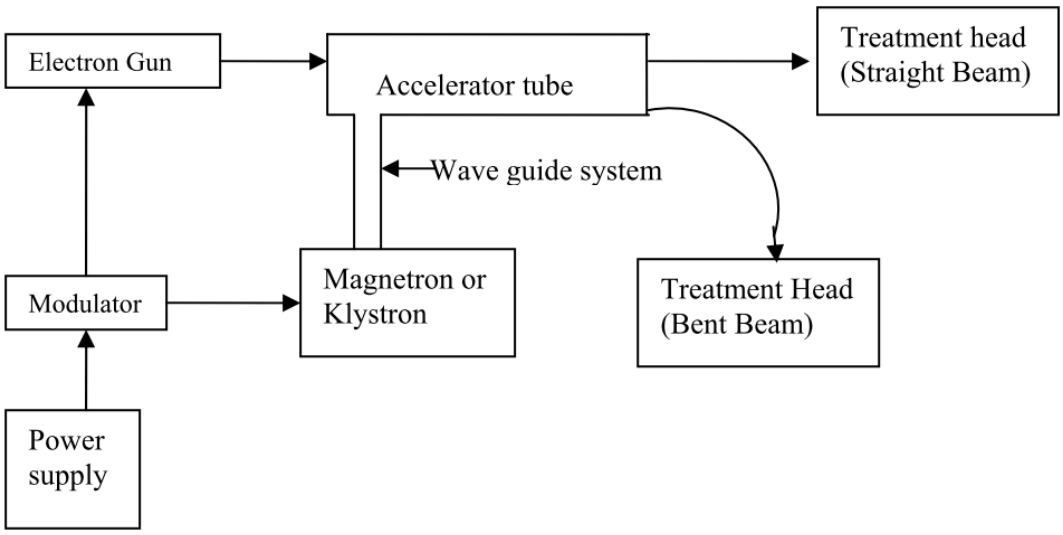


**Figure 2.6:** Block diagram of typical medical linac (Khan 2003)

The microwaves are electromagnetic waves traveling at the speed of light. Therefore, if an electron is injected into the microwaves at the right phase, the electron interacts with the electromagnetic field of the microwaves and is accelerated to a velocity close to the speed of light. Accelerated electrons from the linac waveguide are directed to converge towards the target/scattering foil by bending and steering magnets as a pencil beam of about 3mm in diameter (Khan 2003). In electron therapy, the electrons are scattered by a thin scattering foil to provide a widened beam with uniform electron fluence across the treatment field, or they strike a bremsstrahlung target in which x-rays are generated for photon therapy. X-rays are produced through bremsstrahlung as electrons undergo Coulombic interactions with atomic nuclei in the target. High-Z targets such as tungsten (W) are used due to their high bremsstrahlung efficiency and resistance to heat deformation.

The target is sufficiently thick to absorb most of the incident electrons. The electron energy is converted into a spectrum of x-ray energies with maximum energy equal to the

incident electron energy. These photons are subsequently collimated into a beam that impinges upon the tumor.

## 2.8 Electron interactions

All charged particles, such as electrons, protons and alpha (α) particles basically lose their KE through Coulombic field interactions with the electric field of the orbital electrons or nuclei of the absorber atoms. Energy losses are characterized by *stopping power*, whilst scattering is described by *scattering power*. High–energy electrons experience numerous collisions in the absorber medium before coming to rest, and therefore their behaviour is described by a statistical theory of *multiple scattering* (Podgorsak 2005).

As an energetic beam of electrons travels through a medium, the energy is continually degraded until the electrons reach thermal energies and are eventually absorbed in the medium (Metcalfe, Hoban and Kron 1997). Most of the interactions individually transfer only a small fraction of the electron's KE gradually in a process often referred to as the *continuous slowing down approximation* (CSDA).

### 2.8.1 Stopping power

The rate of KE loss by the charged particle per unit path length $x$ of the medium is known as the stopping power (S), or

$$S = \frac{\mathrm{d}E_k}{dx} \tag{14}$$

The density-independent quantity $(S/\rho)_{tot}$ is called the *mass stopping power*, where $\rho$ is the density of the medium and is usually expressed in MeV.cm²/g (Johns 1969).

Stopping power has two components:

- *Mass collision stopping power* $(S/\rho)_{col}$ – results from Coulombic interactions between the incident electron and the orbital electrons of the medium (Podgorsak 2005). Mass collision stopping power is experienced by both heavy and light

charged particles and results in energy transfer to orbital electrons (atomic ionizations and excitations).

- *Mass radiative stopping power* $(S/\rho)_{rad}$ – results from Coulombic interactions between the incident electron and the absorber nuclei (Podgorsak 2005). Radiative collisions are much more likely for light charged particles (electrons and positrons) and particles experience appreciable energy losses through these interactions (bremsstrahlung production).

In general, the total mass stopping power is the sum of the two components;

$$(S/\rho)_{tot} = (S/\rho)_{rad} + (S/\rho)_{col} \tag{15}$$

The total distance an electron travels in a material before expending all its energy is called its *range* and is dependent on the initial energy of the electron and the medium density. Electrons with equal energy have the same range in a specific material.

### 2.8.2 Scattering power

A beam of electrons traversing a medium suffers multiple scattering mostly through elastic collisions with the nuclei of absorber atoms. Due to their smaller mass, electrons suffer greater multiple scattering than do heavier particles (Khan 2003). The multiple scattering of electrons traversing a path length $l$ through an absorber is characterized by the mean square scattering angle $\overline{\theta^2}$ that is related to the mass thickness $\rho l$ of the medium. Just like the stopping power, the mass scattering power $T/\rho$ is similarly defined by the ICRU (1980) as:

$$\frac{\mathrm{T}}{\rho} = \frac{1}{\rho}\frac{\mathrm{d}\overline{\theta^2}}{dl} \tag{16}$$

The scattering power is proportional to the square of the atomic number Z and inversely proportional to the square of the KE of the electron. Therefore, low energy electrons will

be scattered more readily than high energy electrons; and high atomic number materials will cause more scattering than low Z material (e.g., as in scattering foils) (Khan 2003).

# 3. Design and Properties of Hip Prostheses

## 3.1 Background

To produce lifelong, innocuous hip joint prostheses, hip materials are selected according to their mechanical strength, resistance to corrosion and fatigue, lubricating properties and biocompatibility. Other factors include the patient's age and activity level, as well as the surgeon's preference. The design of HPs, as well as the physical properties of common materials used for total hip replacement (THR) and their pathological effects in host tissue is discussed in this chapter.

## 3.2 Design and composition

There are various designs of HPs to cater for different patient needs. The selection is influenced by factors such as femoral geometry, patient's age, gender, and bone quality. A common design in THR includes a prosthetic acetabular cup around a femoral head which is inserted into the pelvis. The acetabular component consists of a polyethylene core supported by either a titanium (Ti) or cobalt-chromium-molybdenum (Co-Cr-Mo) outer shell alloy. The femoral component usually consists of a stem that fixes into the femur and a solid or hollow head, made of Co-Cr-Mo, Ti or steel alloy (Reft *et al.* 2003). The femoral ball that fits inside the socket is to enable the articulation of hip joint like a mechanical bearing. The size of the femoral head generally ranges between 22–40 mm in diameter (Zhang, Kiat & Pramanik 2009).

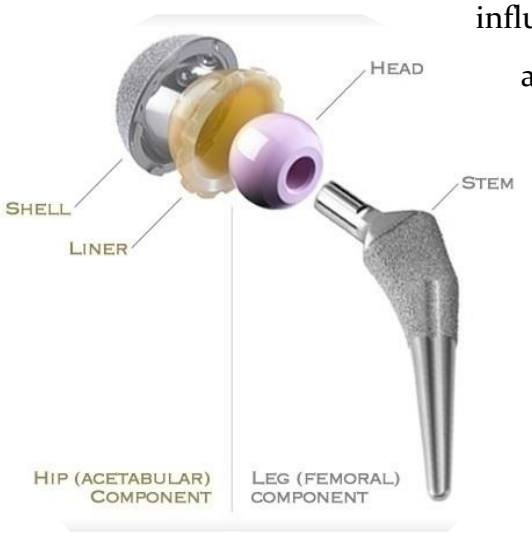


**Figure 3.1:** The fundamental hip joint bearing components (Waring *et al*. 2013)

Another consideration is the means of achieving adhesion of the prosthesis into the femur. One method is to use cemented joint prostheses, which are fixed into the femur with polymethyl methacrylate cement, or to use cementless prostheses which are naturally fixed in the femur. Their fixation depends upon bone in growth into the hydroxyapatite coating of the stem and adhere to it over time.

## 3.3 Material selection for THR components

HPs are most commonly made from cobalt-chrome (Co-Cr), stainless steel and titanium alloys. A summary of the materials used for the individual hip components is tabulated in table 3.1.

**Table 3.1:** Materials commonly used for THR components (Holzwarth & Cotogno 2012)

| Component | Material class | Most used material(s) |
|---|---|---|
| Femoral stem | Metal | Co-Cr-Mo wrought, Ti alloys, stainless steel |
| Femoral head | Metal | Co-Cr-Mo cast, stainless steel |
| | Ceramic | Alumina (pure or zirconia-toughened), zirconia |
| Acetabular cup liner | Polymer | UHMWPE, XLPE (crosslinked UHMWPE) |
| | Metal | Co-Cr-Mo cast |
| | Ceramic | Alumina (pure or zirconia-toughened), zirconia |
| Acetabular cup shell | Metal | Commercially pure Ti, stainless steel |

HPs are most commonly made from cobalt-chrome (Co-Cr), stainless steel and Ti alloys. Table 3.2 gives some physical properties, such as physical density, mass attenuation coefficient, effective atomic number, and electron density for the 3 hip prosthesis materials used in this study.

**Table 3.2:** Physical properties of hip prostheses used in this study (Reft *et al.* 2003)

| Hip prosthesis material | Cross-sectional dimension thickness x width (mm) | Physical density, $\rho$ ($g/cm^3$) | Mass attenuation coefficient at 4MV ($cm^2/g$) | Effective atomic number | Electron density ($e^-/cm^3$) ($\times 10^{24}$) | Relative electron density |
|---|---|---|---|---|---|---|
| SS316L | 11.4 x 20.0 | 8.10 | 0.047 | 26.7 | 2.30 | 6.83 |
| Ti6Al4V | 13.6 x 15.0 | 4.30 | 0.048 | 21.4 | 1.20 | 3.60 |
| UHMWPE | - | 0.95 | 0.034 | 5.44 | 0.32 | 0.94 |

Since dose perturbation is also sensitive to the size, shape, hollowness and composition of the prosthetic material, the simulation data in this report is not meant to be prescriptive and must be carefully applied when dealing with other implant types.

### 3.3.1 Titanium hip prostheses

Titanium is one of the most biocompatible metals, which has enabled its successful use in hip balls and sockets. A biocompatible material can be defined as:

> "any material used to make devices to replace a part or a function of the body in a safe, reliable, economic, and physiologically acceptable manner" (Park & Lakes 2007).

Ti is a light metal with relatively low density and a high strength-to-weight ratio e.g., it is as strong as steel but 45% lighter. Ti is not as rigid as other alloys like Co-Cr. This is desirable because bones too are not absolutely rigid. A very stiff metal prosthesis can cause "stress shielding".

However, pure Ti is costly and its poor mechanical properties such as a small Young's modulus and low fracture stress have restricted its use in THR (Pilliar 2009). Ti alloys, such as Ti6Al4V and Ti6Al7Nb, have improved mechanical properties and can be used for the production of uncemented femoral stems. However, these alloys have a diminished

biocompatibility due to the presence of potentially toxic elements, such as vanadium (V) and aluminium (Al). Another limitation of Ti and its alloys is the great reduction of its outstanding corrosion resistance under friction conditions.

### 3.3.2 Stainless steel hip prostheses

Stainless steel was used for the femoral component in the earlier hip replacements, but it is still used in some implants today. It is an alloy of iron, chromium and usually cobalt and nickel. Stainless steel is corrosion-resistant, abundant and relatively affordable.

Austenitic stainless steels contain chromium (Cr), molybdenum (Mo), nickel (Ni) and nitrogen (N) as the main alloying elements and generally demonstrate good corrosion resistance. ISO 5832-1 stainless steel alloys are less costly but have low resistance against localized crevice corrosion. In addition, their high Ni content represents a potential source of Ni sensitization for patients with stainless steel hip prostheses. ISO 5832-9 stainless steel with relatively higher N content show improved mechanical characteristics and corrosion resistance, but this demands more sophisticated manufacturing procedures and greater cost (Park & Lakes 2007). Some patients also have nickel allergies, which may cause adverse reactions after hip replacement. Stainless steel is still used in femoral implants, notwithstanding its tendency to corrosion and lower fatigue strength (Mirza *et al*. 2010).

### 3.3.3 UHMWPE hip prostheses

UHMWPE is a type of polymer, which is basically a molecule made up of many (poly) parts (mer) linked together by covalent bonds. The individual parts or segments are referred to as monomers, and in the case of UHMWPE, the monomers (ethylene) in the material are all the same. The UHMWPE chain has a molecular weight of 6 000 000 g/mol and can consist of as many as $n$ = 200 000 repeated ethylene units. The structure of UHMWPE is shown in figure 3.2.

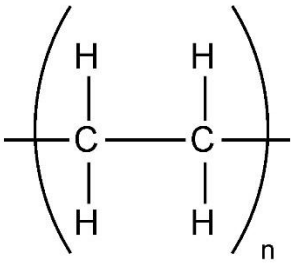


**Figure 3.2:** Molecular structure of UHMWPE

There are several benefits of using UHMWPE for THR. UHMWPE is biocompatible and has a low coefficient of friction as well as a non-stick self-lubricating surface. It is also shown to have the highest impact strength in comparison with other plastic materials, and is demonstrated to be very tough, allowing it to withstand large amounts of compression and tension forces without cracking. Another important advantage is its high resistance to abrasion, which is unsurpassed by any other polymers (Kurtz *et al.* 1998).

One drawback is the non-biocompatibility of particle debris due to wear. The debris can react with the tissue surrounding bone, which may lead to loosening of the prosthesis and eventually the need for revision surgery.

### 3.3.4 Other materials

In addition to the use of metals for prosthetic materials, ceramic and synthetic materials are sometimes used for surgical implants. Densely sintered, high-purity alumina (aluminium oxide, $Al_2O_3$), with a mass density of 3.97 g/cm$^3$ has been used for prosthetic parts. Zirconia (zirconium oxide, $ZrO_2$), with a lower hardness but higher fracture toughness than alumina has also been used in orthopaedics since 1985. A composite ceramic of alumina and zirconia (alumina-toughened zirconia) has also been developed to eliminate the brittleness of $Al_2O_3$. Notwithstanding the brittle nature of ceramics, the hardness and the wettability of ceramic surfaces yield excellent resistance to wear and abrasion (Zietz *et al.* 2011). In addition, the dosimetric complications associated with ceramic prostheses are anticipated to be slighter than those reported on metallic

prostheses because of the lower electron density and effective atomic number (Reft *et al.* 2003).

## 3.4 Implants and pathology

Most hip prostheses have a limited lifespan ranging from about 5 to 15 years. Loosening, dislocation, infection and wear are some of the complications.

Hip prostheses must be physiologically innocuous. However, all implants shed debris as they wear out over time, and this may induce host reactions. The body may recognize polyethylene debris as invaders or a source of infection. As the body starts to attack them, this leads to osteolysis, a "dissolution of bone", which may prompt implant replacement (revision surgery). Rejection reactions may range from mild irritation or inflammation to death. The ideal biomaterial for joint replacement must be highly biocompatible; that is, it must produce a minimum degree of rejection.

One of the concerns associated with metal-on-metal implants (in which the ball and socket are both made from metal) is the accumulation of metal ions in the body. The wearing out of metal-on-metal implants causes the release of metal ions which can be detected in blood and urine samples, and their levels tend to rise with time. However, long-term studies investigating the adverse effects of these metal ions over the course of time are still in progress, and the final results are unknown.

To reduce the risk of host reaction, hip prostheses must also have a high thermal and oxidative stability, chemical and biological inertness, hydrophobic nature, non-adhesiveness to tissue and a low surface roughness.

# 4. Hip Prostheses and Pelvic Radiotherapy

## 4.1 Overview

Hip replacement, or arthroplasty, is an orthopaedic surgical procedure in which the diseased parts of the hip joint are resected and replaced with new, artificial parts called prostheses (Prabhakar *et al.* 2013). Degenerative arthritis (osteoarthritis), rheumatoid arthritis, osteonecrosis, injury, hip fracture, and bone tumours are some of the main etiological factors leading to pain and loss of function of the hip joint and the eventual need for arthroplasty. Joint replacement surgery reduces hip pain, and relieves the physical and psychological sequelae associated with hip dysfunction by producing a more stable hip with better mobility and performance than the preoperative arthritic or fractured hip. A diagrammatic representation of hip arthroplasty is shown in figure 4.1.

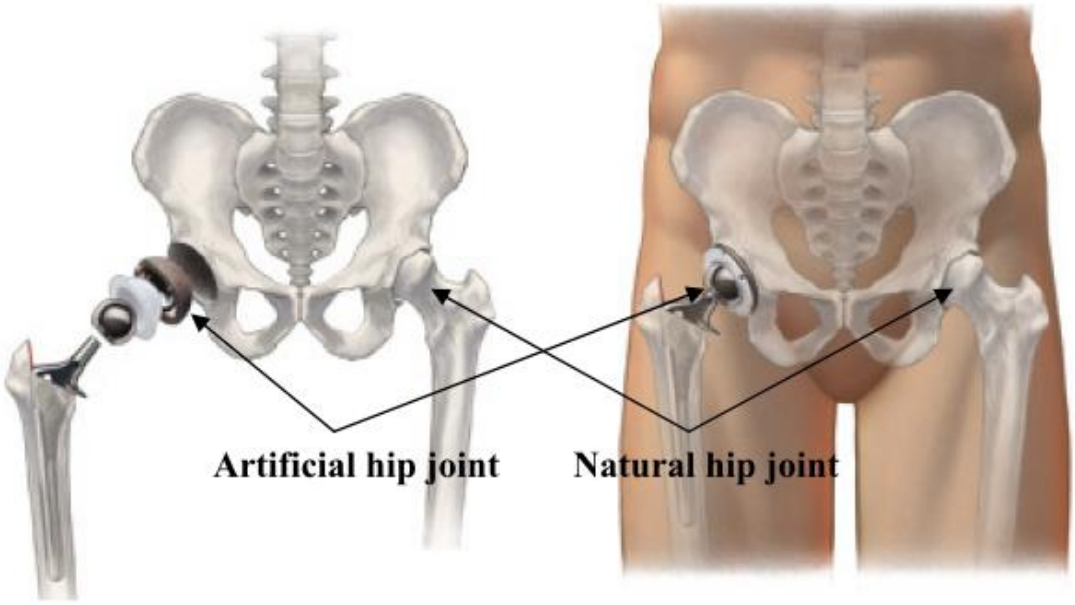


**Figure 4.1:** Diagram showing total hip replacement (Zhang, Kiat & Pramanik 2009)

With the aging of the population, hip replacements are becoming a relatively common procedure, with more than 90% of artificial hips lasting 20 years or longer. Due to the

rising incidence of prostate cancer above the age of 50 (Hankey *et al.* 1999), a small but extensively growing number of patients with prosthetically augmented hips are being referred for prostate RT.

Designing a RT treatment plan for a prostate patient with bilateral prosthetic hips composed of high–Z and high density materials is complicated by the presence of streak artefacts in the CT dataset which makes target delineation difficult, and by inhomogeneous dose distribution within the target volume due to beam attenuation and dose scattering effects of hip prostheses (Rosewall *et al.* 2009; Prabhakar *et al.* 2013). This may create unacceptable dose distributions in the PTV and compel planners to compromise between target coverage and avoidance of beam entry through the prostheses (Martin *et al.* 2012). Even in the absence of hip prostheses, bony tissue can obstruct the path of bi-lateral beams. Consequently, knowledge of the dose perturbations caused by tissue inhomogeneities along a radiation beam traversing through the heterogeneity is very crucial.

## 4.2 Dosimetric properties of prostheses

Treatment of pelvic malignancies normally includes the use of lateral, arc, or rotational fields. The presence of hip prostheses in these treatment fields will perturb the absorbed dose distribution. Dose perturbations take place as a result of beam attenuation by the prosthesis and interactions at the interface between bone and metal. Several research groups have evaluated the dose perturbation by measuring or by calculating dose in patients and in anthropomorphic phantoms containing hip prostheses (Hazuka, Ibbott & Kinzie 1988; Sibata *et al.* 1990; Erlanson *et al.* 1991; Carolan *et al.* 2000; Ma *et al.* 2000; Ding & Christine 2001; Reft *et al.* 2003; Laub & Nüsslin 2004; Buffard *et al.* 2006).

### 4.2.1 Hip prostheses and radiation therapy

Megavoltage (MV) photon RT is an effective treatment modality for prostate cancers because it offers the flexibility of adequately treating lesions at distal depths whilst

sparing superficial tissues. An important aspect of TP is to achieve dose uniformity in the PTV with minimal dose to adjacent critical structures.

Hip prostheses have higher atomic number and higher density than normal tissue, resulting in beam attenuation discrepancies between the two media. The radiopacity of these materials can greatly perturb the dose delivered to the prescription point and to tissue shielded by the prosthesis due to their differential fluence attenuation rates and alterations in the electron scattering pattern. These processes depend on the densities and the Z–numbers of the media in the electron beam path (Podgorsak 2005). The densities, effective atomic numbers as well as electron densities of muscle and bone are given in table 4.1.

**Table 4.1:** The physical properties of muscle and bone (Hendee & Ritenour 2002)

| Material | Density, $\rho$ ($g/cm^3$) | Effective atomic number | Electron density (electrons/kg) |
|---|---|---|---|
| Muscle | ≈ 1.00 | ≈ 7.4 | $3.36 \times 10^{26}$ |
| Bone | ≈1.85 | ≈ 13.8 | $3.10 \times 10^{26}$ |

Scatter perturbations disturb the dose distribution in the neighborhood of the heterogeneity. As a result, considerable deviations in the treatment outcome from the prescribed radiation dose can occur, leading to under-dosing or over-dosing of the tumor load.

The complex dosimetry at the interface between tissue and a high-Z medium is a well–documented problem and numerous publications demonstrated quantitatively that dose perturbations exist between two dissimilar media with different atomic compositions (Werner *et al.* 1987; Das & Kahn 1989; Werner, Das & Salk 1990; Das 1997, Cheng *et al.* 2005). Podgorsak (2005) states that the dose perturbation magnitude depends on the composition, geometry and thickness of the prosthesis as well as the radiation beam characteristics.

Ding and Christine (2001), using a single 18 MV photon beam passing through the implant, found dose increases of 15% in tissue at the tissue–metal implant interface and dose reductions of 5–25% and 10–45% in the shadow of the hip prosthesis made of 0.5–3cm thick titanium and steel alloy respectively.

Gullane (1991) measured interface doses using a wall-less ionization chamber for stainless steel and titanium for both single and parallel-opposed beams. The interface doses increased by as much as 50% at the proximal surface of the metallic inhomogeneity.

Erlanson *et al.* (1991), using small Si diodes, measured the dose increase at the distal site behind a titanium alloy prosthesis in a water phantom for photon energies of 6, 20, and 50 MV. They concluded that the mean dose close to the prosthesis is below the prescription dose of 65 Gy and below the critical level of complications for radiation therapy in the pelvic region using a four-field box technique.

Dose enhancement occurs at the proximal tissue-metal interface whilst beam attenuation is observed in the shadow of the implant. Dose perturbation at the tissue–high Z boundary is comparable to that at the bone–prosthesis interface, though the magnitude of the effects will be reduced in the latter case, owing to the closer match between the Z-numbers of the two materials (Reft *et al.* 2003)**.**

Unfortunately, conventional TPSs do not accurately account for high-Z prosthetic inhomogeneities, particularly at boundaries due to limitations of the planning system in modelling secondary particle production and photon scattering off various materials, causing significant errors during dose calculations (Erlanson *et al.* 1991; Burleson *et al.* 1991; Carolan *et al.* 2000). MC simulation however has the ability to predict the dosimetric influence of hip prostheses during RT (Reft *et al.* 2003).

Another salient problem associated with beam irradiation through the prosthesis is non–uniform attenuation of the radiation beam due to the non–uniform thickness of the inhomogeneity. Therefore, even if the TPS can perform accurate inhomogeneity corrections for the device attenuation, it may produce a plan with non-homogenous

target coverage (Kung *et al.* 2002). This is a planning challenge, and not so much just the high-Z inhomogeneity. Even bony tissue can result in non-homogenous irradiation of the target volume. Fortunately, the complex geometry of prostheses has little effect on the dose distribution in the shadow of the inhomogeneity, except for the actual material thickness through which the beam passes (Ding & Christine 2001).

The concern that needs to be addressed is whether the presence of the prosthetic device would impair local tumour control in patients undergoing radical treatment of tumours in the pelvic region due to the reduced target dose from shadowing of the prosthesis, or an increase in complication rates due to the dose scattering by the presence of the radiation-exposed metallic implant.

Due to the complex dosimetry associated with MV irradiation of high-Z prosthetic devices, most teletherapy treatment techniques for pelvic cancer are not suitable for a patient with b-HP (Sibata *et al.* 1990). While avoiding the hip prostheses as per AAPM TG 63 circumvents the dosimetric complications arising from the shadowing effect of the metallic heterogeneity, the feasibility of oblique beam orientation is further limited by its escalation of bladder and rectal tissue dose (Biggs & Russell 1988; Hazuka, Ibbott & Kinzie 1988; Erlanson *et al.* 1991; Carolan *et al.* 2000; Brooks, Cheung & Kudchadker 2010). Therefore, it is a challenging task to achieve dose uniformity across the PTV whilst respecting the rectal and bladder dose–volume constraints. Therefore, for patients having undergone hip augmentation with prosthetic devices, external photon beams of bilateral incidence are usually delivered to prostate cancer, which lies between the prostheses (Eng 2000).

For beam setups involving passage of radiation through the prosthesis, the AAPM TG 63 recommends taking into consideration the estimated amount of dose perturbation due to the inhomogeneity, the dose to critical organs and the ability of the TPS to accurately estimate the dose distribution. If the type of the prosthesis is known, a protocol for dose calculation and verification is also included (Martin *et al.* 2012).

Dose calculation or measurement within the inhomogeneity is complex, but dose perturbations when RT beams pass through various high–Z and high–density inserts have been extensively studied by several experimental and computational investigations (Hudson, Crawley & Samarasekera 1984; Biggs & Russell 1988; Hazuka, Ibbott & Kinzie 1988; Sibata *et al.* 1990; Burleson *et al.* 1991; Hazuka *et al.* 1993). Dose reduction in a MV x–ray beam due to the presence of high–Z materials can reach up to 64% for the target volume on the distal side of the prosthesis (Sibata *et al.* 1990; Ding & Christine 2001; Mesbahi & Nejad 2007).

Convolution methods, pencil beam and MC techniques have been used to predict the dose in heterogeneous medium (Mackie, Scrimger & Battista 1985; Wieslander & Knöös 2003). The MC method is widely recognized as the most accurate tool available in computing dose distributions for clinical RT in non–tissue–equivalent materials. Recent MC-based TPSs predict the dose within, and on the proximal and distal side of the prosthetic device with excellent accuracy (Wieslander & Knöös 2003).

### 4.2.2 Treatment planning for patients with b-HP

Several TP options for patients with b-HP undergoing teletherapy of prostate cancer have been suggested or used to reduce the attenuation effect of hip prostheses. IMRT is currently the standard treatment technique used in prostate cancer treatment in the presence of metallic HP (Prabhakar *et al.* 2013). Coplanar and non-coplanar beam arrangements of four, five, six or more uniform beams of different energies, ranging from 6 to 18 MV depending on the size of the patient have also been proposed or used (Khan & Potish 1998; Webb 2001; Lin *et al.* 2002). To reduce the attenuation effect of hip prostheses, Eng (2000) suggested a 6F conformal technique with high-energy photon beams, increasing the anterior-posterior/posterior-anterior beam weighting in a conventional 4F technique or bilateral rotational arcs. Ding and Christine (2001) also stated that by using an 8–field technique with proper lateral beam weighting and compensation, acceptable dose distributions can be achieved.

Hip prostheses can be totally avoided using an oblique 4F technique (Eng 2000) or a 3-field coplanar technique (Agapito 2001). However, plans utilizing fewer lateral fields to avoid the prosthesis in the BEV may result in elevated doses to critical structures contiguous to the PTV. Bilateral beams are often used for prostate RT due to their excellent ability to minimize direct rectum and bladder irradiation (Ding & Christine 2001). An additional treatment strategy that can be used is brachytherapy.

Another strategy involves the use of boost fields or compensators to correct the dose distribution in the target. This is however labour intensive and the dosimetry may be dependent on patient set up errors. One can also use beams that give an acceptable dose distribution when heterogeneity corrections are applied during dose calculation. However, this method poses many complications if the TPS uses a non–MC dose calculation algorithm, which cannot account for interface dose accurately (Kung *et al.* 2002).

Efforts have also been made to demonstrate the use of advanced treatment techniques, such as volumetric modulated arc therapy (VMAT) for prostate patients presenting with hip prostheses (Prabhakar *et al.* 2013).

### 4.2.3 Hip prostheses and imaging

Optimization of therapeutic gain depends on maximizing the target dose whilst minimizing the dose to normal tissues. This requires accurate, 3D localization of both the PTV and the OARs, with an excellent ability to differentiate between subtle differences in tissues. However, target localization is complicated by high–Z inserts, whose radiopacity interferes with the diagnostic visualization of abnormal masses that are frequently an indicator of malignancy.

Accurate and reproducible contour delineation is a very crucial step in RT planning. Even though CT imaging is able to give detailed information about the geometry and density of internal structures in most clinical cases, high–density and high–Z prostheses create artefacts, which are usually perceived as starburst streaking and blurring in kilovoltage

computed tomography (kVCT) images (Morin & Raeside 1982; Wang *et al.* 1996; Robertson *et al.* 1997).

Filtered back projection, which is the standard image reconstruction technique, gives characteristic streak artefacts due to aliasing when attempting to create images from patients with high–Z materials. These artefacts degrade the diagnostic quality of CT images by obscuring anatomical structures, and therefore impair accurate contour delineation of target volumes and surrounding critical organs (Rosewall *et al.* 2009; Martin *et al.* 2012). Figure 4.2 shows the transversal view of a CT slice showing bilateral metallic hip prostheses and artifacts.

To reduce the magnitude of CT delineation uncertainties due to image artefacts introduced by metallic inhomogeneity, a number of techniques have been used, e.g., co-registered or fused magnetic resonance imaging (MRI) (Martin *et al.* 2012).

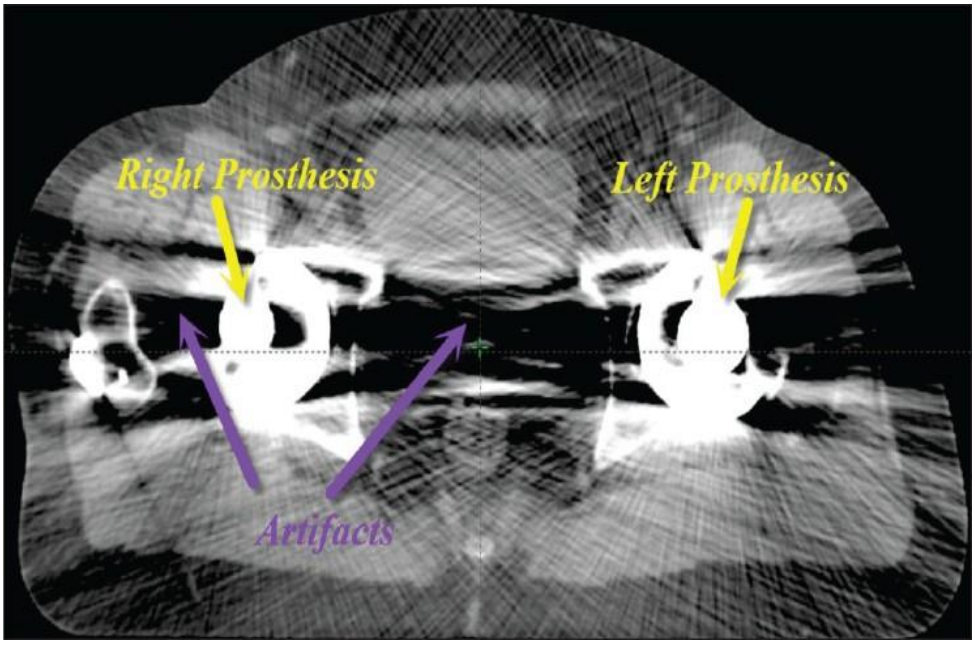


**Figure 4.2:** Transversal view of a patient image with metal artefacts (Rana & Pokharel 2014)

Artefacts also degrade the ability of CT images to provide accurate information about the electron density of structures. Incorrect Hounsfield numbers yield erroneous electron density information needed for dose calculation. Consequently, serious dose calculation

errors arise in the computer TPS (Ding & Christine 2001; Chapman *et al.* 2014). Evaluation of the effect of prosthetic devices on target delineation is however beyond the scope of this study.

Besides aliasing scatter, low signal-to-noise ratio behind the prosthesis, beam hardening, and any other phenomenon that reduces the linearity of CT detector response to attenuation will degrade the image. MV imaging using tomotherapy or cone beam reconstructions or more robust numerical algorithms may help diminish streak-artefacts (Reft *et al.* 2003).

### 4.2.4 Effect of radiation on prostheses

According to published data, radiation doses of the order of megagray (MGy) are required to disturb the mechanical properties of hip materials. Therefore, it is not of concern to investigate the effect of radiation on prosthetic devices in clinical situations (Reft *et al.* 2003).

### 4.2.5 Tissue inhomogeneity

Tissues with densities and Z-numbers different from those of water are referred to as tissue inhomogeneities (also called heterogeneities). Tissue inhomogeneities affect the dose deposition in the patient/phantom and may result in isodose distributions that differ considerably from those obtained in water.

Unfortunately, standard depth dose tables, isodose charts and most of the guidelines (Landberg *et al*. 1993; Wambersie & Landgerg 1999; IAEA 2000) for accuracy and consistency in radiation dosimetry provide information for homogenous unit density media, whereas the human body consists of many naturally occurring internal inhomogeneities whose physical and radiological properties deviate significantly from water, e.g., lungs, air cavities, teeth and bone. Additionally, foreign materials may also be introduced into the body, such as surgical rods, mandibular plates for reconstruction,

spinal cord fixation devices, dental fillings and other metallic prostheses (Reft *et al.* 2003). This study focuses on hip prostheses.

The effects of tissue heterogeneities on radiation dose distributions depend on the amount, the type (density and Z-number) of the inhomogeneity as well as on the photon beam quality. The main effects due to the presence of inhomogeneities in the beam path are:

1) Different attenuation rates in various tissues which depend on the densities of the tissues involved (changes in the absorption of the primary beam and associated scattered photons).
2) Changes in the electron scattering pattern, which depend on the Z-number of the tissue in the electron beam path (changes in secondary electron fluence). These scatter perturbations may affect the dose distribution in the neighborhood of the inhomogeneity.

The relative importance of each effect depends on the position of the region of interest with respect to the heterogeneity. In the MV energy range, Compton scattering is the predominant interaction mode and its cross-section (therefore beam attenuation) is dependent on the electron density (Podgorsak 2005). On the proximal side of the inhomogeneity, the dose is not affected by the heterogeneity since the primary beam in this area is not affected, neither is the scatter component, except near the boundary. Inside the heterogeneity, the dose is largely affected by alterations in the secondary electron fluence and to a minor degree by alterations in the primary beam attenuation. In electronic equilibrium conditions, the ratio of absorbed dose in two different media is equal to the ratio of mass energy absorption coefficients for the two media. On the distal side of the heterogeneity, the dose is predominantly affected by alterations in the primary beam attenuation and to a smaller degree by changes in scatter (Khan 2003).

Adjacent to interfaces the dose distribution is more complex e.g., for MV beams there may be a partial loss of electronic equilibrium in the lower-density medium and an

accompanying reduction in dose. For superficial and orthovoltage x-rays, the main effect is energy absorption in high-Z inhomogeneities caused by an increase in the electron fluence arising from photoelectric absorption in the high-Z medium (Khan 2003).

Tissue heterogeneity causes less accurate dose calculation along the beam, especially for prostate cancer patients undergoing THR (Lin *et al.* 2002). To maximize the therapeutic benefit of RT, it is thus necessary that the absorbed dose delivered to tissues in the presence of heterogeneities be accurately predicted.

# 5. The Monte Carlo Method

## 5.1 Overview

Although the physics of the interactions of radiation with matter is well understood, it is generally impossible to develop an analytic expression to describe particle transport in a medium, due to the complex and random behavior of radiation in matter. Analytical dose calculations through media can be performed only in very simple geometries and under severe approximations. Electrons can create bremsstrahlung/characteristic x-rays and knock-on (delta) electrons and photons can produce both electrons and positrons (Rogers 2002). For problems of practical interest, numerical techniques are used.

One widely used technique involves MC simulation of radiation transport, which uses knowledge of probability distributions governing the individual interactions of particles in matter to simulate their individual random trajectories (Rogers & Bielajew 1990). Due to the dependence on random numbers of

the probability distributions, the term Monte Carlo was devised by von Newmann and Ulam in 1947 (Metropolis 1987; Bielajew 2001).

In contrast to other common radiation transport methods, MC starts from first principles and tracks individual particle histories, taking into account the production of secondary particles. MC-based TPSs simulate radiation transport with great accuracy so that a more realistic dose distribution is obtained in heterogeneous media (Caccia *et al.* 2007).

Due to the vast development in computer processor technology, the availability of general–purpose and specialized code systems optimized for RT calculations and variance reduction techniques, the MC method has become a fast, more widely used, and the current state-of-the-art technique in computational dosimetry, e.g., for modelling

linear accelerators and phantoms in medical physics. The MC method can be applied to many scientific fields of interest. However, discussion will be limited to radiation dosimetry.

## 5.2 Why Monte Carlo?

The accuracy of currently available dose computation models for planning of radiation treatments is limited and discrepancies compared to true dose distributions may be clinically significant in many cases.

MC has been widely regarded as the most accurate tool available in computing fluence and dose distributions for clinical RT, particularly in heterogeneous patient tissues where the effects of electron transport cannot be accurately handled with conventional, deterministic dose algorithms (Deng *et al.* 2000; Rogers 2002; Kim *et al.* 2006; Chetty *et al.* 2007; Chatzigiannis *et al.* 2011). The MC technique faithfully simulates radiation transport in a medium to give accurate dose distributions in regions of tissue heterogeneities, such as lung, bone and irregular surface contours (Fix *et al.* 2004). In particular, MC techniques can handle backscatter from prostheses and bone, or scatter perturbations by air cavities much more accurately than any of the other current methods (Rogers *et al.* 1995).

MC methods also have a unique ability in modeling non-local deposition of charged-particle energy released by photon radiation and charged particle disequilibrium situations, such as the build-up region, near beam boundaries, and near low-density heterogeneities. Therefore, MC-based TPSs produce a more realistic dose distribution in heterogeneous media (Caccia *et al.* 2007).

MC techniques have the fundamental advantage of more accurately representing the geometry and the nuclear data and can handle complex geometries and continuous cross section data as well as backscatter from high density materials more accurately than deterministic methods. Deterministic techniques give a highly exact solution to a

significantly simplified approximation of the problem, while MC techniques provide an approximate solution to a highly exact representation of the problem (Rogers *et al.* 1995).

## 5.3 The technique

MC is a model–based dose calculation method that uses well-established probability distributions governing individual particle interactions to simulate radiation transport in a medium (Reda *et al.* 2006).

MC simulates the stochastic paths and interactions of individual particles in any material by ray-tracing method. In this method, MC tracks individual particles and computes how a particle of given energy propagates through a defined geometry of source and medium according to fundamental principles of radiation physics. This is done by sampling appropriate dynamical quantities from probability density functions derived from atomic cross sections, and using computer–generated random numbers to determine which interaction will occur by comparing probabilities (i.e. cross-sections) of each interaction. Each particle is tracked until it deposits all its energy in the medium or escapes from the region of interest (Rogers & Bielajew 1990; Ali 2009).

The code simulates the distance travelled by a particle before interaction, the type of interaction undergone, the initial energy, the change in direction and energy, the angle of emission of secondary particles etc., and this information is stored in a memory stack (Heath & Seuntjens 2003). For photons, it accounts for coherent and incoherent scattering, the possibility of fluorescent emission after photoelectric absorption, absorption in pair production with local emission of annihilation radiation, and bremsstrahlung (Krstic *et al.* 2012).

MC simulation characterizes the clinical beam emanating from the radiation source, but can also be used to calculate dose distributions in a given patient and treatment geometry. To practically employ the MC method in RT, accurate modelling of the

materials and geometrical components of the radiation treatment unit (in this case linac head) and patient geometry (in this case CT data) is required. This requires thorough understanding of the machine specifications provided by the manufacturer (Ali 2009).

MC is widely considered as the most accurate method available in computing dose distributions in non-tissue-equivalent-materials (TEMs) due to its capacity to faithfully describe the underlying physical interactions between radiation and matter. The accuracy of MC results depends on the detailed specification of the geometry, the accuracy in the cross section libraries and the number of events (called histories) simulated (Reynaert *et al.* 2007). Since MC is a statistical process, a large number of particle histories must be simulated in order to accurately approximate actual physical processes that may be experimentally determined.

The traditionally long calculation times previously associated with MC simulations rendered this method as a clinically unfeasible approach for routine clinical TP. However, with the development of faster codes optimized for RT calculations, advances in computer processor technology and variance reduction techniques, the MC method is becoming a fast, powerful, and standard practical approach in computational dosimetry. The MC user-codes BEAMnrc and DOSXYZnrc have been extensively used by several groups for linac head simulation and phantom dose calculation, respectively (Ding & Christine 2001; Lin *et al.* 2002; Wieslander and Knöös 2003; Keall *et al.* 2003; Buffard *et al.* 2006).

## 5.4 The EGSnrc code system

The EGSnrc code system, released in February 2000 (Rogers, Walters and Kawrakow 2001), is a general-purpose software package for MC simulations of coupled electron–photon transport, and particle energies ranging from 1 keV to 10 GeV. It is a joint development of the NRC and the Stanford Linear Accelerator Centre (SLAC) (Nelson, Hirayama & Rogers 1985) as an extension of the popular EGS4 system. The EGSnrc implementation improved charged particle transport mechanics and multiple scattering

algorithms/atomic scattering cross-section data (e.g., to include electron relativistic spin effects in elastic scattering cross-sections) and has the ability to simulate atomic relaxations after Compton and photoelectric events (Kawrakow 2000). It also includes a C++ geometry library for defining the geometry of complex simulation environments or particle sources. All these improvements increase the accuracy of EGSnrc over EGS4, particularly at lower energies.

The EGSnrc system consist of BEAMnrc, DOSXYZnrc, DOSRZnrc, FLURZnrc, CAVRZnrc, SPRRZnrc and other simulation codes that come as a package under license to the NRC (Rogers *et al.* 2003). All MC simulations reported in this study were performed with the EGSnrc–based BEAMnrc and DOSXYZnrc packages.

Other MC algorithms that have been developed during the past few decades include EGS5 (Nelson, Hirayama & Rogers 1985; Bielajew *et al.* 1994; Hirayama *et al.* 2010), GEANT4 (Agostinelli *et al*. 2003), PENELOPE (Baró *et al.* 1995; Sempau *et al*. 1997) and MCNP (Briesmeister 2000).

### 5.4.1 BEAMnrc

BEAMnrc is an EGSnrc-based general-purpose MC user-code designed to simulate RT sources, including low-energy x-rays, and photon and electron beams from a wide variety of accelerators as well as Co-60 units (Ali 2009). The BEAMnrc code is capable of developing a detailed 3D model of a medical linac treatment head and dosimetric calculations in complex geometries and material combinations, while producing data that can be closely matched to realistic clinical beams.

BEAMnrc was developed as part of the Ottawa Madison Electron Gamma Algorithm (OMEGA) project to develop 3D TP for RT (Rogers, Walters and Kawrakow 2001). It has been extensively benchmarked against measured data for a variety of accelerators over a wide range of beam parameters and treatment geometry.

#### 5.4.1.1 Component modules (CMs)

One of the key design features of BEAMnrc is that each part of the radiation unit is considered to be an independent component module (CM) which takes up a horizontal slab portion of the accelerator and communicates with the rest of the system in specific ways. A CM can be considered as a block with a 'front' and a 'back' surface (Rogers, Walters and Kawrakow 2001).

An accelerator is built by simulating each piece of the linac with many such blocks available in BEAMnrc. The gap between blocks is usually filled with air by the BEAMnrc main routine, as is the case in a real accelerator. Each CM can be used for a wide variety of applications, for example, the JAWS CM is well suited to simulating a wedge as well as the secondary collimators. Other CMs include SLABS – generally used for simulating the target, CONESTAK – for modelling the primary collimator, FLATFILT for the flattening filter etc.

#### 5.4.1.2 Phase space files

MC simulations with BEAMnrc allows for generation of a phase space (PS) file on each scoring plane directly below a CM.

The generated PS data characterizes the beam emanating from the treatment unit. The PS file is a data set containing all the information relating to the incident beam e.g., particle type, energy, position, charge, direction, weight, and a tag that records the particle history for every particle crossing a specified scoring plane in the simulated geometry (Rogers *et al.* 1995; Ding & Christine 2001).

These PS files may require a large amount of computer disk space. Each particle crossing the scoring plane requires 32 bytes of data, and to attain low statistical uncertainties, several million particles are required in the PS file (Rogers *et al.* 2005).

### 5.4.2 BEAMDP

BEAMDP (BEAM Data Processor) is an interactive program that was also originally developed for the OMEGA project, to analyze the PS data and to derive spectral and planar fluence distributions for use by beam characterization models (Ma & Rogers 1995).

BEAMDP can be used to analyze the PS parameters of a clinical beam generated from the radiation machine using BEAMnrc and can also be used as a utility program to derive the data required by multiple-source models for use in MC RT treatment planning (Ma & Rogers 2004). BEAMDP can also be used to derive energy distribution or fluence plots, angular distributions, scatter plots and also to combine PS files.

### 5.4.3 Variance reduction methods

MC simulations attempting to simulate the full stochastic development of radiation transport through the simulated accelerator head can, if a low variance is required, be very time consuming. Uushona (2009) defined variance reduction as:

> "the modification of the faithful analogue simulation of particle histories in order to obtain an increase in the precision of the result per unit central processing unit time"

The uncertainty in a MC simulation is determined by dividing the simulation into batches of equal particle histories. In EGSnrc, 10 batches are usually used. The mean energy in each voxel is calculated together with the associated uncertainty. The uncertainty ($\sigma$) for number of histories per voxel ($N$) is given as:

$$\sigma = \frac{1}{\sqrt{N}} \tag{17}$$

Therefore, 1% uncertainty requires $N \approx 10\,000$. The main variance reduction techniques used in BEAMnrc include range rejection, bremsstrahlung splitting, photon forcing and Russian roulette.

#### 5.4.3.1 Range Rejection

The basic idea of range rejection is to compute the range of a charged particle and terminate its history (depositing all of its energy at that point) if its residual range is smaller than the distance to the nearest boundary or scoring region. This can save a considerable amount of computing time during simulations, since the range and distance to boundaries are already calculated by the EGSnrc code (Kawrakow & Rogers 2000). The electron range is calculated as the path length travelled until the electron slows down to the cut–off energy, if it does not undergo any discrete interactions (Rogers *et al.* 1995).

As bremsstrahlung photons can be generated by the slowing down electron, the main approximation in range rejection is that, in terminating a charged particle's history and depositing all of its energy in the current region, it neglects any escape of bremsstrahlung photons from that region and their non-local energy deposition, far from the site of bremsstrahlung production.

The effects resulting from this approximation can be minimised using the input variable ESAVE – defining the maximum charged particle energy at which range rejection is considered. An electron having energy > ESAVE is not considered for range rejection since they may have enough energy to exit the current region. It is important to switch off range rejection in regions were the bremsstrahlung process is an important interaction mechanism, for example, in the linac target.

Range rejection can save 10–17% on computing time for 5 $mm^3$ voxels, but for smaller voxels, it saves less time (3–4% for 2.5 $mm^3$ voxels).

#### 5.4.3.2 Photon forcing

BEAMnrc also provides an option whereby the user can force photons to interact in specified CMs. This option helps to improve statistics of scattered photons in regions where photon interactions are sparse (e.g., in thin material slabs or in low density

materials). This option helps to study the generation of contaminant electrons in a photon beam. In short, a photon forced to interact in a CM is "*split*" into a scattered photon whose weight is equal to the interaction probability and an unscattered photon with the residual weight. The unscattered photon proceeds as if no interaction occurred, and cannot be forced to interact again within the specified forcing zone. Nevertheless, as soon as it exits the forcing region, it may interact again depending on the sampled path length. The scattered photon can be forced again in the forcing region depending on how many forced interactions are allowable (Rogers, Walters and Kawrakow 2004).

#### 5.4.3.3 Bremsstrahlung splitting and Russian roulette

Bremsstrahlung splitting gives the user another variance reduction technique to improve the statistics of bremsstrahlung photons resulting from electron interactions. There are three different bremsstrahlung splitting options in BEAMnrc: uniform bremsstrahlung splitting (UBS), selective bremsstrahlung splitting (SBS) and directional bremsstrahlung splitting (DBS). The simulations in this work were performed with UBS because it is easier to implement than SBS and DBS.

UBS uses the input variables **IBRSPL** (= 1 for UBS) and **NBRSPL** (the splitting number). Each bremsstrahlung event produces NBRSPL photons, each with a weight = $\frac{1}{\text{NBRSPL}}\times$ weight of electron that underwent the splitting. The photon energies and directions are sampled individually for each photon according to the relevant probability distributions. The primary electron energy is decreased by the energy of one of the photons. This is necessary to preserve the effects on energy straggling but it means that energy is not conserved on a given history but it is conserved on average over many histories.

The splitting number is not applied to higher-order bremsstrahlung and annihilation photons unless Russian roulette is turned on. This saves simulation time by avoiding the tracking of many higher-order photons of vanishing weight. UBS is now handled by the EGSnrc system using a more efficient internal bremsstrahlung splitting feature. So, other

than input, there is no longer any coding in BEAMnrc related to this except for the feature which turns it off for higher orders (Rogers, Walters & Kawrakow 2004).

If the prime interest of the simulation is bremsstrahlung photons, BEAMnrc can implement Russian roulette on secondary electrons generated by the split photons to reduce the CPU time while still preserving the variance reduction benefits of bremsstrahlung splitting. Russian roulette is implemented by setting a survival threshold for secondary charged particles. The survival threshold is always the inverse of the photon splitting number (Ns for UBS), or the inverse of the variable splitting number (NBR for SBS). For each particle, a random number RN is chosen and if RN < the survival threshold, the particle survives, and its weight is increased by a factor of Ns for uniform splitting or NBR for selective splitting, otherwise the charged particle's history is terminated.

#### 5.4.3.4 Transport cut-off energies

The most common technique for reducing computing time in MC simulations is by using electron and photon cutoff energies, ECUT and PCUT, below which the particles are stopped and their residual energy is deposited in their current region.

ECUT defines the global cutoff energy for electron transport in MeV, and results in the termination of the electron's history and its energy deposited in the current region as soon as its total energy falls below the cutoff energy. The calculation time is strongly dependent on the ECUT value and thus it is important to use a value as high as possible. Similarly, PCUT is the photon equivalent of ECUT but the value of PCUT is not critical since low PCUT values do not lead to a longer simulation time. A PCUT value of 0.01 MeV is generally used.

Energy cutoffs must be chosen in a way that will not affect the calculated result, i.e. the particle's range should be, at the most, as short as its distance to the boundaries of its current region. Since photons have relatively large ranges, even at low energies, PCUT must be smaller than ECUT (Rogers *et al.* 2005).

### 5.4.4 PEGS4

EGSnrc codes run using the cross-section data of different materials stored in a PEGS4 file. The files 521icru.pegs4dat and 700icru.pegs4dat contain data for a large number of commonly used materials. The numbers in the file identifiers correspond to the lower electron energy limits for cross section calculation, AE = 521 and AE = 700, i.e. kinetic energy thresholds for secondary electron production of 10 and 189 keV respectively. Both files contain data for the photon energy from 0.01 MeV up to 55 MeV (Rogers *et al.* 2005).

This data can be generated using the PEGS4 code in the EGSnrc program package, where the user specifies the lower energy cut-off for the production of knock-on electrons and photons, AE and AP, respectively (Kawrakow & Rogers 2000). The code includes cross–section libraries for the radiation interaction processes for all elements from which the cross section data for body tissues are then evaluated according to their density and elemental composition (Reda *et al.* 2006).

### 5.4.5 DOSXYZnrc

DOSXYZnrc is a general-purpose Cartesian coordinate EGSnrc-based MC simulation user-code for calculating 3D absorbed dose distributions in a rectilinear voxel phantom and is based directly on the DOSXYZ code developed for the EGS4 code system. It can use the PS data file generated by BEAMnrc as input (Lin *et al.* 2002). DOSXYZnrc simulates particle transport in a rectilinear geometry and scores the energy deposition in the designated voxels (Walters, Kawrakow & Rogers 2005). The voxel dimensions are variable in all three dimensions and each voxel can have different materials with varying densities for use with CT data.

The code allows a wide variety of source configurations such as a monoenergetic parallel or diverging beam, PS data generated from a BEAMnrc simulation, or a model–based beam reconstruction produced by BEAMDP.

DOSXYZnrc simulation produces an output file that stores the calculated 3D dose distribution data (normalized per incident history) and the corresponding dose uncertainties. The 3D dose file produced by DOSXYZnrc can be analysed to extract PDD and DPs from 3D dose. DOSXYZnrc simulation can accurately predict detailed dose distributions inside a phantom where experimental measurements are difficult or impossible to perform.

## 5.5 Applications of Monte Carlo in medical physics

MC is a numerical tool commonly used in research areas involving stochastic event modelling e.g., radiation transport in matter, in disciplines such as nuclear medicine, radiation protection, diagnostic radiology, radiation shielding and dosimetry (Andreo 1998; Zaidi 1999; Abdullah, Nabil & Akhtar 2005).

In medical physics, the MC method can be used as a dose calculation engine for TP (Heath & Seuntjens 2003). MC is used to compute dose distributions in non-TEMs and to provide 3D dose distributions in complex, heterogeneous targets where it might be difficult to perform accurate measurements. Furthermore, the MC method is a very useful tool in output calibration, providing critical correction factors e.g., for TG–51 (Almond *et al.* 1999). MC linac head simulation gives results of unmatched accuracy and detail of the character of the RT beam and has therefore proven to be instrumental in linac head design.

MC is showing to be an essential tool for development in image-guided radiotherapy (IGRT), including design of flat panels for portal imaging, and improving contrast in MV x-ray beams. In the future, MC simulation may well be routinely used in the clinic to support IGRT, mixed beam RT (IMRT with combined electron and x-ray fields), and dose-effect planning.

The successful application of MC methods in TP with unprecedented accuracy has demonstrated that MC can be used as a benchmarking tool to verify other dose

calculation algorithms (Ding & Christine 2001; Solberg *et al.* 2001; Wieslander & Knöös 2003; Laub & Nüsslin 2004; Farajollahi & Mesbahi 2006).

## 5.6 Drawbacks of the Monte Carlo method

MC methods require a large amount of computational resources that may be unavailable in hospitals. The current limitation of MC simulations is the long computation time needed to calculate the large number of particle histories required to achieve a reasonable level of statistical accuracy i.e., to reduce stochastic or random uncertainties to acceptable levels. To speed up the dose calculation, radiation transport modelling has to be simplified, and this may lead to less accurate results. However, faster codes do exist and have been benchmarked against EGSnrc. The type of analyses required would prompt which code is to be used.

One drawback to the implementation of MC codes in RT dose calculation is the need of a general and accurate radiation source model that will allow a user with an arbitrary linac to commission a MC dose-calculation algorithm that meets the standard accuracy requirements. Fortunately, generalized source models are now commercially available that can be modified to match the output of a general linac and have been shown to compare well with EGSnrc (Fippel *et al.* 2003).

MC techniques are statistical in nature and do not provide exact solutions to the problem. All results represent estimates with associated uncertainties. Another recurring problem in MC simulations is numerical round off errors as particles cross boundaries.

# 6. Materials and Methods

## 6.1 Overview

Several software tools were used to complete most of the aspects of this study. The software used was either freeware or it was written in order to perform a specific task. The software and hardware used in this study include: *BEAMnrc* for linac modelling, *DOSXYZnrc* for phantom dose calculation, *EGSnrcMP* for generating PEGS4 data, *BEAMDP* for beam analysis, *Grace* for graph plotting, *MCSHOW* for phantom modification and dose extraction, *Fortran* for combining dose files, *IDL* for modifying material density, *Excel spreadsheets* for calculating collimator apertures, *XiO TPS* for generating treatment plans, a Linux platform as the MC dose calculation engine and an emergency power supply system.

## 6.2 Monte Carlo Simulations

The MC technique used to calculate the dose distribution in the vicinity of the prosthesis is currently a two-step process – simulating the clinical linear accelerator and then simulating the dose distribution in a mathematical phantom. In the first step, BEAMnrc was used to build a virtual model of a medical linac. In the second stage, DOSXYZnrc was used to calculate 3D absorbed dose distributions in a CT–based phantom from scanned patient images. MC was used due to its versatility, its ability to handle complex geometries and its recognition as the most accurate dose calculation algorithm available.

### 6.2.1 Linac head simulation

The MC radiation software package BEAMnrc was used to simulate the accelerator head, based on the geometric and material specifications provided by the manufacturer. The detailed cross–sectional view and composition of the Elekta Precise linac head components is shown in figure B.1 and table B.1.

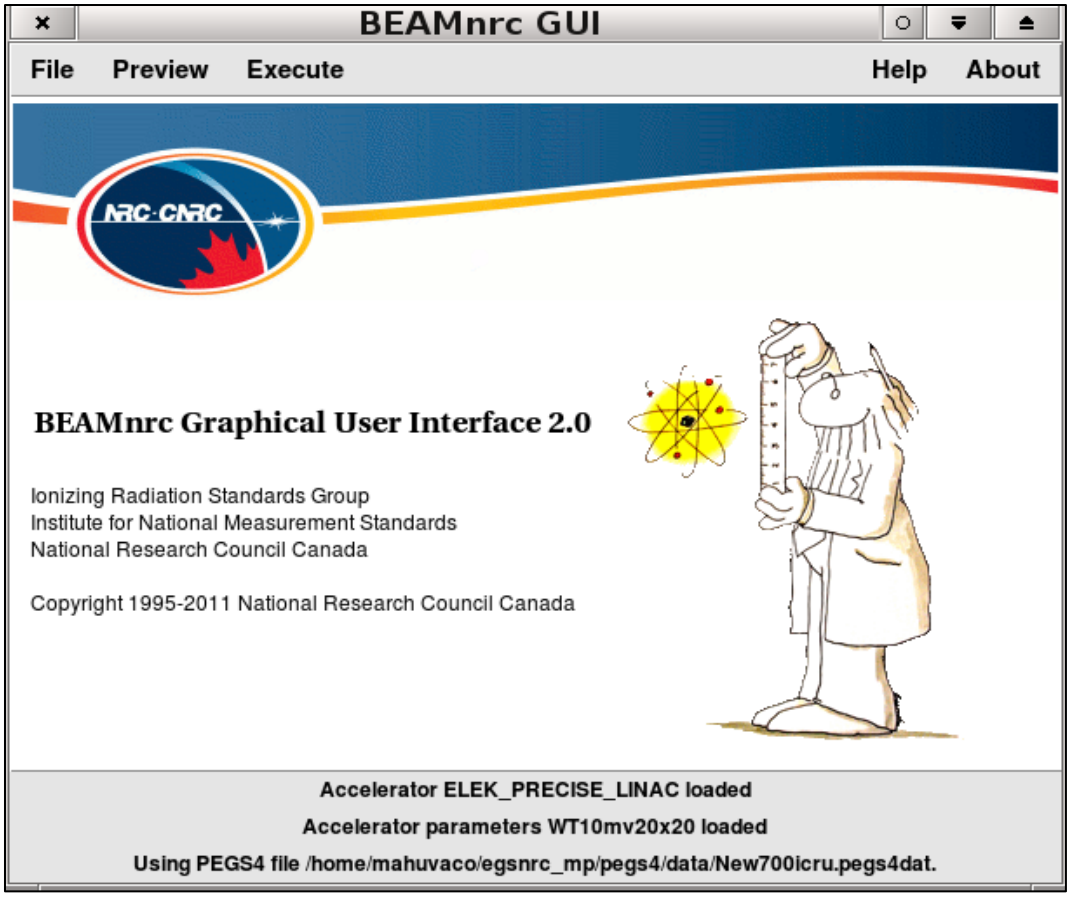


**Figure 6.1:** BEAMnrc graphical user interface

The BEAMnrc GUI (figure 6.1) has the option to preview individual components of the linac separately or to preview the whole linac structure. BEAMnrc can run multiple jobs in parallel as a queue batch.

The linac model used in this study is that of a multi-energy Elekta Prec*i*se unit working in three nominal photon energy modes of 6, 10, 15 and 20 MV and seven electron energies of 4, 6, 8, 10, 12, 15 and 20 MeV. The linac is installed at the RT department of Universitas Academic Hospital Annex, Bloemfontein, South Africa. The Elekta Prec*i*se linac structure is shown in figure 6.2.

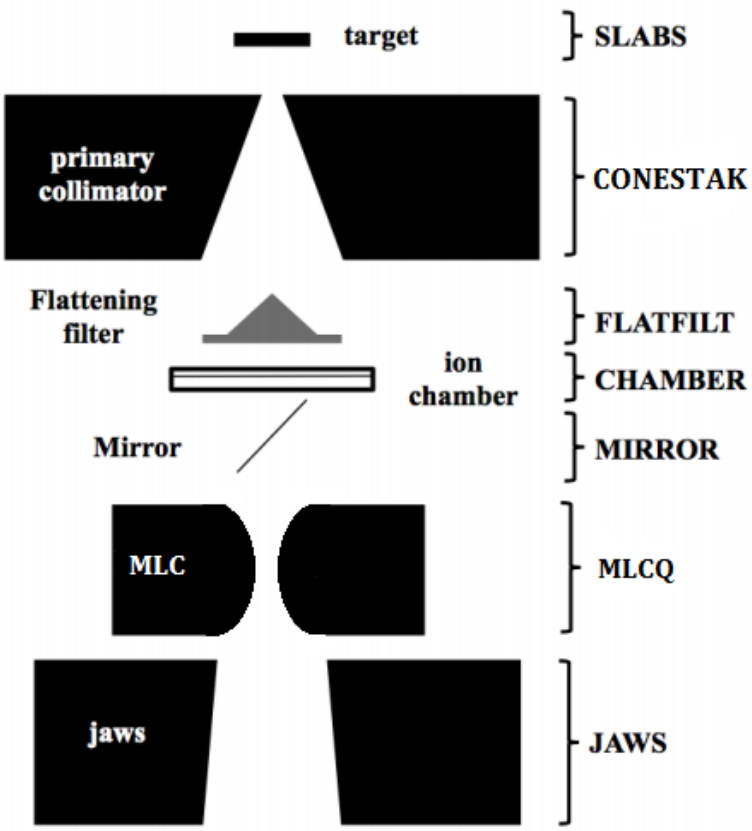


**Figure 6.2:** Geometry used for modelling the Elekta Precise linac head in BEAMnrc (Lye 2012)

The A-A' plane in figure 6.2 separates the upper (invariant) part of the linac head from the lower (field defining) part of the linac head. CMs are shown in brackets. The incident parallel electron beam impinging perpendicularly on a 3 mm thick bremsstrahlung target was simulated by a spot size of 2 mm in diameter with uniform spatial distribution at nominal accelerating potentials of 6, 10, 15 and 20 MV. The target was an alloy of tungsten (W) and rhenium (Re) and was modelled with the SLABS CM. Immediately below the target; a primary conical collimator composed of an alloy of tungsten (W), nickel (Ni) and iron (Fe) was modelled with the CONESTAK CM with top and bottom radius of 1.0 cm and 3.5 cm respectively. A stainless steel flattening filter just below the primary collimator was also simulated with FLATFILT CM, whose dimensions depend on the beam energy used. The atomic compositions of the linac components modelled are shown in table 6.1.

**Table 6.1:** Compositions of Elekta Precise linac head components simulated (Nedaie *et al.* 2014)

| Linac head component | Materials | Percentage (%) | Density (g/cm$^3$) |
|---|---|---|---|
| Target | W/Re | 90/10 | 19.4 |
| Primary collimator | W/Ni/Fe | 95/3.75/1.25 | 18.0 |
| Flattening filter | C/Si/Ni/Cr/Mn/Fe | 0.15/0.85/9/18/2/70 | 7.80 |
| Secondary collimator | Pb/Sb/W | – | 18.0 |

The lower (field-defining) part of the linac head consists of a heavy metal alloy multi-leaf collimator (MLC) with 40 leaf pairs of rounded ends for conformal RT and heavy metal alloy secondary collimator X–Y jaws below the MLCs. The MLC leaves were modelled with the MLCQ CM and the jaws were modelled with the JAWS CM. The PS data was scored just below the secondary collimator jaws to be used as a 'radiation source' in phantom simulations. Each CM in BEAMnrc is designed to model a specific geometric shape, and the user arranges these CMs along the z-axis inside a module file that defines the whole linac structure. The linac is then 'built' by simulating each linac component with the existing CM describing its geometry. Only the linac components in the radiation beam path were modelled as shown in table 6.2.

**Table 6.2:** The linac components modelled in BEAMnrc

| Order of CM | CM type | Beam-line component modelled |
|---|---|---|
| 1 | SLABS | bremsstrahlung Target |
| 2 | CONESTAK | primary collimator |
| 3 | FLATFILT | flattening filter |
| 4 | CHAMBER | ion chamber |
| 5 | MLCQ | multi-leaf collimator |
| 6 | JAWS | secondary collimator jaws |

In the input file, the user also inputs the cross-section data and the geometry characteristics for each CM as well as specifications of the simulation parameters and the output. Upon execution of the code, an output is generated - which could be a PS file, an output listing or a graphical output. The overall steps required to perform an accelerator simulation are summarized in the schematic in figure 6.3.

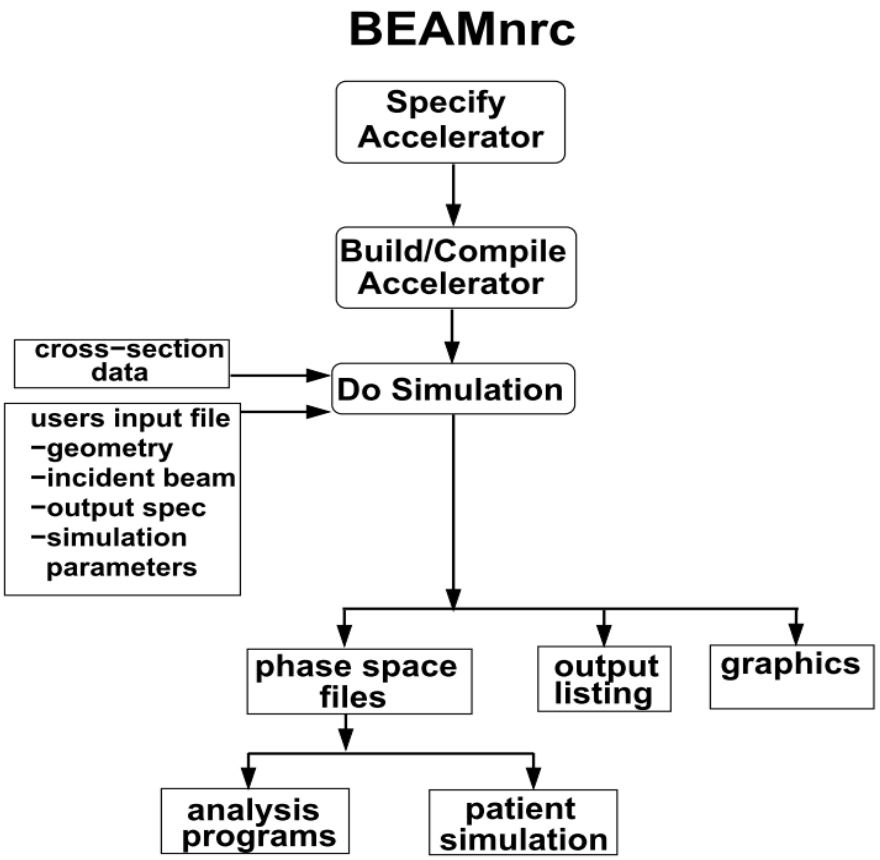


**Figure 6.3:** Steps involved in using the BEAMnrc system (Rogers *et al.* 1995)

The PS output data can be useful as a model of the fixed part of the linac head when scored behind stationary components, such as below the flattening filter and then used as a source to the moving components in the treatment head, such as MLCs and jaws. This can be more time efficient than re-running a simulation of the full accelerator when a parameter is changed, for example, the field size (FS).

In this study, the electron and photon energy cut-offs, ECUT and PCUT, were 0.7 and 0.01 MeV, respectively (Rogers, Walters and Kawrakow 2004). The value of the maximum

fractional energy a charged particle can lose per step, ESTEPE was set to its default value of 25%. The cross-section data of materials used was obtained from the ICRU PEGS4 cross-section data available in EGSnrc. However, new materials were generated in EGSnrcMP and appended to the ICRU700 PEGS4 data file. To keep the uncertainty below 1%, the total number of photon histories varied between $3 \times 10^8$ and $5 \times 10^8$ particle histories depending on the field size and energy mode of the simulation. Russian roulette was switched on and uniform bremsstrahlung splitting with a splitting factor of 50 was used in all BEAMnrc simulations. All other transport control parameters were set to their default values. Range rejection was not used because it only saves 3–4% of the computing time for 2.5 $mm^3$ voxels, and even less time for smaller voxels used in this study.

#### 6.2.1.1 Simulating the 20 MV photon beam

The physical linac being simulated has only three nominal photon energies – 6, 10 and 15 MV. However, this study involved investigating the dose attenuation effect of hip prostheses at energies up to 20 MV. Therefore, the Precise linac model was modified, particularly the dimensions of the flattening filter (other linac components remain invariant), to create a 20 MV virtual machine. Podgorsak (2005) states that standard linac specifications generally require that the beam flatness must be less than 3% when measured in a water tank at 10 cm depth and a source-to-surface distance (SSD) of 100 cm for the largest field size available. Therefore, a flattening filter having the optimum dimensions required to satisfy the above flatness requirement for a 20 MV photon beam was determined. This was performed using a trial and calculation method i.e., by simulating various flattening filter thicknesses and calculating their corresponding beam profiles in water until the profile flatness at 10 cm depth ≤ 3%.

#### 6.2.1.2 BEAMDP

The PS data generated from BEAMnrc characterizes the treatment unit; therefore by analysing this PS file, the characteristics of the incident beam can be obtained. The PS file contains all the information relating to the incident beam for all particles crossing a

defined plane e.g., particle energy, position, charge, direction, LATCH information etc. (Rogers *et al.* 1995; Ding & Christine 2001). LATCH contains information about the origin of a particle i.e., the region numbers where the particle has been to, has interacted, or was created if it is a secondary particle. A photon's origin is considered to be the region where it is created or last scattered and for a charged particle it is the last non-air region it has been to before crossing the scoring plane (Ma & Rogers 1995).

BEAMDP was used in this study to perform simple analysis of the PS parameters of the clinical beam generated from the linac head. The source parameter data extracted with BEAMDP e.g., the energy, angular, and spatial distribution of particles was then plotted with *Grace* for 6, 10, 15 and 20 MV photon beams of various FS. Beam characterization is required for patient dose calculations in modern dose calculation algorithms. BEAMDP can also be used to derive the data required by a multiple-source model for beam representation and beam reconstruction for use in MC RT planning (Ma & Rogers 1995).

BEAMDP can derive the following from PS data: particle and energy fluence vs. position, spectral distribution, energy fluence distribution, mean energy distribution, angular and particle weight distribution. It can also combine two PS files into one.

### 6.2.2 DOSXYZnrc simulation

The second stage of the calculation involved using DOSXYZnrc, which is a Cartesian coordinate EGSnrc-based MC simulation user-code for calculating 3D absorbed dose distributions in a rectilinear voxel phantom (Lin *et al.* 2002, Walters & Rogers 2004). DOSXYZnrc was used in this study to calculate the dose distribution in a patient model (with and without HPs) built from actual CT images of the patient using the PS data generated by BEAMnrc as the radiation source. DOSXYZnrc was also used to calculate the dose distribution in a homogenous cubic water tank (WT) for photon beam standardization prior to CT-based simulations. The DOSXYZnrc GUI (figure 6.4) was used to compile and run phantom simulations. DOSXYZnrc can be run interactively or as a queue batch (as a parallel run).

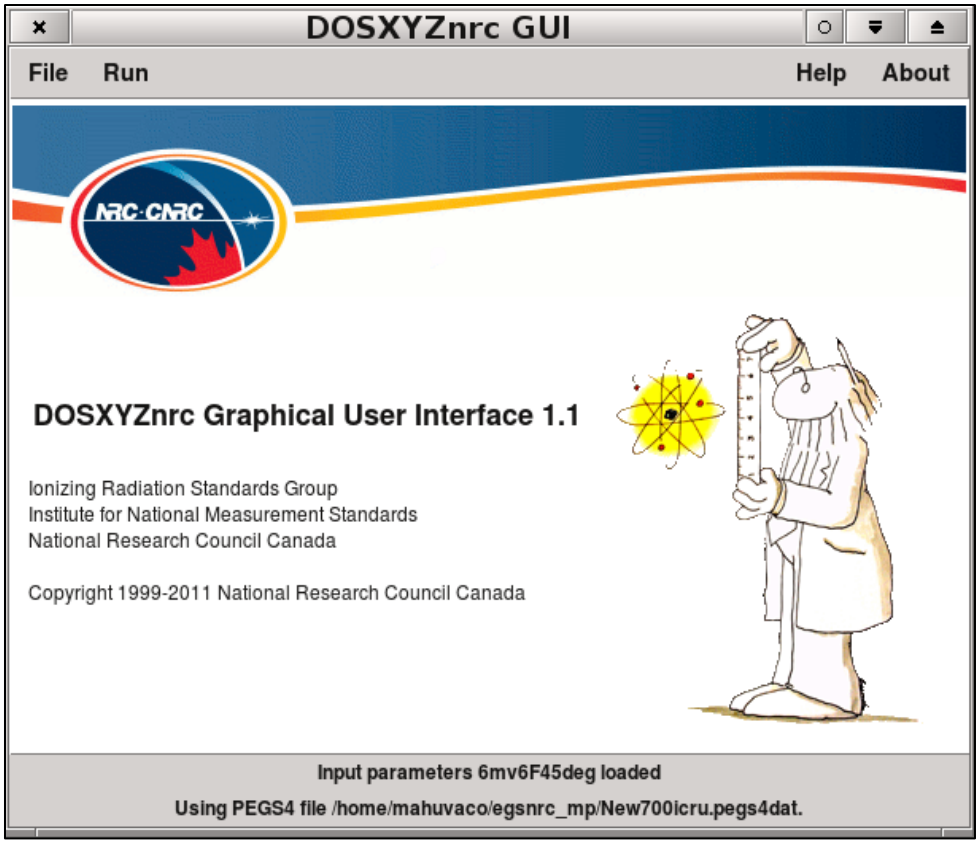


**Figure 6.4:** DOSXYZnrc graphical user interface

The 3D dose files produced by DOSXYZnrc were analysed by MCSHOW software for extracting percentage depth dose, dose profile and dose volume histogram data. Microsoft Excel and *Grace*, which is short for "GRaphing, Advanced Computation and Exploration of data", and a derivative of Xmgr, were used as the plotting tools.

The computing times to calculate the dose distributions in the phantom depend on the dose uncertainties required and number of histories used. In this study, the maximum statistical uncertainty associated with DOSXYZnrc simulations was reduced to below 1%. A 2.40 GHz Intel(R) Xeon(R) CPU with 16 GB RAM was used to simulate 3 billion histories in a CT-based phantom. The ECUT and PCUT values used were 0.7 and 0.01 MeV respectively. No other variance reduction parameters were set.

### 6.2.2.1 Water tank simulations

For analysis of photon beam characteristics and model validation, a homogenous water phantom with dimensions $40 \times 40 \times 40\ cm^3$ was simulated under the linac treatment head at 100 cm SSD (see figure 6.5). Small voxels of size $0.2 \times 0.2 \times 0.2\ cm^3$ were used in penumbral regions to obtain a good resolution of the dose and $0.5 \times 0.5 \times 0.5\ cm^3$ voxel sizes were used near the central axis (CAX). The secondary collimator jaws and MLC openings were set to create several sizes of x-ray fields: $5 \times 5\ cm^2$, $10 \times 10\ cm^2$, $15 \times 15\ cm^2$ and $20 \times 20\ cm^2$ on the phantom surface.

Simulations were performed for 6, 10, 15 and 20 MV photon beams incident perpendicularly on the WT surface. CAX PDD plots normalized at $d_{max}$ were presented for a given photon energy and different field sizes. In-plane and cross-plane dose profiles at 10 cm depth were also plotted on the same axes at varying field sizes and energies. The MC linac model was validated by comparing these simulated dosimetric features (PDD and dose profile data) with measured water tank dose values.

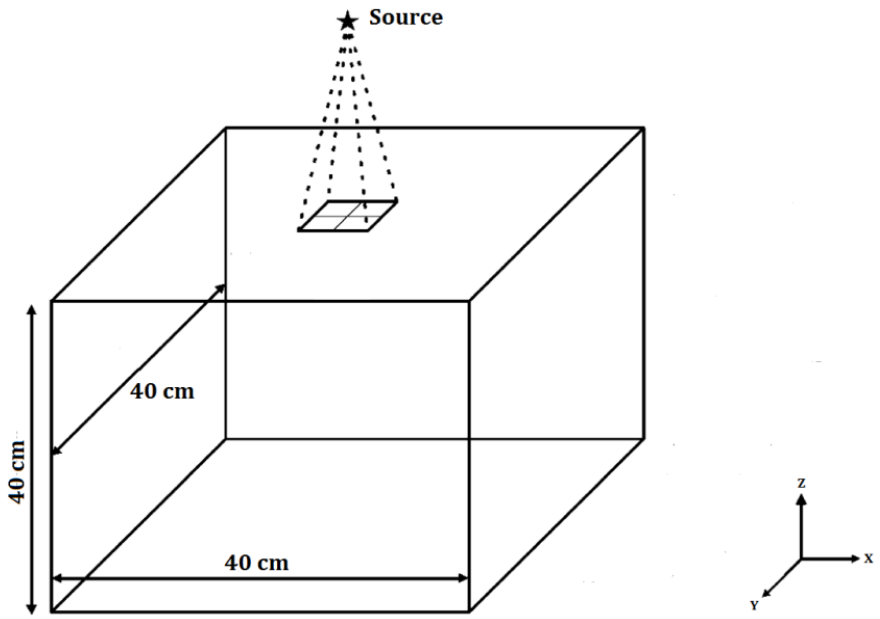


**Figure 6.5:** Geometry used in DOSXYZnrc water tank simulations for beam characterization. The source is located 100 cm (SSD) from the WT surface.

### 6.2.2.2 Photon beam quality

Most studies pertaining irradiation of prosthetically augmented hips have poorly-specified parameters regarding beam characteristics used during irradiation. Parameters such as beam flatness and symmetry are needed to validate results since dose perturbations due to tissue inhomogeneity also depend on the photon beam quality. The *beam flatness* ($F$) was calculated using the formula:

$$F = 100 \times \frac{\mathrm{D_{max}} - \mathrm{D_{min}}}{\mathrm{D_{max}} + \mathrm{D_{min}}} \tag{18}$$

Where $\mathrm{D_{max}}$ and $\mathrm{D_{min}}$ are the respective maximum and minimum dose point values on the beam profile within the central 80% of the full width at half maximum (FWHM) (see figure 6.6).

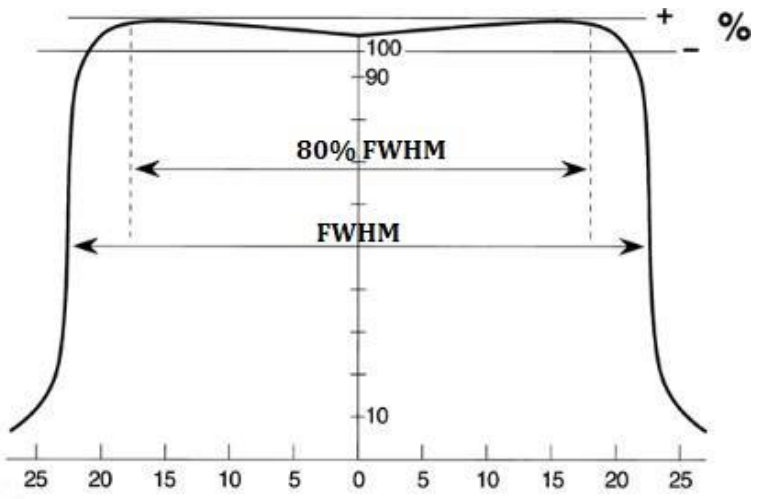


**Figure 6.6:** Definition of beam flatness on a photon beam profile (Khan 2010)

The *beam symmetry* ($S$) was calculated in using the formula:

$$S = 100 \times \frac{|\mathrm{area_{left}} - \mathrm{area_{right}}|}{|\mathrm{area_{left}} + \mathrm{area_{right}}|} \tag{19}$$

Where $area_{left}$ and $area_{right}$ are areas under the beam profile on each side of the CAX extending to the 50% dose level when normalized to 100% at the CAX point(Podgorsak 2005) (see fig. 6.7).

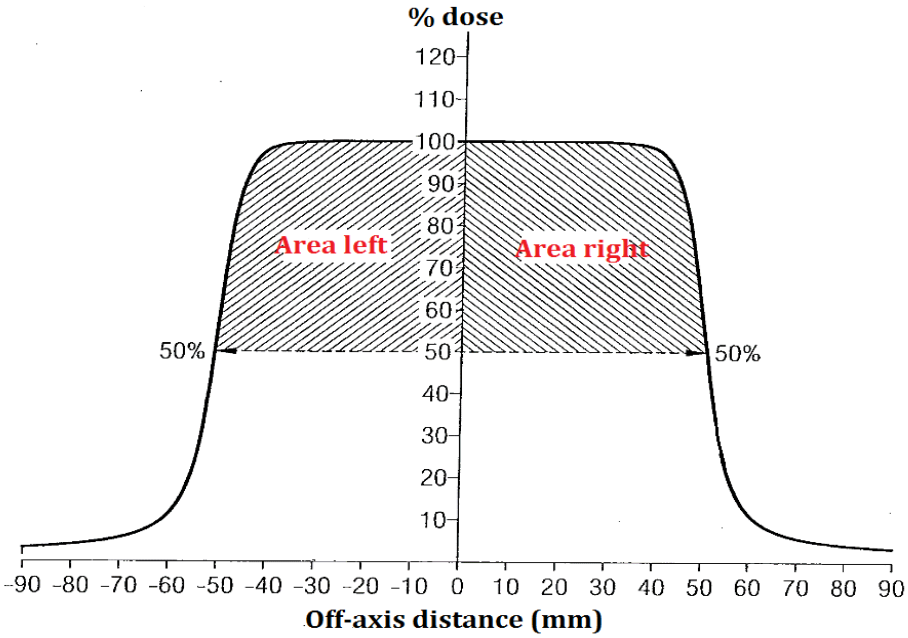


**Figure 6.7:** Definition of beam symmetry on a photon beam profile

The AAPM TG-40 protocol (Kutcher *et al.* 1994) recommends that the x-ray beam flatness must be ≤ 2% and the beam symmetry must be ≤ 3% within the central 80% of the largest field size in a water phantom.

### 6.2.2.3 CT-based simulations

A pelvic CT-based virtual phantom was used as the patient model. A transverse slice of the CT phantom used in this study is displayed in MCSHOW GUI in figure 6.8. The phantom was imported into DOSXYZnrc as an **.egsphant* file for dose calculations. The phantom had a regular voxel size of 0.2 × 0.2 × 0.2 $cm^3$. The output dose distribution data was stored in **.3ddose* files whence PDD, DVH and dose profile data was extracted.

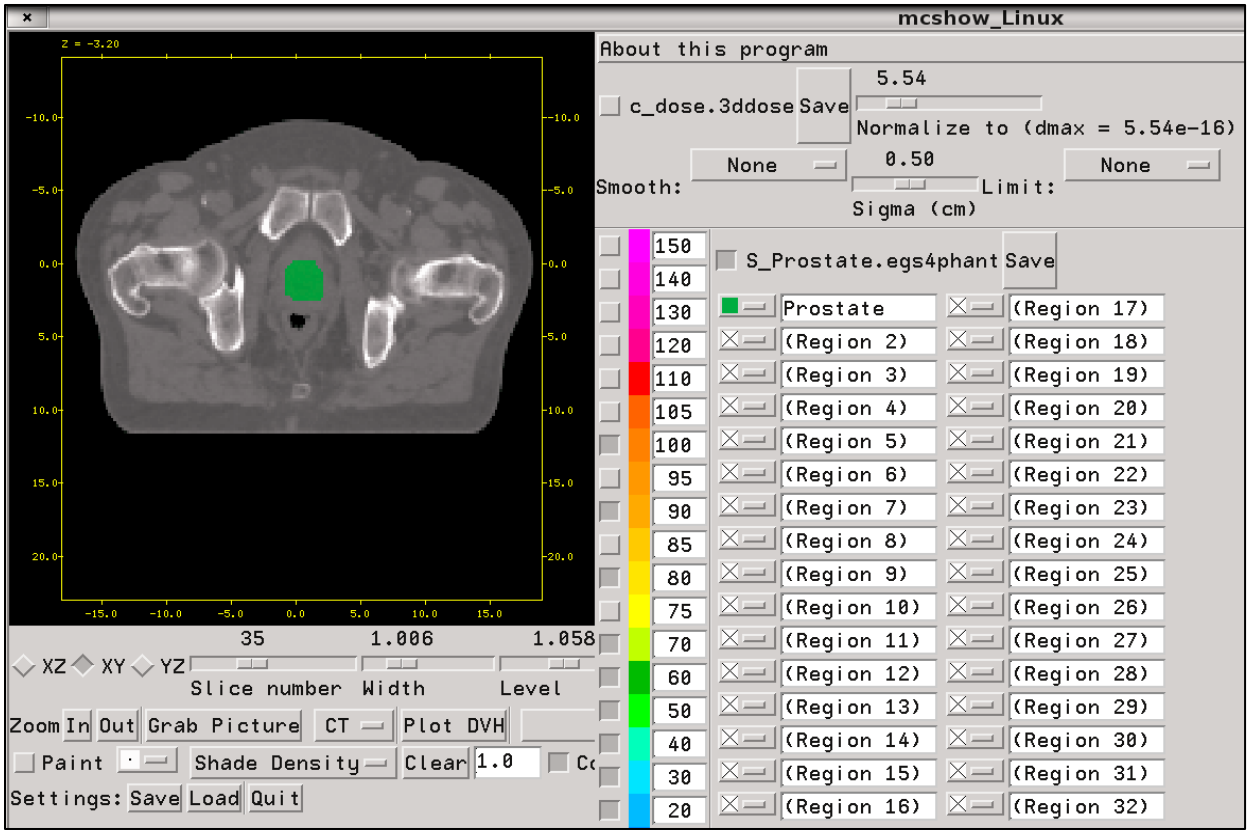


**Figure 6.8:** MCSHOW GUI showing a transverse slice of the original CT data (without HP) used in DOSXYZnrc simulations. The green region is the prostate.

#### 6.2.2.4 Combining **.3ddose* files

A FORTRAN code (*dcombine.f*) (see Appendix C.1) was developed and used to combine the **.3ddose* files produced from DOSXYZnrc phantom simulations. Each treatment field in a multiple-field plan (e.g., 4F box) produces a **.3ddose* output file during DOSXYZnrc simulation. These individual dose files were combined by the FORTRAN code into a single dose file that contains the total dose distribution from all the treatment fields in the plan.

### 6.2.3 Generating a CT–based phantom with hip prostheses

The method used in this study enables the complete exclusion of imaging artifacts since the prosthesis is synthetically introduced into the femur of the raw patient-CT data by substituting bone tissue with the prosthesis material using a masking method. Generating

a CT phantom with HP in this study was a two-step process; contouring the shape of the prosthesis into the femur of a normal pelvis and then converting the density of the drawn volume to the density of the desired HP. An IDL code was developed to produce artefact-free CT-based phantoms containing HPs. The dimensions of the hip prostheses were approximated by overriding bony tissue media in the pelvis using a masking method.

#### 6.2.3.1 Delineating prosthesis contours

As discussed in Chapter 5, CT imaging of patients with high-Z devices is hampered by streak artefacts on the image sets. As a result, it is difficult to get an artefact-free CT image of a patient with metallic HPs. To circumvent this problem, the CT dataset of a patient without HPs was modified to obtain an artefact-free CT phantom implanted with hip prostheses.

MCSHOW was used to delineate a hip prosthesis in the patient and an IDL code was used to convert the delineated volume into a tissue type to re-write the *.*egs4phant* file for use in DOSXYZnrc, thus eliminating streak artefacts from CT scan in the presence of prostheses. The HPs were manually inserted into the CT patient model by drawing the shape of a HP into the femur of an existing CT dataset of a patient with normal hips on MCSHOW GUI (see figure 6.9).

MCSHOW is a Unix-based phantom and dose display package adapted from dosxyz_show by Ma *et al.* (2002) at Fox Chase Cancer Center to display isodose distributions on patient CT datasets. It can read and modify the *.*egs4phant* format of CT-based phantoms exported by CTCREATE. CTCREATE is a stand-alone program which converts DICOM, CADPLAN, AAPM, and ADAC Pinnacle CT file formats from patient scan into *.egsphant formats that can be read by DOSXYZnrc to perform a simulation. The MCSHOW GUI allows for contouring, slice by slice, the shape of the prosthetic implant, reproduced from a CT dataset of a patient with a HP, onto the CT dataset of the actual patient *.*egs4phant* file. Two patient models were generated: one with uHP and another with bHPs. Both models were elaborated from the same CT dataset and were made to represent THR.


**Figure 6.9:** MCSHOW GUI showing transversal delineation of bHPs into the original CT data

Features on MCSHOW include the following: extracting depth dose and dose volume histogram data, smoothing dose distributions, comparing two dose distributions, modifying structure information, changing material density, capturing image and saving files, displaying isodose only, generating CT phantoms etc.

### 6.2.3.2 Converting contours into prosthesis material

Having delineated HP contours and saving the resulting phantom in *.*egs4phant* format, the drawn volumes were converted into the desired prosthesis material using a locally-developed IDL code (*editegs4phantfile.pro*) (see Appendix C.2). The code reads in an *.*egs4phant* file, the phantom media, the media density data, as well as the mask (delineated HP volume) media data. The code then changes the mask media type into the HP media as well as the mask physical density into the physical density of the desired prosthesis material and write the output as a new phantom file which is exported to

DOSXYZnrc for irradiation (see figure 6.10). (DOSXYZnrc reads phantom files in *egsphant* format; MCSHOW reads phantom files in *.*egs4phant* format.)

This flexibility to add any materials of any desired shape into the phantom allows one to perform MC simulations for several implant models and patient geometry. This illustrates another powerful application of the MC method in studying complex dosimetric problems.

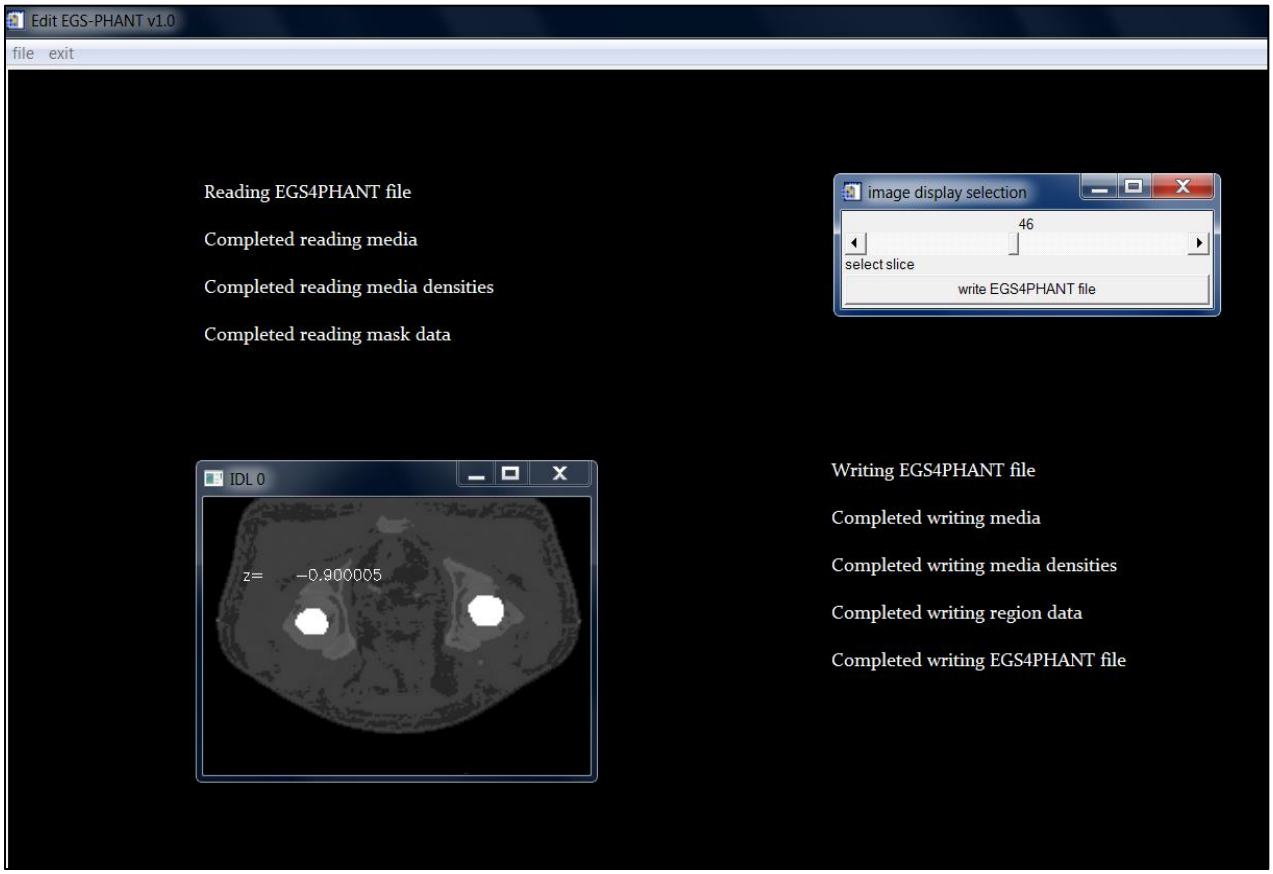


**Figure 6.10:** IDL output showing how the code generates a phantom with bHPs

The materials for HPs used in this study were stainless steel (SS316L), titanium alloy (Ti6Al4V) and UHMWPE. Specific PEGS4 data were calculated for each one. The detailed compositions of the materials are needed to generate cross-section data for MC simulation. Table 6.3 gives the composition of Ti6Al4V, SS316L and UHMWPE.

**Table 6.3:** Material compositions used to generate implant PEGS4 data (Alvarado *et al.* 2003)

| | Ti6Al4V | SS316L | UHMWPE |
|---|---|---|---|
| Mass density ($g/cm^3$) | 4.34 | 8.10 | 0.95 |
| Composition (% by weight) | H 0.012 | Cr 16-18 | $(C_2H_4)_n$ |
| | C 0.01 | Fe balance | |
| | O 0.11 | Mn 2 max. | |
| | Ti 89.947 | Mo 2-3 | |
| | V 3.92 | Ni 10-14 | |
| | Al 5.80 | P 0.045 max. | |
| | Fe 0.18 | Si 1 max. | |
| | Y 0.001 | S 0.03 max | |

*where n in $(C_2H_4)_n$ is the number of monomer units

The PEGS4 data for these HPs were generated on EGSnrcMP GUI (see figure 6.11). The user inputs the percentage compositions (by weight) of each of the elements that comprise the material, the mass density of the material, the medium type as well as the energy cut-offs.

The program then generates the material cross-section data based on the user inputs and writes a new PEGS4 data file or appends the output data to an existing data file which will be read by the DOSXYZnrc code during phantom simulation.

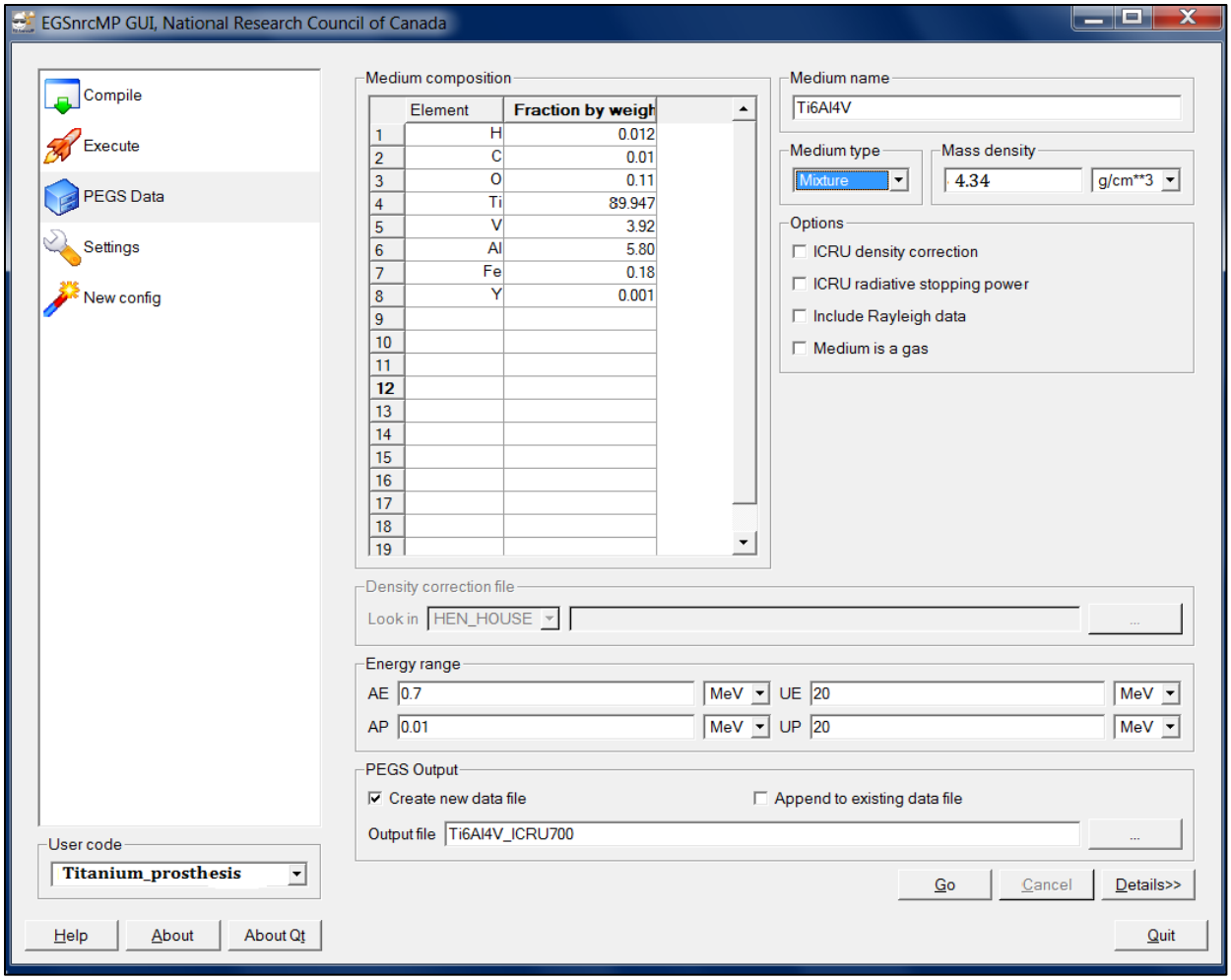


**Figure 6.11:** EGSnrcMP GUI showing how a composite material is generated

### 6.2.3.3 CTCREATE

CTCREATE is a stand-alone program which converts CT dataset from patient scan into the data needed by DOSXYZnrc to perform a simulation (i.e. material and density in each voxel). At the present time it handles DICOM, CADPLAN, AAPM, and ADAC Pinnacle CT file formats, converting them into *.*egsphant* formats that can be read by DOSXYZnrc. In this study, three *.*egsphant* files were generated from DICOM CT files; one phantom file with the prostate, another with the bladder (first OAR) and the third with the rectum (second OAR). All CT phantoms had voxels of size $0.2 \times 0.2 \times 0.2$ cm$^3$.

### 6.2.4 Hardware

A 16-core Linux computer equipped with Intel(R) Xeon(R) CPUs, each with clock speed of 2.40 GHz and 16 GB RAM was used as the MC dose calculation engine and to run the FORTRAN code which combined *.*3ddose* files generated from each treatment field. A dual-core Windows 7 computer with Intel(R) Pentium(R) D CPUs, each with clock speed of 3.60 GHz and 4 GB RAM was also used to run the IDL code which was used for modifying the mask density information in a CT phantom. XiO TPS, which is a CMS trademark application, was used to generate plans, i.e., to calculate appropriate MLC and jaw settings for conformal prostate treatment.

In case of temporary power outages, an uninterruptible power supply was used to provide emergency power for a period of about 15 minutes. This gives the user the time to save all files, record all important data and quit the simulations, or to fix the cause of the power outage before the uninterruptible power supply power gets depleted. All other hardware, including printing equipment and all stationery were locally available at Universitas Academic Hospital Annex.

## 6.3 Treatment planning

PTV irradiation was performed with 3DCRT fields at 100 cm source-to-axis distance. The radiation isocenter was always located at the centre of the target volume. The mid-leaf positions of the MLCs conform to the PTV in each port's beams-eye-view. All plans were generated on the same patient's anatomy from a planning CT scan for 6, 10, 15 and 20 MV photon beams. The prostate was delineated as the clinical target volume (CTV). All plans were coplanar, and were designed to encompass 100% of the PTV with 1 cm isotropic margin around the prostate alone (excluding seminal vesicles). This margin size is commonly used in prostate treatments (Kung *et al.* 2002; Su *et al.* 2005). The plans were prepared on XiO TPS. The plans in this study were adapted from Reft *et al.* (2003), who presented them as techniques for treating of prostate cancer in patients with hip

prostheses. The beams were forced to intercept the prostheses because the aim was to evaluate the attenuation effect of prostheses during complete HP irradiation.

### 6.3.1 Six field plan

This treatment plan was composed of 6 isocentric equiangular fields in a standard pelvic configuration. The gantry angles were set at 45°, 90°, 135°, 225°, 270° and 315°, i.e. two opposed lateral fields and two pairs of opposed oblique fields (see figure 6.12).

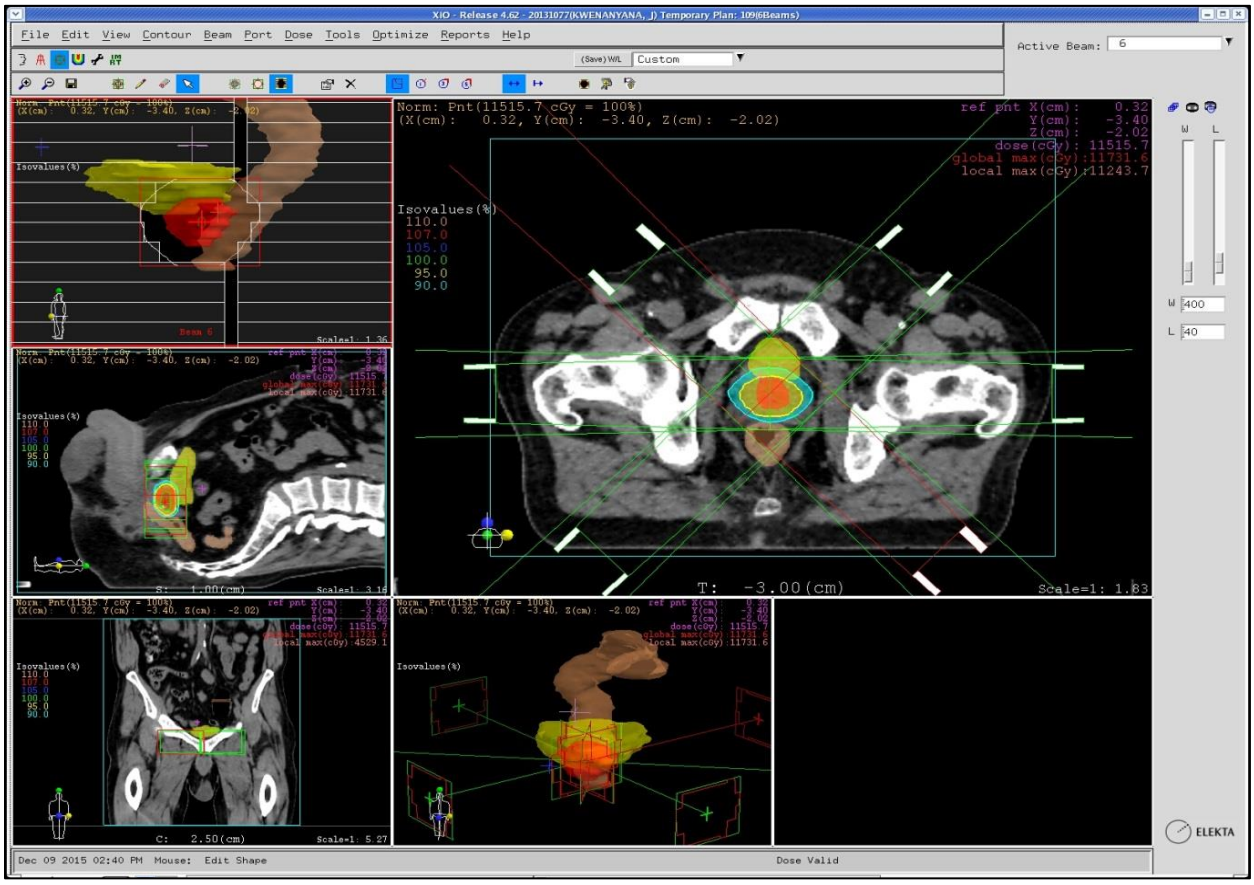


**Figure 6.12:** XiO TPS showing the 6F plan to be incorporated into MC simulations

An XiO TPS was used to define treatment beam portals for prostate 3DCRT to allow translation of the beam setup to DOSXYZnrc for phantom simulations. MLC and jaw aperture data was imported into BEAMnrc for simulating 3DCRT linac beams incident on the phantom. The gantry angle, collimator angle, couch angle, and isocenter position

were imported into DOSXYZnrc for each of the treatment fields. However, MC simulations using data from TPS–generated plans require transformation of beam orientations to the EGSnrc coordinate system. This is described in section 6.4.

Collimator aperture values from XiO TPS were then converted to actual field settings on an Elekta Preci*s*e linac in BEAMnrc on an excel spreadsheet.

The phantom (*.*egs4phant*) file and total dose distribution (*3ddose*) file for each treatment plan and energy were imported into MCSHOW. The *.*egs4phant* file is an ASCII file containing all the relevant information needed by DOSXYZnrc to simulate the phantom, including the number of media in the phantom, the media names and their ESTEPE vales, the number of voxels and their boundaries in each of the Cartesian directions and the media density in each voxel. The *.*3ddose* file contains the 3D dose information generated by DOSXYZnrc. MCSHOW superimposes the isodose distribution on the phantom and allows the user to extract dose profile data at any depth, the dose volume histogram data as well as depth dose data, and also to normalize the dose values to a set value. The output dose data was plotted using Grace.

### 6.3.2 Five–field plan

XiO TPS was also used to construct five equiangular fields at gantry angles 54°, 126°, 198°, 270° and 342° i.e., all beam portals in this plan are 72° apart. The 5F plan is useful for a patient with a left uHP to avoid intersection through the HP and is also effective for a patient with bilateral prostheses since, unlike the 6F plan, the 270° beam is not affected by the addition of the second HP.

### 6.3.3 Four–field box plan

A four-field box (4F box) technique was constructed at gantry angles 0°, 90°, 180° and 270° i.e. two bilateral portals passing through the pelvis and two anterior-posterior/posterior-anterior beams for a regular supine head-first patient setup.

## 6.4 Coordinate transformations from DICOM to DOSXYZnrc

DICOM format is the existing standard for communications between different diagnostic and therapeutic modalities. It is the format in which plans from a TPS are usually exported (Pianykh 2009). However, the MC packages used for linac head modelling and RT dose calculation, BEAMnrc and DOSXYZnrc, have their own definition of beam orientation which is non-compliant to the DICOM coordinate system (see Figure 6.13). The EGSnrc code system cannot read plans in DICOM format. Therefore, MC simulations that utilize data imported from TPS–generated plans demand transformation of the coordinate system from DICOM to DOSXYZnrc to convert the patient setup and beam arrangement information. However, the extraction of information and conversion of parameters from DICOM to DOSXYZnrc is non-trivial (Zhan, Jiang and Osei 2012).

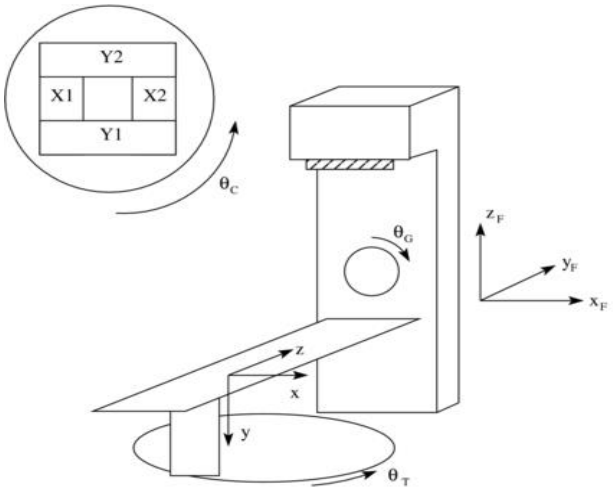


**Figure 6.14:** Illustration of the DICOM coordinate system (Zhan, Jiang and Osei 2012). X1/X2 and Y1/Y2 are the collimator jaws which define the field opening in the x and y–directions respectively. ($X_F$, $Y_F$, $Z_F$) is a fixed coordinate system, fixed with respect to the machine.

The most compact and easily understandable coordinate transformation equations were derived by Zhan, Jiang and Osei (2012) and were computationally implemented and verified on plans generated from Eclipse and Pinnacle TPS. By taking $\theta_G$ as the gantry

angle and $\theta_T$ as the treatment couch angle as shown in figure 6.13, the polar angle $\theta$ and the azimuthal angle $\varphi$ were derived:

$$\theta = \cos^{-1}(\sin\theta_T \sin\theta_G) \tag{20}$$

$$\varphi = \tan^{-1}\left(\frac{-\cos\theta_G}{\cos\theta_T \sin\theta_G}\right) \tag{21}$$

BEAMnrc does not use similar coordinates in its generated PS as DOSXYZnrc; the BEAMnrc PS source must be mapped into the equivalent DOSXYZnrc coordinates. By taking this into account, this transformation yields a collimator rotation angle of:

$$\phi_{\text{col}}^{(\text{beam})} = \frac{3\pi}{2} - \theta_C - \tan^{-1}\left(\frac{-\sin\theta_T \cos\theta_G}{\cos\theta_T}\right) \tag{22}$$

Equations (20) to (22) were used to transform TPS angles in the CT data to their DOSXYZnrc equivalents in MC simulations as shown in table 6.4 below.

**Table 6.4:** DICOM beam arrangements and their conversion to DOSXYZnrc

| | | DICOM | | | DOSXYZnrc | | |
|---|---|---|---|---|---|---|---|
| Treatment plan | Beam | $\theta_G$ | $\theta_T$ | $\theta_C$ | $\theta$ | $\varphi$ | $\phi_{\text{col}}^{(\text{beam})}$ |
| 4F box | 1 | 0 | 0 | 0 | 90 | -90 | 270 |
| | 2 | 90 | 0 | 0 | 90 | 0 | 270 |
| | 3 | 180 | 0 | 0 | 90 | 90 | 270 |
| | 4 | 270 | 0 | 0 | 90 | 180 | 270 |
| 6F plan | 1 | 45 | 0 | 0 | 90 | -45 | 270 |
| | 2 | 90 | 0 | 0 | 90 | 0 | 270 |
| | 3 | 135 | 0 | 0 | 90 | 45 | 270 |
| | 4 | 225 | 0 | 0 | 90 | 135 | 270 |
| | 5 | 270 | 0 | 0 | 90 | 180 | 270 |
| | 6 | 315 | 0 | 0 | 90 | 225 | 270 |

## 6.5 Dose perturbation factors

The back-scattered dose perturbation factor (BSDF) at the entrance side of the high-Z material and the forward dose perturbation factor (FDPF) on the exit side of the inhomogeneity were calculated. The BSDF may be defined as the ratio of the dose at a given distance from the interface to the dose at the same point with no HP for identical setup conditions. Mathematically, BSDF (or FDPF) $= D_i/D_h$ where $D_i$ and $D_h$ are the respective doses with and without the presence of the implant. These dose perturbation factors were calculated at points along the horizontal line passing through the isocentre.

# 7. Results and discussion

## 7.1 Overview

In this chapter, results are presented in form of central axis PDD curves, lateral dose profiles, dose volume histograms and dose perturbation factors. The MC model of the Elekta Prec*i*se linac head and beam production for 6–20 MV high energy x-rays beams simulated by BEAMnrc is also presented and the beam parameters were benchmarked against the machine's commissioning data from water tank measurements.

The 3D absorbed dose distributions were calculated in a CT-based phantom model implanted with HPs. The dose calculation sites were within and near the inhomogeneity for 6, 10, 15 and 20 MV conformal photon beams at different beam arrangements. Beam parameters for MC dose calculation were cloned from three treatment plans generated by a XiO TPS namely: 4F box, 5F plan and 6F plan.

The utility of the 5F plan was evaluated for a patient with bilateral hip prostheses. Both unilateral and bilateral HP models of SS316L, Ti6Al4V and UHMWPE were considered in the simulations and dose perturbation factors were calculated on the proximal and distal interfaces. The PTV dose reduction due to lateral beam attenuation was evaluated for all the HPs. The dependence of the shadowing effect, electron backscatter and forward scatter on beam energy and implant material density was also assessed.

## 7.2 Linac modelling

A full model of the Elekta Prec*i*se linac treatment head built by BEAMnrc is displayed in figure 7.1 as rendered by the BEAMnrc accelerator preview. This machine was used as the radiation source in all MC simulations. The PS data used in phantom simulations was scored below the secondary collimator jaws.

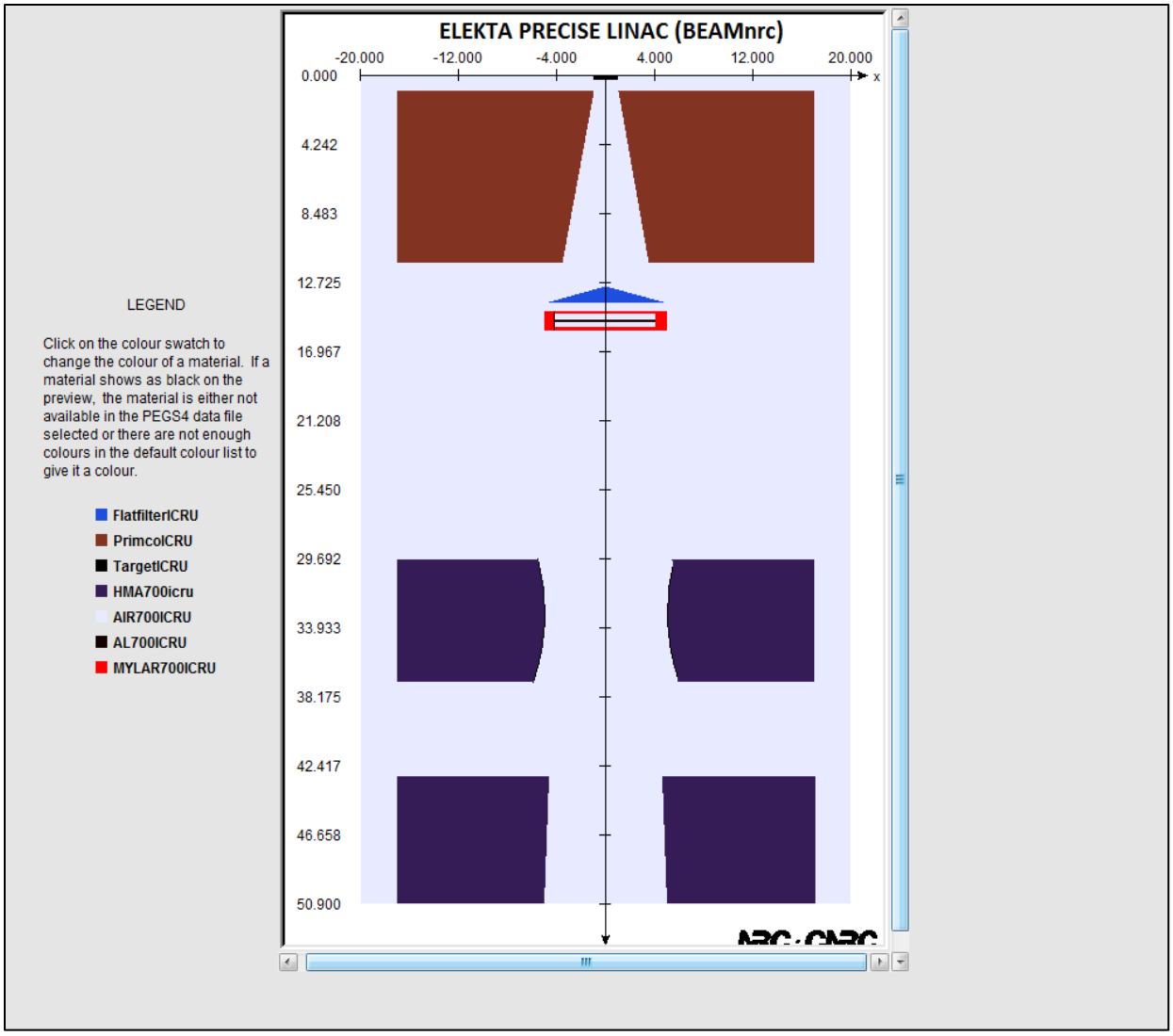


**Figure 7.1:** Cross-sectional view of the BEAMnrc Elekta Prec*i*se linac model

The field mirror and wedge were omitted in the simulations since they are not relevant to this study.

## 7.3 Phantom modelling

Two phantom simulations were performed: WT simulations for photon beam characterization and CT-based simulations to calculate the dose distribution in the pelvic region of a CT phantom with prosthetic hips.

### 7.3.1 Water tank simulations

For analysis of incident photon beam characteristics and linac model validation, simulations in a homogenous water tank were performed using the phase space data scored at the linac head exit window as the 'source'. The MC linac model was validated by comparing simulated dosimetric features (PDDs and dose profiles) with water bath measurements. Presented below are simulated in-plane and cross-plane beam profiles in the water phantom for different field sizes and energies. The profiles were measured at 10 cm depth and were normalized to $d_{max}$. Average dose smoothing was implemented on the simulated water tank data. The 20 MV beam profiles do not seem typical of clinical data because they are simulated from a virtual machine. Comparisons between MC–simulated and measured dose profile and CAX PDD plots are given in Appendix D.11.

#### 7.3.1.1 In-plane dose profiles

Figures 7.2 (a – d) present the simulated in-plane dose profiles for the given range of beam energies and field sizes (FS) in a water tank. In this study, an in-plane profile is defined as being along the beam data y-axis and a cross-plane profile is along the x-axis. The 20 MV data is an additional beam energy that was simulated and is not found on the linac. The purpose thereof was to expand this study to higher photon beam energies.

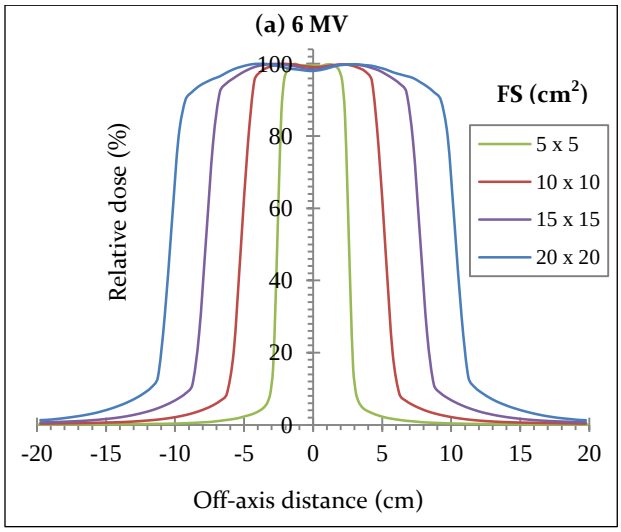


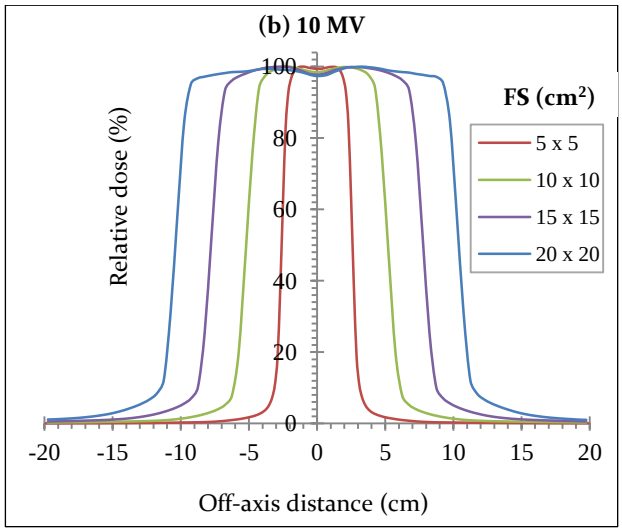

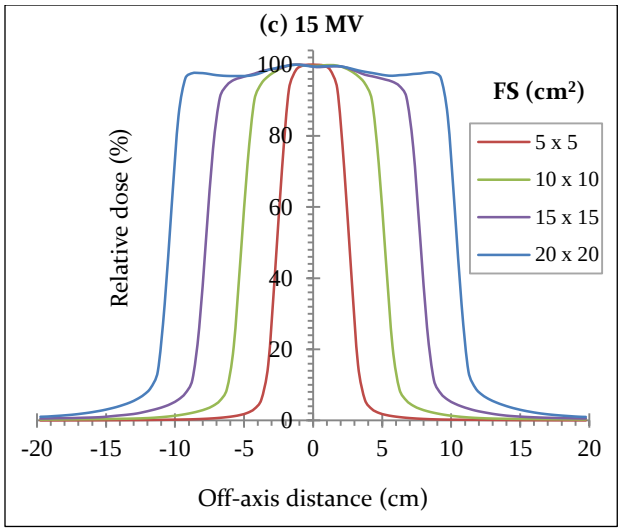


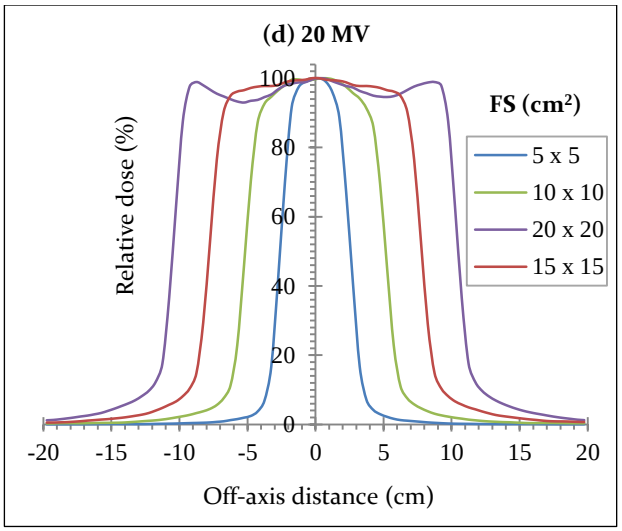


**Figure 7.2:** Simulated in-plane dose profiles for 6 - 20 MV photon beams at various FS in a water tank. The profiles were measured at 10 cm depth and were normalized to $d_{max}$.

### 7.3.1.2 Cross-plane dose profiles

Figures 7.3 (a – d) present the simulated cross-plane dose profiles for the given range of beam energies and FS in a water tank.

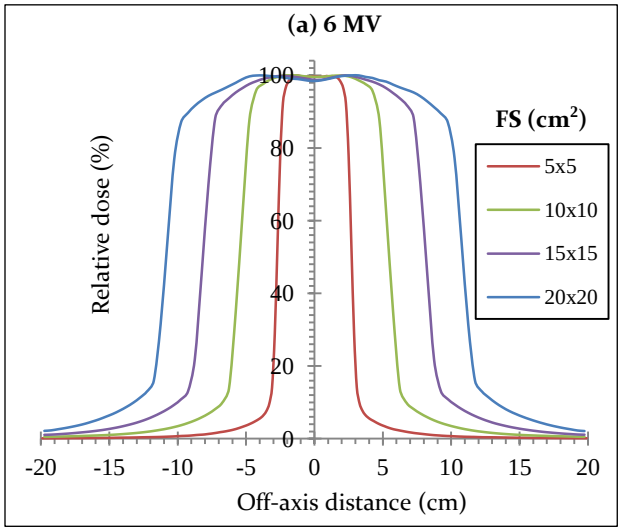


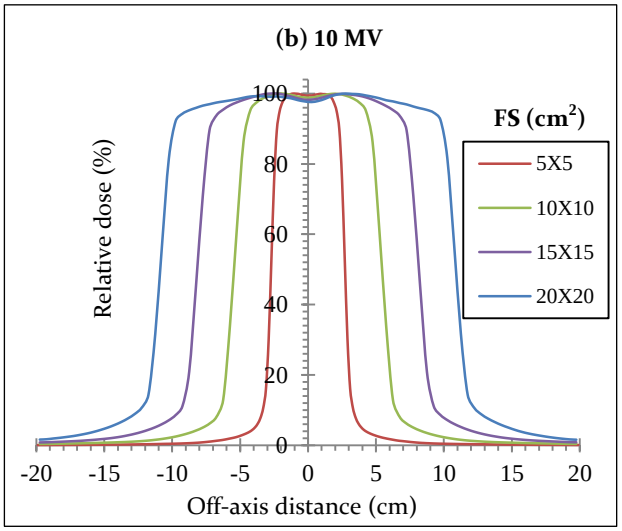

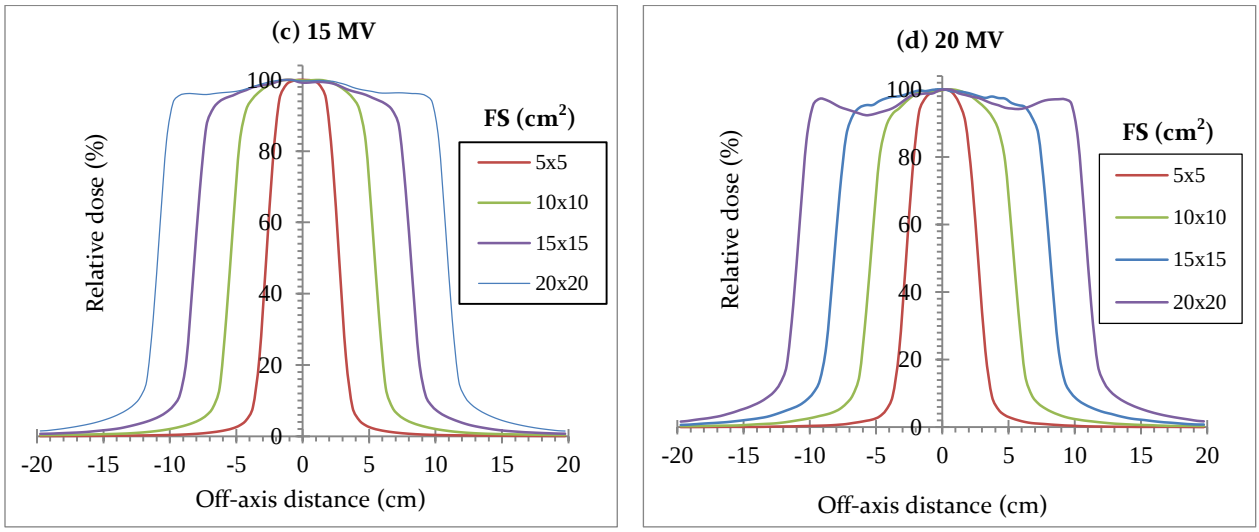


**Figure 7.3:** Simulated cross-plane dose profiles for 6 - 20 MV photon beams at various FS in a water tank. The profiles were measured at 10 cm depth and were normalized to $d_{max}$.

### 7.3.1.3 Beam quality

The AAPM TG-40 protocol (Kutcher *et al.* 1994) recommends that the x-ray beam flatness must be ≤ 2% in a water phantom at z = 10 cm and 100 cm SSD within the central 80% of the largest field size, and the beam symmetry must be ≤ 3% over 80% of the field. Flatness and symmetry values were calculated at 10 cm depth for the largest field simulated ($20 \times 20$ cm$^2$) for both in-plane and cross-plane profiles as part of the characterization process of the BEAMnrc linac. The results are presented in table 7.1 (a) and (b).

**Table 7.1:** In-plane and cross-plane (a) beam flatness and (b) beam symmetry values at 6 – 20 MV and $20 \times 20$ cm$^2$ field in a WT. All tolerance values are according to the AAPM TG-40 protocol.

| | (a) Beam flatness (%) @ 10cm depth | | |
|---|---|---|---|
| **Energy (MV)** | In-plane | Cross-plane | Tolerance |
| 6 | 1.6 | 1.7 | 2.0 |
| 10 | 1.7 | 1.9 | 2.0 |
| 15 | 1.8 | 2.0 | 2.0 |
| 20 | 2.2 | 2.3 | 2.0 |

| | (b) Beam symmetry (%) @ 10cm depth | | |
|---|---|---|---|
| **Energy (MV)** | In-plane | Cross-line | Tolerance |
| 6 | 1.3 | 1.5 | 3.0 |
| 10 | 1.4 | 1.8 | 3.0 |
| 15 | 1.9 | 1.9 | 3.0 |
| 20 | 2.4 | 2.5 | 3.0 |

All beam flatness and symmetry values were within the tolerance levels except for the beam flatness values of the 20 MV virtual linac model.

### 7.3.1.4 Percentage depth dose curves

Figures 7.4 (a – d) present the simulated central axis PDD curves at photon beam energies ranging from 6 to 20 MV at various field sizes in a virtual water phantom.

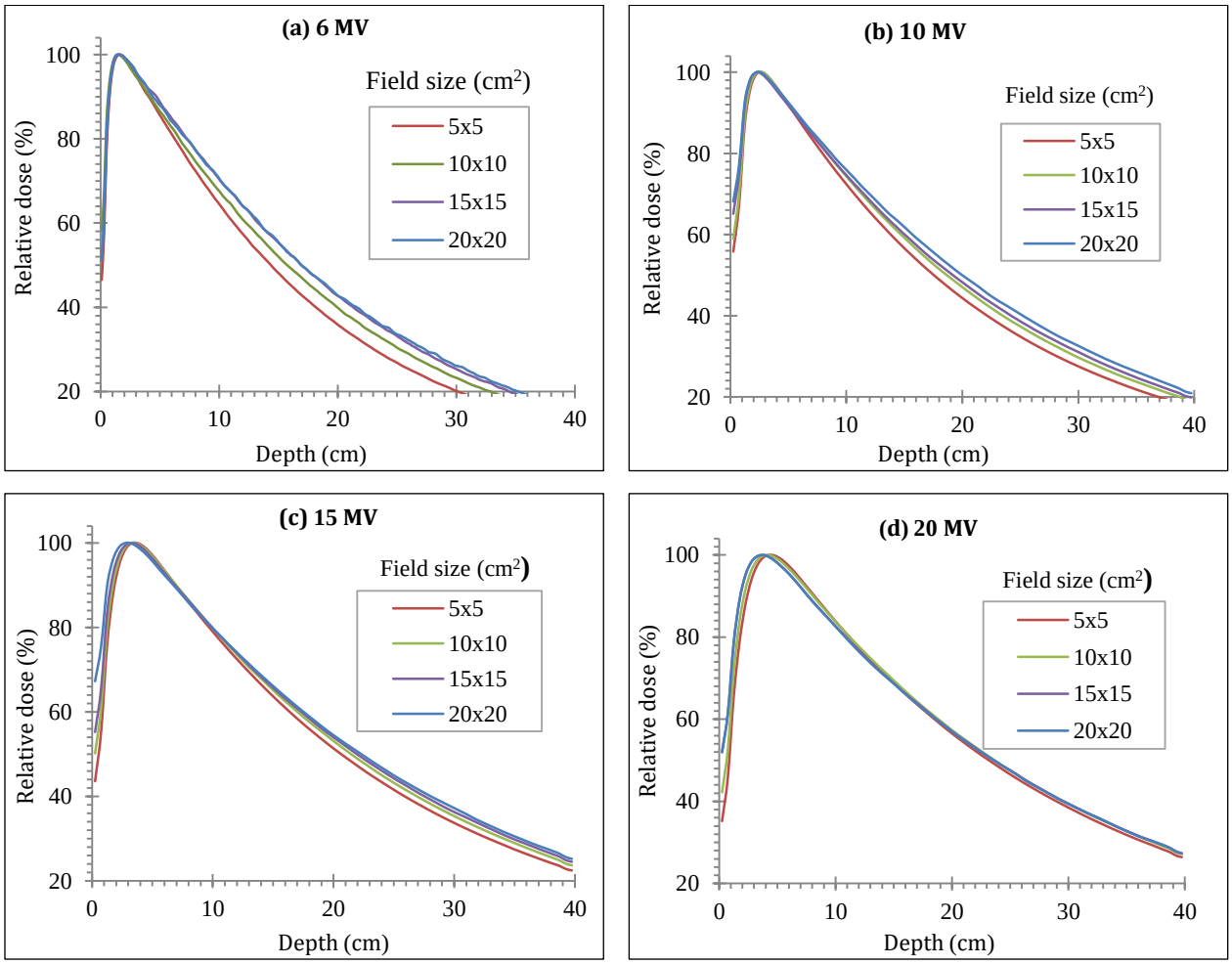


**Figure 7.4:** MC–simulated CAX PDD curves from 6 – 20 MV at various FS in a WT. All PDDs in were normalized to the local $d_{max}$ value. At higher beam energies, changing the FS has a diminished effect on the depth dose curves. PDDs were normalized at $d_{max}$.

Table 7.2 shows the simulated percentage doses at 10 cm depth ($PDD_{10cm}$) for all field sizes and beam energies used as well as the depth of dose maximum ($d_{max}$) values in a homogenous water phantom.

**Table 7.2:** $d_{max}$ and $PDD_{10cm}$ values for all field sizes and beam energies used

| | | **$PDD_{10cm}$ (%)** | | | |
|---|---|---|---|---|---|
| Energy (MV) | $d_{max}$ (cm) | 5 × 5 $cm^2$ | 10 × 10 $cm^2$ | 15 × 15 $cm^2$ | 20 × 20 $cm^2$ |
| 6 | 1.7(1.7) | 63.7 | 67.3(67.9) | 70.0 | 70.2 |
| 10 | 2.5(2.5) | 71.6 | 73.8(73.3) | 74.3 | 75.2 |
| 15 | 2.9(3.0) | 75.0 | 76.5(75.9) | 77.8 | 77.9 |
| 20 | 3.5( –) | 81.9 | 82.6( –) | 83.8 | 83.8 |

The simulated values shows good agreement (within 1%) with measured values (in brackets) obtained from the Elekta Prec*i*se unit commissioning data.

### 7.3.2 CT–based simulations (bHP patient model)

All beams used in this study are equally weighted, equally-spaced coplanar photon beams. 'Equally weighted' here means that the same dose was delivered to the isocenter for each radiation beam. A dose of 75 Gy was prescribed to the PTV with at least 95% of the prescription dose covering the entire target volume. (The dose was scaled since the prescription is not in line with ICRU). This protocol was based on the ICRU 50 guideline that stipulates that an optimal treatment plan is one wherein the total PTV receives between 95% and 107% of the prescription dose (Landberg *et al*. 1993). The x, y and z coordinates of the isocenter (0.56, 1.19, -3.9) were positioned at the centre of the PTV. Treatment plans were compared for target coverage in the presence of HPs and dose to critical organs for the same target expansion (prostate + 1 cm margin). The clinical simulations were performed with a certain number of histories in DOSXYZnrc, and then repeated for the same number of histories, only with the HP introduced. Since MCSHOW, by default, normalizes the dose distribution to the global maximum dose value in the **.3ddose* file, re-normalizations of the DVH or dose profile data were performed in Excel. The normalization point was the isocentre dose with no prosthesis

for that particular beam energy. The data is presented to show under- or over-dosage that occurs if the prosthesis is not accounted for.

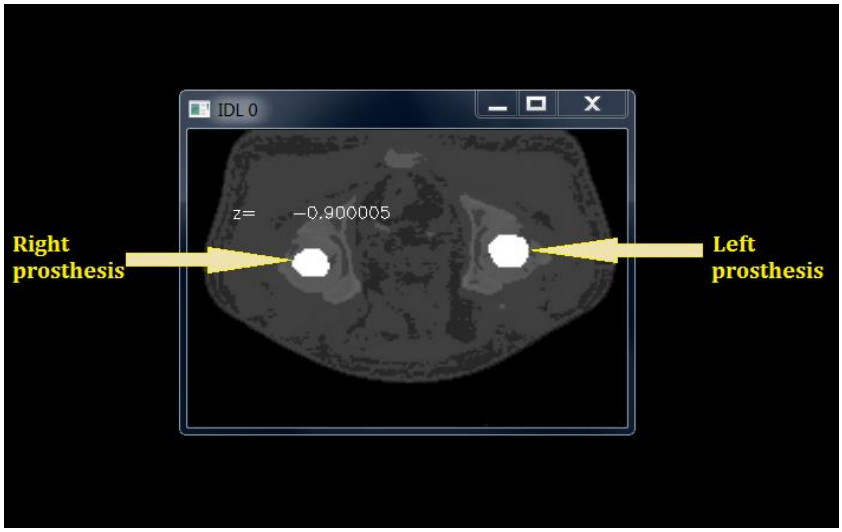


**Figure 7.5:** IDL output showing the transverse slice of a patient model fitted with bHPs

It would also have been interesting to show the data from the TPS for the same patient even if it was calculated for all CT numbers set to zero (water-equivalence). However, this was a purely Monte Carlo study and the TPS was only used to generate MLC and jaw settings for translation to DOSXYZnrc and not to compare TPS data with MC results. The bHP patient model used is shown in figure 7.5. The thickness of the left prosthesis through the isocenter is 2.9 cm (from $x$ = 11.6 cm to $x$ = 14.5 cm) and the thickness of the right prosthesis is 2.7 cm (from $x$ = −13.37 cm to $x$ = −10.67 cm), where $x$ is the lateral beam direction. All beam profiles were drawn for beams that traversed through the head of the prosthesis, which is the thickest aspect of the implant.

#### 7.3.2.1 Four–field box plan

The isodose distribution in a conventional 4F box with 2 bilateral portals passing through the pelvis and 2 anterior-posterior/posterior-anterior beams is shown in figure 7.6.

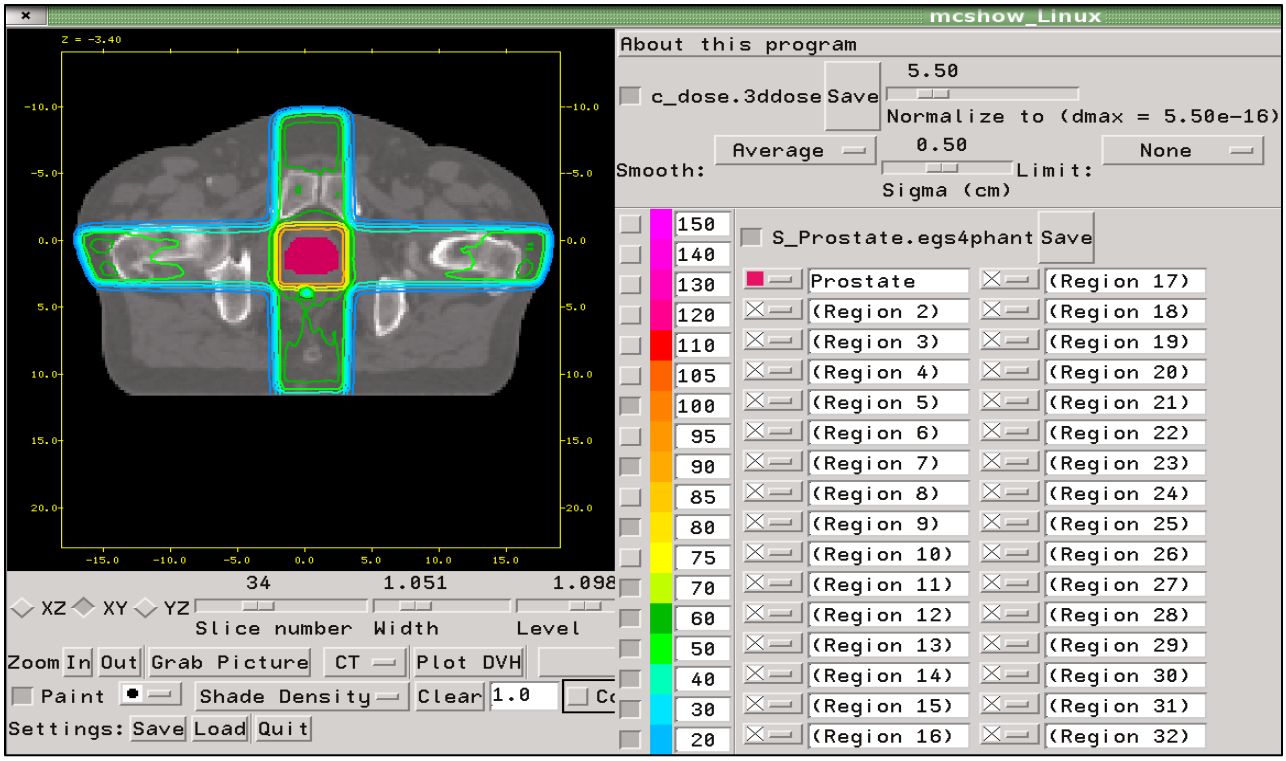


**Figure 7.6**: MCSHOW GUI showing the transverse isodose distribution of 4F box obtained from DOSXYZnrc simulations in a patient with no prostheses.

The PTV lies in the shadow of the prostheses with respect to the two lateral beams. The effect of various bilateral prostheses on the cumulative DVHs for the PTV, bladder and rectum using a 4F box technique is demonstrated in figs. 7.7-7.10. Interface effects are also evaluated on lateral DPs intersecting the implant materials.

It is evident that maximum dose perturbation occurs for the steel alloy, followed by titanium alloy, and lastly the thermoplastic HP. From the rectal and bladder DVHs, it can be noted that the rectum generally receives less absorbed dose than the bladder for a given fractional volume of the organ. In fact, the rectum DVH is almost completely unaffected by the presence of HPs for this patient, except at doses above 60 Gy. This observation applies for all beam energies in this 4F plan.

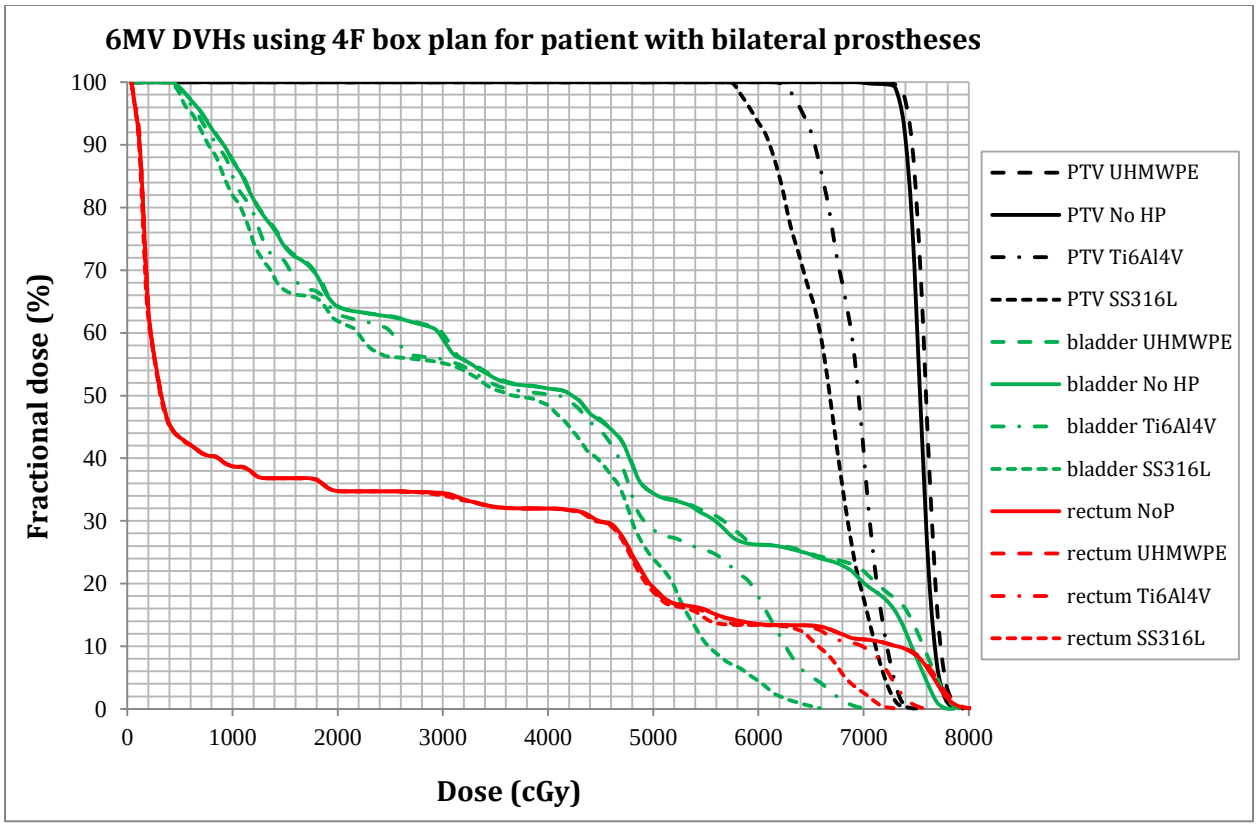


**Figure 7.7:** Comparison of DVHs for various bHPs using a 4F box plan at 6 MV

The 2 principal photon attenuation mechanisms in the MV energy range are Compton scattering and pair production. By taking a closer look at reaction cross sections and linear attenuation coefficients for Compton scattering and pair production, it can be noted that at 6MV, Compton scattering dominates. The Compton scattering attenuation coefficient, being independent of the atomic number of materials (see table 2.1), will not contribute to photon attenuation disparities as a result of differences in atomic number between HP and bone. However, the material density (ρ), which is the only term appearing in the Compton scattering linear interaction coefficient, is slightly lower for UHMWPE and much higher for steel and titanium compared to bone. The net effect is reduced Compton attenuation in UHMWPE and increased attenuation in steel and titanium, although the Compton reduction in UHMWPE is less pronounced due to the closer match in ρ between UHMWPE and bone as opposed to metallic alloys.

Consequently, SS316L and Ti6Al4V alloys yield a greater absorbed dose reduction in the target volume.

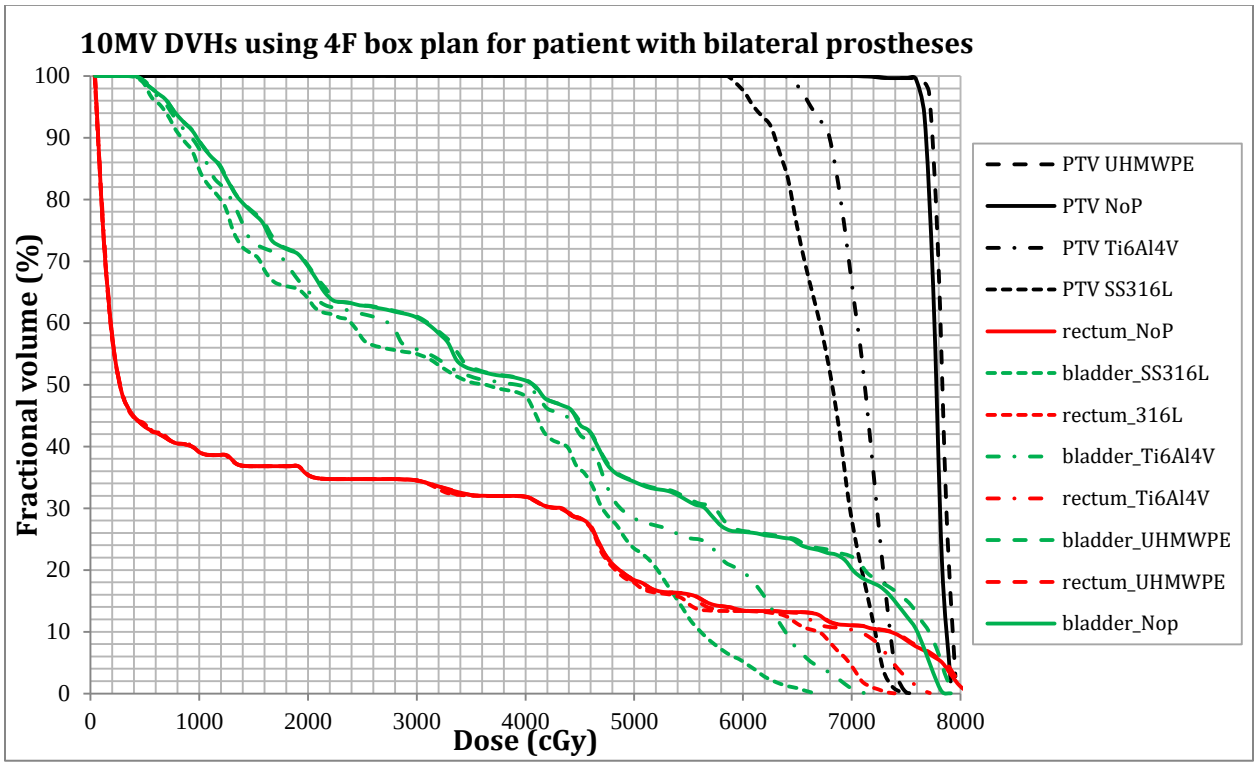


**Figure 7.8:** Comparison of DVHs for various bHPs using a 4F box plan at 10 MV

In the high photon energy region (above 10 MV), pair production dominates. Pair production is more efficient in high-Z and high-ρ materials, with ρ and Z having an equal weighting in the pair production attenuation coefficient. SS316L, having the highest effective atomic number and density, will cause the greatest dose attenuation.

The fractional volume of the PTV receiving at least 95% of the prescribed dose ($V_{95\%}$) in the presence of bilateral SS316L alloy with this 4F plan is as low as 10% for the 6 MV beam. This means up to 90% of the PTV volume is underdosed. The underdosed fractional volume for a patient with titanium alloy bHPs reaches up to 76%, and no underdosage occurred for UHMWPE. The values of $V_{95\%}$ for all HP materials and energies are summarized in table 7.3. Although $V_{95\%}$ remains constant (100%) when beams pass through UHMWPE, there is an overall PTV dose escalation since the UHMWPE DVHs overlay the DVHs with no prosthesis, owing to the greater dose transmission through

UHMWPE compared to bone. This can be quantitatively verified by looking at other dosimetric endpoints, like V105.

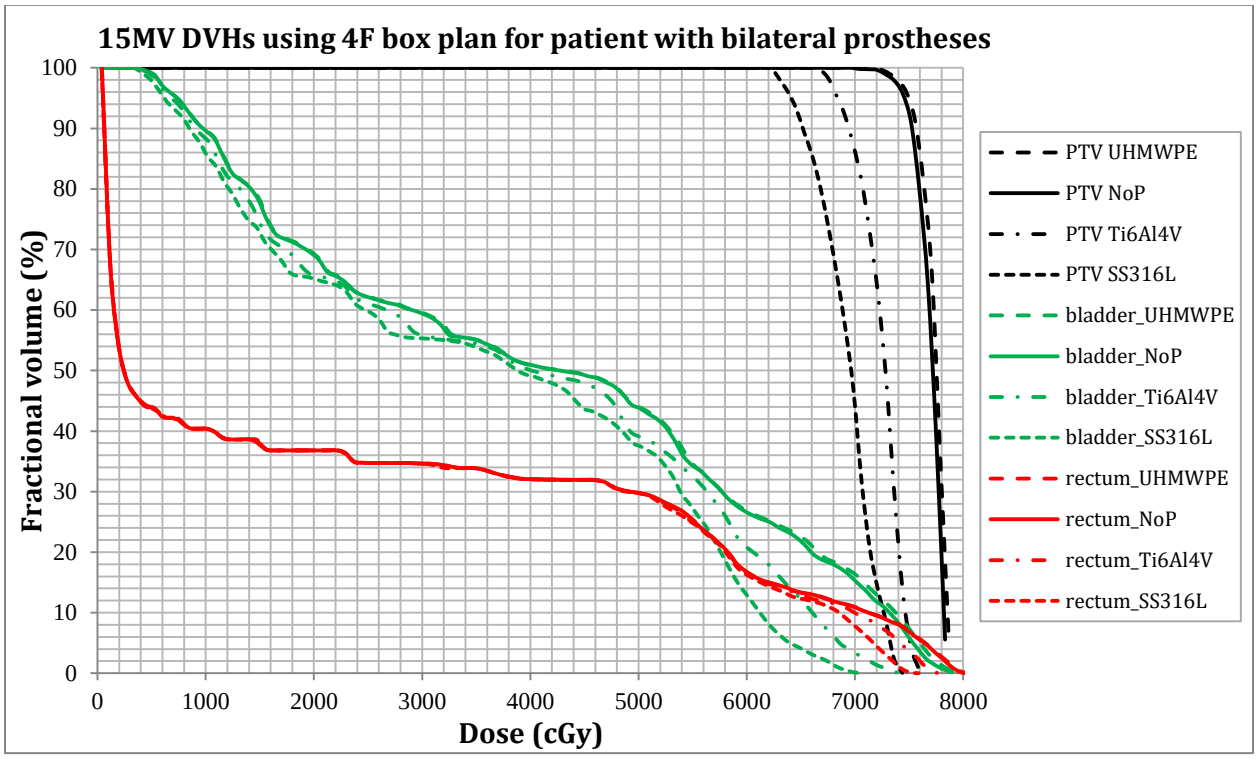


**Figure 7.9:** Comparison of DVHs for various bHPs using a 4F box plan at 15 MV

The target coverage at various energies and HPs was quantified by comparing $V_{95\%}$ values in the PTV obtained from DVHs in figures 7.7-7.10. Less than 4% of the PTV volume received < 1 Gy beyond the upper dose limit i.e., above 107% of the prescription dose (~ 80.3 Gy). This slight overdose was only observed for a patient with UHMWPE at 20 MV.

**Table 7.3:** $V_{95\%}$ vs. beam energy in the PTV for various hip prostheses

| | **$V_{95\%}$: 4F box (%)** | | | |
|---|---|---|---|---|
| Energy (MV) | SS316L | Ti6Al4V | UHMWPE | No prosthesis |
| 6 | 10.5 | 24.3 | 100.0 | 100.0 |
| 10 | 17.2 | 53.1 | 100.0 | 100.0 |
| 15 | 24.1 | 74.2 | 100.0 | 100.0 |
| 20 | 46.5 | 85.8 | 100.0 | 100.0 |

High–energy photon beams have greater penetrating power, hence the observed increase in $V_{95\%}$ with energy. It is therefore reasonable to increase the beam energy to help overcome the attenuation effects of metallic HPs and thus improve target coverage.

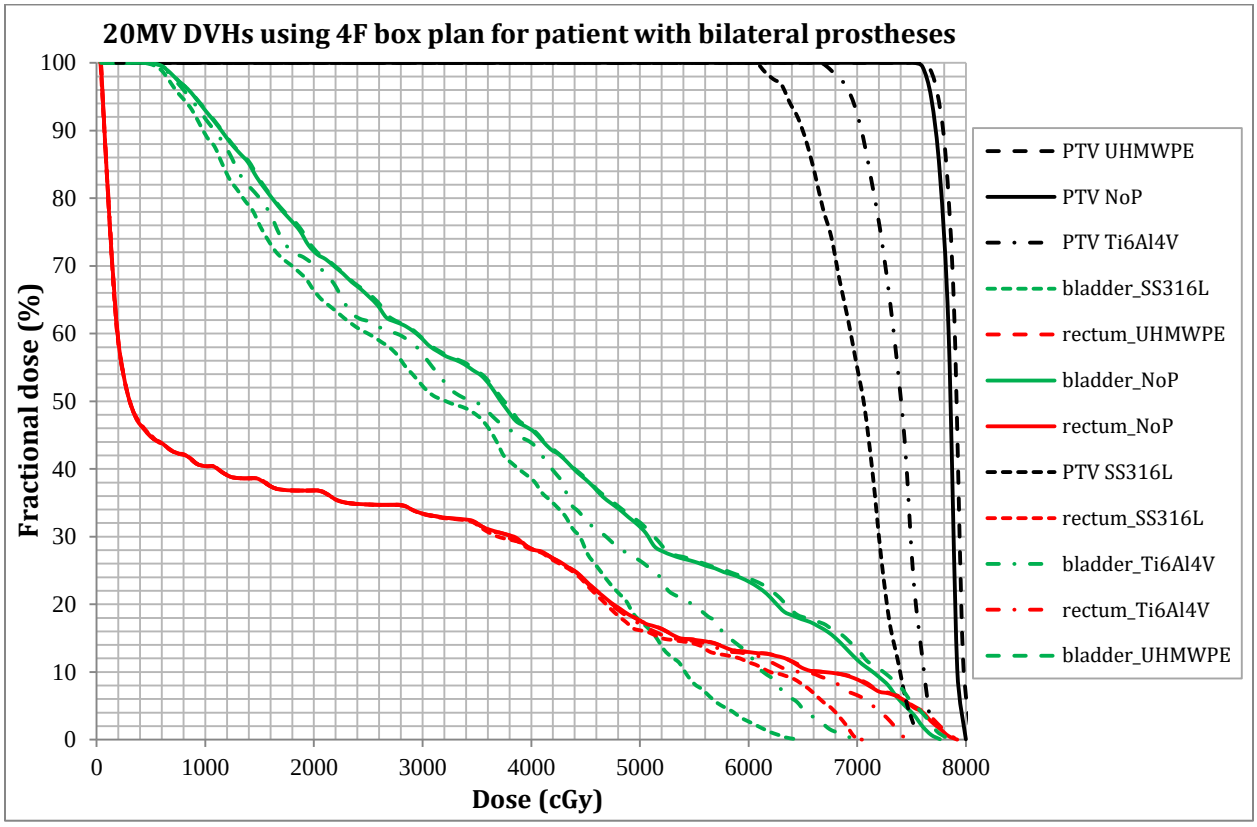


**Figure 7.10:** Comparison of DVHs for various bHPs using a 4F box plan at 20 MV

To evaluate the dose–volume effect to OARs with this 4F plan, the volume of the bladder and rectum receiving at least 60 Gy ($V_{60Gy}$) was determined and presented in table 7.4 (60 Gy is 80% of the prescription dose).

**Table 7.4:** $V_{60Gy}$ vs. beam energy in OARs for a 4F plan

| | **4F box** | |
|---|---|---|
| Energy (MV) | Rectum | Bladder |
| 6 | 14.0 | 26.8 |
| 10 | 13.6 | 26.8 |
| 15 | 16.0 | 26.8 |
| 20 | 13.2 | 24.0 |

The maximum rectal and bladder volume receiving at least 80% of the prescription dose in this 4F plan is 16% and 27%, respectively. Figures 7.11 – 7.14 show the dose distribution along the lateral parallel–opposed beams CAX for this 4F technique.

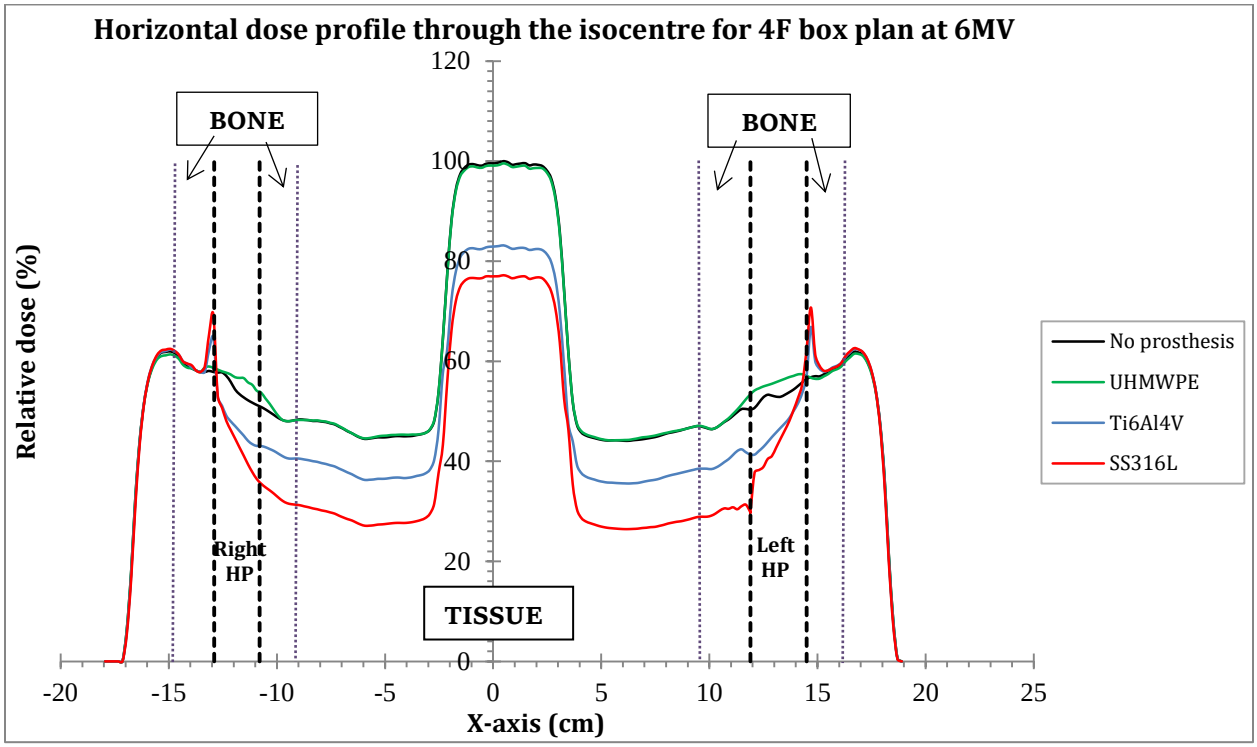


**Figure 7.11:** Comparison of DPs along the *x*–axis for a 4F box plan at 6 MV.Doses to the isocenter are ~ 23% lower for a steel alloy and ~ 17% lower for a titanium alloy. The dose attenuation by UHMWPE is negligible (< 1%). Interface regions are marked by the broken lines.

It can be observed that dose perturbation does not only occur for points in the shadow of the implant, but also in the vicinity of the metallic prosthesis, and these local dose perturbations are known as interface effects. Transition zone dosimetry is more complex and results from electronic disequilibrium that occurs between two materials with different densities.

When a photon beam is incident on a phantom, transient charged particle equilibrium (TCPE) exists at all depths except at $d_{max}$. When the beam passes through an inhomogeneity in the phantom, TCPE is perturbed at the inhomogeneity–tissue–equivalent material boundary. The 'horns' in figure 7.11-7.14 are due to electrons released

from the surface of the high density implant on the proximal interface relative to each lateral beam.

The backscattered dose perturbation factor (BSDF) = $D_p$(with HP)/$D_p$(no HP) at distance *P* from the interface was calculated at 6 MV on the beam entrance side for the 3 types of prostheses used and presented in table 7.5.

**Table 7.5:** BSDF vs. distance from interface for different HPs at 6 MV

| | **BSDF (proximal interface)** | | |
|---|---|---|---|
| Distance *P* (mm) | SS316L | Ti6Al4V | UHMWPE |
| 0 | 1.24 | 1.18 | 0.99 |
| 2 | 1.08 | 1.06 | 0.99 |
| 4 | 1.04 | 1.03 | 1.00 |
| 6 | 0.99 | 1.00 | 1.00 |

MC demonstrates that up to 24% local dose increase is observed at the bone–SS316L boundary and up to 18% dose increase for the bone–Ti6Al4V proximal interface for a plan with bilateral beams. At 6 MV, backscatter radiation from the HPs contributes a small peak extending ~ 5 mm, which is the order of the range of secondary electrons scattered from the surface of the metallic implants. It can also be observed that backscatter perturbation is dependent on density and its highest value is for the SS316L HP, showing a rapid dose fall–off with increasing distance from the interface.

The two competing processes at the distal bone–prosthesis interface are; altered transmission of primary photons through the prosthesis and changes in forward scatter of secondary electrons from the HP. The occurrence of dose disturbances at the distal interface is attributed to the rapid build down from the high–Z material not being compensated for rapidly enough by the new scatter contribution from the low–Z material. Although the build up of dose in bone at the interface occurs on both the beam entrance and beam exit side of the metal implant, dose enhancement at the beam exit side from forward scatter is not obvious due to the substantial dose attenuation by the prosthesis. The change in the disequilibrium magnitude at the beam exit interface of the

heterogeneity was quantified by the forward dose perturbation factor (FDPF), evaluated as a function of beam energy and tabulated in table 7.6 below.

**Table 7.6:** FDPF calculated vs. energy for different HPs at the distal interface

| | **FDPF (distal interface)** | | |
|---|---|---|---|
| Energy (MV) | SS316L | Ti6Al4V | UHMWPE |
| 6 | 0.62 | 0.84 | 1.08 |
| 10 | 0.75 | 0.87 | 1.02 |
| 15 | 0.80 | 0.94 | 1.02 |
| 20 | 0.93 | 1.04 | 0.99 |

At 6 MV, secondary electrons produced in the HP close to the beam exit interface by incident photon interactions have lower energy and a wide angular distribution because the primary photon interaction mode at 6 MV is Compton scattering which produces lower–energy electrons with a large angular distribution.

The dose changes on the distal boundary are less pronounced than on the beam entrance side. The forward scatter effect is more pronounced for higher energy beams (> 10 MV) and this is attributed to the increased contribution of pair production, especially in the high–Z prostheses (Ti6Al4V and SS316L). Similar dose perturbation effects have been reported by Reft *et al.* (2003), who calculated the FDPF at bone, lead and steel interfaces in a water equivalent phantom.

Back-scatter effects for a 10 MV beam extend a distance of approximately 0.9 cm from the prosthesis (towards the beam entry side) (see table 7.7). Inside the HP, the local dose reduction is due to the fact that electrons that are scattered out from the high–Z media are not compensated for. There is a faster dose drop-off in SS316L due to the high density of stainless steel followed by titanium, bone and lastly UHMWPE. The half-value layer and the linear absorption coefficient for metallic HPs and bone are very different, which means that the degree of backscatter and radiation absorption by the prosthesis and phantom are also different.

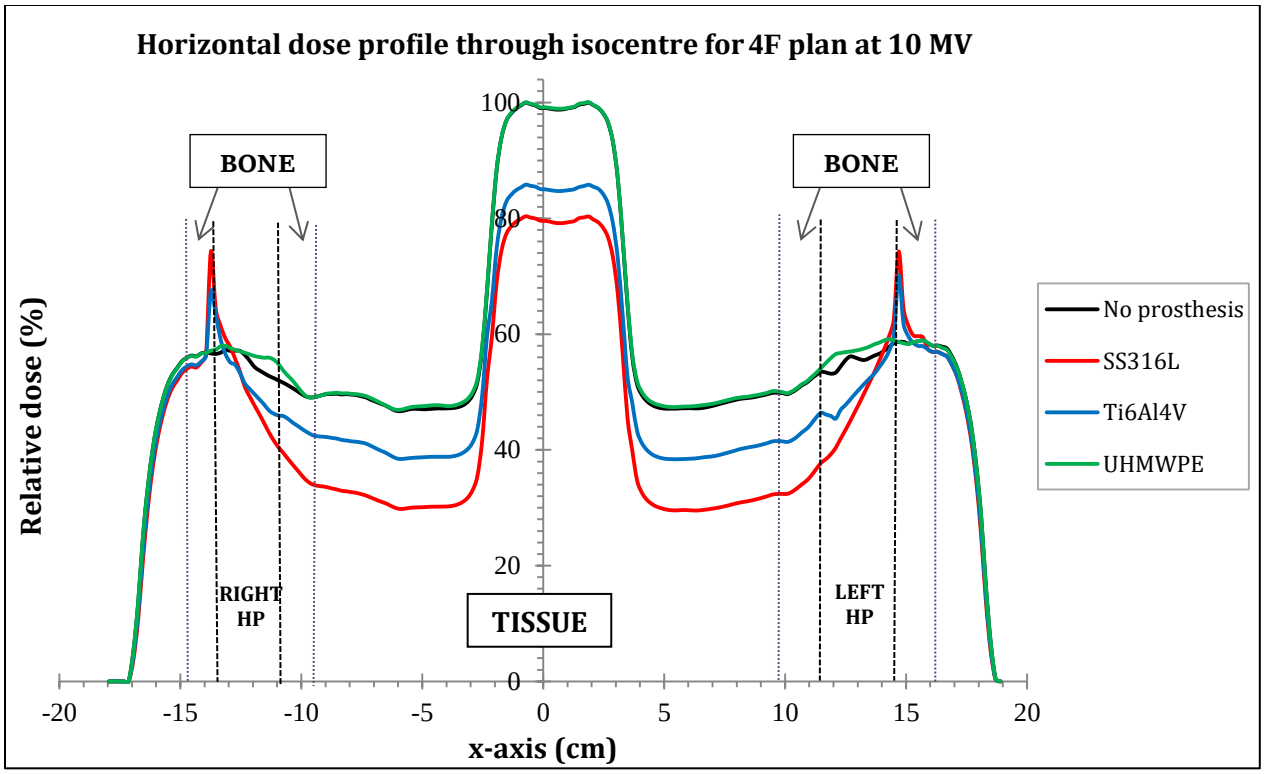


**Figure 7.12:** Comparison of DPs along the *x*–axis for a 4F box plan at 10 MV. The isocenter dose is ~21% lower for a steel alloy and ~ 12% lower for a titanium alloy

Emerging secondary electrons deposit their energy within a few cm away from the surface of the metallic implant. For a steel HP, backscatter effects at 15 MV extend a distance of up to 1.2 cm from the prosthesis (see table 7.8). Beyond the steel and titanium heterogeneity, dose is reduced and remains reduced at all depths.

**Table 7.7:** BSDF vs. distance from interface for different HPs at 10 MV

| | **BSDF (bone–HP interface)** | | |
|---|---|---|---|
| Distance *P* (mm) | SS316L | Ti6Al4V | UHMWPE |
| 0 | 1.27 | 1.20 | 0.99 |
| 3 | 1.10 | 1.05 | 0.99 |
| 6 | 1.02 | 1.02 | 1.00 |
| 9 | 1.00 | 1.00 | 1.00 |

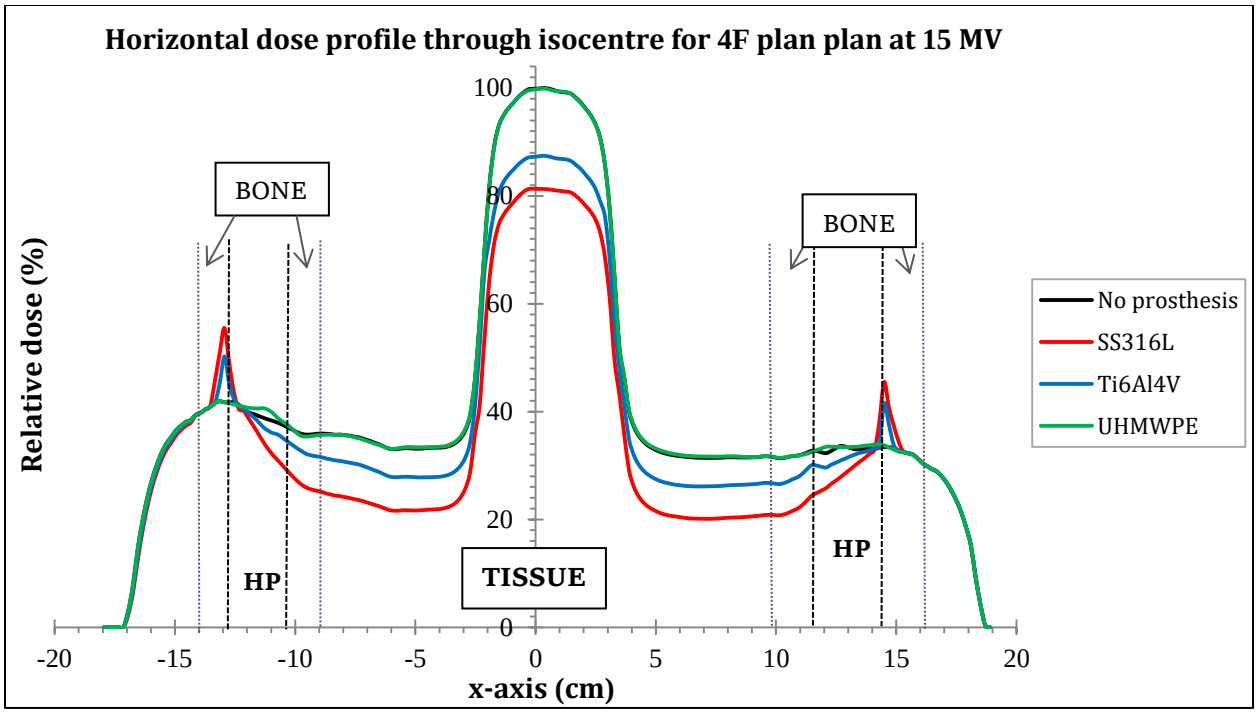


**Figure 7.13:** Comparison of DPs along the *x*–axis for a 4F box plan at 15 MV.The isocenter dose is ~19% lower for a steel alloy and ~ 11% lower for a titanium alloy

**Table 7.8:** BSDF vs. distance from interface for different HPs at 15 MV

| | **BSDF (bone–HP interface)** | | |
|---|---|---|---|
| Distance *P* (mm) | SS316L | Ti6Al4V | UHMWPE |
| 0 | 1.32 | 1.21 | 0.99 |
| 5 | 1.21 | 1.08 | 1.00 |
| 10 | 1.07 | 1.00 | 1.00 |
| 12 | 1.00 | 1.00 | 1.00 |

Interface effects for a 20 MV beam extend a distance of between 1.00 – 1.5 cm from the front of the prosthesis (see table 7.9). This effect should be taken into account since the range of these hot spots can extend to tissue volumes at high beam energies.

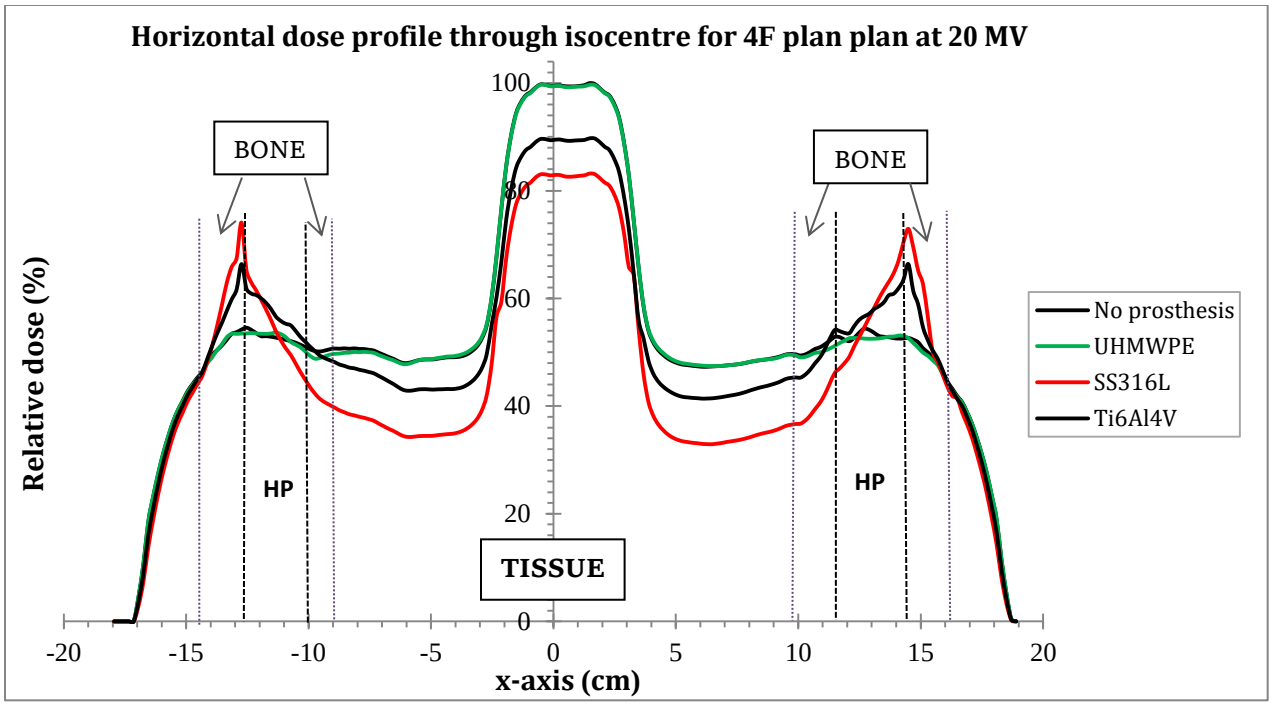


**Figure 7.14:** Comparison of DPs along the *x*–axis for a 4F box plan at 20 MV.The isocenter dose is ~17% lower for a steel alloy and ~ 12% lower for a titanium alloy

**Table 7.9:** BSDF vs. distance from interface for different HPs at 20 MV

| | **BSDF (bone–HP interface)** | | |
|---|---|---|---|
| Distance *P* (mm) | SS316L | Ti6Al4V | UHMWPE |
| 0 | 1.38 | 1.25 | 1.00 |
| 5 | 1.25 | 1.13 | 0.99 |
| 10 | 1.08 | 1.00 | 0.99 |
| 15 | 1.00 | 1.00 | 1.00 |

A substantial dose decrease is observed in the area that lies in the shadow of the metallic prostheses relative to lateral beams. The dose reduction at the isocenter in the presence of bilateral stainless steel implant for the 4F box ranges from 17% – 23%, and for titanium alloy it ranges from 11% – 17%. The isocenter dose perturbation in the presence of UHMWPE is below 1%. Lateral DPs with and without UHMWPE in the phantom essentially overlap for all x-ray energies (isocenter dose perturbation due to UHMWPE < 1% for all energies). This indicates that, with MV beams used for external prostate

irradiation, the thermoplastic implant has effectively comparable radiolucency to the pelvic bone and to tissue. The isocenter dose reduction due to beam attenuation by HPs is shown in table 7.10 as a function of beam energy.

**Table 7.10:** Isocenter dose perturbation vs. energy for different bHPs in a 4F box plan

| | **% dose reduction** | | **% dose enhancement** |
|---|---|---|---|
| Energy (MV) | SS316L | Ti6Al4V | UHMWPE |
| 6 | 22.8 | 16.8 | < 1 |
| 10 | 20.4 | 14.8 | < 1 |
| 15 | 18.5 | 12.7 | < 1 |
| 20 | 16.9 | 10.6 | < 1 |

Our results suggest that for a 4F box the dependence of dose distribution on beam energy at the isocenter is weak, ranging only from 22.8 to 16.9% from 6 to 20 MV, except in the vicinity of the HP. Erlanson *et al.* (1991) reported a decrease in the target dose ranging from 9.8% to 8.1% for equally-weighted beams between 6 and 50 MV using a 4F box. Even though Erlanson's results differ by more than 50% from the results in this study, Erlanson also suggested that for a four-field technique, the dose distribution is nearly independent of beam energy at the centre of the target, which is almost synonymous to what was found in this dissertation.

It can be observed that interface dose enhancement is more pronounced at higher incident beam energies and at high-Z due to increased contribution by pair production reactions at the interface and that the energy deposited per scattered electron is higher.

#### 7.3.2.2 Five–field plan

The isodose distribution in a 5F plan with beam portals at gantry angles 54°, 126°, 198°, 270° and 342° is shown in figure 7.15. The right lateral beam intersects the prosthesis.

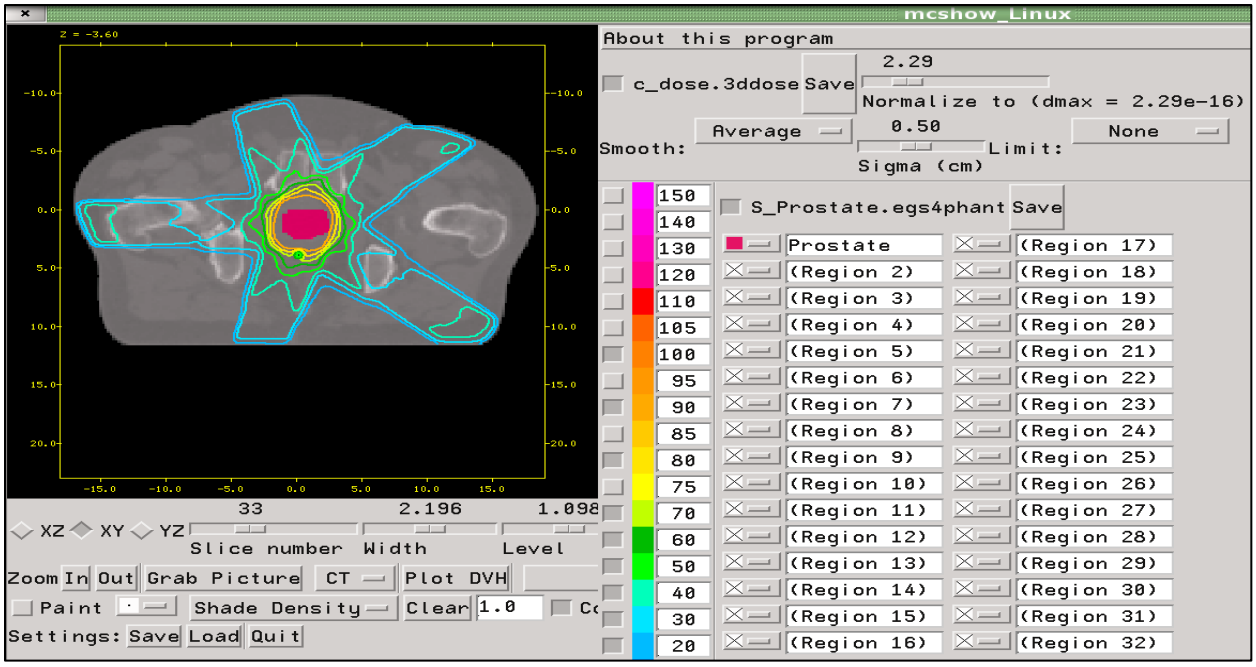


**Figure 7.15:** MCSHOW GUI showing the beam arrangements in a 5F plan obtained from DOSXYZnrc simulations in a patient with no prostheses. All beams portals are 72° apart.

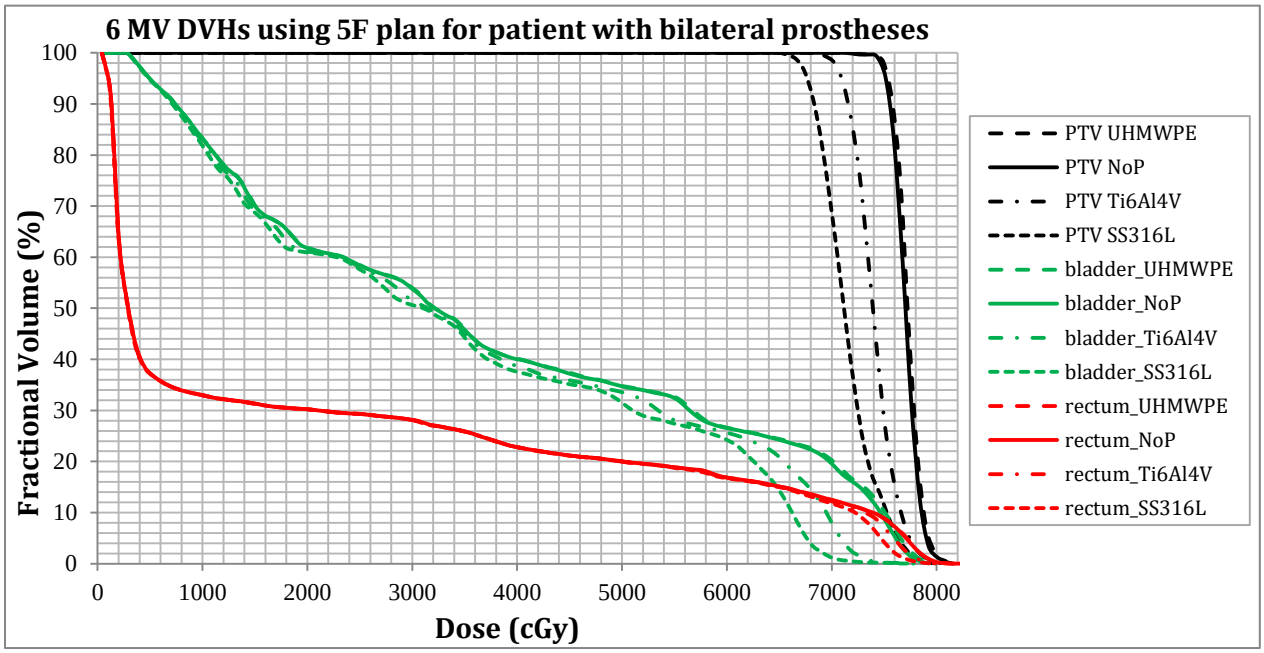


**Figure 7.16:** Comparison of DVHs for various bHPs using a 5F plan at 6 MV

DVHs in figures 7.16-7.19 were used to calculate $V_{95\%}$ and $V_{60Gy}$ values in tables 7.11 and 7.12 respectively. The dose reduction is exactly the same for the unilateral hip prosthesis since only one beam intersects a HP at 270°.

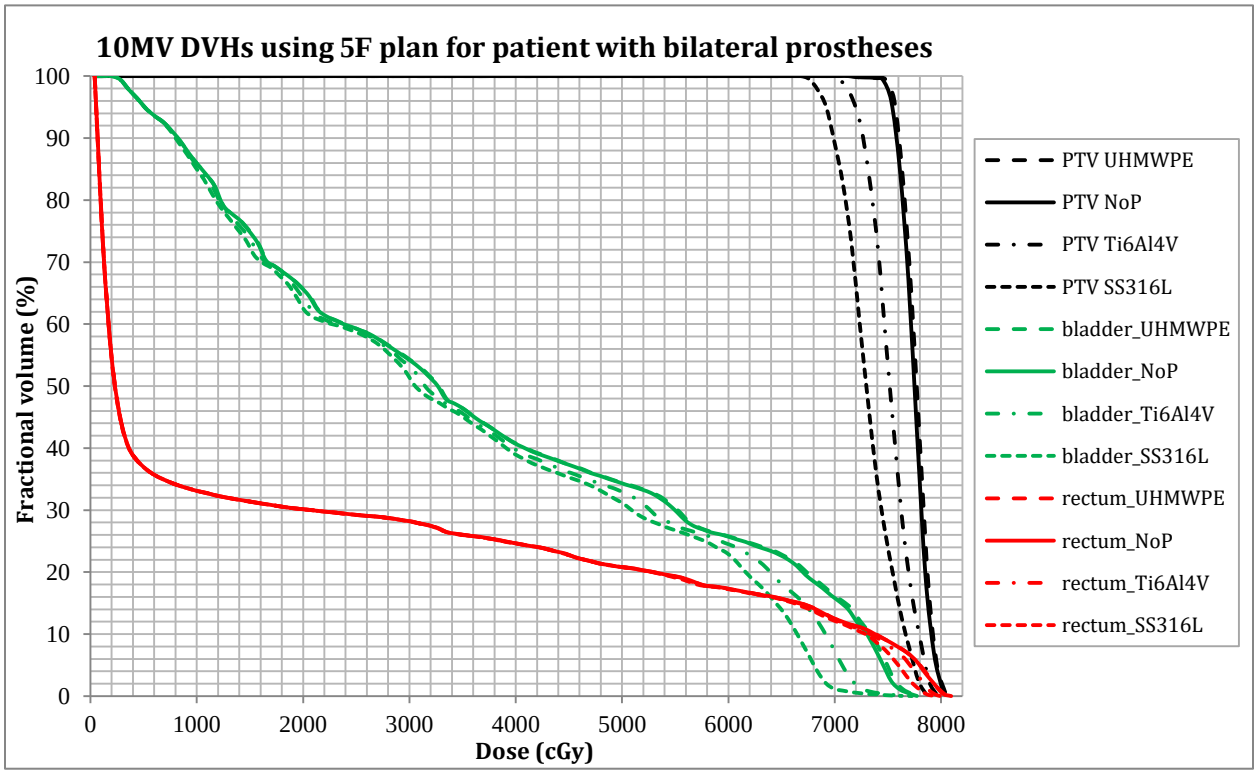


**Figure 7.17:** Comparison of DVHs for various bHPs using a 5F plan at 10 MV

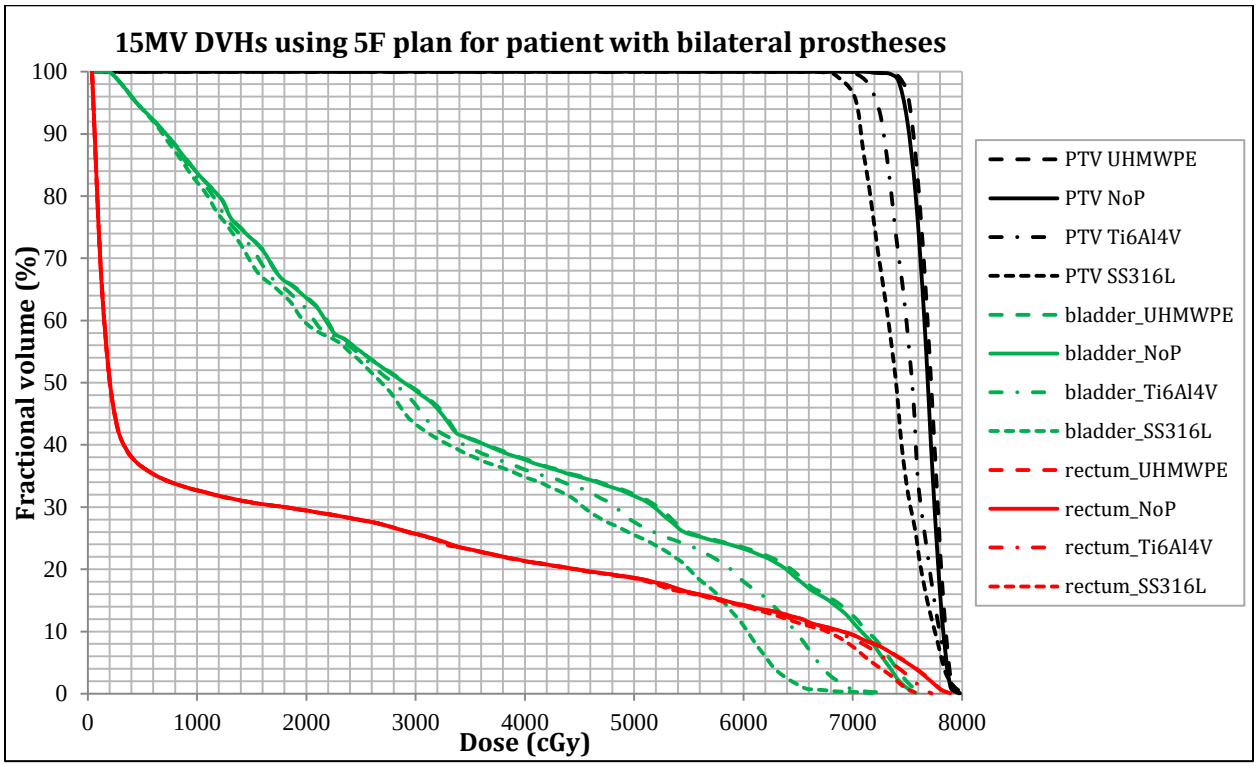


**Figure 7.18:** Comparison of DVHs for various bHPs using a 5F plan at 15 MV

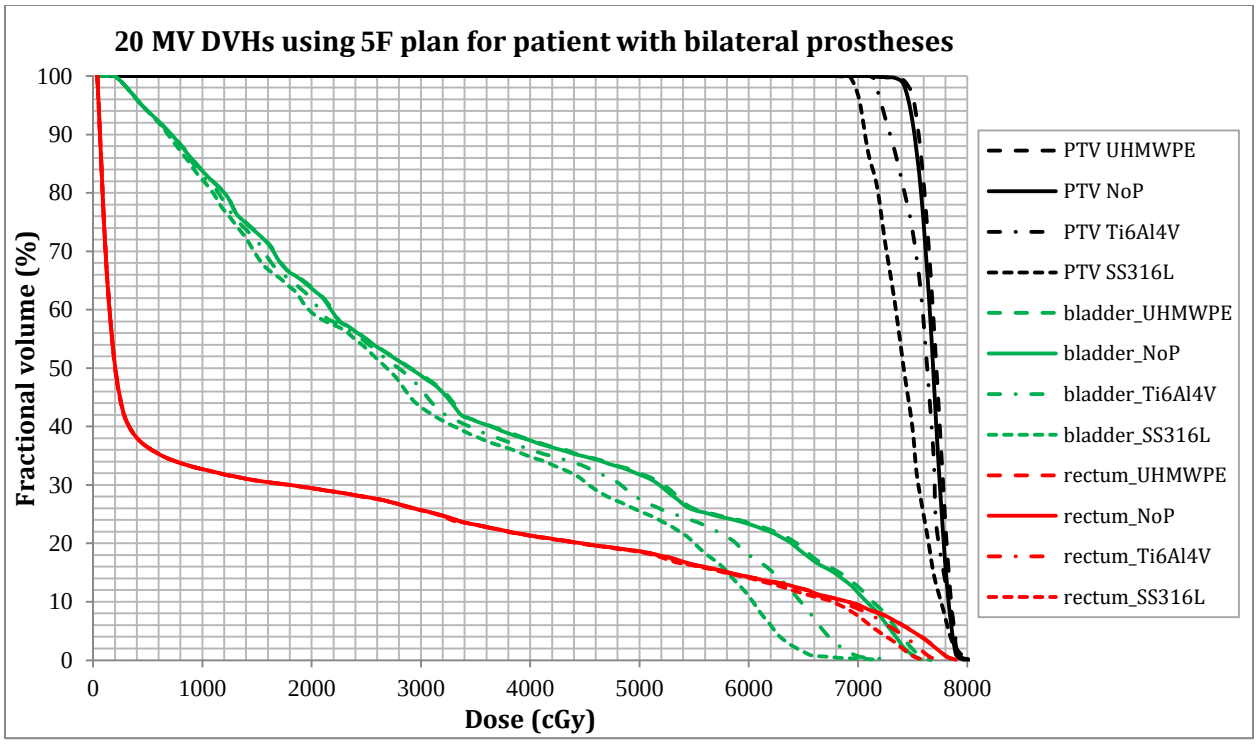


**Figure 7.19:** Comparison of DVHs for various bHPs using a 5F plan at 20 MV

An interesting observation is that above 10 MV, increasing the beam energy does not cause a significant increase in target coverage, with $V_{95\%}$ increasing only from 81% to 86% from 10 MV to 20 MV in the presence of a steel prosthesis. This is a significant increase in beam energy, though the PTV is still underdosed.

**Table 7.11:** $V_{95\%}$ vs. beam energy in the PTV for a 5F plan

| | **$V_{95\%}$: 5F plan** | | | |
|---|---|---|---|---|
| Energy (MV) | SS316L | Ti6Al4V | UHMWPE | No Prosthesis |
| 6 | 48.5 | 94.3 | 100.0 | 100.0 |
| 10 | 80.0 | 96.8 | 100.0 | 100.0 |
| 15 | 83.3 | 98.3 | 100.0 | 100.0 |
| 20 | 91.5 | 99.2 | 100.0 | 100.0 |

The 5F plan gives a better target coverage in the PTV compared to a 4F box plan. This is because the 5F plan has four beams avoiding the prostheses, and only one lateral beam passing through the prostheses. Up to 44% of the PTV volume is underdosed in the presence of bilateral steel alloy with this 5F plan. The corresponding underdosed volume

for a patient with titanium alloy in this plan reaches only up to 5%. No significant PTV volume received any dose below 95% of the prescription dose or above 107% of the prescription dose for UHMWPE prostheses.

**Table 7.12:** $V_{60Gy}$ vs. beam energy in OARs for a 5F plan

| Energy (MV) | **5F plan** | |
|---|---|---|
| | Rectum | Bladder |
| 6 | 16.8 | 26.8 |
| 10 | 17.2 | 26.0 |
| 15 | 14.4 | 23.6 |
| 20 | 14.0 | 23.9 |

The maximum rectal and bladder volume receiving at least the prescription dose in this 5F plan is 17% and 27%, respectively.

The MC simulation predicts underdosages of about 19% and 14% in the target (isocenter) due to the attenuation effect of SS316L and Ti6Al4V at 6MV in this 5F plan. However, the dose changes in this study are relatively lower than those reported in other studies due to the closer match between the Z–numbers and densities of bone and HP compared to water and high–Z materials used in most investigations. For example, Mesbahi & Nejad (2007), using MC simulations, found dose attenuations of 32% and 55% for titanium and steel alloys, respectively, at 5 cm distance from a $4 \times 4 \times 4$ $cm^3$prosthesis in a cubic water tank using 9 MV lateral photon fields. Several authors used metallic HPs immersed in a WT and irradiated with a single beam, or used IMRT beams in real patient situations. Very few studies have investigated the dose changes in a CT–based phantom irradiated with 3DCRT beams and, to the best knowledge of this author, no previous study has evaluated the dosimetric effect of UHMWPE on radiotherapy beams.

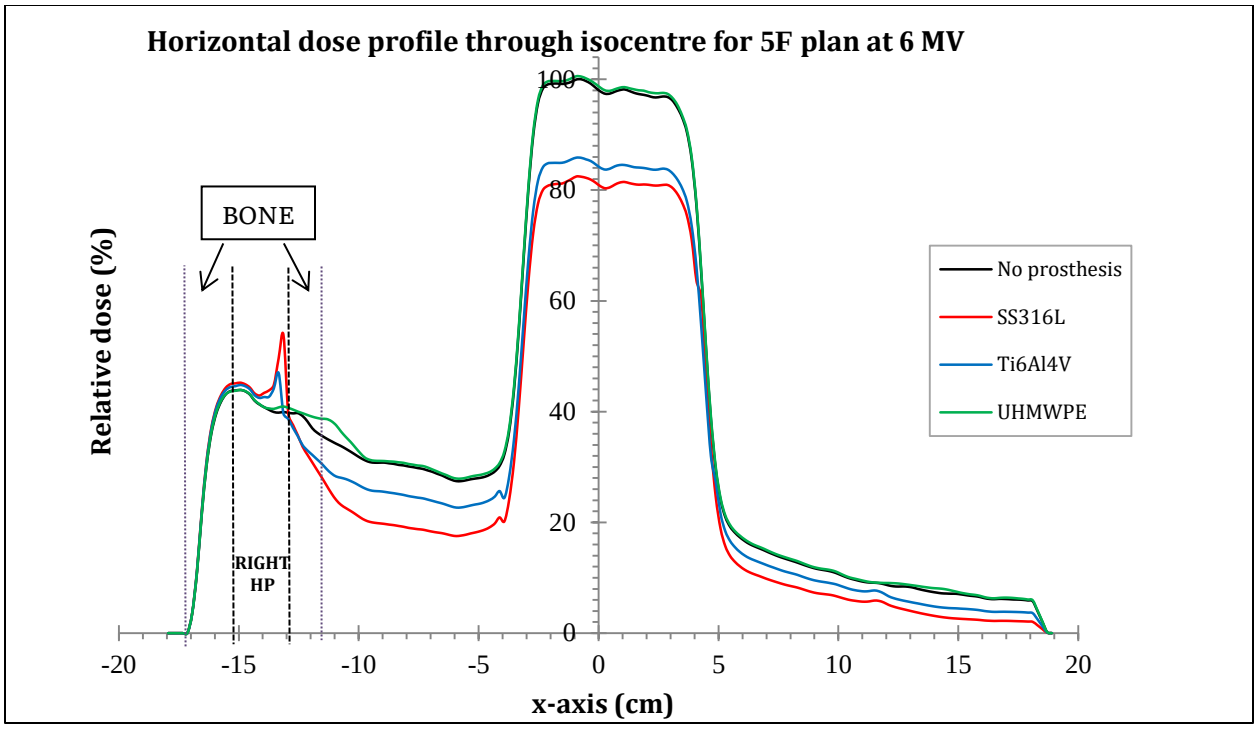


**Figure 7.20:** Comparison of DPs along the *x*–axis for a 5F plan at 6 MV. The isocenter dose is ~19% lower for a steel alloy and ~ 14% lower for a titanium alloy

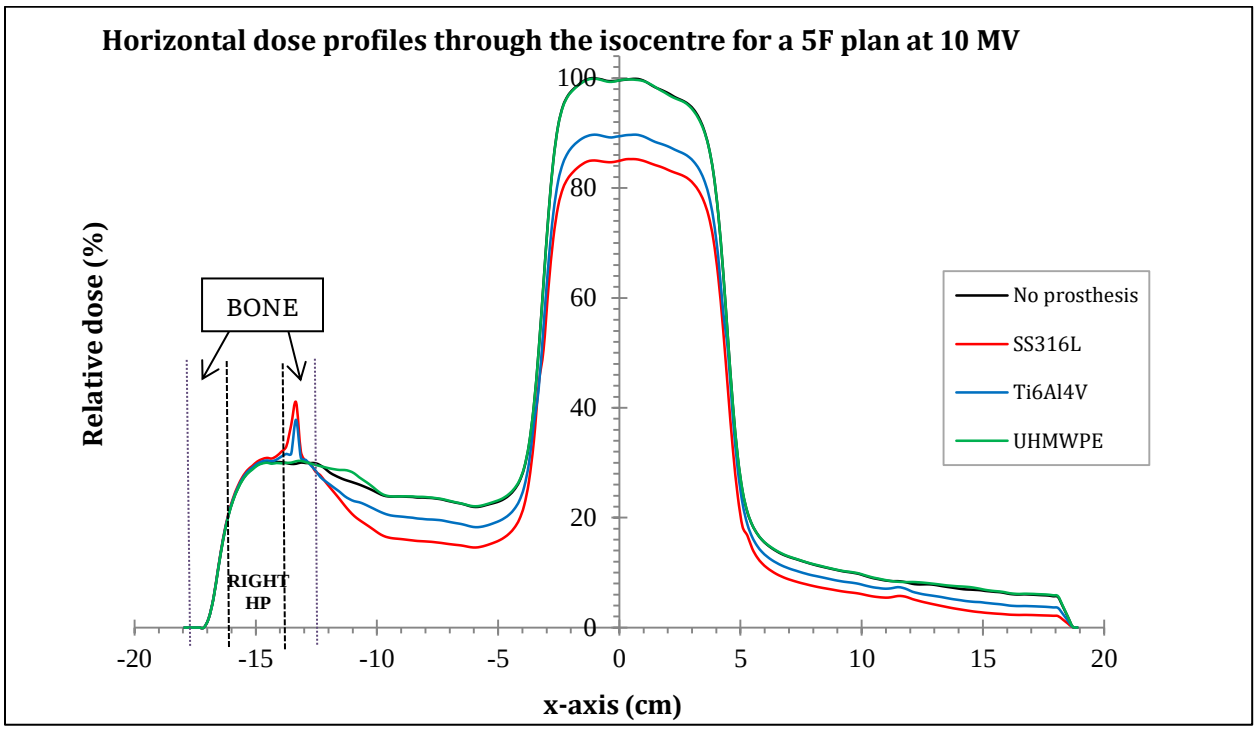


**Figure 7.21:** Comparison of DPs along the *x*–axis for a 5F plan at 10 MV. The isocenter dose is ~16% lower for a steel alloy and ~ 11% lower for a titanium alloy.

**Table 7.13:** Isocenter dose perturbation vs. energy for different HPs in a 5F plan

| | % dose reduction | | % dose enhancement |
|---|---|---|---|
| Energy (MV) | SS316L | Ti6Al4V | UHMWPE |
| 6 | 14.2 | 11.0 | < 1 |
| 10 | 9.6 | 7.5 | < 1 |
| 15 | 5.3 | 4.2 | < 1 |
| 20 | 2.3 | 1.1 | < 1 |

Figures 7.20 – 7.23 show the dose distribution along the lateral beam CAX for this 5F technique. The 5F plan gives a more diminished dose reduction in the PTV compared to a 4F box plan for all the beam energies used as seen in table 7.13. This is because the 5F plan has 2 out of 5 fields (20%) passing through the prostheses and for the 4F field it is 2 out of 4 fields (50%).

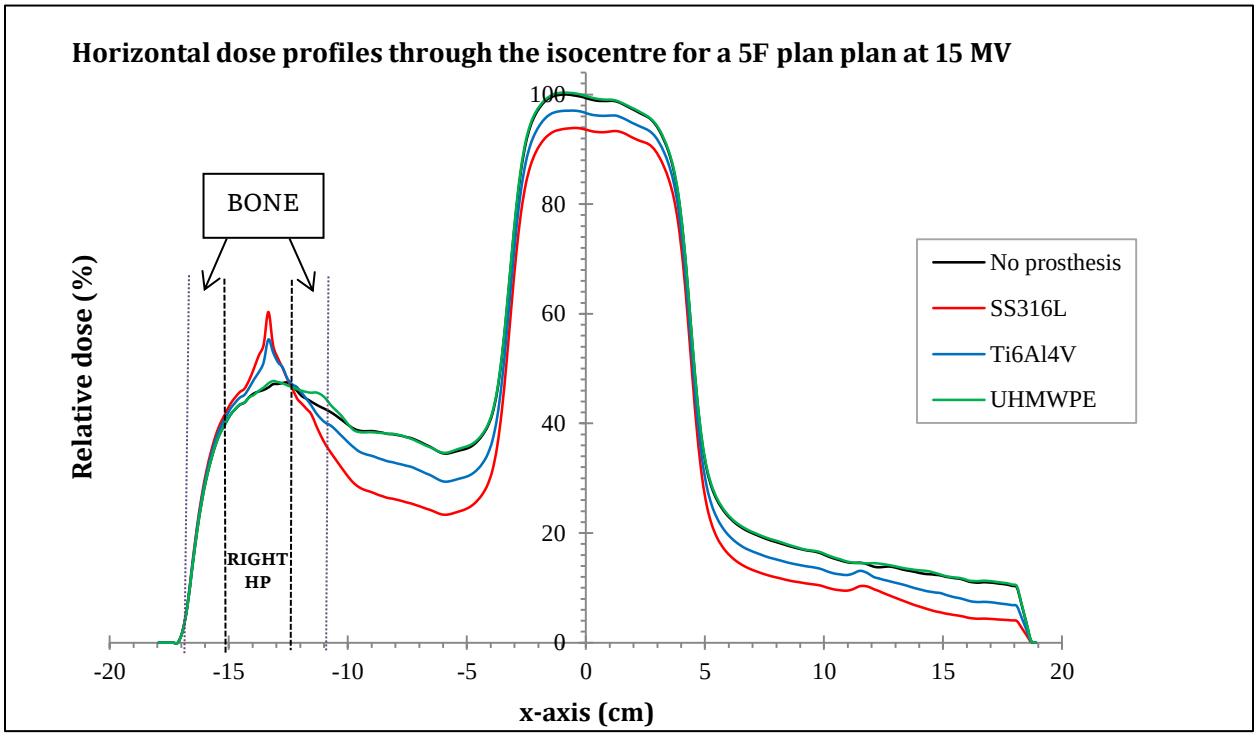


**Figure 7.22:** Comparison of DPs along the *x*–axis for a 5F plan at 15 MV. The isocenter dose is ~7% lower for a steel alloy and ~ 4% lower for a titanium alloy.

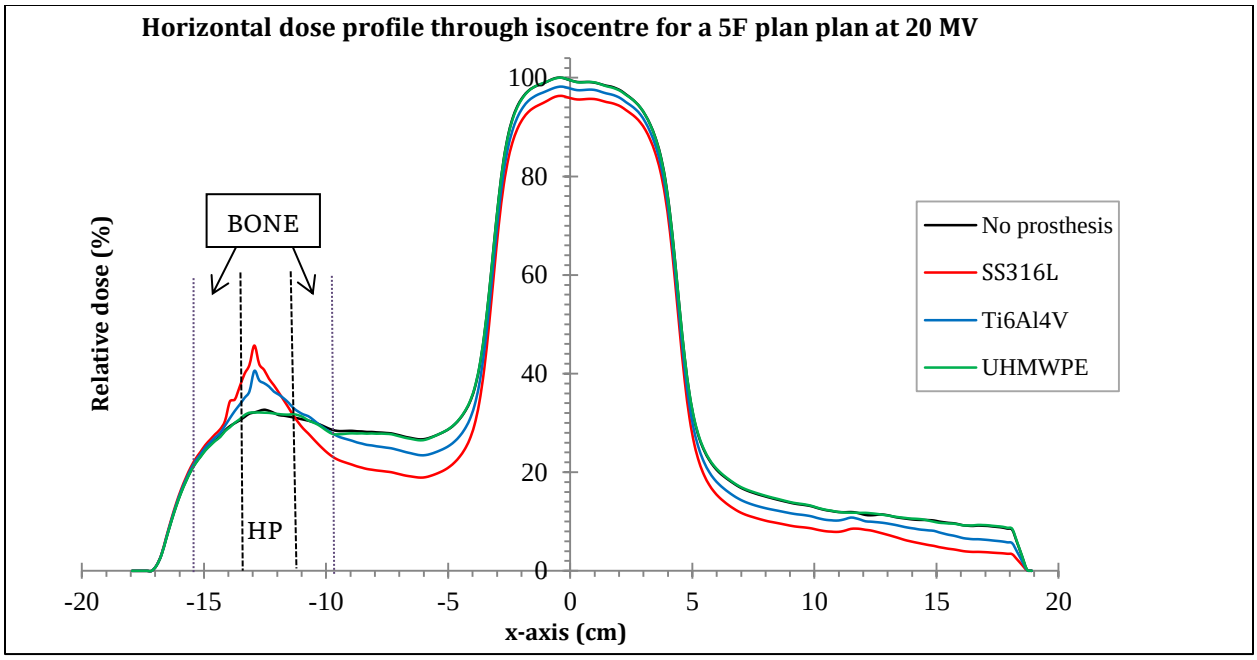


**Figure 7.23:** Comparison of DPs along the *x*–axis for a 5F plan at 20 MV. The isocenter dose is ~4% lower for a steel alloy and ~ 2% lower for a titanium alloy.

### 7.3.2.3 Six–field plan

Figure 7.24 shows the isodose distribution of a 6F plan in a patient with no hip prostheses.

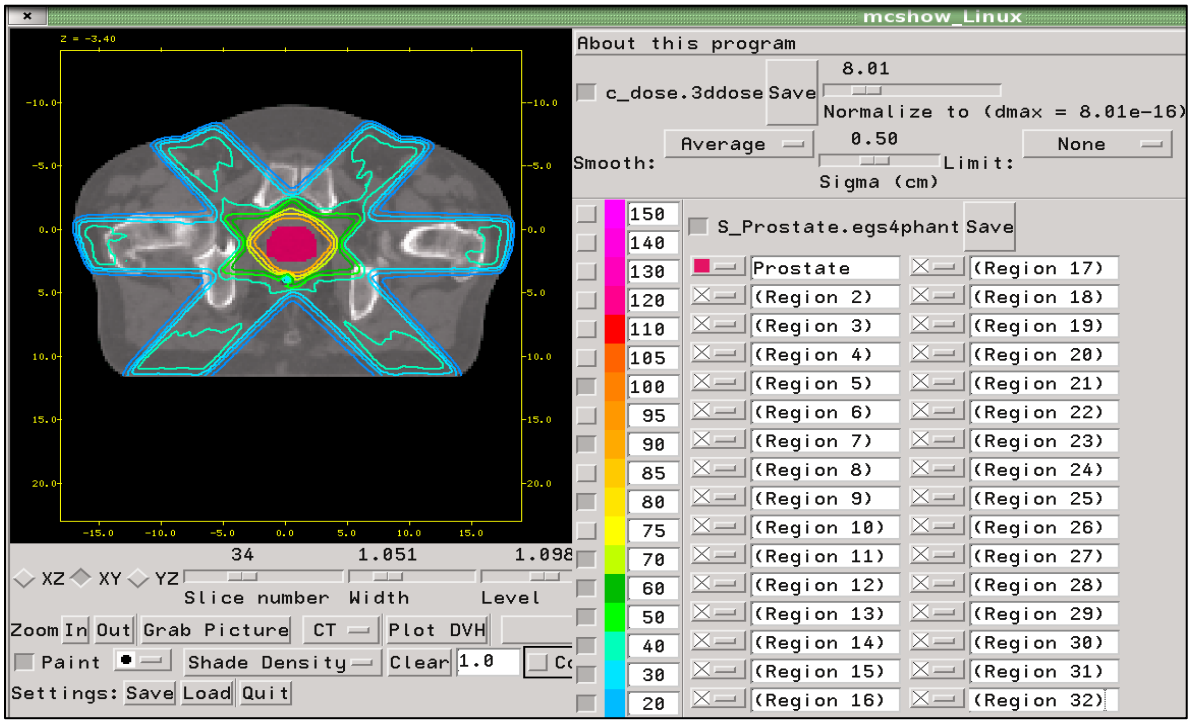


**Figure 7.24:** MCSHOW GUI showing the isodose distribution of a 6F plan obtained from DOSXYZnrc simulations in a patient with no prostheses

The effect of bilateral prostheses on the DVHs for the PTV, bladder and rectum using this 6F box technique is demonstrated in figs. 7.25-7.28. The 6F plan produces better PTV dose conformity, as well as less pronounced dose perturbation in the target compared to the 4F box plan. This is because the 6F plan has 2 out of 6 fields (33%) passing through the prostheses and 2 out of 4 fields (50%) passing through the prostheses in a 4F box plan. Comparing the 5F and the 6F plans for a patient with a single hip prosthesis, the 5F plan has 20% (one out of five) of its fields going through the HP whilst the 6F plan has only 17% (one out of six) intersecting the prosthesis. This is why the 6F plan has a reduced dose perturbation for a unilateral HP. However, in a patient with bilateral prostheses, the 6F plan has 33% of its beam portals intersecting the HPs compared to 20% in a 5F plan, and therefore the dose perturbation would be worse for a 6F plan in this case.

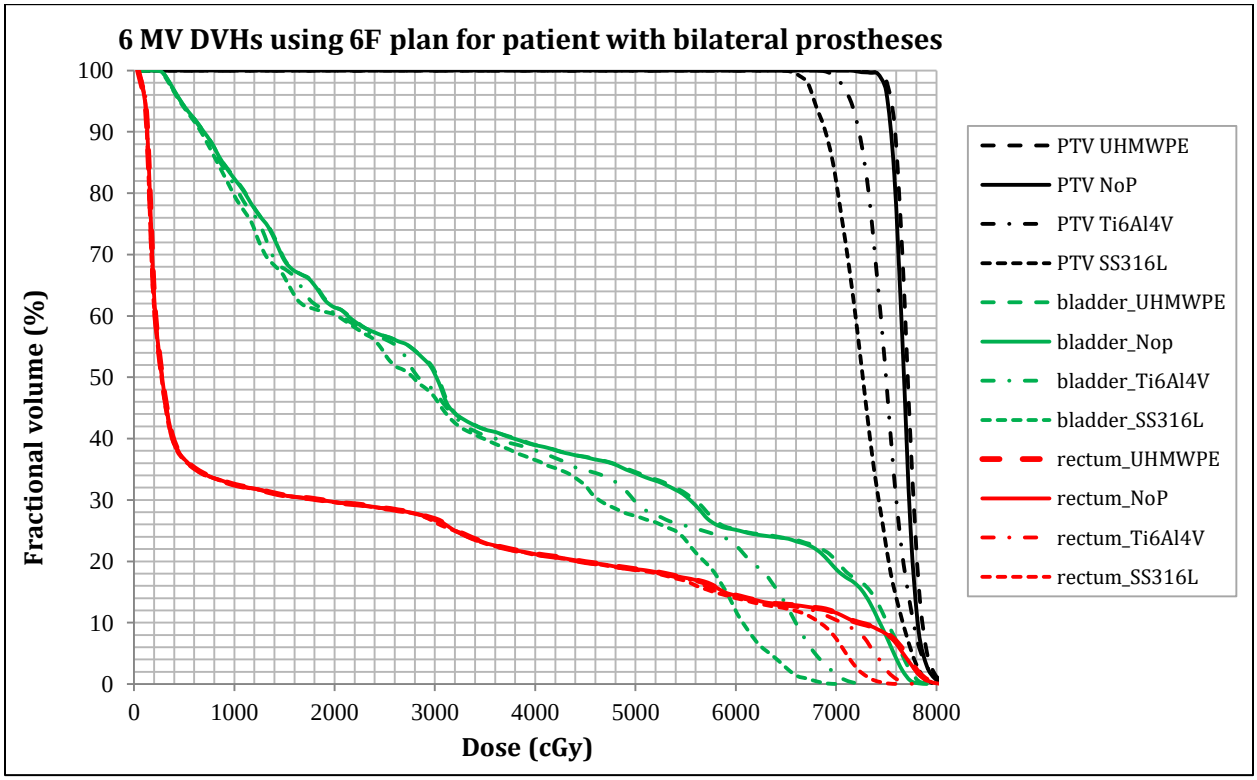


**Figure 7.25:** Comparison of DVHs for various bHPs using a 6F plan at 6 MV

It is also noticeable that the attenuation effect of metallic HPs not only reduces the dose to the target volume, but also results in lower dose to the rectum and bladder. The opposite, dose increase, is observable for the polymer HP.

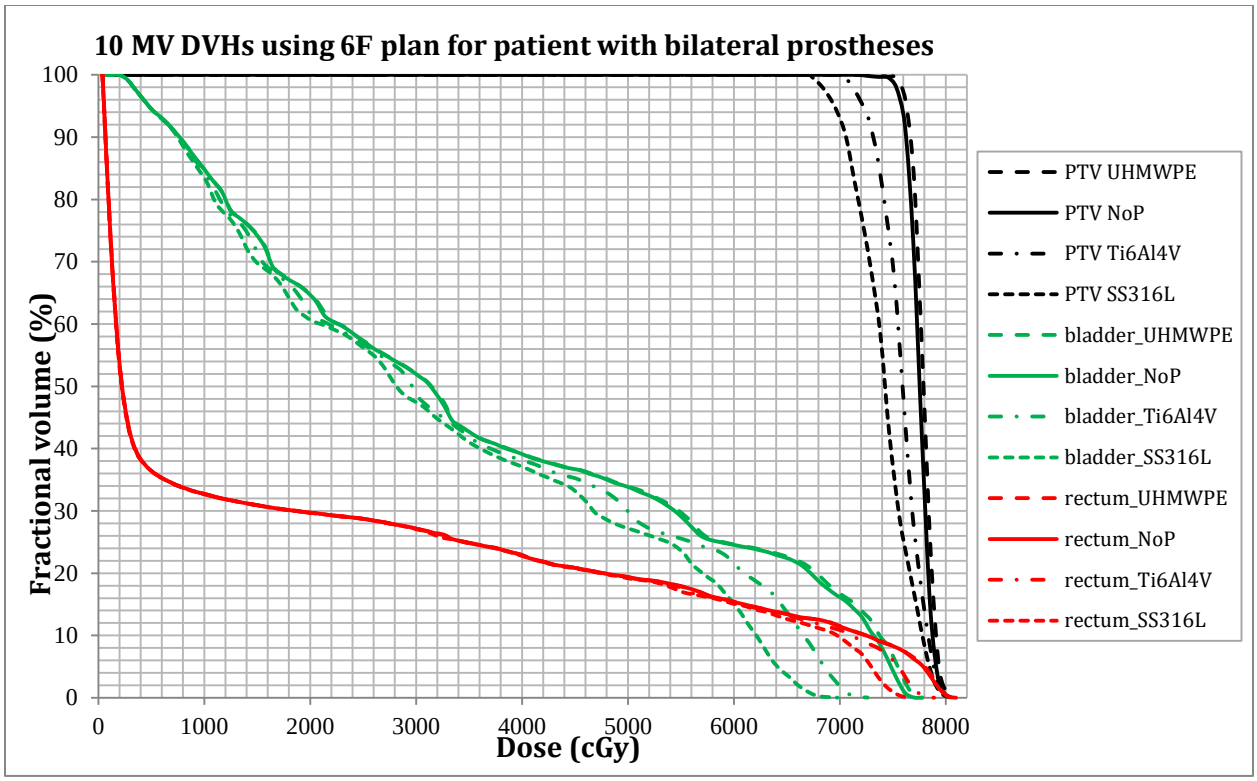


**Figure 7.26:** Comparison of DVHs for various bHPs using a 6F plan at 10 MV

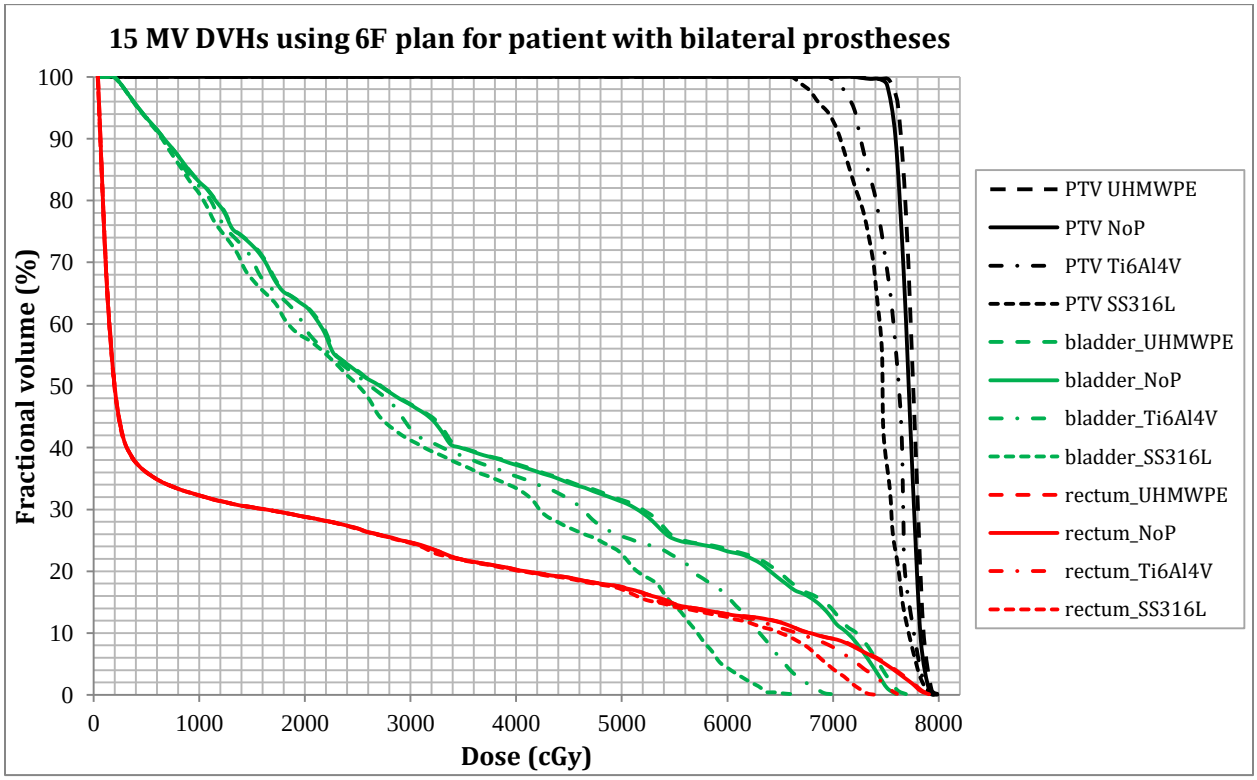


**Figure 7.27:** Comparison of DVHs for various bHPs using a 6F plan at 15 MV

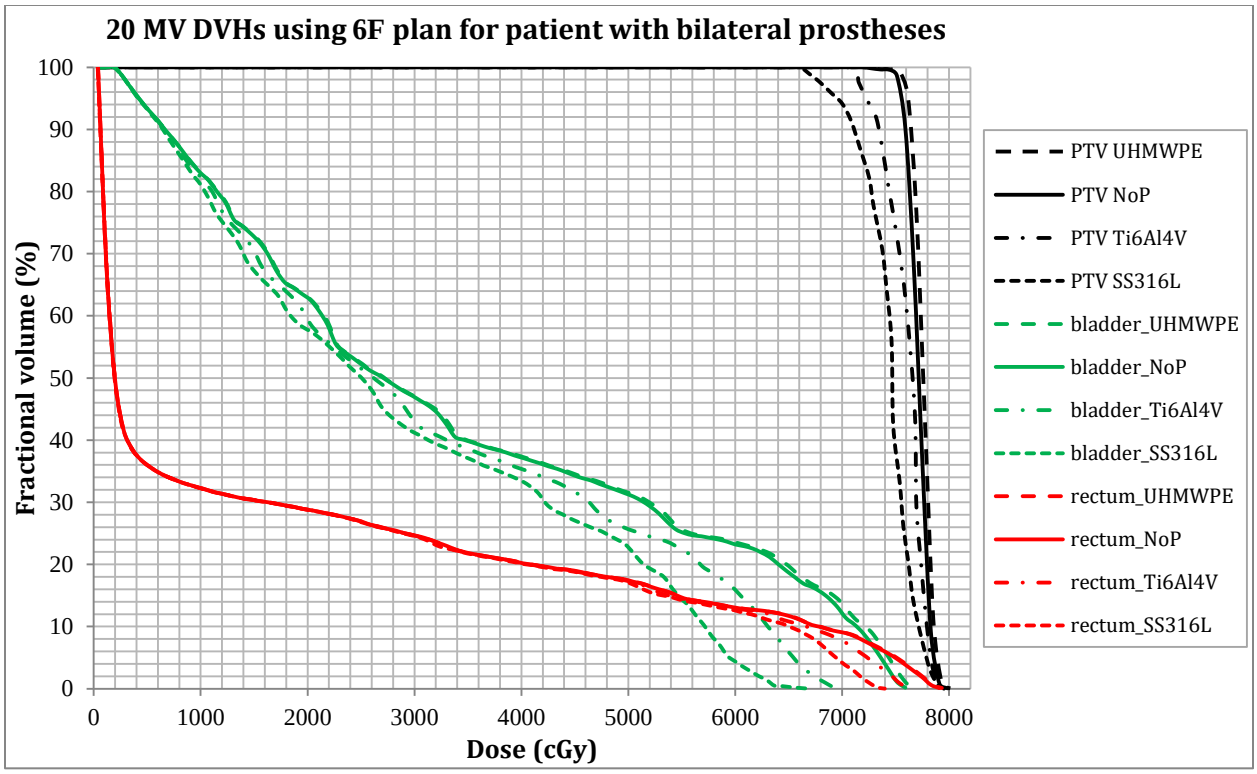


**Figure 7.28:** Comparison of DVHs for various bHPs using a 6F plan at 20 MV

In this 6F plan, up to 30% of the PTV volume is underdosed due to radiation absorption by SS316L and less than 4% was underdosed for a patient with titanium alloy. Again, UHMWPE prostheses showed negligible dose attenuation. This is summarized in table 7.14.

**Table 7.14:** $V_{95\%}$ vs. beam energy in the PTV for a 6F plan

| | **$V_{95\%}$: 6F plan** | | | |
|---|---|---|---|---|
| Energy (MV) | SS316L | Ti6Al4V | UHMWPE | No Prosthesis |
| 6 | 70.0 | 96.1 | 100.0 | 100.0 |
| 10 | 82.3 | 98.5 | 100.0 | 100.0 |
| 15 | 85.8 | 98.7 | 100.0 | 100.0 |
| 20 | 90.0 | 100.0 | 100.0 | 100.0 |

The dose effect of this 6F plan to the rectum and bladder at various energies is shown in table 7.15. It appears that the dose to critical organs is independent of the beam energies used, or at least no general trend is noticeable in these results.

**Table 7.15:** $V_{60Gy}$ vs. beam energy in OARs for a 6F plan

| | **6F plan** | |
|---|---|---|
| Energy (MV) | Rectum | Bladder |
| 6 | 14.0 | 25.2 |
| 10 | 15.2 | 23.8 |
| 15 | 13.5 | 23.8 |
| 20 | 13.5 | 23.8 |

The dose perturbation at the isocenter due to beam attenuation by the HPs in this 6F plan is shown in table 7.16. The maximum isocenter dose reduction in the presence of bilateral stainless steel alloy is 13%, and for titanium alloy it is 9% at 6 MV. The maximum PTV dose increase in the presence of UHMWPE is below 1%.

**Table 7.16:** Isocenter dose perturbation vs. energy for different HPs (6F plan)

| | **% dose reduction** | | **% dose enhancement** |
|---|---|---|---|
| Energy (MV) | SS316L | Ti6Al4V | UHMWPE |
| 6 | 15.1 | 12.6 | < 1 |
| 10 | 10.1 | 8.9 | < 1 |
| 15 | 7.2 | 4.8 | < 1 |
| 20 | 4.0 | 2.6 | < 1 |

By comparing the 4F box, 5F and 6F plans, the general trend is that increasing the number of beam portals improves the plan quality. Figures 7.29 (a) and (b) show the relationship between the number of beams in a plan and the target coverage for a patient fitted with bilateral titanium alloy at 6 and 15 MV.

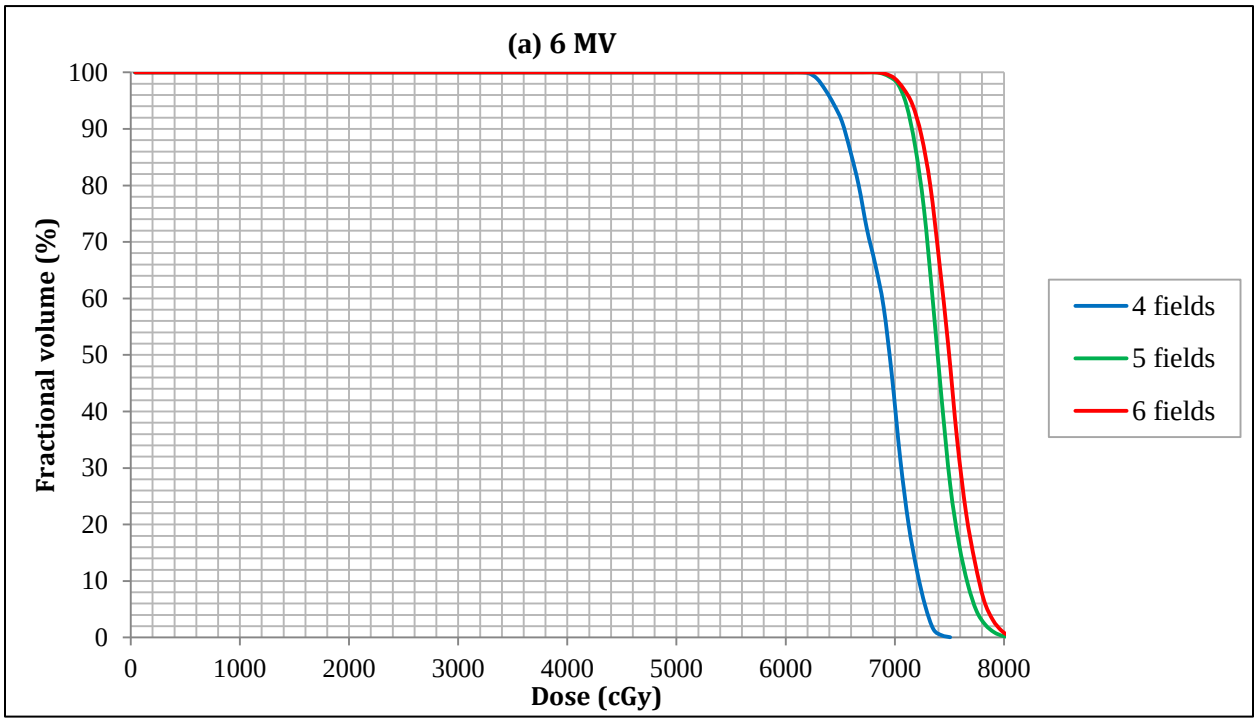


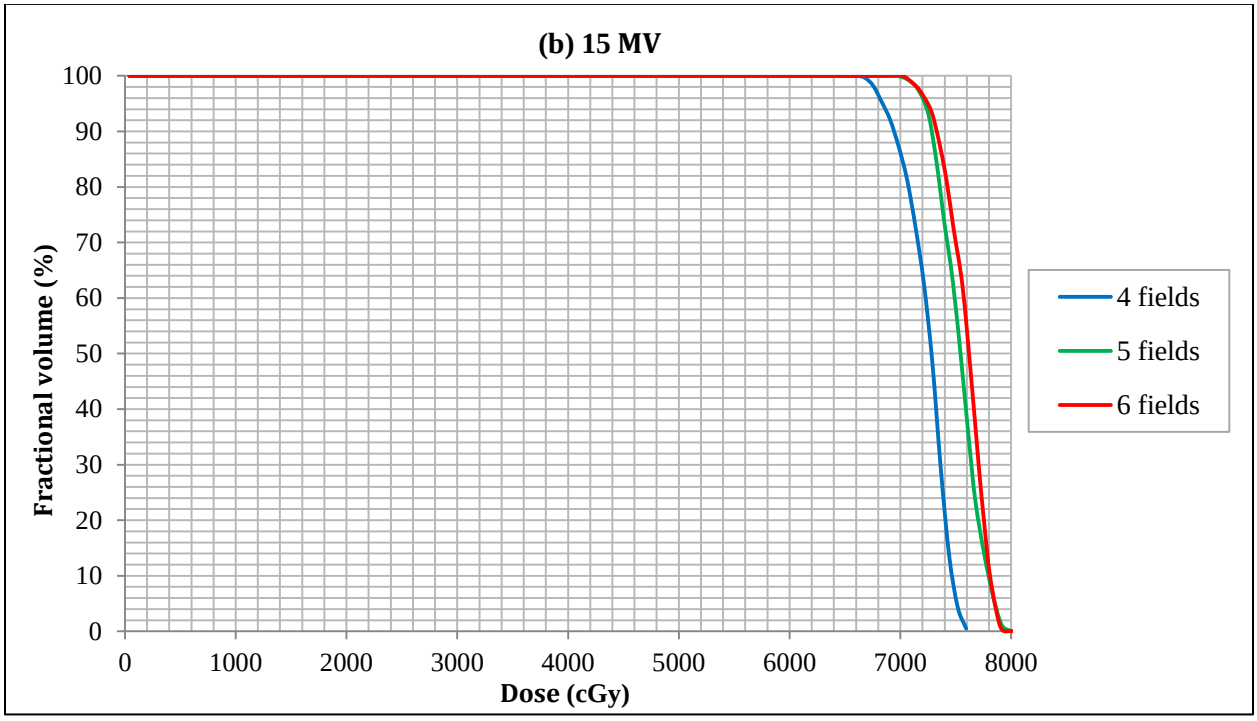


**Figure 7.29:** Relationship between the number of beams and target coverage for (a) 6 MV and (b) 15 MV photon beams in a patient with bilateral titanium hip prostheses. More beams produce a better dose distribution.

The 6F plan gives the best PTV coverage. It can also be noted that there is a closer match in dose distribution between the 5–field and the 6–field plan compared to the 4–field box plan and this match is more pronounced at the higher beam energy. Therefore, this study recommends plans with a larger number of beams that would allow avoiding the hip inhomogeneity in order to effectively compensate for dose attenuated in fields passing through HPs.

### 7.3.3 CT–based simulations (uHP patient model)

In this model, the same original CT dataset was elaborated and the same geometry as well as the same thickness of the prosthesis used in the bHP model was used for comparison purposes. The uHP model used is shown in figure 7.30.

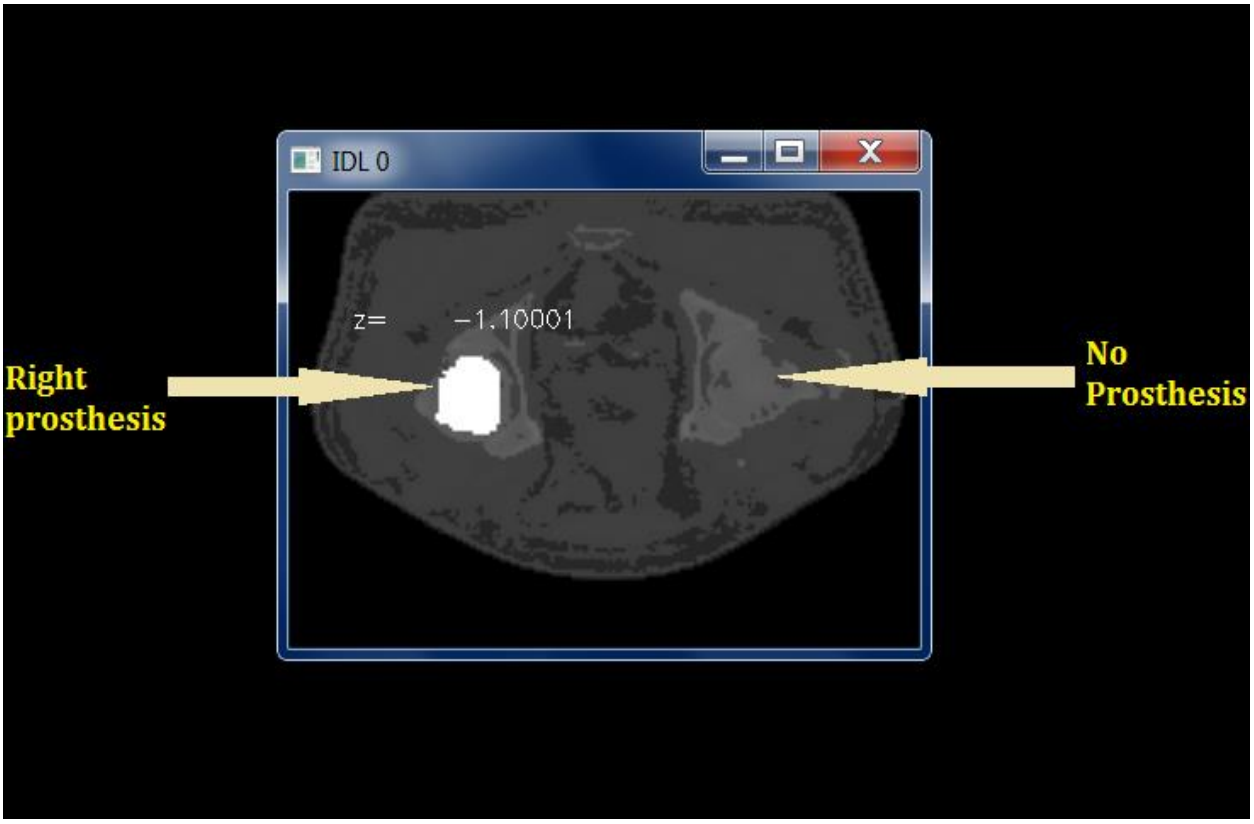


**Figure 7.30:** IDL output showing the transverse slice of a patient model fitted with uHP

### 7.3.3.1 Four–field box plan

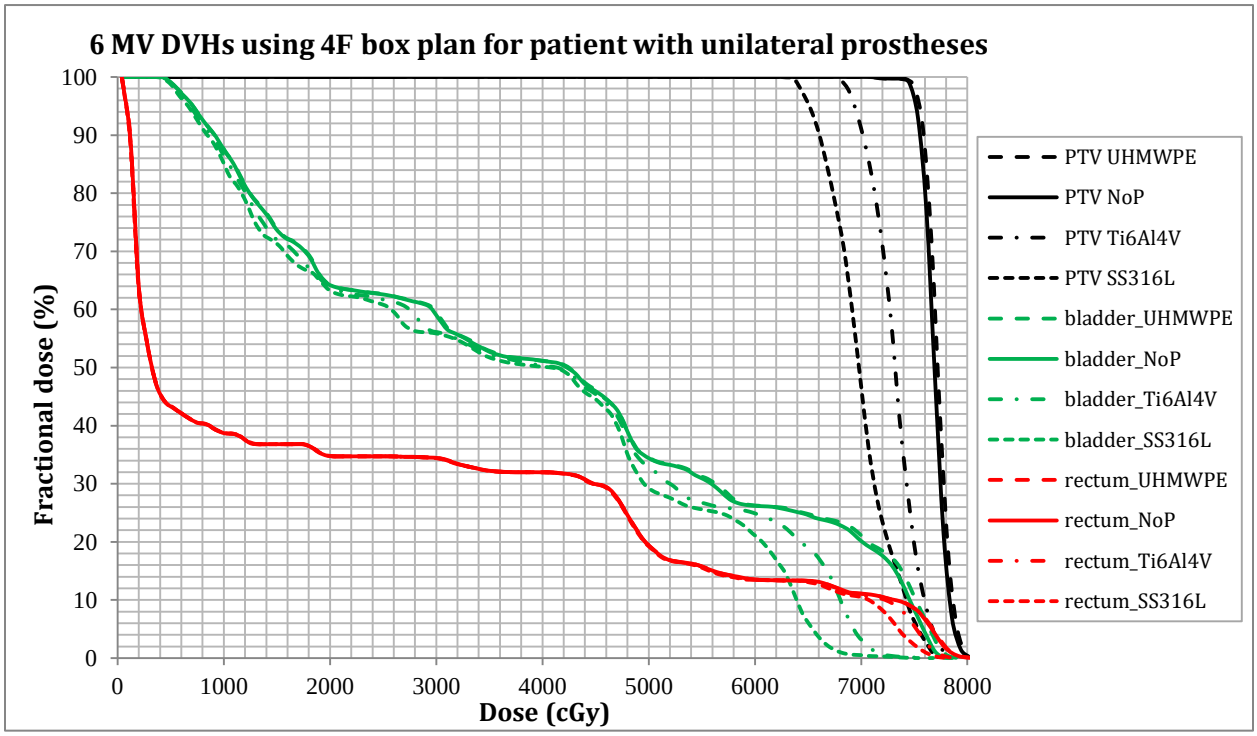


**Figure 7.31:** Comparison of DVHs for various uHPs using a 4F box plan at 6 MV

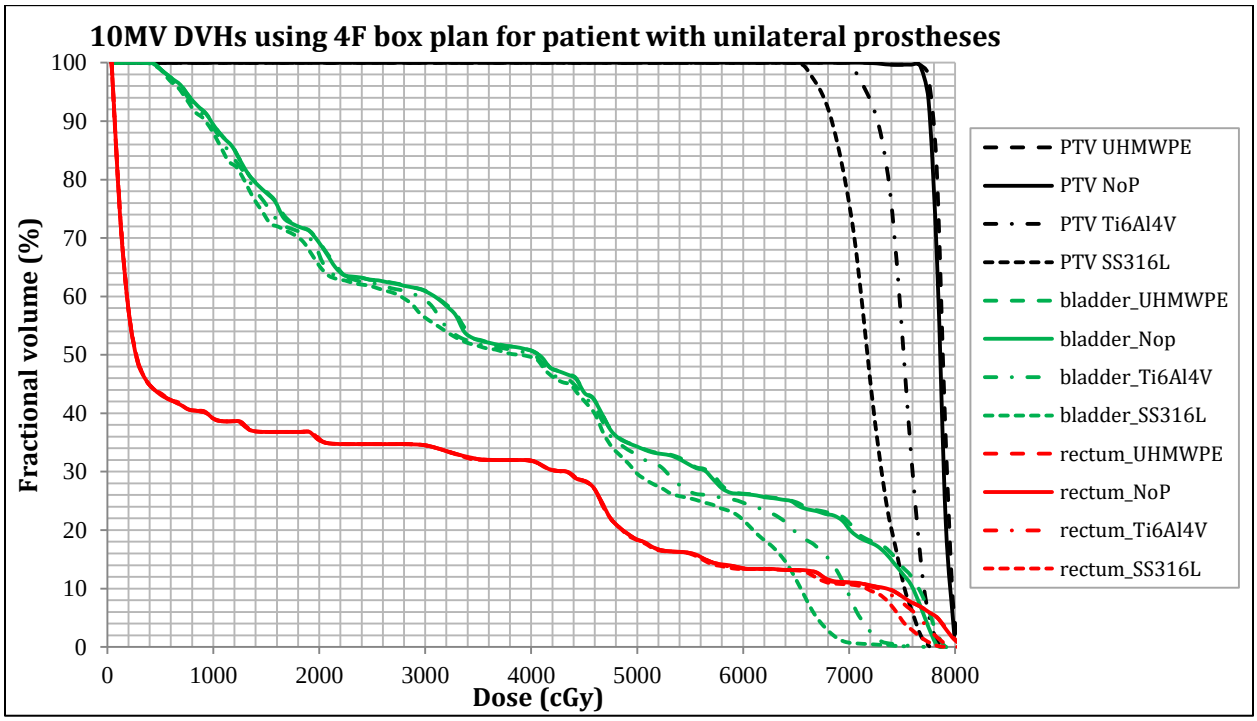


**Figure 7.32:** Comparison of DVHs for various uHPs using a 4F box plan at 10 MV

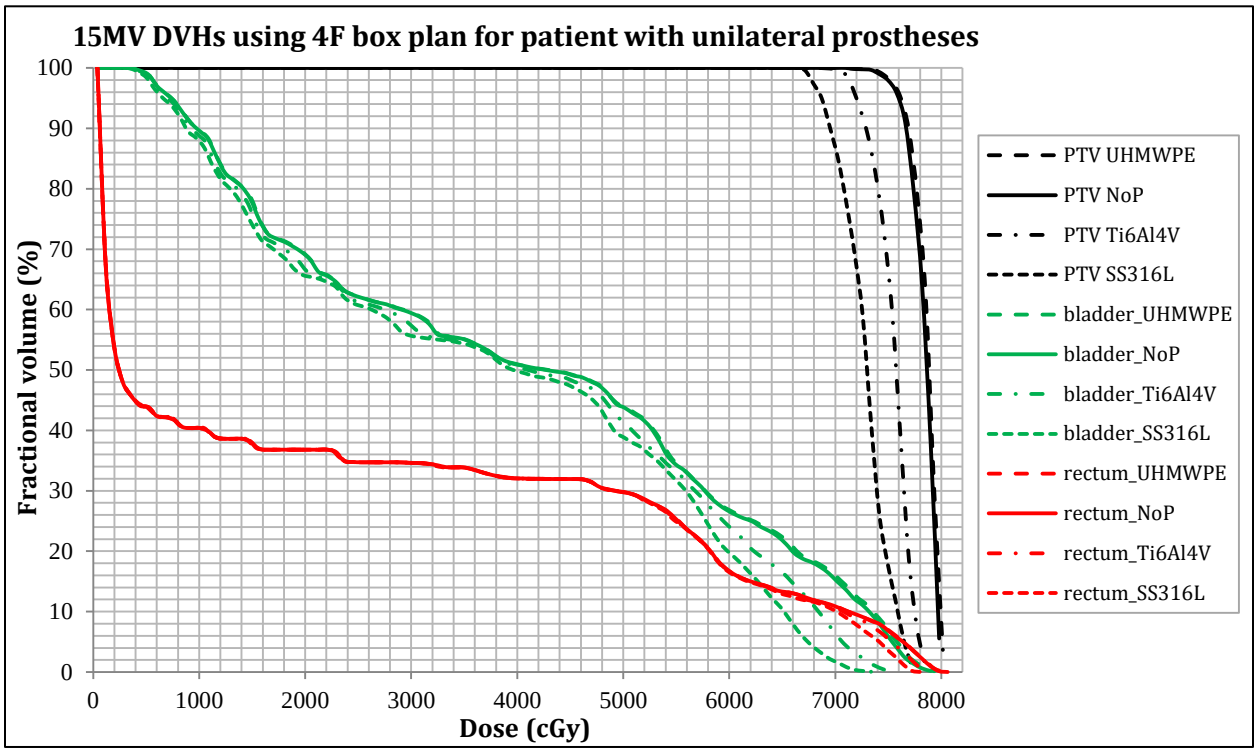


**Figure 7.33:** Comparison of DVHs for various uHPs using a 4F box plan at 15 MV

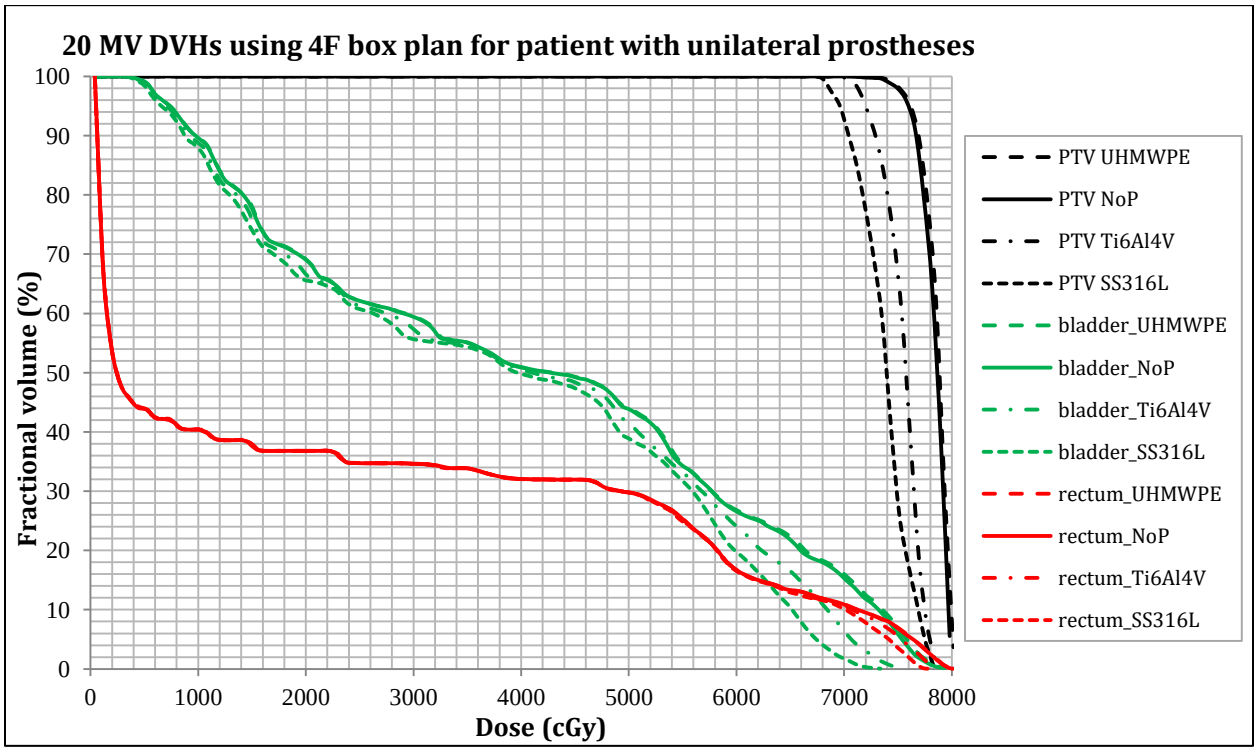


**Figure 7.34:** Comparison of DVHs for various uHPs using a 4F box plan at 20 MV

The maximum underdosed volume of the PTV in the presence of a unilateral SS316L and Ti6Al4V alloy with this 4F plan reaches up to 69% and 19%, respectively. The values of $V_{95\%}$ extrapolated from figures 7.31-7.34 for all HP materials and energies are summarized in table 7.17.

**Table 7.17**: $V_{95\%}$ vs. beam energy in the PTV for a 4F box with uHPs

| | **$V_{95\%}$: 4F box (%)** | | | |
|---|---|---|---|---|
| Energy (MV) | SS316L | Ti6Al4V | UHMWPE | No Prosthesis |
| 6 | 31.0 | 80.3 | 100.0 | 100.0 |
| 10 | 58.1 | 95.8 | 100.0 | 100.0 |
| 15 | 76.4 | 98.0 | 100.0 | 100.0 |
| 20 | 84.9 | 99.0 | 100.0 | 100.0 |

The dose reduction at the isocenter in the presence of unilateral stainless steel implant for the 4F box ranges from 7% – 19%, and for titanium alloy it ranges from 3% – 12%. The dose perturbation at the isocenter due to beam attenuation by single HPs is shown in table 7.18. The PTV dose reduction in a patient with a single hip prosthesis is markedly lower than for bilateral prostheses.

**Table 7.18:** Isocenter dose perturbation vs. energy for different uHPs (4F box)

| | **% dose reduction** | | **% dose enhancement** |
|---|---|---|---|
| Energy (MV) | SS316L | Ti6Al4V | UHMWPE |
| 6 | 18.6 | 12.3 | < 1 |
| 10 | 15.1 | 9.5 | < 1 |
| 15 | 10.3 | 5.6 | < 1 |
| 20 | 6.8 | 2.5 | < 1 |

### 7.3.3.2 Five–field plan

The isocenter dose perturbation as well as the $V_{95\%}$ values in the 5F configuration used is exactly the same as in the bilateral model as only one HP blocks the field.

### 7.3.3.2 Six–field plan

The effect of various unilateral hip prostheses on the cumulative DVHs for the PTV, bladder and rectum using a 6F box technique is demonstrated in figs. 7.35-7.38. The values of $V_{95\%}$ for all HP materials and energies are summarized in table 7.19.

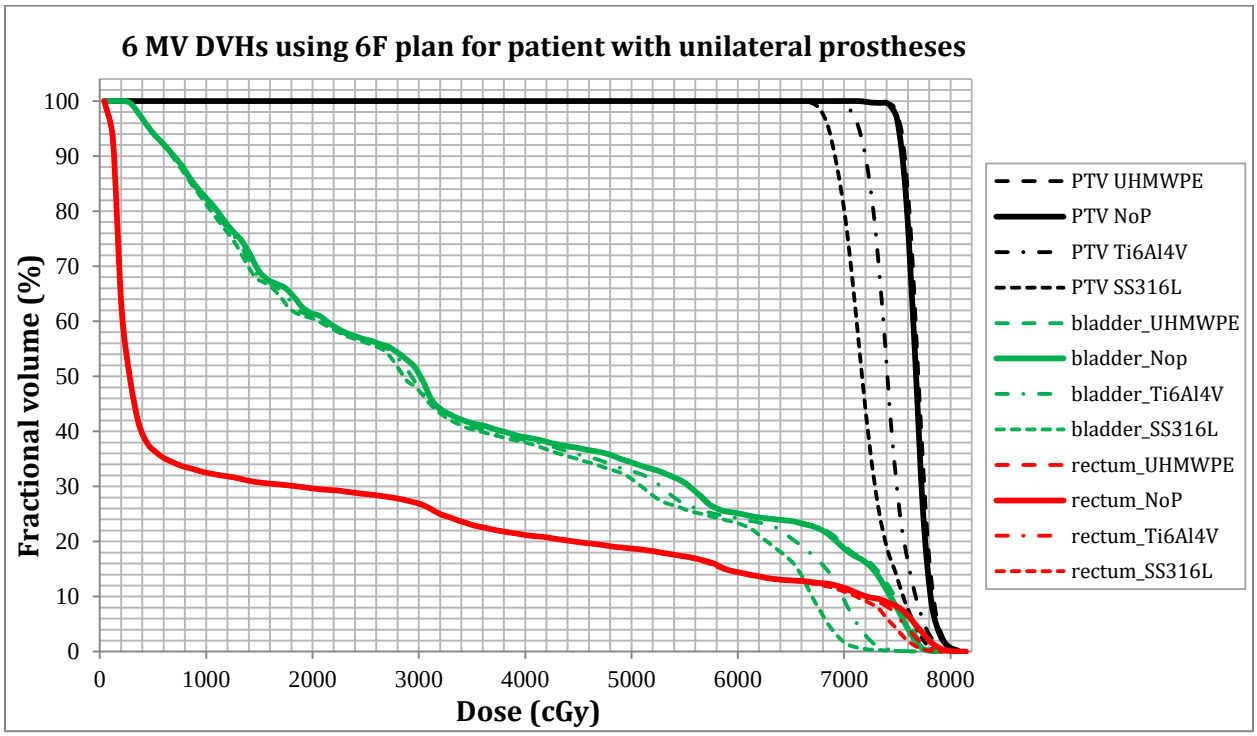


**Figure 7.35:** Comparison of DVHs for various bHPs using a 6F plan at 6 MV

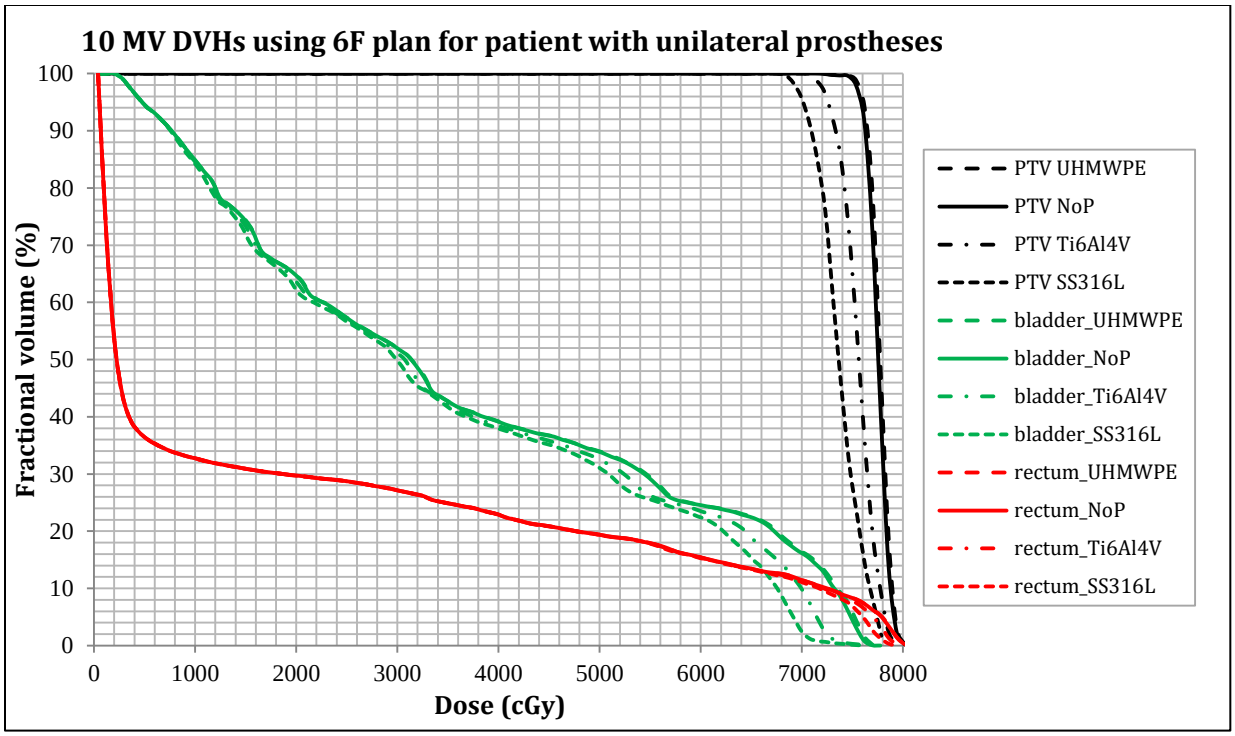


**Figure 7.36:** Comparison of DVHs for various bHPs using a 6F plan at 10 MV

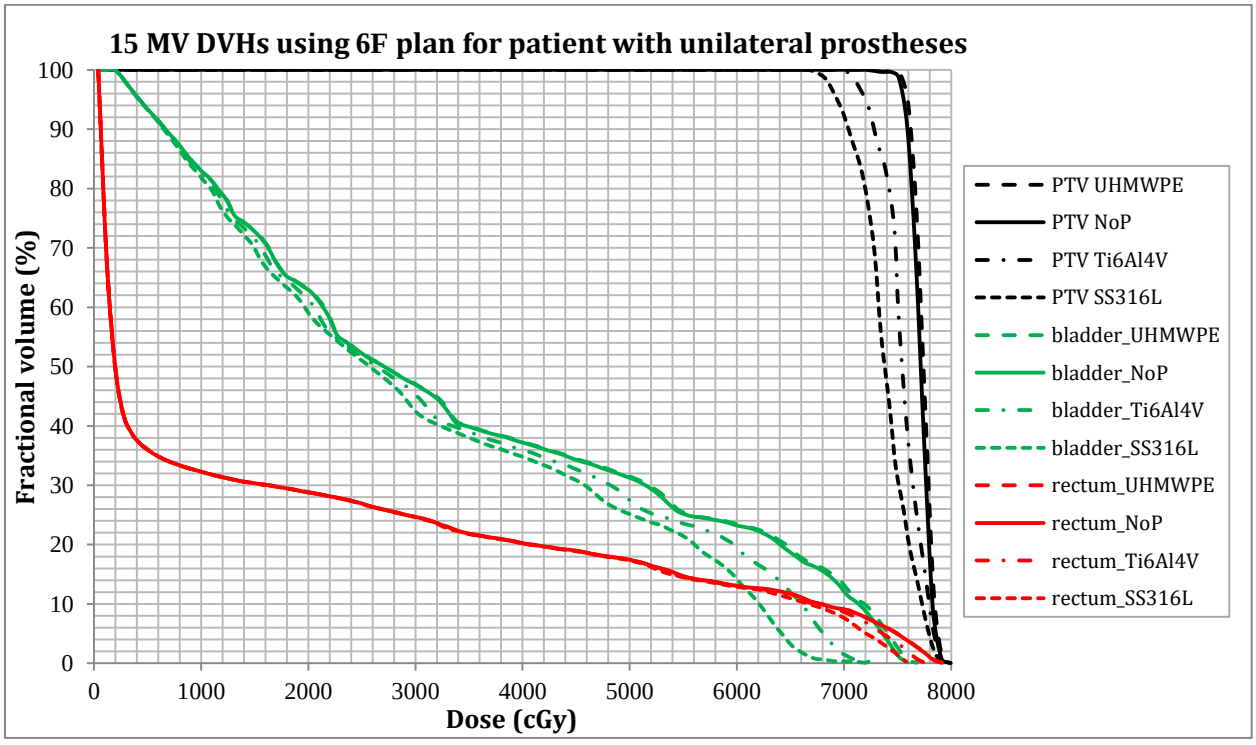


**Figure 7.37:** Comparison of DVHs for various bHPs using a 6F plan at 15 MV

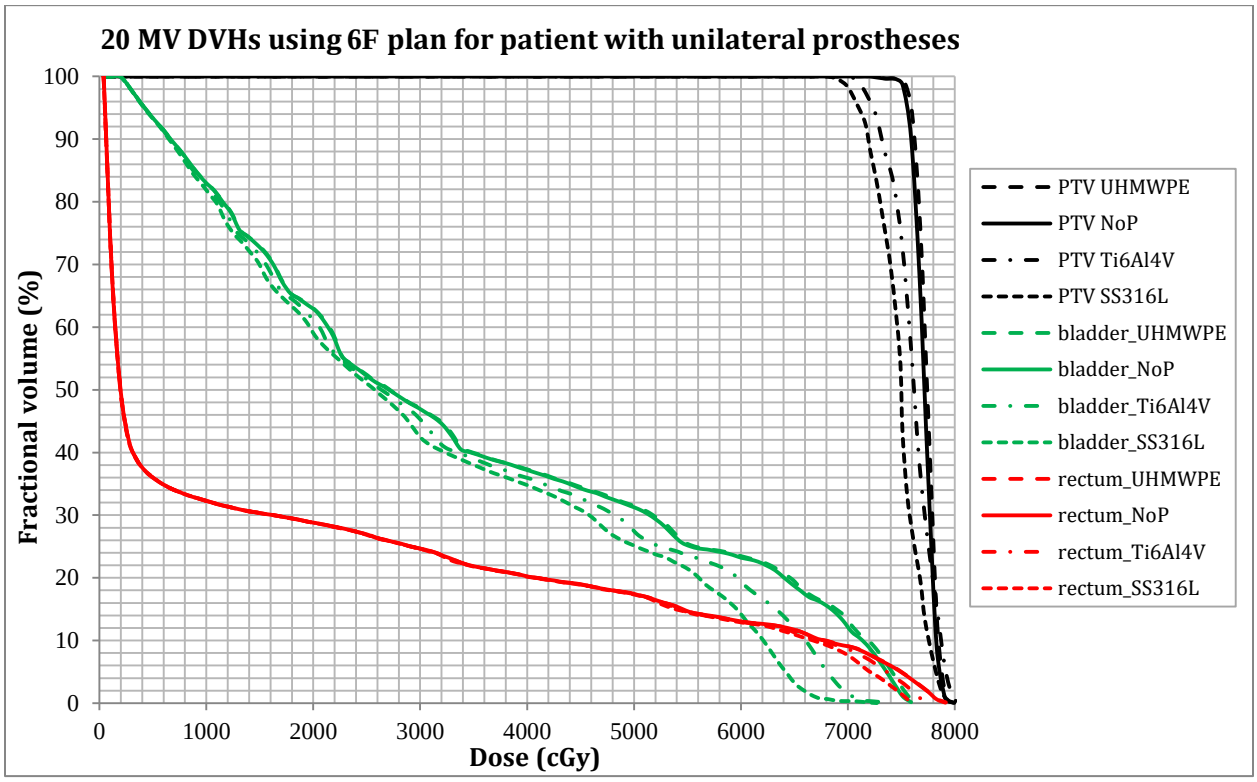


**Figure 7.38:** Comparison of DVHs for various bHPs using a 6F plan at 20 MV

The largest PTV volume underdosed in the presence of unilateral SS316L and Ti6Al4V implants with this 6F plan is 40% and 4%, respectively. Maximum underdosage occurs at 6 MV.

**Table 7.19:** $V_{95\%}$ vs. beam energy in the PTV for a 6F plan with uHPs

| | **$V_{95\%}$: 6F plan (%)** | | | |
|---|---|---|---|---|
| Energy (MV) | SS316L | Ti6Al4V | UHMWPE | No Prosthesis |
| 6 | 73.0 | 95.5 | 100.0 | 100.0 |
| 10 | 84.2 | 98.4 | 100.0 | 100.0 |
| 15 | 86.6 | 99.0 | 100.0 | 100.0 |
| 20 | 95.7 | 100.0 | 100.0 | 100.0 |

The dose reduction in the PTV in the presence of a single stainless steel implant for the 6F plan is below ~11%, and for titanium alloy it is below ~ 7%. No observable dose changes occur for UHMWPE. These results are tabulated in table 7.20.

**Table 7.20:** Isocenter dose perturbations for different uHPs (6F plan)

| | **% dose reduction** | | **% dose enhancement** |
|---|---|---|---|
| Energy (MV) | SS316L | Ti6Al4V | UHMWPE |
| 6 | 10.3 | 6.2 | < 1 |
| 10 | 6.9 | 4.2 | < 1 |
| 15 | 3.5 | 2.4 | < 1 |
| 20 | 2.1 | 1.0 | < 1 |

The MV photon dose distribution in several studies indicated similar patterns of implant-tissue interface effects for various implant types. The dose change at the bone-HP interface is comparable to that at a tissue-high-Z boundary, although the degree of the perturbation will be lessened due to a closer match between the Z-numbers of the two media as reported by Reft *et al.* (2003).

## 7.5 Limitations

There were a few problems encountered in this study, most of which are based on the nature of MC simulations.

A common problem associated with MC simulations is the long simulation time; it took ≈ 21 hours to simulate $3 \times 10^8$ particle histories in BEAMnrc linac modelling and ≈ 54 hours to simulate $3 \times 10^9$ histories in DOSXYZnrc CT phantom modelling. This long simulation time increased the chances of encountering an electrical interruption. Therefore, simulations had to be 'broken down' into numerous runs with smaller histories, whose PS output files were combined using BEAMDP. This was a very labour intensive process.

Lack of detailed specifications for linac components (e.g. material compositions) was another challenge. The detailed mechanic drawings and compositions of a linac are usually confidential and secured by the manufacturer to prevent others from directly adopting their models for subsequent research. Thus, our linac was a generic model of an Elekta Prec*i*se linac head. However, the model was validated by analysing the photon beam characteristics of the beam generated in a water phantom and comparing with standard dose distributions.

A large storage space was needed for PS files generated, especially at high energies and large fields. More than 100 Gigabytes were needed to store all the PS files generated in this study.

One disadvantage of using cumulative DVHs for dose comparisons is the lack of spatial information; only the magnitude of dose changes can be known but not where the changes occured.

# 8. Conclusions

## 8.1 Summary of results

The main goal of this work was to evaluate the dosimetric influence of hip prostheses on the mid axial slice and in some volumes in a CT–based phantom using MC simulations. The effects of radiation absorption and scatter by the metallic or thermoplastic implants in the shadow of the HP and on the bone–prosthesis interfaces were determined.

The Monte Carlo simulation of a full Elekta Prec*i*se linear accelerator head design and beam production for 6–20 MV high energy x-rays beams was successfully performed and the beam parameters were benchmarked against the machine's commissioning data from water tank measurements. Beam parameter data were within one percent of measured PDD data.

Results indicate that the depth dose within and beyond the metallic inhomogeneity drops significantly due to beam attenuation. For patients with bilateral Ti6Al4V and SS316L HPs (~3 cm thick), the PTV dose reductions using a 4F box ranged from 11 – 17% and 17 – 23%, respectively. For a uHP patient model, the respective dose reductions ranged from 3 – 12% and 7 – 19% for titanium and steel alloys. The dose perturbation was always <1% for a patient fitted with UHMWPE. The PTV dose reduction diminished for plans with more beam portals, dropping below 5% in a bHP model and below 2% in a uHP patient model irradiated with 6 conformal treatment fields at 20 MV. The results indicate that metallic prostheses cause a clinically significant absorbed dose reduction throughout the area lying in the shadow of the HP whereas thermoplastic implants like UHMWPE pose no significant dose perturbation in the shadow of the implant and on the interface with tissue or bone. Adequate dose distribution may be achieved by using high–energy photon

beams to reduce beam attenuation by metallic HPs and using plans with more beam portals to improve target coverage.

MC was also used to examine the dosimetric influence of electronic disequilibrium at the bone–prosthesis interface and DPFs were calculated in the close vicinity of the interfaces. It was found that scatter radiation from denser materials was significant and dose escalation at the proximal interface between metallic HPs and bone existed in patients undergoing lateral beam irradiation for pelvic malignancies. The degree of this perturbation is highly dependent on the beam energy and the effective atomic number of the heterogeneity. The maximum local dose enhancement (DEF ~ 1.38) ranging a distance of up to 1.5 cm from the bone–steel proximal interface and rapidly falling off with increasing distance from the interface was observed at 20 MV. This dose build up is due to backscatter perturbation that exists at the interface of two materials with different densities and resulted in normal tissue proximal to the beams for the stainless steel device receiving very near prescribed dose – this is an important finding. Increased doses distal to the high–Z implant were observed for beam energies above 10 MV due to pair production interactions in the metal. These dose perturbations are comparable to that at tissue–metal boundaries, though the magnitude of the effects is reduced, owing to the closer match between the Z–numbers of bone and metal.

The range of secondary electrons backscattered from the high–Z prosthesis is less than the distance to tissue. Therefore, there are no major concerns about creating 'hot spots' in tissue regions adjacent to the prosthesis. Furthermore, the volume irradiated immediately contiguous to the metallic prosthesis is too small to arouse any concerns about bone necrosis.

Simulations reveal that the dose escalation at the proximal interface is greater than the dose reduction at the distal interface. The exit boundary dose is diminished as the electron build-up in bone scattered from the HP does not fully compensate for the increased primary beam absorption through steel and titanium alloys.

The 4F box plan produced the greatest dose reduction in the tumor load, underdosing 54 – 90% of the PTV volume in the presence of bilateral steel alloy and 15 – 76% for a patient with titanium prostheses. Using beam portals that do not traverse the HP is recommended, if possible. These results also highlight the significant influence of the implant's composition and the beam position relative to the HP as well as beam energy on the dose distribution.

Though the reduction of OAR dose occurs when high–Z materials are used for HP in these chosen treatment plans, it was not the planning intent to reduce/spare OAR doses and therefore little can be said about the OAR dose reduction.

It has been established that MC can provide dose information that a conventional TPS might not be able to calculate accurately. Therefore, this study recommends using MC–based TPSs for accurate dose calculation in the presence of metallic heterogeneities. MCSHOW GUI allowed the addition of HP contours into patient CT images, thus allowing us to evaluate the effect of different implant materials and models in patient CT dataset without metal artefacts.

This study confirmed the results in other studies of the same topic. The advantage, as stipulated in the dissertation, was the exclusion of imaging artefacts due to the fact that heterogeneous media was introduced into the patient-CT phantom in a synthetic way. This skill allows several other future studies to be performed.

## 8.2 Future research

The results of this study are highly dependent on other variables not investigated, such as the field size, the thickness of the prosthesis and the angle of beam incidence. Therefore, the recommendations given in this report are not meant to be prescriptive, but only general guidelines on how to minimize the undesired dosimetric effects of HPs during pelvic RT.

This work used equally-spaced, equally weighted coplanar photon beams and 3 THR models of ~3 cm thickness. Further studies are needed to determine whether the same conclusions hold even when using different implant sizes and more sophisticated, non-coplanar beam arrangements with lateral beam weighting and compensation.

Further focus can also be on comparing the dosimetric effect of a cephalic prosthesis with a total hip prosthesis during pelvic RT and other implant materials like cobalt–chromium, ceramics, and synthetic materials.

Another interesting study would be to investigate other parameters affecting dose perturbation; including the area of the prosthesis relative to the beam, depth of the interface from the surface, beam angle relative to the implant (i.e., perpendicular vs. oblique beam incidence), the prescribed dose, patient anatomy and the treatment volume (i.e., whether or not seminal vesicles are included in the PTV).

Another research study could be investigating the effectiveness of cements used to coat hip prostheses in reducing dose perturbations at the bone–HP interface to help protect the bone from necrosis, as proposed by Carolan *et al.* (2000).

Virtually all studies investigating the dosimetric effect of HPs lack the biological component. Only when clinically reliable dose-volume data for normal tissue complication probability calculation can be incorporated for each OAR will a plan evaluation become absolutely quantitative. As computing power continues to increase, the research emphasis can be directed on studying the biological effects of increased dose in the vicinity of the bone–HP boundary.

This work could also be improved by performing film measurements to validate the MC results and corroborate the accuracy of our conclusions.

# 9. References


Abdullah, A.K., Nabil, M., and Akhtar, A.N., 2005. The use of MCNP code for radiation transport and dosimetry calculations in training medical physics student. *Int. J. Sci. Res.,* Vol. 15, pp. X-Y.

Agapito, J., 2001. Radical radiation therapy for carcinoma of the prostate in patients with a single hip prosthesis: a technique analysis using dose-volume histograms. *Medical Dosimetry*, *26*(3), pp.243-250.

Agostinelli, S., Allison, J., Amako, K.A., Apostolakis, J., Araujo, H., Arce, P., Asai, M., Axen, D., Banerjee, S., Barrand, G. and Behner, F., 2003. Geant4–a simulation toolkit. *Nuclear instruments and methods in physics research section A: Accelerators, Spectrometers, Detectors and Associated Equipment*, *506*(3), pp.250-303.

Al Kafi, A., Maalej, N. and Naqvi, N., 2006. The use of MCNP Code for Radiation Transport and Dosimetry Calculations in Training Medical Physics Students. *J. Scientific Research*, *16*, pp.195-200.

Ali, O.A., 2009. *Monte Carlo Characterisation of Electron Beams Transported Through a Photon Multi-leaf Collimator for Use in Modulated Electron Radiation Therapy*. Doctoral thesis, University of the Free State, Bloemfontein, South Africa.

Almond, P.R., Biggs, P.J., Coursey, B.M., Hanson, W.F., Huq, M.S., Nath, R. and Rogers, D.W.O., 1999. AAPM's TG-51 protocol for clinical reference dosimetry of high-energy photon and electron beams. *Medical physics*, *26*(9), pp.1847-1870.

Alvarado, J., Maldonado, R., Marxua ch, J. and Otero, R., 2003. Biomechanics of hip and knee prostheses. *Applications of Engineering Mechanics in Medicine*, pp.6-22.

Andreo, P., 1998. Monte Carlo applications in radiotherapy. *Radiation Physics and Chemistry*, *53*(3), pp.350-351.

Baró, J., Sempau, J., Fernández-Varea, J.M. and Salvat, F., 1995. PENELOPE: an algorithm for Monte Carlo simulation of the penetration and energy loss of electrons and positrons in matter. *Nuclear Instruments and Methods in Physics Research Section B: Beam Interactions with Materials and Atoms*, *100*(1), pp.31-46.

Bielajew, A.F., 2001. Fundamentals of the Monte Carlo method for neutral and charged particle transport. *The University of Michigan.*

Bielajew, A.F., Rogers, D.W.O., Nelson, W.R. and Hirayama, H., 1994. History, overview and recent improvements of EGS4. In *Presented at* (No. SLAC-PUB-6499).

Biggs, P.J. and Russell, M.D., 1988. Effect of a femoral head prosthesis on megavoltage beam radiotherapy. *International Journal of Radiation Oncology* Biology* Physics*, *14*(3), pp.581-586.

Briesmeister, J.F., 2000. MCNPTM-A general Monte Carlo N-particle transport code. *Version 4C, LA-13709-M, Los Alamos National Laboratory*.

Brooks, C., Cheung, R.M. and Kudchadker, R.J., 2010. Intensity-modulated radiation therapy with non-coplanar beams for treatment of prostate cancer in patients with bilateral hip prosthesis–a case study. *Medical Dosimetry*, *35*(2), pp.87-91.

Buffard, E., Gschwind, R., Makovicka, L. and David, C., 2006. Monte Carlo calculations of the impact of a hip prosthesis on the dose distribution. *Nuclear Instruments and Methods in Physics Research Section B: Beam Interactions with Materials and Atoms*, *251*(1), pp.9-18.

Burleson, W.D., Stutzman, C.D., Stitt, J.A., Karlsson, U.L. and Mian, T.A., 1991. In vivo isocenter dose in two hip prosthesis patients. *International Journal of Radiation Oncology* Biology* Physics*, *20*(6), pp.1347-1352.

Caccia, B., Mattia, M., Amati, G., Andenna, C., Benassi, M., d'Angelo, A., Frustagli, G., Iaccarino, G., Occhigrossi, A. and Valentini, S., 2007. Monte Carlo in radiotherapy: experience in a distributed computational environment. In *Journal of Physics: Conference Series* (Vol. 74, No. 1, p. 021001). IOP Publishing.

Carolan, M., Dao, P., Fox, C. and Metcalfe, P., 2000. Effect of hip prostheses on radiotherapy dose. *Australasian radiology*, *44*(3), pp.290-295.

Chapman, D., Smith, S., Barnett, R., Bauman, G. and Yartsev, S., 2014. Optimization of tomotherapy treatment planning for patients with bilateral hip prostheses. *Radiation Oncology*, *9*(1), p.1.

Chatzigiannis, C., Lymperopoulou, G., Sandilos, P., Dardoufas, C., Yakoumakis, E., Georgiou, E. and Karaiskos, P., 2011. Dose perturbation in the radiotherapy of breast cancer patients implanted with the Magna-Site: a Monte Carlo study. *Journal of Applied Clinical Medical Physics*, *12*(2).

Cheng, C.W., Mitra, R., Li, X.A. and Das, I.J., 2005. Dose perturbations due to contrast medium and air in MammoSite® treatment: An experimental and Monte Carlo study. *Medical physics*, *32*(7), pp.2279-2287.

Chetty, I.J., Curran, B., Cygler, J.E., DeMarco, J.J., Ezzell, G., Faddegon, B.A., Kawrakow, I., Keall, P.J., Liu, H., Ma, C.M.C. and Rogers, D.W.O., 2007. Report of the AAPM Task Group No. 105: Issues associated with clinical implementation of Monte Carlo-based photon and electron external beam treatment planning. *Medical physics*, *34*(12), pp.4818-4853.

Curry, T.S., Dowdey, J.E. and Murry, R.C., 1990. *Christensen's physics of diagnostic radiology*. Lippincott Williams & Wilkins.

Das, I.J. and Kahn, F.M., 1989. Backscatter dose perturbation at high atomic number interfaces in megavoltage photon beams. *Medical physics*, *16*(3), pp.367-375.

Das, I.J., 1997. Forward dose perturbation at high atomic number interfaces in kilovoltage x-ray beams. *Medical physics*, *24*(11), pp.1781-1787.

Deng, J., Jiang, S.B., Kapur, A., Li, J., Pawlicki, T. and Ma, C.M., 2000. Photon beam characterization and modelling for Monte Carlo treatment planning. *Physics in medicine and biology*, *45*(2), p.411.

Ding, G.X. and Christine, W.Y., 2001. A study on beams passing through hip prosthesis for pelvic radiation treatment. *International Journal of Radiation Oncology* Biology* Physics*, *51*(4), pp.1167-1175.

Eng, T.Y., 2000. Dose attenuation through a titanium alloy hip prosthesis. *Medical Dosimetry*, *25*(1), pp.7-8.

Erlanson, M., Franzén, L., Henriksson, R., Littbrand, B. and Lofroth, P.O., 1991. Planning of radiotherapy for patients with hip prosthesis. *International Journal of Radiation Oncology* Biology* Physics*, *20*(5), pp.1093-1098.

Farajollahi, A. and Mesbahi, A., 2006. Monte Carlo dose calculations for a 6-MV photon beam in a thorax phantom. *Radiation medicine*, *24*(4), pp.269-276.

Fern`andez, J.E. and Scot, V., 2007. Deterministic and Monte Carlo codes for multiple scattering photon transport with arbitrary polarization states. *Spectrochimica Acta Part B: Atomic Spectroscopy*, *62*(6), pp.517-528.

Fippel, M., Haryanto, F., Dohm, O., Nüsslin, F., and Kriesen, S., 2003. A virtual photon energy fluence model for Monte Carlo dose calculation. *Medical Physics*, 30(3), pp. 301–311.

Fix, M.K., Keall, P.J., Dawson, K. and Siebers, J.V., 2004. Monte Carlo source model for photon beam radiotherapy: photon source characteristics. *Medical physics*, *31*(11), pp.3106-3121.

Gullane, P.J., 1991. Primary mandibular reconstruction analysis of 64 cases and evaluation of interface radiation dosimetry on bridging plates. *Laryngoscope* 101(6 Pt. 2), pp.1–24.

Hankey, B.F., Feuer, E.J., Clegg, L.X., Hayes, R.B., Legler, J.M., Prorok, P.C., Ries, L.A., Merrill, R.M. and Kaplan, R.S., 1999. Cancer surveillance series: interpreting trends in prostate cancer—part I: evidence of the effects of screening in recent prostate cancer incidence, mortality, and survival rates. *Journal of the National Cancer Institute*, *91*(12), pp.1017-1024.

Hazuka, M.B., Ibbott, G.S. and Kinzie, J.J., 1988. Hip prostheses during pelvic irradiation: effects and corrections. *International Journal of Radiation Oncology* Biology* Physics*, *14*(6), pp.1311-1317.

Hazuka, M.B., Stroud, D.N., Adams, J., Ibbott, G.S. and Kinzie, J.J., 1993. Prostatic thermoluminescent dosimeter analysis in a patient treated with 18 MV X rays through a prosthetic hip. *International Journal of Radiation Oncology* Biology* Physics*, *25*(2), pp.339-343.

Heath, E. and Seuntjens, J., 2003. Development and validation of a BEAMnrc component module for accurate Monte Carlo modelling of the Varian dynamic Millennium multi leaf collimator. *Physics in medicine and biology*, *48*(24), p.4045.

Hendee, W.R., and Ritenour, E.R., 2002. *Medical imaging physics*. 4th ed. New York: Wiley-Liss, Inc. p120.

Hirayama, H., Namito. Y., Bielajew, A.F., *et al*., 2010. The EGS5 code system Stanford Linear Accelerator Centre. *Report SLAC-R-730*

Holzwarth, U. and Cotogno, G., 2012. Total Hip Arthroplasty: State of the art, prospects and challenges.

Hudson, F.R., Crawley, M.T. and Samarasekera, M., 1984. Radiotherapy treatment planning for patients fitted with prostheses. *The British journal of radiology*, *57*(679), pp.603-608.

IAEA, T., 2000. 398. Absorbed dose determination in external beam radiotherapy: An International Code of Practice for Dosimetry based on standards of absorbed dose to water. *Vienna International Atomic Energy Agency*.

ICRU, R.Q. and Units, I.C.R.U., 1980. Report 33. *Int. Comm. Radiation Units and Measurements, Washington DC*.

Johns, H.E., 1969. CUNNINGHAM JR: The Physics of Radiology. *Charles C. Thomas, Springfield, Ill*, p.457.

Kawrakow, I. and Rogers, D., 2000. The EGSnrc code system: Monte Carlo simulation of electron and photon transport.

Kawrakow, I., 2000. Accurate condensed history Monte Carlo simulation of electron transport. I. EGSnrc, the new EGS4 version. *Medical physics*, *27*(3), pp.485-498.

Keall, P.J., Siebers, J.V., Jeraj, R. and Mohan, R., 2003. Radiotherapy dose calculations in the presence of hip prostheses. *Medical Dosimetry*, *28*(2), pp.107-112.

Khan, F.M., 2003. The physics of radiation therapy, Third edition. Lippincott Williams and Wilkins, Philadelphia.

Khan, F.M., 2010. The Physics of Radiation Therapy, Third edition. Lippincott Williams and Wilkins, Philadelphia.

Khan, F.M., Potish, R.A., 1998. Treatment Planning in Radiation Oncology. *William & Wilkins, Baltimore*, pp. 369–386.

Kim, H.K., Han, S.J., Kim, J.L., Kim, B.H., Chang, S.Y. and Lee, J.K., 2006. Monte Carlo simulation of the photon beam characteristics from medical linear accelerators. *Radiation protection dosimetry*, *119*(1-4), pp.510-513.

Krstic, D., Nikezic, D., Markovic, V.M. and Vucic, D., 2012, September. Absorbed fractions in sensitive regions of human respiratory tract calculated by mcnp5/x software for electrons and beta particles due to radon progeny. In *Paper presented at the First East European Radon Symposium–FERAS*.

Kung, J.H., Reft, C., Jackson, W. and Abdalla, I., 2002. Intensity-modulated radiotherapy for a prostate patient with a metal prosthesis. *Medical Dosimetry*, *26*(4), pp.305-308.

Kurtz, S.M., Pruitt, L., Jewett, C.W., Crawford, R.P., Crane, D.J. and Edidin, A.A., 1998. The yielding, plastic flow, and fracture behaviour of ultra-high molecular weight polyethylene used in total joint replacements. *Biomaterials*, *19*(21), pp.1989-2003.

Kutcher G.J., Coia, L., Gillin, M., Hanson, W.F., Leibel S, Morton, R.J., Palta, J,R., Purdy, J.A., Reinstein, L.E., Svensson, G.K., *et al*., (1994). Comprehensive QA for radiation oncology: report of AAPM Radiation Therapy Committee Task Group 40. *Med Phys* 21:581–618

Landberg, T., Chavaudra, J., Dobbs, H.J., Hanks, G., Johansson, K.A., Möller, T. and Purdy, J., 1993. Prescribing recording and reporting photon beam therapy *ICRU Report*, *50*.

Laub, W.U. and Nüsslin, F., 2004. Monte Carlo dose calculations in the treatment of a pelvis with implant and comparison with pencil-beam calculations. *Medical Dosimetry*, *28*(4), pp.229-233.

Lin, S.Y., Chu, T.C., Lin, J.P. and Liu, M.T., 2002. The effect of a metal hip prosthesis on the radiation dose in therapeutic photon beam irradiations. *Applied radiation and isotopes*, *57*(1), pp.17-23.

Lye, J.E., 2012. *Monte Carlo evaluation of the dosimetric uncertainty in matched 6 MV Elekta and Varian linear accelerators*. Masters dissertation, RMIT University, Melbourne, Australia.

Ma, C.M. and Rogers, D., 2004. BEAMDP as a general-purpose utility.

Ma, C.M. and Rogers, D.W.O., 1995. BEAMDP user's manual. *NRC Report PIRS-0509 (D)*.

Ma, C.M., Li, J.S., Pawlicki, T., Jiang, S.B., Deng, J., Lee, M.C., Koumrian, T., Luxton, M. and Brain, S., 2002. A Monte Carlo dose calculation tool for radiotherapy treatment planning. *Physics in medicine and biology*, *47*(10), p.1671.

Ma, C.M., Pawlicki, T., Jiang, S.B., Li, J.S., Deng, J., Mok, E., Kapur, A., Xing, L., Ma, L. and Boyer, A.L., 2000. Monte Carlo verification of IMRT dose distributions from a commercial treatment planning optimization system. *Physics in medicine and biology*, *45*(9), p.2483.

Mackie, T.R., Scrimger, J.W. and Battista, J.J., 1985. A convolution method of calculating dose for 15-MV x rays. *Medical physics*, *12*(2), pp.188-196.

Martin, D.A., Hruby, G., Whitaker, M.K. and Foo, K.Y.M., 2012. Constrained-beam inverse planning for intensity-modulated radiation therapy of prostate cancer patients with bilateral hip prostheses. *Journal of medical imaging and radiation oncology*, *56*(6), pp.703-707.

Mayles, P., Nahum, A., Rosenwald, J. and Papanikolaou, N., 2008. Handbook of Radiotherapy Physics: Theory and Practice. *Medical Physics*, *35*(9), pp.4281-4281.

Mesbahi, A. and Nejad, F.S., 2007. Dose attenuation effect of hip prostheses in a 9-MV photon beam: commercial treatment planning system versus Monte Carlo calculations. *Radiation medicine*, *25*(10), pp.529-535.

Metcalfe, P., Hoban, P. and Kron, T., 1997. *The physics of radiotherapy X-rays from linear accelerators*. Medical Physics Publishing.

Metropolis, N., 1987. The beginning of the Monte Carlo method. *Los Alamos Science*, *15* (584), pp.125-130.

Mirza, S.B., Dunlop, D.G., Panesar, S.S., Naqvi, S.G., Gangoo, S. and Salih, S., 2010. Basic science considerations in primary total hip replacement arthroplasty. *The Open Orthopedics Journal*, 4:169-80.

Morin, R.L. and Raeside, D.E., 1982. Removal of streaking artifact in computed tomography. *Journal of medical systems*, *6*(4), pp.387-397.

Nedaie, H.A., Darestani, H., Banaee, N., Shagholi, N., Mohammadi, K., Shahvar, A. and Bayat, E., 2014. Neutron dose measurements of Varian and Elekta linacs by TLD600 and TLD700 dosimeters and comparison with MCNP calculations. *Journal of medical physics/Association of Medical Physicists of India*, *39*(1), p.10.

Nelson, W.R., Hirayama, H. and Rogers, D.W.O., 1985. The EGS4 code system Stanford Linear Accelerator Center. *Report SLAC-265*.

Park, J. and Lakes, R.S., 2007. *Biomaterials: an introduction*. Springer Science & Business Media.

Patra, S.R., Sinha, S.P., Mishra, S.C. and Mallick, B., 2014. X-Ray Fibre Diffraction Analysis of 6 MV Photon-Induced Mimosa pudica. *Advanced Science Letters*, *20*(3-4), pp.733-736.

Pianykh, O.S., 2009. *Digital imaging and communications in medicine (DICOM): a practical introduction and survival guide*. Springer Science & Business Media.

Pilliar, R.M., 2009. Metallic biomaterials. In *Biomedical materials* (pp. 41-81). Springer US.

Podgorsak, E.B., 2005. Radiation oncology physics. *A handbook for teachers and students/EB Podgorsak.–Vienna: International Atomic Energy Agency*, *657*.

Prabhakar, R., Kumar, M., Cheruliyil, S., Jayakumar, S., Balasubramanian, S. and Cramb, J., 2013. Volumetric modulated arc therapy for prostate cancer patients with hip prosthesis. *Reports of Practical Oncology & Radiotherapy*, *18*(4), pp. 209-213.

Rana, S.B. and Pokharel, S., 2014. A dosimetric study of volumetric modulated arc therapy planning techniques for treatment of low-risk prostate cancer in patients with bilateral hip prostheses. *South Asian journal of cancer*, *3*(1), p.18.

Reda, S.M., Massoud, E., Hanafy, M.S., Bashter, I.I. and Amin, E.A., 2006. Monte Carlo dose calculations for breast radiotherapy using 60Co gamma rays. *Journal of nuclear and radiation physics*, *1*(1), pp.61-72.

Reft, C., Alecu, R., Das, I.J., Gerbi, B.J., Keall, P., Lief, E., Mijnheer, B.J., Papanikolaou, N., Sibata, C. and Van Dyk, J., 2003. Dosimetric considerations for patients with HIP prostheses undergoing pelvic irradiation. Report of the AAPM Radiation Therapy Committee Task Group 63. *Medical physics*, *30*(6), pp.1162-1182.

Reynaert, N., Van der Marck, S.C., Schaart, D.R., Van der Zee, W., Van Vliet-Vroegindeweij, C., Tomsej, M., Jansen, J., Heijmen, B., Coghe, M.A.R.C. and De Wagter, C., 2007. Monte Carlo treatment planning for photon and electron beams. *Radiation Physics and Chemistry*, *76*(4), pp.643-686.

Robertson, D.D., Yuan, J., Wang, G. and Vannier, M.W., 1997. Total hip prosthesis metal-artifact suppression using iterative deblurring reconstruction. *Journal of computer assisted tomography*, *21*(2), pp.293-298.

Rogers, D., 2002. Monte Carlo techniques in radiotherapy. *Physics in Canada*, *58*(2), pp.63-70.

Rogers, D.W.O., Faddegon, B.A., Ding, G.X., Ma, C.M., We, J. and Mackie, T.R., 1995. BEAM: a Monte Carlo code to simulate radiotherapy treatment units. *Medical physics*, *22*(5), pp.503-524.

Rogers, D.W.O., Walters, B. and Kawrakow, I., 2001. BEAMnrc users manual. *NRC Report PIRS*, *509*.

Rogers, D.W.O., Walters, B. and Kawrakow, I., 2004. BEAMnrc users manual NRC Report PIRS 509 (a) revH. *Ionizing Radiation Standards (NRC, Ottawa, Ont, 2005)*.

Rosewall, T., Kong, V., Vesprini, D., Catton, C., Chung, P., Ménard, C. and Bayley, A., 2009. Prostate delineation using CT and MRI for radiotherapy patients with bilateral hip prostheses. *Radiotherapy and Oncology*, *90*(3), pp.325-330.

Sempau, J., Acosta, E., Baro, J., Fernández-Varea, J.M. and Salvat, F., 1997. An algorithm for Monte Carlo simulation of coupled electron-photon transport. *Nuclear Instruments and Methods in Physics Research Section B: Beam Interactions with Materials and Atoms*, *132*(3), pp.377-390.

Sibata, C.H., Mota, H.C., Higgins, P.D., Gaisser, D., Saxton, J.P. and Shin, K.H., 1990. Influence of hip prostheses on high energy photon dose distributions. *International Journal of Radiation Oncology* Biology* Physics*, *18*(2), pp.455-461.

Solberg, T.D., DeMarco, J.J., Chetty, I.J., Mesa, A.V., Cagnon, C.H., Li, A.N., Mather, K.K., Medin, P.M., Arellano, A.R. and Smathers, J.B., 2001. A review of radiation dosimetry applications using the MCNP Monte Carlo code. *Radiochimica Acta International journal for chemical aspects of nuclear science and technology*, *89*(4-5), p.337.

Su, A., Reft, C., Rash, C., Price, J. and Jani, A.B., 2005. A case study of radiotherapy planning for a bilateral metal hip prosthesis prostate cancer patient. *Medical Dosimetry*, *30*(3), pp.169-175.

Uushona, N.V., 2009. *The effect of silicone gel breast prosthesis on the electron beam dose distribution*. Master's dissertation, University of Limpopo, Medunsa, South Africa.

Walters, B., Kawrakow, I. and Rogers, D.W.O., 2005. DOSXYZnrc user's manual. *NRC Report PIRS*, *794*.

Wambersie, A. and Landgerg, T., 1999. ICRU Report 62: prescribing, recording and reporting photon beam therapy. *International Commission on Radiation Units and Measurements, Bethesda, USA: (supplement to ICRU Report 50)*.

Wang, G., Snyder, D.L., O'Sullivan, J.A. and Vannier, M.W., 1996. Iterative deblurring for CT metal artifact reduction. *Medical Imaging, IEEE Transactions on*, *15*(5), pp.657-664.

Waring, A., Melles, M., Goossens, R.H.M., Lancaster, J. and Vehmeijer, S.B.W., 2013, October. Development of a Tool for Component Positioning in THA Surgeries. In *DMD Europe 2013: Design of Medical Devices Conference-Europe Edition 2013, Delft, The Netherlands, 7-9 October 2013*.

Werner, B.L., Das, I.J. and Salk, W.N., 1990. Dose perturbations at interfaces in photon beams: secondary electron transport. *Medical physics*, *17*(2), pp.212-226.

Werner, B.L., Das, I.J., Khan, F.M. and Meigooni, A.S., 1987. Dose perturbations at interfaces in photon beams. *Medical physics*, *14*(4), pp.585-595.

Wieslander, E. and Knöös, T., 2003. Dose perturbation in the presence of metallic implants: treatment planning system versus Monte Carlo simulations. *Physics in medicine and biology*, *48*(20), p.3295.

Xu, X.G., Chao, T.C. and Bozkurt, A., 2000. VIP-Man: an image-based whole-body adult male model constructed from color photographs of the Visible Human Project for multi-particle Monte Carlo calculations. *Health Physics*, *78*(5), pp.476-486.

Zaidi, H., 1999. Relevance of accurate Monte Carlo modelling in nuclear medical imaging. *Medical Physics*, *26*(4), pp.574-608.

Zhan, L., Jiang, R. and Osei, E.K., 2012. Beam coordinate transformations from DICOM to DOSXYZnrc. *Physics in medicine and biology*, *57*(24), p.N513.

Zhang, L.C., Kiat, E.C.S. and Pramanik, A., 2009, October. A briefing on the manufacture of hip joint prostheses. In *Advanced Materials Research* (Vol. 76, pp. 212-216).

Zietz, C., Kluess, D., Bergschmidt, P., Haenle, M., Mittelmeier, W. and Bader, R., 2011, December. Tribological aspects of ceramics in total hip and knee arthroplasty. In *Seminars in Arthroplasty*, 22(4) pp. 258-263.

# Appendices

## A. Glossary

Biocompatibility – the capability of coexistence with living tissues or organisms without causing toxic, injurious, or immunological response in living tissue.

Dosimetry – the accurate measurement of doses, especially of radiation.

Half value layer – the thickness of the material at which the intensity of radiation entering it is reduced by 50%.

Interstitial brachytherapy – the radiation sources are placed directly in the target tissue of the affected site, such as the prostate or breast.

Osteoarthritis – a type of joint disease that results from breakdown of joint cartilage and underlying bone resulting in pain and stiffness. Also called wear–and–tear or degenerative arthritis.

Osteonecrosis – disease caused by inadequate blood supply to the ball portion of the hip joint leading to cellular death of bone components. Also knows as avascular necrosis, aseptic necrosis, bone infarction, or ischemic necrosis.

Phase space – an ideal space in which the coordinate dimensions represent the variables that are required to describe a system or substance.

Physiologically innocuous – not biologically harmful or offensive.

Prostheses – an artificial substitute for a missing body part, such as an eye, tooth or breast; used for functional or cosmetic reasons or both.

Radical prostatectomy – is a surgical procedure to remove the prostate gland and some of the tissue around it. It is done to remove prostate cancer.

Radiolucent – permitting the passage of radiant energy, such as x-rays, with little attenuation.

Radiopacity/radiodensity – the relative inability of electromagnetic radiation, particularly x-rays, to pass through a particular material.

Rheumatoid arthritis – a chronic progressive disorder caused by an overactive immune system, produces an inflammation type that can erode bone and cartilage and deform joints.

Tissue equivalent material – a substance with absorbing and scattering properties for a given radiation that sufficiently match those of a certain biological tissue.

Teletherapy – (also called external beam radiation therapy) is treatment in which the source of the therapeutic agent (such as radiation) is at a distance from the body.

# B. Elekta Precise linac specifications

## B.1 Linac head geometry

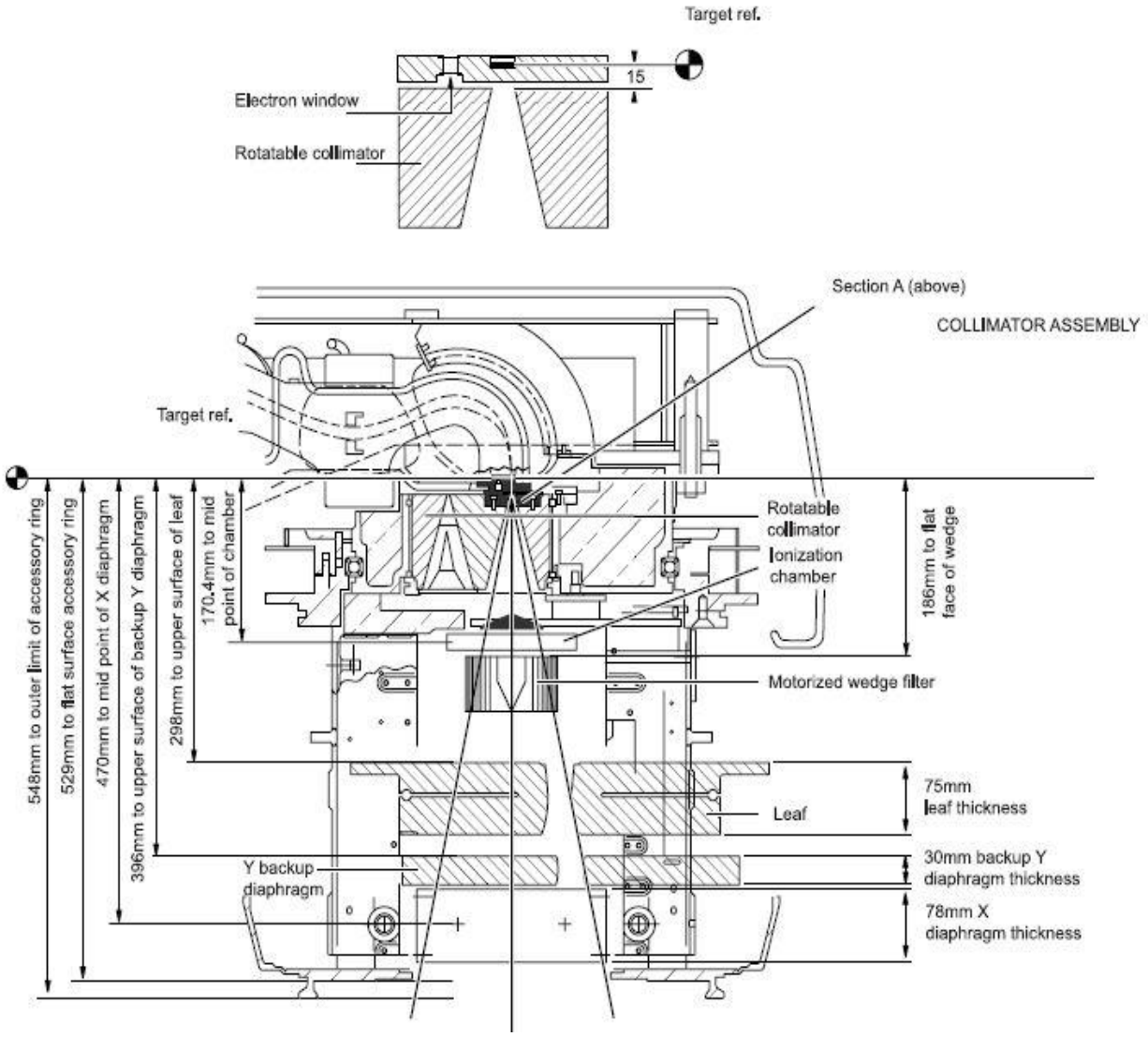


**Figure B.1:** Cross–sectional view of the Elekta Precise linac head components.

# B.2 Material composition

**Table B.1:** Compositions and densities of Elekta Precise linac components simulated

| *Linac head components* | *Elekta Precise* |
|---|---|
| Target | W/Re |
| Percentage | 90/10 |
| Density (g $cm^{-3}$) | 19.4 |
| Target cover | Cu |
| Percentage | 100 |
| Density (g $cm^{-3}$) | 8.96 |
| Primary collimator | W/Ni/Fe |
| Percentage | 95/3.75/1.25 |
| Density (g $cm^{-3}$) | 18.0 |
| Flattening filter | C/Si/Ni/Cr/Mn/Fe |
| Percentage | 0.15/0.85/9/18/2/70 |
| Density (g $cm^{-3}$) | 7.8 |
| Secondary collimator | Pb/Sb/W |
| Percentage | - |
| Density (g $cm^{-3}$) | 18 |

## Technical information

Number of MLC leaf pairs: 40

Leaf width: 1.0 cm

Leaf thickness: 7.5 cm

Leaf ends: rounded

# C. Codes

## C.1 FORTRAN code (*dcombine.f*)

```
c   dcombine.f
c   Code combines .3ddose files

    Integer IMAX,JMAX,KMAX,nfiles,nf
    Real dose(340,340,340),errors(340,340,340)
    Real xbound(340),ybound(340),zbound(340)
    Real dosecomb(340,340,340), errcomb(680,680,680)
    Real err(680,680,680)
    Character*60 fnam(40)

    write(*,*) 'Number of files to add:'
    read(*,*) nfiles

        do nf=1,nfiles

        write(*,*) 'Give name of file',nf,':'
        read(*,*) fnam(nf)

    Open(unit=12,file=fnam(nf),access='sequential',status='unknown')

        Read(12,*)IMAX,JMAX,KMAX

        Read(12,*)  (xbound(I),I=1,IMAX+1)
        Read(12,*)  (ybound(I),I=1,JMAX+1)
        Read(12,*)  (zbound(I),I=1,KMAX+1)

        Read(12,*)  (((dose(i,j,k),i=1,IMAX),j=1,JMAX),k=1,KMAX)
        Read(12,*)  (((errors(i,j,k),i=1,IMAX),j=1,JMAX),k=1,KMAX)

        write(*,*) nf,'succesfully read'

    Close(12)

    Do 110 i = 1, IMAX+1
    Do 210 j = 1, JMAX+1
    Do 310 k = 1, KMAX+1

    dosecomb(i,j,k) = dosecomb(i,j,k) + dose(i,j,k)
    err(i,j,k) = err(i,j,k)**2 + errors(i,j,k)**2

310 Continue
210 Continue
110 Continue

    enddo

    Do 410 i = 1, IMAX+1
    Do 510 j = 1, JMAX+1
    Do 610 k = 1, KMAX+1

    errcomb(i,j,k) = (sqrt(err(i,j,k))) / nfiles

610 Continue
510 Continue
410 Continue

    Open(unit=13,file='c_dose.3ddose',access='sequential',
     &  status='unknown')

        Write(13,*)IMAX,JMAX,KMAX

        Write(13,*)  (xbound(I),I=1,IMAX+1)
        Write(13,*)  (ybound(I),I=1,JMAX+1)
        Write(13,*)  (zbound(I),I=1,KMAX+1)

        write(13,*)  (((dosecomb(i,j,k),i=1,IMAX), j=1,JMAX),k=1,KMAX)

        write(13,*)  (((errcomb(i,j,k),I=1,IMAX),J=1,JMAX),K=1,KMAX)

    Close(13)

    write(*,*) 'Dose combined in file: c_dose.3ddose'

    End
```

Figure C.1: FORTRAN code to combine 3D dose files in a multiple-field set-up

## C.2 IDL code (*editegs4phantfile.pro*)

```
pro egs4phant,event
common block1,rho
common block2, med, region
common block3, dimxyz
common block4, xbound,ybound,zbound
common block11, tarx,tarz
common block12, cnt
common block21, angle
common block41, sliceindex
common block40, copyflag,x1arrow,y1arrow,x2arrow,y2arrow
common block47, nmed, media, estepe,medq,regq,rhoq
common block77, mask, medm
;
file = dialog_pickfile(/read,path = 'C:\Users\Medphys\Desktop\IDL_CODE',filter='*.egs4phant')
;
;*************************readegsphant***********************************
;* To read egs4phant data
;*****************************************************************************
;
dimxyz = intarr(3)
nmed = intarr(1)
rhor = fltarr(10000000)
estepe = fltarr(30)
newrhor = fltarr(300,300,300)
newregion = bytarr(300,300,300)
kindex = intarr(300)
fileindex = intarr(300)
;Open egsphantfile
xyouts, 0.7, 0.25,'Reading EGS4PHANT file',/normal
openr, 1, file, /get_lun
readf,1, nmed
media = strarr(nmed)
estepe = fltarr(nmed)                    ;number of media
readf,1, media
readf,1, estepe
readf,1, dimxyz
print, nmed
print, dimxyz
xbound = fltarr(dimxyz(0)+1)
ybound = fltarr(dimxyz(1)+1)
zbound = fltarr(dimxyz(2)+1)
med = bytarr(dimxyz(0),dimxyz(1),dimxyz(2))
mask = bytarr(dimxyz(0),dimxyz(1),dimxyz(2))
medq = bytarr(dimxyz(0))
medm = bytarr(dimxyz(0))
region = intarr(dimxyz(0),dimxyz(1),dimxyz(2))
regq = intarr(dimxyz(0))
rho = fltarr(dimxyz(0),dimxyz(1),dimxyz(2))
rhoq = fltarr(dimxyz(0))
space = strarr(1)
tarx = fltarr(3000)
tarz = fltarr(3000)
cnt = intarr(1)
;
readf,1, xbound
readf,1, ybound
readf,1, zbound
;print,xbound
;print,ybound
;print,zbound
voxsize = abs(xbound(1)-xbound(2))
voxyzize = abs(ybound(1)-ybound(2))
zvoxelsize = abs(zbound(1)-zbound(2))
;
;read in the media data
;
for k = 0, dimxyz(2)-1 do begin
for j = 0, dimxyz(1)-1 do begin
READF, 1, $
   FORMAT = '(300I1)', medq
for i = 0, dimxyz(0)-1 do begin
med(i,j,k) = medq(i)
endfor
endfor
```

```
readf,1,space
endfor
;readf,1,space
xyouts, 0.7, 0.2,'Completed reading media',/normal
;
;Reading in media density data
;
for k = 0, dimxyz(2)-1 do begin
for j = 0, dimxyz(1)-1 do begin
READF, 1, rhoq
for i = 0, dimxyz(0)-1 do begin
rho(i,j,k) = rhoq(i)
endfor
endfor
readf,1,space
endfor
;readf,1,space
xyouts,0.7, 0.15,'Completed reading media densities',/normal
;
;Reading in volumes to change media data of EGS4PHANT file.
;
for k = 0, dimxyz(2)-1 do begin
for j = 0, dimxyz(1)-1 do begin
READF, 1, $
   FORMAT = '(300I2)', medm
for i = 0, dimxyz(0)-1 do begin
mask(i,j,k) = medm(i)
;put Titanium in the mask
if (mask(i,j,k) eq 2) then begin
med(i,j,k) = nmed + 1
rho(i,j,k) = 4.50
endif
endfor
endfor
readf,1,space
endfor
;
xyouts,0.7, 0.1,'Completed reading mask data',/normal
;
;Now we display regions and media in one window and select slices with slider
;
win1=widget_base(title='image display selection',/column)
copyflag = 0
xslider = widget_slider(win1,min = 0, max = dimxyz(2),title = 'select slice',event_pro='showslice',xsize=350)
checkplan3 = widget_button(win1,value='write EGS4PHANT file',event_pro='egs4phantwrite')
widget_control,win1,/realize
state1 = {xslider:xslider}
widget_control, win1,set_uvalue=state1
free_lun,1
END

pro showslice,event
common block1, rho
common block2, med, region
common block3, dimxyz
common block4, xbound,ybound,zbound
common block5, res
common block6, slice
common block11, tarx,tarz
common block12, cnt
common block13, zslice
common block40, copyflag,x1arrow,y1arrow,x2arrow,y2arrow
common block41, sliceindex
common block47, nmed, media, estepe,medq,regq,rhoq
common block77, mask, medm
widget_control, event.top, get_uvalue = state1
widget_control, state1.xslider, get_value = slice
slice = round(slice)
zslice = slice
y = fltarr(10,3000)
z = fltarr(10,3000)
window,0,xsize = dimxyz(0)*2,ysize = dimxyz(1)*2
xs = dimxyz(0)*2 & ys = dimxyz(1)*2
result = congrid(rho(*,*,zslice) + med(*,*,zslice), dimxyz(0)*2, dimxyz(1)*2,/interp)
```

```
tvscl, result
xyouts, 0.1,0.7,string('z=',zbound(zslice))
end

pro egs4phantwrite,event
common block1, rho
common block2, med, region
common block3, dimxyz
common block4, xbound,ybound,zbound
common block5, res
common block6, slice
common block11, tarx,tarz
common block12, cnt
common block13, zslice
common block40, copyflag,x1arrow,y1arrow,x2arrow,y2arrow
common block41, sliceindex
common block47, nmed, media, estepe,medq,regq,rhoq
estepeout = fltarr(nmed+1)
common block77, mask, medm
wset,0
xyouts, 0.1, 0.25,'Writing EGS4PHANT file',/normal
file = 'C:\Users\Medphys\Desktop\IDL_CODE\newphantom.egs4phant'
openw, l, file, /get_lun
printf,l, nmed + 1
printf,l, media(0)
printf,l, media(1)
printf,l, media(2)
printf,l, media(3)
printf,l, media(4)
printf,l,'Ti700ICRU'
estepeout(*) = 1.0000
printf,l, estepeout
printf,l, dimxyz
printf,l, format = '(300(f7.3," "))',xbound
printf,l, format = '(300(f7.3," "))',ybound
printf,l, format = '(800(f7.3," "))',zbound
;
;writing media data
;
for k = 0, dimxyz(2)-1 do begin
for j = 0, dimxyz(1)-1 do begin
for i = 0, dimxyz(0)-1 do begin
medq(i) = med(i,j,k)
endfor
printf, l, $
   FORMAT = '(300I1)', medq
endfor
printf,l,' '
endfor
;
xyouts, 0.2, 0.2,'Completed writing media',/normal
;
;Reading in media density data
;
for k = 0, dimxyz(2)-1 do begin
for j = 0, dimxyz(1)-1 do begin
for i = 0, dimxyz(0)-1 do begin
rhoq(i) = rho(i,j,k)
endfor
printf,l,format='(300(f8.2," "))',rhoq
endfor
printf,l,' '
endfor
;
xyouts,0.3, 0.15,'Completed writing media densities',/normal
;
;Reading in DVH regions of interest
;
for k = 0, dimxyz(2)-1 do begin
for j = 0, dimxyz(1)-1 do begin
for i = 0, dimxyz(0)-1 do begin
regq(i) = region(i,j,k)
endfor
printf,l,format='(300(I1," "))',regq
```

```
endfor
printf,1,' '
endfor
;
xyouts,0.4, 0.1,'Completed writing region data',/normal
xyouts,0.3, 0.1,'Completed writing EGS4PHANT file',/normal

end

pro exit,event
widget_control,event.top,/destroy
exit
end

pro editegs4phantfile
common block1,rho
common block5, res
temp = strarr(2)
temp(0) = 'nul'
res = intarr(2)
res = get_screen_size()
nocompflag = 0
opencheck = 0

windows1=widget_base(title='Edit EGS-PHANT v1.0',mbar=menu,/column)
drw = widget_draw(windows1, xsize=res(0),ysize=0.7*res(1))
checkplan = widget_button(menu,value='file')
checkplan3 = widget_button(checkplan,value='open egs4phant file',event_pro='egs4phant')
checkplan2 = widget_button(menu,value='exit',event_pro='exit')
checkplan4 = widget_button(checkplan2,value='exit',event_pro='exit')
widget_control,drw,/realize
xmanager,'Complanner v1.0', windows1
end
```

**Figure C.2:** IDL code to modify material density information in a phantom

# D. Measured dose values

The graphs below (figures D.1 to D.10) show the measured DPs and PDD data for photon beams of various energies and field size in a WT irradiated with an Elekta Prec*i*se linac head at 100 cm SSD.

## D.1 6 MV 5 × 5 cm² dose profile @ z = 5 cm

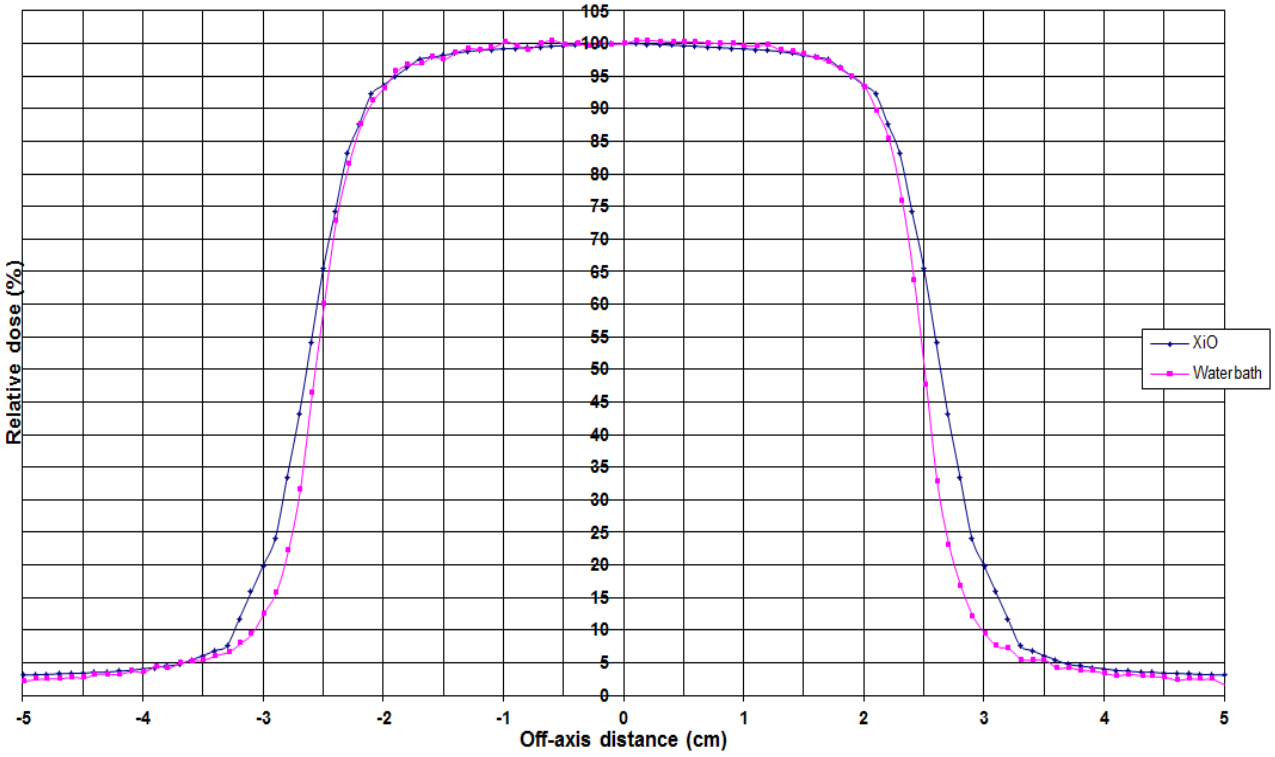


**Figure D.1:** Measured profiles at z = 5 cm for a 6 MV beam & 5 × 5 cm$^2$ FS.

## D.2 6 MV 10 × 10 cm² dose profile @ z = 10 cm

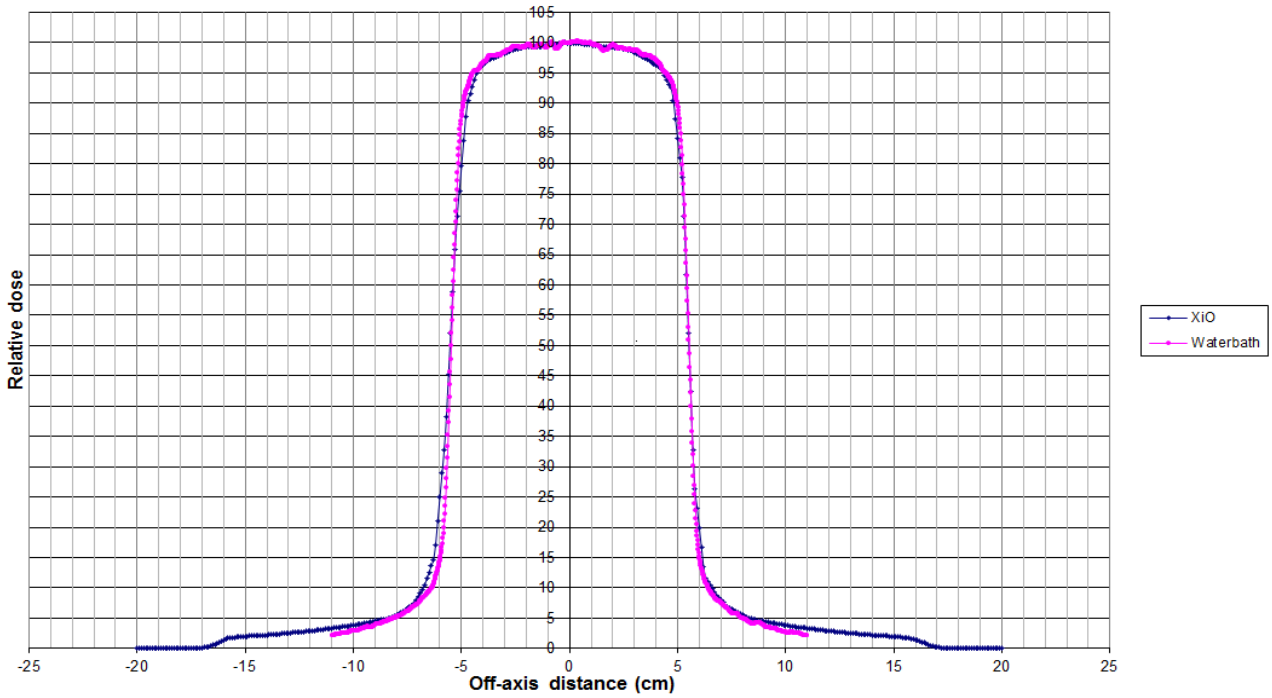


**Figure D.2:** Measured profiles at z = 10 cm, energy 6 MV & 10 × 10 cm$^2$ FS

## D.3 6 MV 10 × 10 cm² dose profile @ z = 20 cm

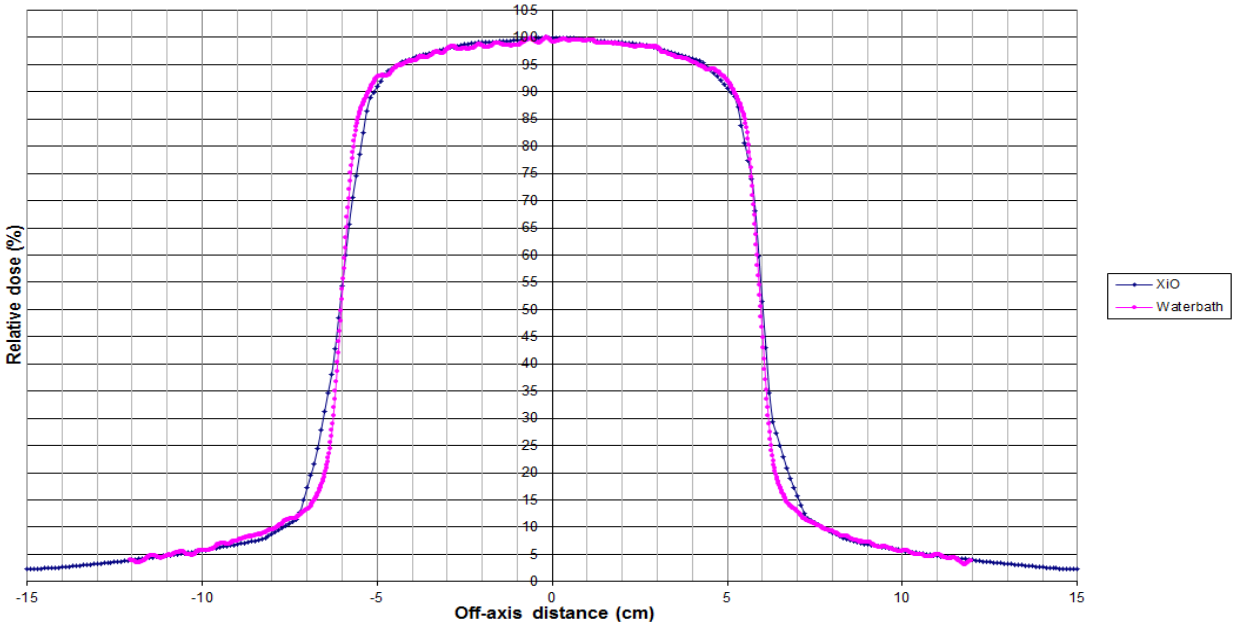


**Figure D.3:** Measured profiles at z = 20 cm for 6 MV beam & 10 × 10 cm$^2$ FS

## D.4 6 MV 10 × 10 cm² dose profile @ z = $d_{max}$

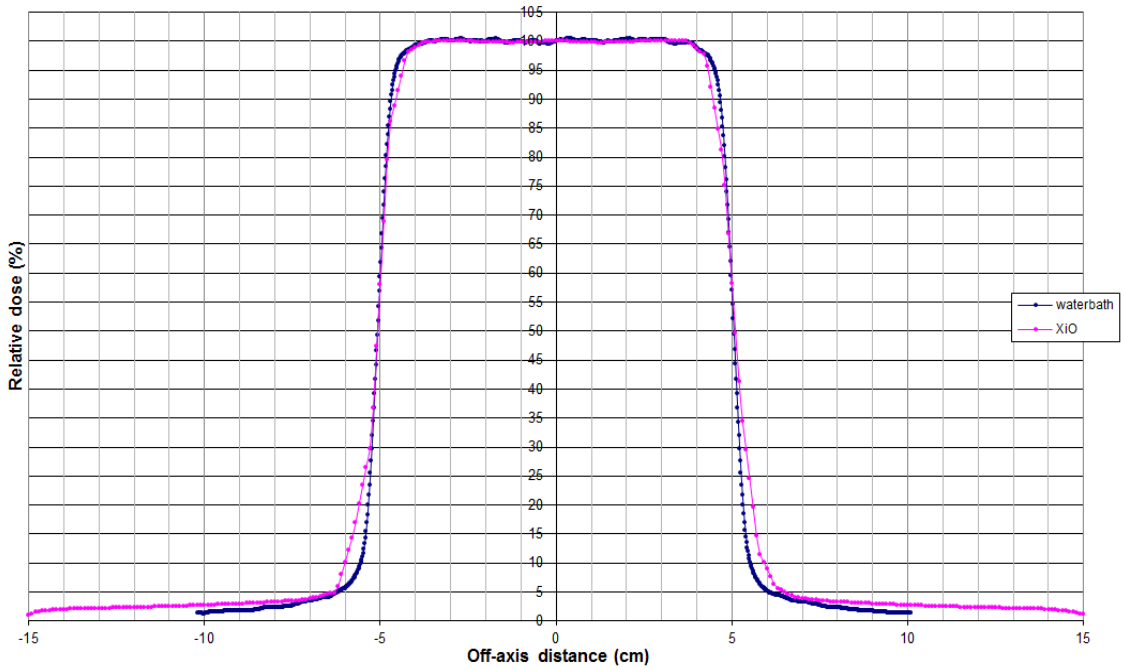


**Figure D.4:** Measured profiles at z = $d_{max}$ for a 6 MV beam at 10 × 10 cm² FS

## D.5 15 MV 10 × 10 cm² dose profile @ z = 10 cm

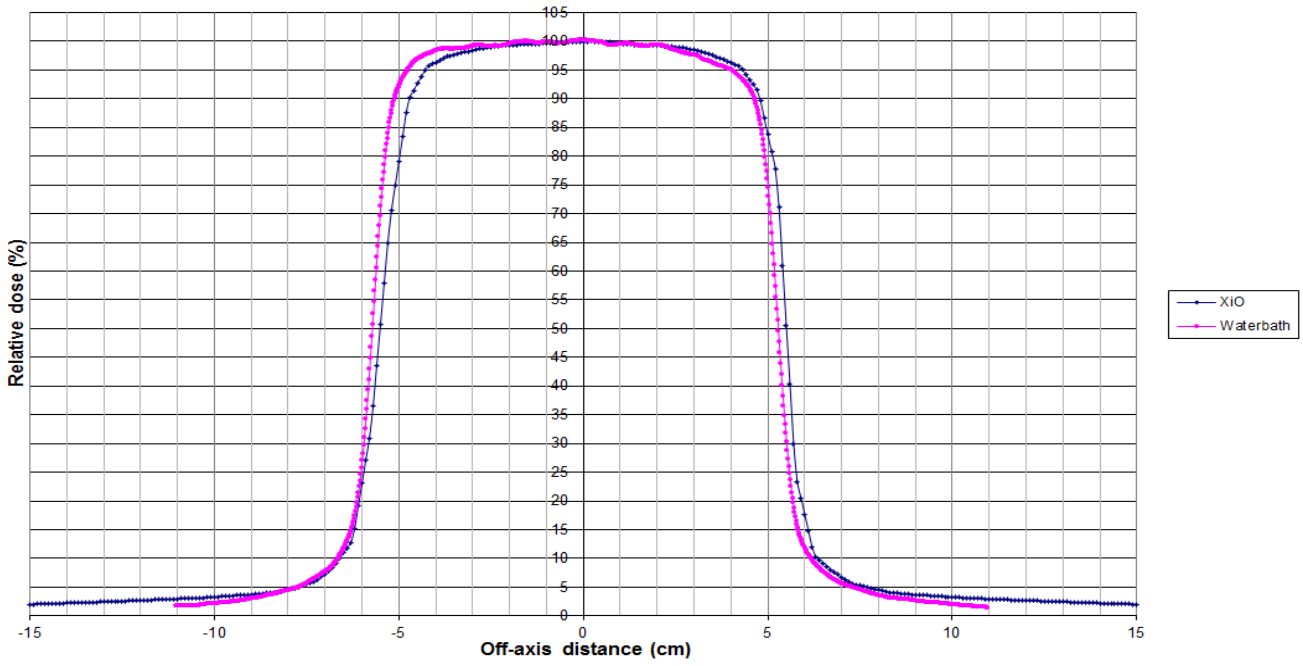


**Figure D.5:** Measured profiles at z = 10 cm, energy 15 MV & 10 × 10 cm² FS

## D.6 15 MV 10 × 10 cm² dose profile @ z = 20 cm

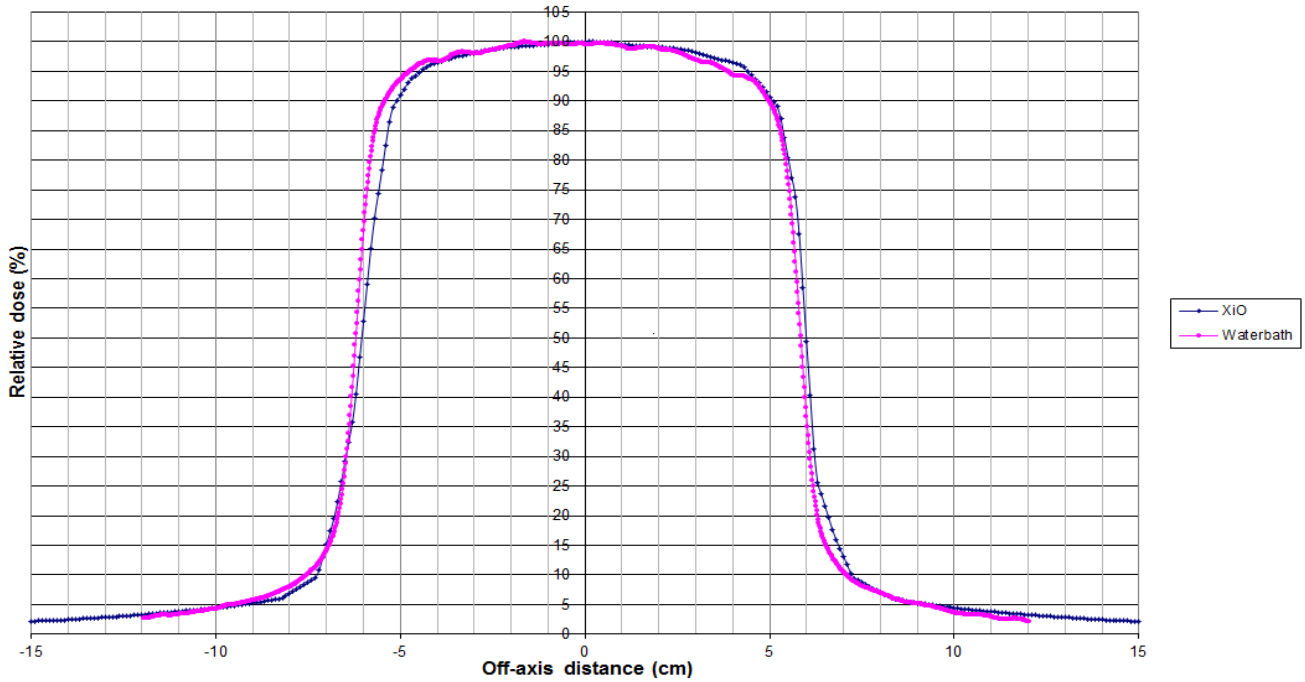


**Figure D.6:** Measured profiles at z = 20 cm, energy 15 MV & 10 × 10 cm² FS

## D.7 15 MV 10 × 10 cm² dose profile @ z = $d_{max}$

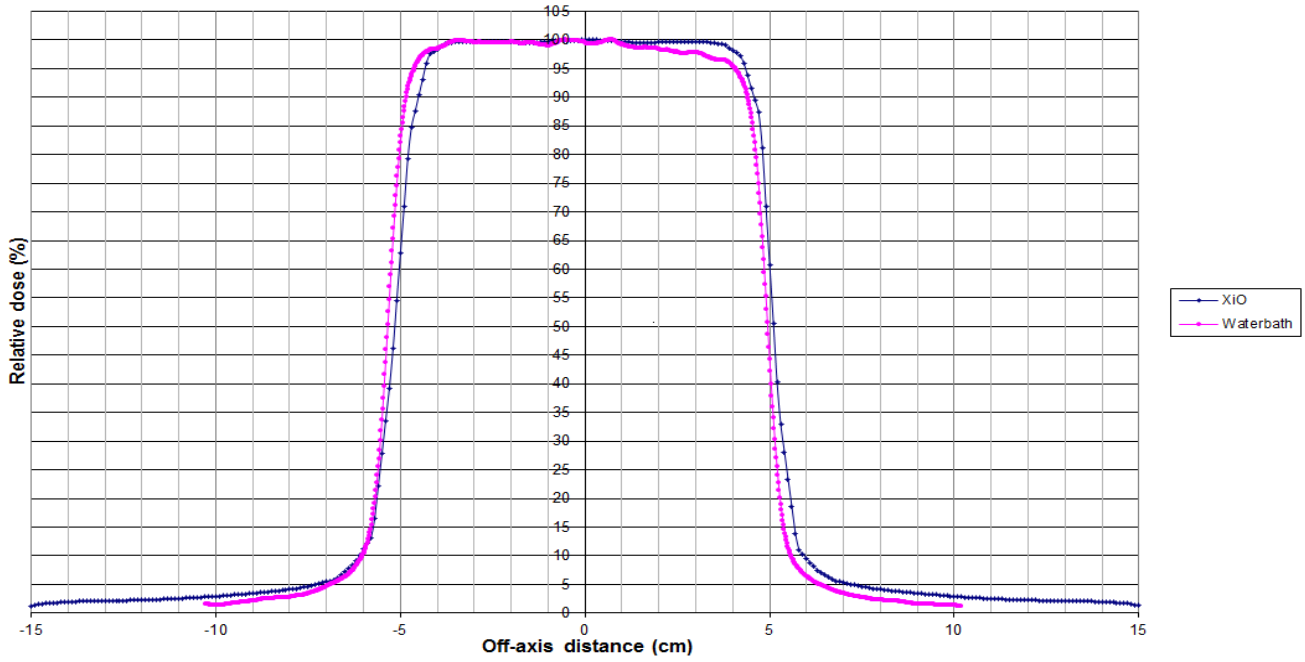


**Figure D.7:** Measured profiles at z = $d_{max}$, energy 15 MV & 10 × 10 cm$^2$ FS

## D.8 6 MV 5 × 5 cm² CAX PDD curves

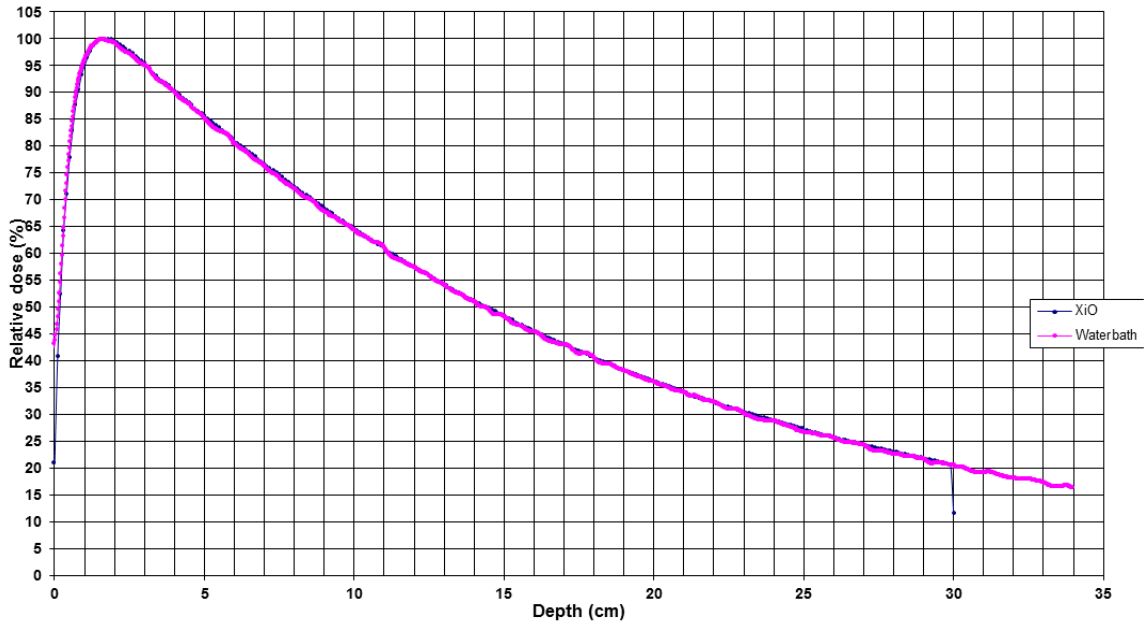


**Figure D.8:** Measured CAX PDD curves in a WT at 6 MV and 5 × 5 cm$^2$ FS

## D.9 6 MV 10 × 10 cm² CAX PDD curves

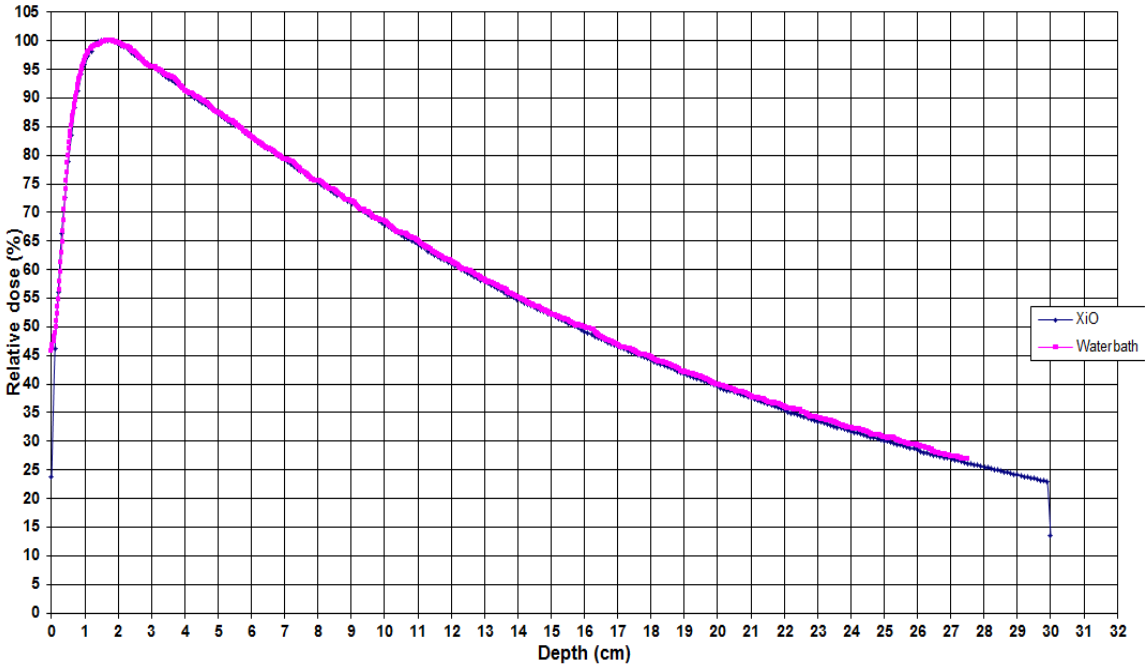


**Figure D.9:** Measured CAX PDD curves for a 6 MV beam at 10 × 10 cm$^2$ FS

## D.10 15 MV 10 × 10 cm² CAX PDD curves

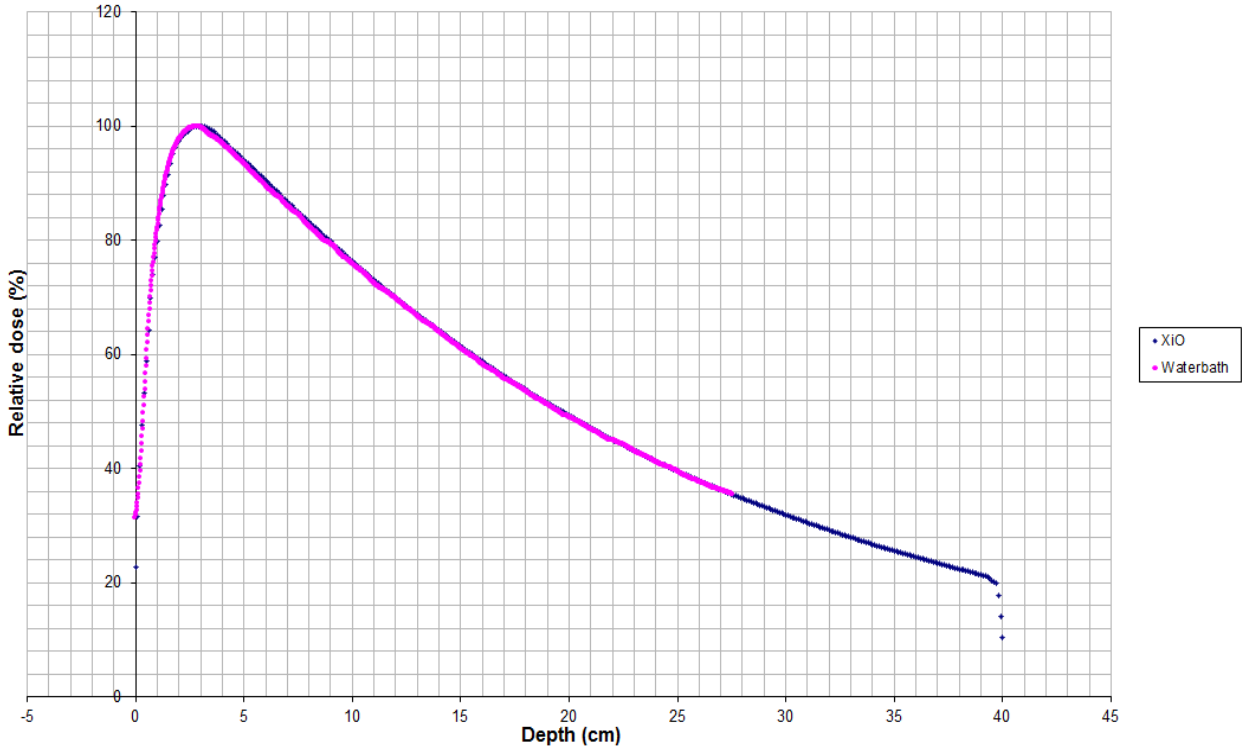


**Figure D.10:** Measured CAX PDD curves for 15 MV beam and 10 × 10 $cm^2$ FS

## D.11 Comparisons between MC and WT measurements

MC–simulated and measured dose profile and CAX PDD plots were also compared to validate the photon beam emanating from the linac head. It can be observed that simulated and measured values agree within reasonable limits, except near the beam edges where the measured profile slightly underestimates the dose. This might be due to limitations of film dosimetry or the voxel–size effect in MC simulations at beam edges. Some of the comparisons are shown in figure D.11-D.19 and table D.1.

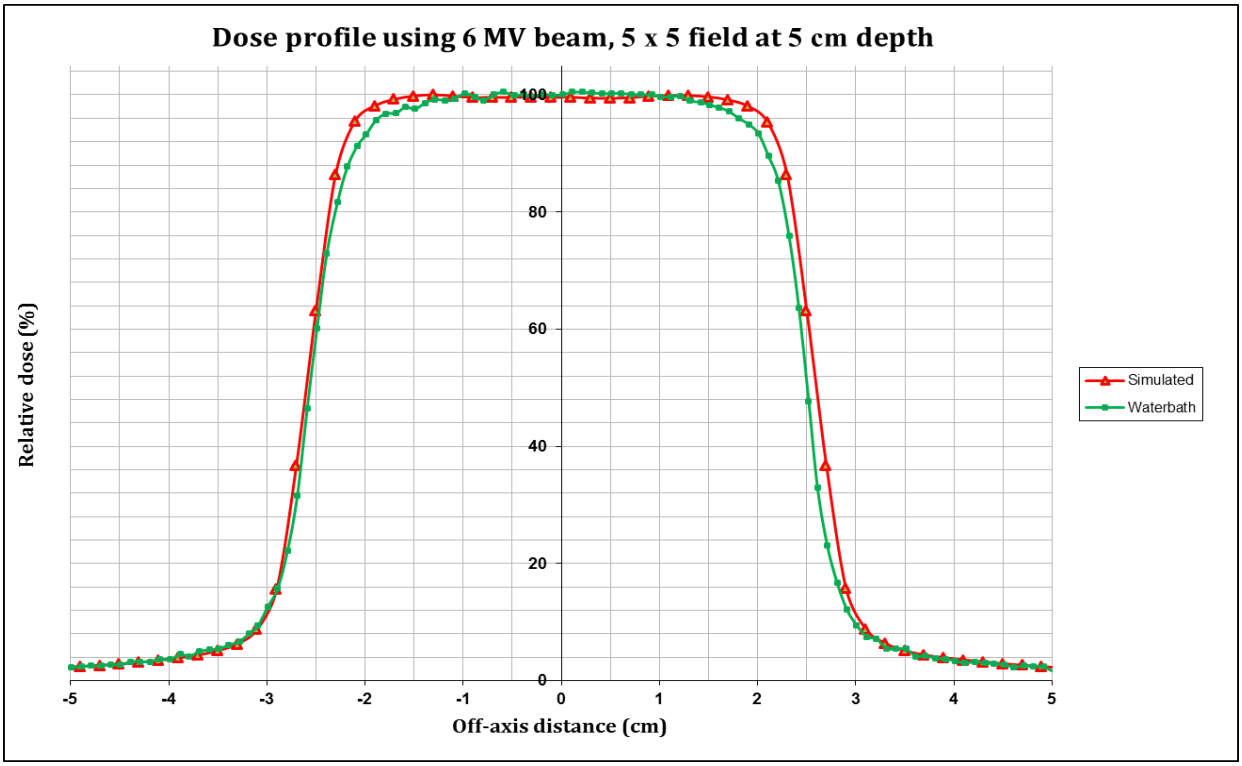


**Figure D.11:** MC & measured DPs at 6 MV, z = 5 cm and 5 x 5 FS

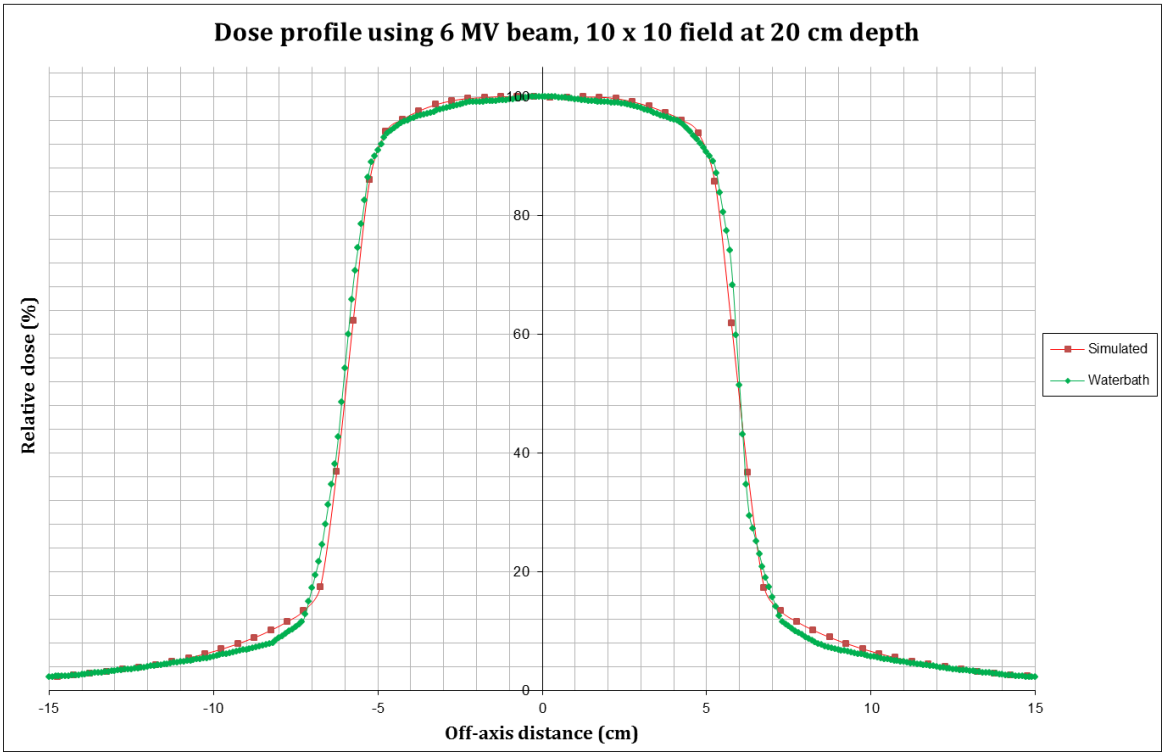


**Figure D.12:** MC & measured DPs at 6 MV using 10 x 10 FS at z = 20 cm

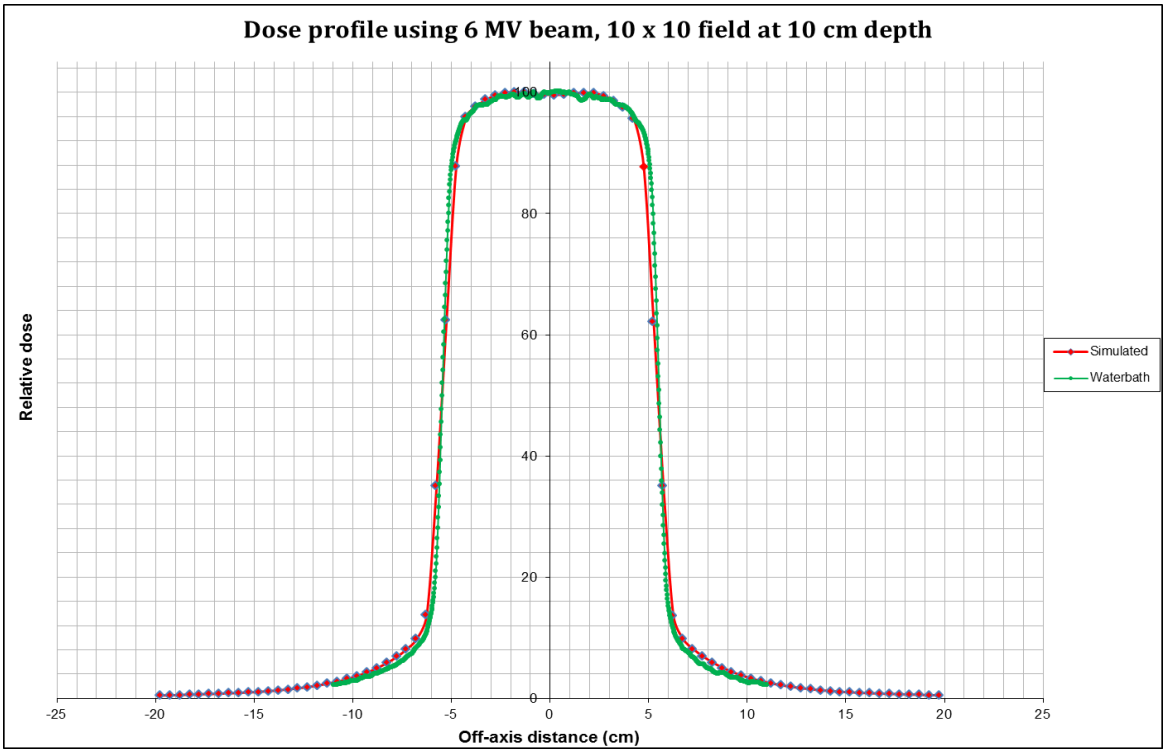


**Figure D.13:** MC & measured DPs at 6 MV using 10 x 10 FS at z = 10 cm

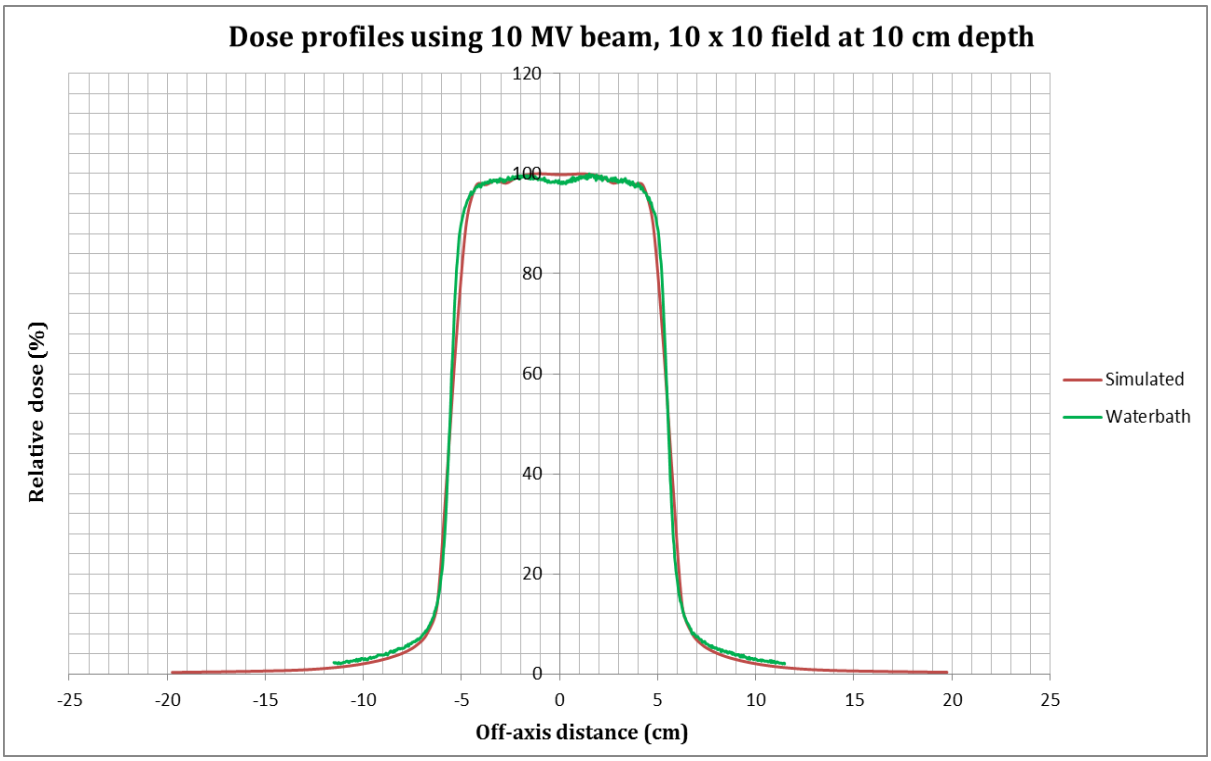


**Figure D.14:** MC & measured DPs at 10 MV using 10 x 10 FS at z = 10 cm

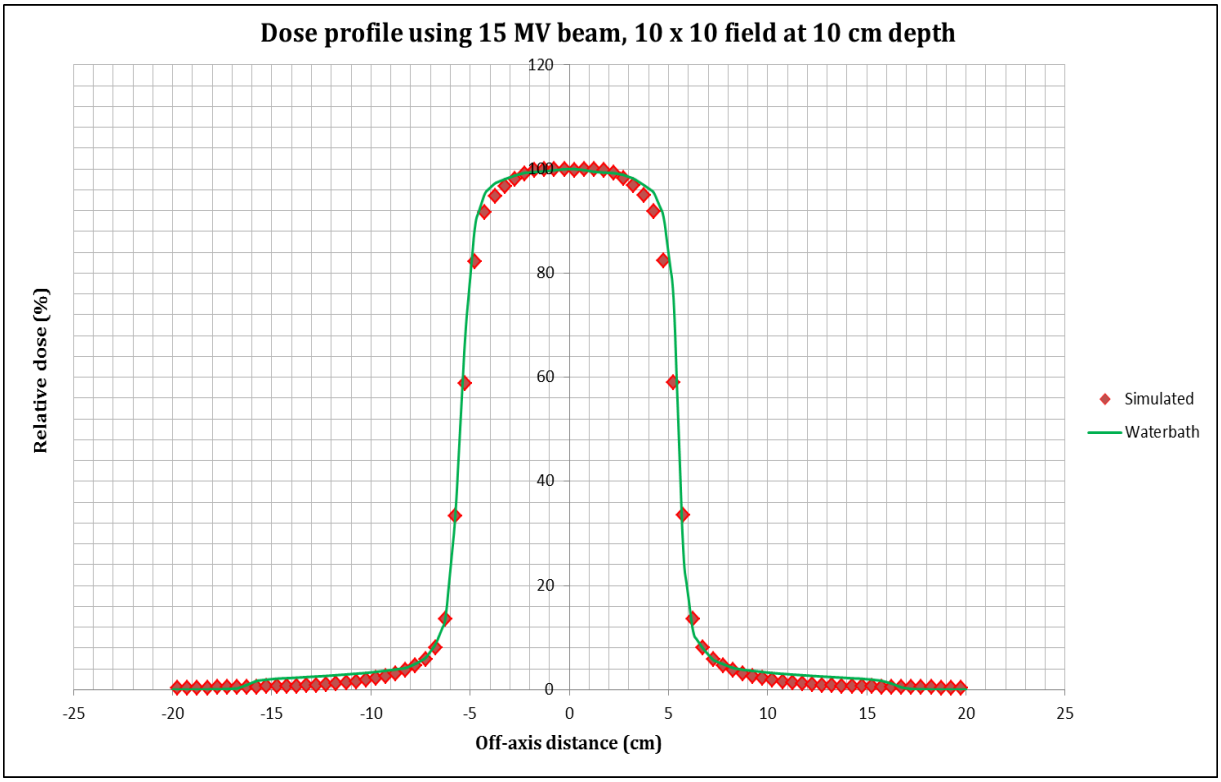


**Figure D.15:** MC & measured DPs at 15 MV using 10 x 10 FS at z = 10 cm

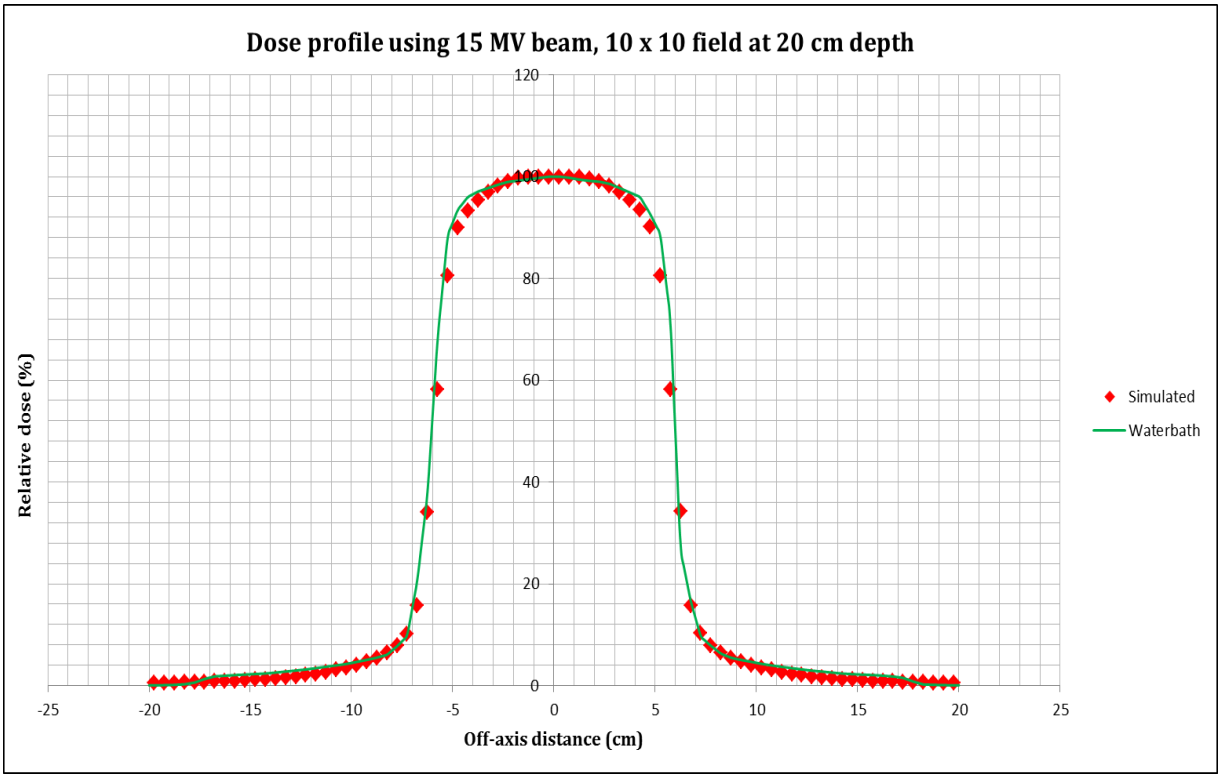


**Figure D.16:** MC & measured DPs at 15 MV using 10 x 10 FS at z = 20 cm

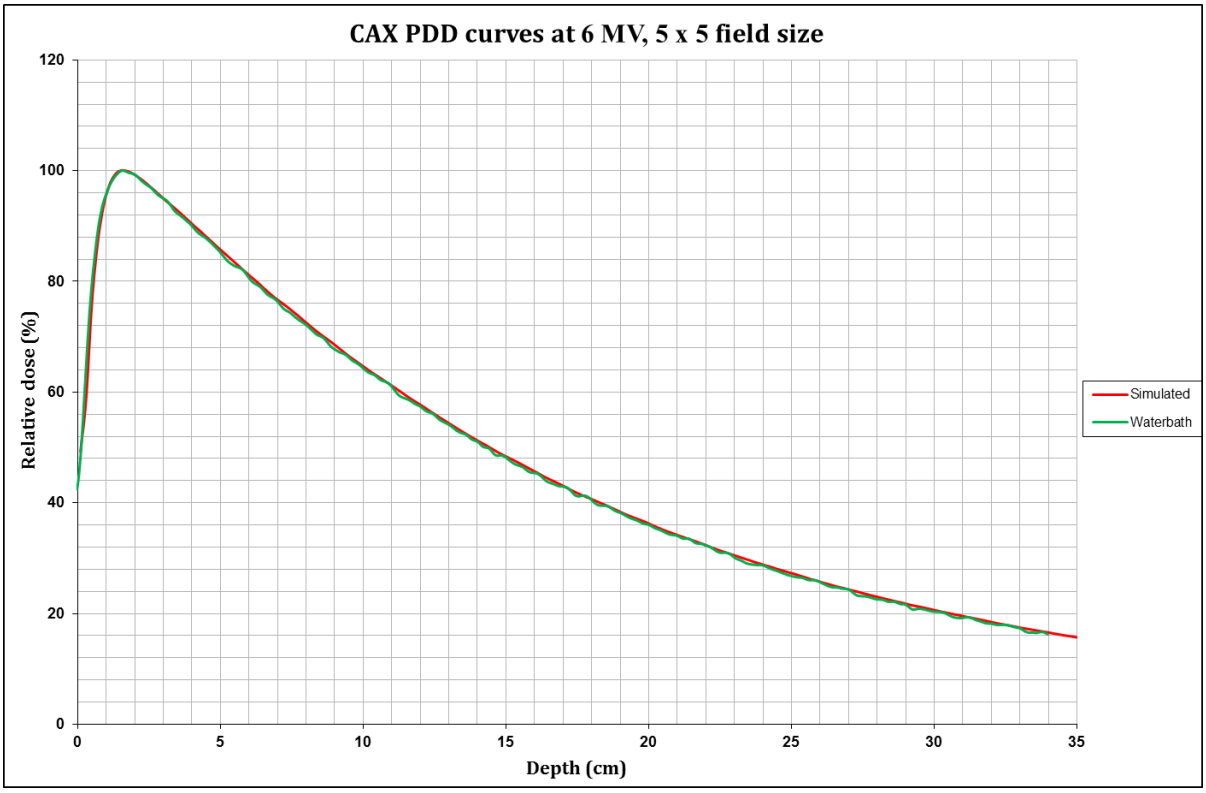


**Figure D.17:** MC & Simulated CAX PDD curves at 6 MV and 5 x 5 FS compared

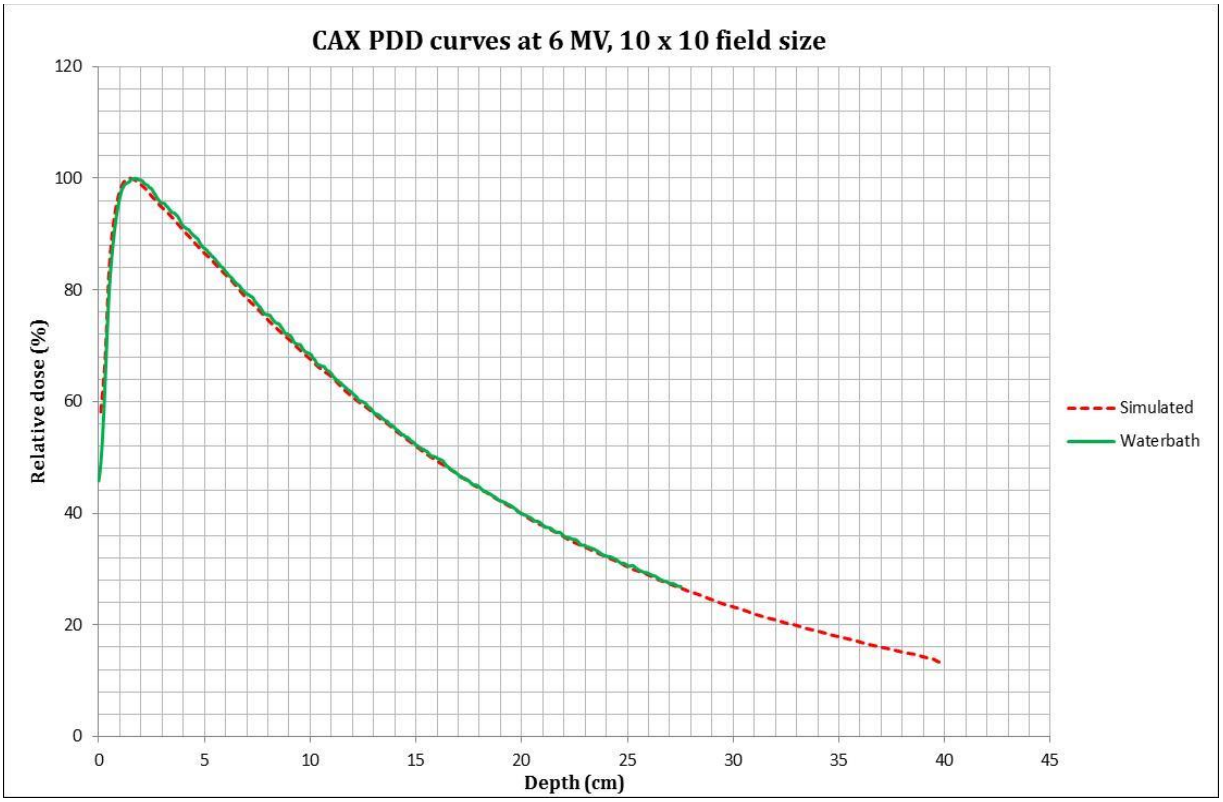


**Figure D.18:** MC & Simulated CAX PDD curves at 6 MV and 10 x 10 FS compared

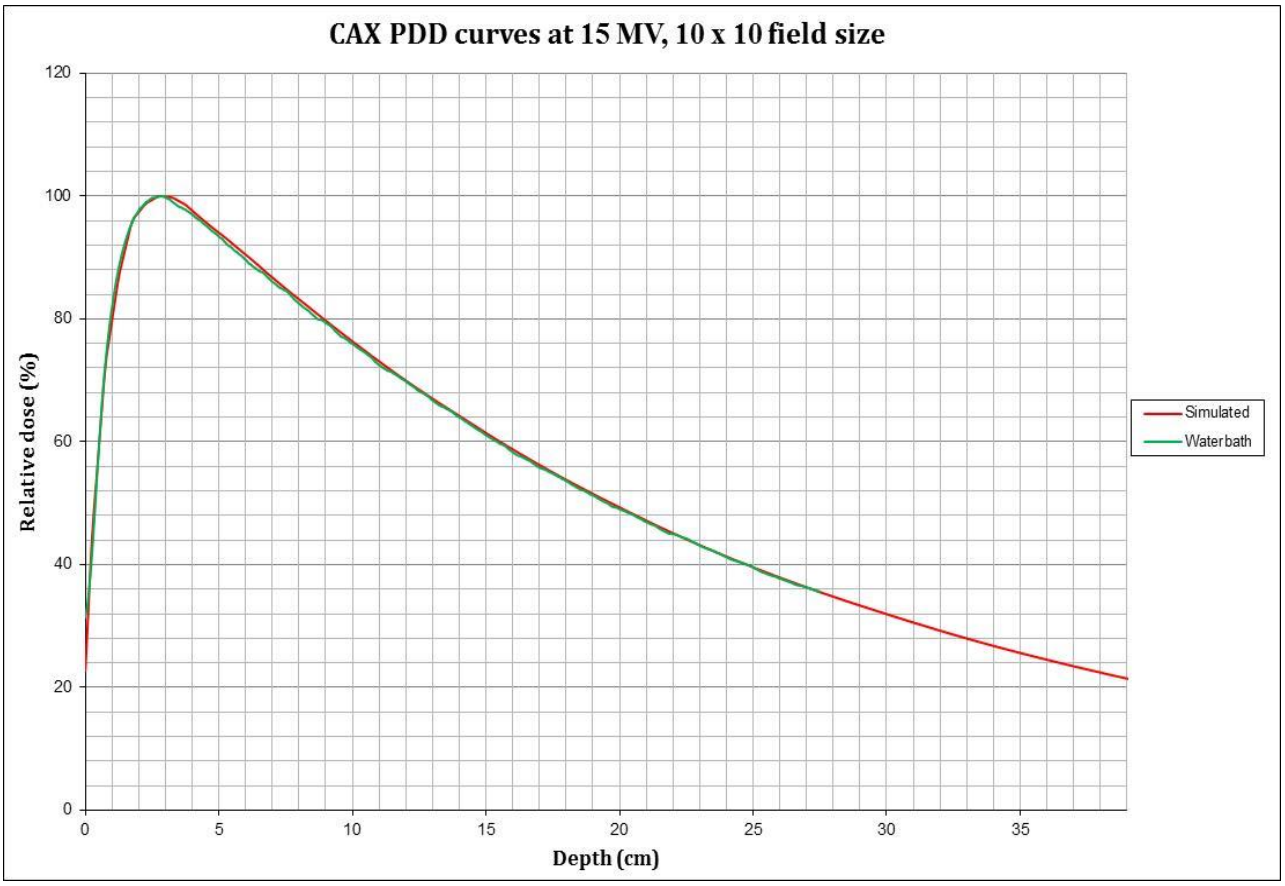


**Figure D.19:** MC & Simulated CAX PDD curves at 15 MV and 10 x 10 FS compared

**Table D.1:** Depth dose comparisons between simulated & measured data

| Energy (MV) | $d_{max}$ (cm) | | (%) | $PDD_{10}$ (%) | | % |
|---|---|---|---|---|---|---|
| | Simulated | Measured | Difference | Simulated | Measured | Difference |
| 6 | 1.7 | 1.7 | 0.0 | 67.4 | 67.8 | 0.6 |
| 10 | 2.5 | 2.5 | 0.0 | 73.8 | 73.2 | 0.8 |
| 15 | 2.9 | 3.0 | 3.4 | 76.5 | 76.4 | 0.1 |

The above comparisons of MC and measured depth dose values were also performed to ensure that the BEAMnrc linac model accurately represents the physical unit. All beams were $10 \times 10$ cm$^2$ in field size.